CANADIAN THESES ON MICROFICHE

I.S.B.N.

THESES CANADIENNES SUR MICROFICHE

National Library of Canada
Collections Development Branch

Canadian Theses on
Microfiche Service

Ottawa, Canada
K1A 0N4

Bibliothèque nationale du Canada
Direction du développement des collections

Service des thèses canadiennes
sur microfiche

NOTICE

The quality of this microfiche is heavily dependent upon the quality of the original thesis submitted for microfilming. Every effort has been made to ensure the highest quality of reproduction possible.

If pages are missing, contact the university which granted the degree.

Some pages may have indistinct print especially if the original pages were typed with a poor typewriter ribbon or if the university sent us a poor photocopy.

Previously copyrighted materials (journal articles, published tests, etc.) are not filmed.

Reproduction in full or in part of this film is governed by the Canadian Copyright Act, R.S.C. 1970, c. C-30. Please read the authorization forms which accompany this thesis.

THIS DISSERTATION
HAS BEEN MICROFILMED
EXACTLY AS RECEIVED

AVIS

La qualité de cette microfiche dépend grandement de la qualité de la thèse soumise au microfilmage. Nous avons tout fait pour assurer une qualité supérieure de reproduction.

S'il manque des pages, veuillez communiquer avec l'université qui a conféré le grade.

La qualité d'impression de certaines pages peut laisser à désirer, surtout si les pages originales ont été dactylographiées à l'aide d'un ruban usé ou si l'université nous a fait parvenir une photocopie de mauvaise qualité.

Les documents qui font déjà l'objet d'un droit d'auteur (articles de revue, examens publiés, etc.) ne sont pas microfilmés.

La reproduction, même partielle, de ce microfilm est soumise à la Loi canadienne sur le droit d'auteur, SRC 1970, c. C-30. Veuillez prendre connaissance des formules d'autorisation qui accompagnent cette thèse.

LA THÈSE A ÉTÉ
MICROFILMÉE TELLE QUE
NOUS L'AVONS REÇUE

NL-339 (r. 82/08)

Canada

VALLEYS AND PEAKS IN HYSTERESIS LOSSES IN TYPE II SUPERCONDUCTORS IN THE COLLINEAR AND NONCOLLINEAR REGIMES

Jean-Pierre Lorrain

Dissertation submitted to the School of Graduate Studies of the University of Ottawa in partial fulfillment of the requirements for the degree

Doctor of Philosophy

1982

DEDICACE

A Gaëtan et Ida.

REMERCIEMENTS

J'aimerais remercier Dr. Marcel LeBlanc, directeur de thèse, pour son excellente supervision, pour son intérêt et pour son encouragement lors de la réalisation de ce travail de recherche.

Je voudrais aussi souligner tout particulièrement le travail admirable, qui passe souvent inaperçu, de Robert Hart, de Ronald Lavigueur et de Léonard Pément qui ont machiné la plupart des pièces nécessaires à l'accomplissement de ce projet.

Et finalement, j'aimerais exprimer toute ma reconnaissance à Mme Lorraine Johnston pour la qualité de son travail et aussi pour la rapidité avec laquelle elle a dactylographié cette thèse.

Ce projet fut réalisé grâce au support du Conseil National des Recherches du Canada.

PENSEES A RETENIR

Ce qui vaut la peine d'être fait, mérite d'être bien fait.

Un événement est aussi important que l'importance qu'on lui accorde.

Alors, est-ce vraiment SI important ...

NOTES

On the door to success it says "push" and "pull".

All men are ordinary: The extraordinary men are those who know it.

We admire the wisdom of people who come to us for advice.

It is better to ask some of the questions than to know all of the answers.

ABSTRACT

Magnetic phenomena and hysteresis losses in ribbons of VTi and Nb subjected to a slowly time varying magnetic field of amplitude h_o directed transverse or tilted with respect to a stationary magnetic field, H_{static}, have been extensively investigated. This arrangement is denoted the noncollinear regime and involves a novel process known as flux cutting. Both h_o and H_{static} are oriented along the broad faces of the ribbon and h_o lies either along the length or the width of the ribbon. The flux configurations and the energy dissipation are determined by monitoring $\langle B_{//} \rangle$ and $\langle B_{\perp} \rangle$, the spatial averages of the magnetic induction threading the ribbon along its length and width, continuously and separately.

The suggestion of Campbell and Evetts that vortices retain their angle of creation as they undergo displacements, compression and decompression, is pursued in detail for a variety of initial magnetic states exploiting standard approximations for the gradient of the flux density including the force free case. Comparison with observations and other considerations show that the concept is not valid.

Extensive data on hysteresis losses, $W(h_o, H_b, H_{//}$ (or $H_{\perp}))$ versus $H_{//}$ (or $H_{\perp}$) for various H_b are presented for the VTi and Nb samples where H_b is the component of H_{static} which lies along h_o, $H_{//}$ and $H_{\perp}$ are orthogonal to h_o and directed along the length and width of the ribbon. Also representative curves of $\langle B_{//} \rangle$ and $\langle B_{\perp} \rangle$ as the time varying magnetic field oscillates over various amplitudes in different H_b and $H_{//}$ (or $H_{\perp}$) are displayed. Deep valleys are observed for W

versus $H_{//}$ (or $H_{\perp}$) for full-wave oscillations ($H_b = 0$) and half-wave oscillations ($H_b = h_o$).

The double critical state concept proposed by Lachaine is applied to the analysis of this vast assortment of results. This idea stipulates that the gradients for the flux density, B(x), and of the spatial variation of the orientation of the flux sheets, $\theta(x)$, are in critical states described by $dB/dx = \pm F_p(B)/B$ and $d\theta/dx = \pm f(B)\, F(\theta)$ where $F_p(B)$ is a bulk pinning function characterizing the sample. Basic cases of this general concept are developed. Specifically, (i) the electrodynamic model where B(x) along the stationary $H_{//}$ (or $H_{\perp}$) is taken as uniform and constant, hence $d\theta/dx = \pm k\, F_p/B^2 \tan\theta$ and (ii) the Boyer model, where $F(\theta) = k$ and $f(B) = F_p(B)/B^2$. Guided by the comparison of these calculations with the data on W, we are led to explore the form $F(\theta) = k/(1 + |\theta|)^2$ and find that this yields the best agreement with all of our observations.

A valley in W vs. H_b for various h_o is observed for the VTi ribbon in the classical collinear regime where only h_o and H_b are present. Invoking only bulk pinning hence neglecting the surface step, and applying the established critical state concept, these data are well reproduced taking $dB/dx = \pm \alpha/B^{1/2}$. In view of the success of this approach we investigate the predictions of three basic approximations, namely $dB/dx = \pm\alpha$, $\pm \alpha/B$ and $\pm \alpha(1 - B/B_{c2})$ for both infinite slab and cylinder geometry on the structure of the valley and the evolution of its minimum as a function of H_b, in the simple framework where the surface step is ignored.

The effect of a B independent surface step (surface barrier)

on hysteresis losses in the collinear regime is investigated computationally. A complete picture of the influence of the surface step is developed by examining a matrix of sixteen cases constructed by considering (i) two radically different types of surface barriers (symmetric and asymmetric), (ii) infinite slab and cylinder geometry, (iii) the basic and extremal approximations $dB/dx = \pm\alpha$ and $\pm\alpha/B$ and (iv) full-wave ($H_b = 0$) and half-wave oscillations ($H_b = h_o$). In all cases, the behaviour is scanned over a broad range of h_o, extending from weak penetration to far beyond full penetration. We find the remarkable result that in many instances reducing the barrier will also reduce the losses.

In the four appendices a large number of new analytic expressions are derived and presented for many of the various situations which are addressed in the body of the thesis.

TABLE OF CONTENT

CHAPTER 1

INTRODUCTION: HYSTERETIC EFFECTS AND LOSSES IN TYPE II SUPERCONDUCTORS

1.1 BACKGROUND REMARKS

Hysteresis losses in type II superconductors has been a subject of continuing interest for theoreticians and experimentalists during the last two decades. This is illustrated by the partial enumeration of references in the bibliography of this thesis (A). This phenomenon has attracted the interest of researchers because of the insight and information it provides on the interaction on a macroscopic scale of flux vortices with various pinning sites in the body or bulk of the material and on the role of surfaces of different degrees of geometric perfection and physical condition in opposing the entry or exit of flux from the specimens.

These investigations also received some impetus because of their importance to applications of these materials in situations where the magnetic field has to vary. For instance, in accelerators, storage rings and experimental halls constructed and under construction for high energy and nuclear physics, the superconducting magnets used in steering and focusing the beam and in track detection in bubble or spark chambers have to be ramped or pulsed and their polarity sometimes reversed. In A.C. superconducting power cables, the transport current and its associated magnetic field change intensity and direction at a chosen low frequency. In magnetomechanical machinery (motors, generators, etc)

because of the lumped nature of the components of the assembly, of mechanical oscillations and imperfect alignments, the magnetic field produced by and bathing the superconducting elements experiences significant ripples in strength. In high speed transport using superconducting magnetic levitation and propulsion, the lateral and vertical motion and even the displacement along the driving circuit and the discrete components of the roadbed, cause variations of magnetic field intensity.

This field of inquiry has until recently been mainly limited to the basic configuration where the persistent current density $\vec{J}$ is perpendicular to the local magnetic induction $\vec{B}$. This means that an increase or decrease in $\vec{J}$ will generate a change $\Delta\vec{B}$ which will be collinear locally to the existing $\vec{B}$. A classic and simple illustration is that of a wire carrying a varying transport current in a transverse (stationary or varying) externally produced magnetic field.

The study of hysteresis losses in type II superconductors appears to be witnessing a resurgence due to a logical and fundamental extension of the scope of the investigations. The new interest and broadened horizons emerge from the realization that a different situation, where $\vec{J}$ has a component parallel to $\vec{B}$, which has been largely ignored by the community of workers, is fraught with intriguing and novel features. The departure from the orthogonality of $\vec{J}$ and $\vec{B}$ and the tilting of these two vectors towards each other culminates in force free configurations where $\vec{J}$ lies perfectly parallel to $\vec{B}$ everywhere in the material. This conceptually simple change in the orientation of these vectors constitutes a crucial modification which brings new processes

into play and leads to a variety of new phenomena. The planes of flux lines cannot now be unidirectional or parallel but vary in orientation with position. The interaction of nonparallel sheets of flux lines opens new vistas not encountered in the parallel arrangement. In particular, the fascinating phenomenon of flux cutting enters into the picture (B). Here a pair of adjacent sheets of vortices, tilted with respect to each other beyond a critical angle, attract and merge by cross-joining of segments. The ensuing bent vortices straighten and driven by mutual repulsion, separate, forming two new sheets with an orientation intermediate between the direction of the original two partners. The microscopic details and macroscopic consequences of such events have scarcely been explored and challenging vistas lie ahead. For instance, the role of pinning sites and of the surface in this drama remains to be elucidated.

Again some of the impetus for investigations of hysteresis losses in this different framework arises from their relevance to developing technology. It is worthwhile at this point to mention the large superconducting Tokamaks envisaged for the next decades. We note that in these devices, the poloidal magnetic field associated with the plasma current ring is locally perpendicular to the toroidal magnetic field mainly responsible for the magnetic confinement of the hot ions. Consequently, the material in the superconducting coils which generate the latter is periodically subjected to an increment in $\vec{B}$, orthogonal to the "steady" toroidal component.

A classic and simple situation where the increment in $\vec{B}$ is not collinear with the initial $\vec{B}$ but orthogonal to the latter is that where a transport current is fed into a long straight wire immersed in a static

externally applied longitudinal magnetic induction, $B_{//}$ (C). We note that here, B_θ, the azimuthal magnetic induction generated by the current I is everywhere orthogonal to $B_{//}$ and the current density $\vec{J}$ has a component along the local total magnetic induction inside the wire. Indeed, if a force-free configuration is adopted in this arrangement, $\vec{J}$ is perfectly collinear with $\vec{B}$ and can be written $\vec{J} = c\vec{B}$ where c is a coefficient which may vary with position in the sample.

1.2 FRAMEWORK AND PERSPECTIVE

As indicated above, magnetic phenomena and hysteresis losses in type II superconductors occur for two radically different configurations, namely where, (i) $\vec{J}$ is always perpendicular to $\vec{B}$ and, (ii) $\vec{J}$ has a component along $\vec{B}$. Since in the former, $\Delta\vec{B}$, the change in $\vec{B}$, is locally parallel to the existing $\vec{B}$, we will refer to this situation as collinear or unidirectional. In our investigations of (ii), $\Delta\vec{H}$, an increment in the applied magnetic field, $\vec{H}$, is directed at some angle with respect to the initial $\vec{H}$. For this reason we will denote the latter situation as noncollinear or tilted. The limit of (ii) where $\vec{J}$ is exactly parallel to $\vec{B}$ everywhere constitutes a special configuration and entails no hysteresis losses since it is force free. The literature on the first configuration is already voluminous. It is fairly extensive on the force free case but the study of the remainder of the spectrum of (ii) is only in its infancy. The bulk of the work in this last area has been carried out in our laboratory. In this thesis we pursue two aspects of the collinear situation and examine the behaviour in planar geometry of noncollinear configurations in considerable detail.

An excellent synthesis of our present phenomenological understanding of magnetic phenomena and energy dissipation in type II superconductors for the $\vec{J}$ perpendicular to $\vec{B}$ configuration (the situation where $\Delta\vec{B}$ and $\vec{B}$ are collinear) has been presented in various articles authored or coauthored by Clem (D). To place our work in perspective, it is useful to sketch the salient features of the prevailing picture developed more fully and quantitatively in the articles just referred to.

Energy dissipation in type II superconductors can arise from two basic mechanisms; the viscous flow of flux lines and hysteresis effects. The former is important at high frequencies-large amplitudes of applied currents or magnetic fields, where the driving forces dictate the velocity of the vortices. In this thesis we are concerned with the domain of slow changes of flux and current configurations where the velocity of migration of the flux lines is inconsequential and hysteresis effects are dominant. In the regime where velocity dependent contributions are negligible it is nevertheless useful to introduce the concept of velocity in the analysis of the magnetic behaviour. This approach is pursued in chapter 3.

The important quasi-macroscopic features which determine hysteretic losses are, a) the sequence of configurations of the magnetic induction or B profiles and, b) the external or applied magnetic field H_a corresponding to each member of the sequence of B profiles. This can be seen by considering the classic expression for the energy dissipation per unit volume and per cyclic variation of H_a,

(1.1) $$W = \oint H_a \, d\langle B \rangle$$

which follows from introducing $\nabla \times \vec{E} = -\frac{\partial \vec{B}}{\partial t}$ into Poynting's vector, $\vec{S} = \vec{E} \times \vec{H}$, and integrating over space and time. Here H_a is the applied magnetic field and $\langle B \rangle = \int \vec{B}.d\vec{A}/A$ is the spatial average of $\vec{B}$ over the cross section A of the specimen. When the velocity dependent (viscous) forces are negligible, the B profiles in the body of the material are viewed as a succession of static critical state configurations where the driving Lorentz force density $\vec{F}_L = \vec{J} \times \vec{B}$ is balanced by the maximum pinning force density $\vec{F}_p$. The average magnetic induction (density of flux lines), B_{si}, a distance of the order of few penetration depths from the surface is generally not the same as the external or applied magnetic induction, $B_a = \mu_o H_a$. The difference, $B_a - B_{si}$, is frequently denoted the surface step, $\mu_o \Delta S$, and arises from the operation of equilibrium or reversible diamagnetism in type II superconductors (internal H in equilibrium with B, the local density of flux lines), and a surface barrier which can oppose the entry or exit of flux. In spite of a substantial effort, the detailed nature of the surface barrier remains to be elucidated (E). Dissipation of energy occurs as flux lines move through pinning sites and traverse the surface barrier. Hysteretic losses can consequently be classified under bulk pinning and surface losses. Energy is released when flux lines of opposite direction meet and annihilate in the superconductor. This phenomenon occurs because flux lines of one polarity are pinned in the material and can subsequently be made to encounter flux lines of the opposite polarity entering the sample. Consequently energy dissipation via flux annihi-

lation can be included with bulk pinning losses.

1.3 THE BASIC INGREDIENTS

A full account of hysteretic losses involves three basic elements: (i) the surface barrier, I_b, (ii) equilibrium diamagnetism or the reversible magnetization, $H_{eq}(B)$, and (iii) the critical current density in the bulk or volume of the material, $J_c(B)$. Equilibrium diamagnetism and the surface barrier play a role in establishing the surface step. Further, for a given B, the barrier against entry of flux, I_b', may differ from the barrier opposing the exit of flux, I_b'', A knowledge of $H_{eq}(B)$, the equilibrium relationship between H and B together with information on the bulk pinning function $F_p(B)$ are required to map out the critical state B profiles. The critical state concept stipulates that the driving Lorentz force is in equilibrium with the maximum pinning force and can be written

$$\vec{J}_c \times \vec{B} + \vec{F}_p(B) = 0 \tag{1.2}$$

Introducing Maxwell's equation $\nabla \times \vec{H} = \vec{J}$ into this leads to

$$(\nabla \times \vec{H}) \times \vec{B} + \vec{F}_p(B) = 0 \tag{1.3}$$

To compute B profiles with this expression we require a knowledge of the relationship between $\vec{H}$ and $\vec{B}$ (i.e. $H_{eq}(B)$ or $B_{eq}(H)$) and data on $F_p(B)$.

At present, first principle expressions are available only for the reversible magnetization, hence $H_{eq}(B)$. The fountainhead for these

formulae is Abrikosov's classic paper of 1957 (111). Many observations on ideal samples have corroborated the essential features of these expressions. In practice however, it is frequently found more convenient to exploit one of several analytic approximations which have been proposed in the literature to reproduce the observed and theoretical H vs. B (or B vs. H) curves (F).

In spite of considerable effort, $J_c(B)$, $I_b'(B)$ and $I_b''(B)$ cannot be calculated from first principles or determined from a few parameters characterizing a material. $J_c(B)$ has been extracted numerically from an analysis of measurements of (i) the critical current, I_c versus H_a, (with I perpendicular to H_a) and (ii) the magnetization curves (G). In these exercises, the role of the surface barrier(s) and $H_{eq}(B)$ should be taken into account unless the data or auxiliary measurements justify neglecting either or both of these contributions. A wealth of empirical expressions have been put forward in the literature for $J_c(B)$, different forms appearing to correspond closely to the particular behaviour encountered in different materials (H). A basic feature which these expressions share is that J_c be a decreasing function of B, or alternatively, that the gradient of the flux density becomes steeper as B decreases. Nevertheless, it is sometimes found adequate in the treatment of data far below H_{c2} to take J_c to be constant for a given material at a fixed temperature. This crude and simple picture is referred to as the Bean-London approximation (2, 13, 117).

Quantitative information on I_b vs. B is however scarce indeed and some ambiguity exists regarding the contribution of I_b'' to the results quoted for I_b'. The existence of the surface barrier(s) is well

established from measurements of <B> (or of the magnetization) versus H_a. The presence of the barrier causes <B> to remain unchanged over a range $H_a' - H_a'' = I_b' + I_b''$. The effect of different surface conditions and surface treatments on the height of the barrier(s) has been explored but no clear picture has yet emerged and much work remains to be done in this area (I). Metallic coatings of Ni, Cr, Cu, Tl and Pb in good contact with the surface have been shown to dramatically reduce the height of the barrier(s) (J).

It is, of course, desirable to measure the spatial distribution and temporal evolution of the B profile directly and accurately. In practice this is extremely difficult. Various workers have obtained such data by inserting suitable magnetic probes in small holes drilled perpendicularly to $\vec{B}$ across the thickness of a ribbon or diameter of a cylindrical sample (138). The probes used have been either magneto-resistive (a segment of a fine bismuth wire) or Hall Effect elements. In spite of the skill and sophistication brought to bear in these efforts, the spatial resolution and sensitivity achieved have not been encouraging. Further, the perturbation of the B profile by the hole, which drastically modifies the pattern of flow of the persistent currents in its vicinity, introduces a significant element of uncertainty in the data.

1.4 VARIOUS EXPERIMENTAL APPROACHES

The first step in the experimental and theoretical investigation of magnetic behaviour and hysteretic losses is the determination of $\Delta\phi$, the change in magnetic flux (or equivalently Δ<B>, the change

in the average magnetic induction) threading the specimen as the external magnetic field H_a is incremented. $\Delta\phi/\Delta H_a$ vs. H_a is denoted, the flux response function. The magnetic flux threading the material can have two sources; (i) an externally applied magnetic field and (ii) a conduction current I fed into the specimen via leads attached to it. For simplicity we consider only idealized geometries (infinite slab and cylinder) where the external magnetic induction is uniform over the surface of the specimen. Under these circumstances the external magnetic induction can arise only from (i) and/or (ii).

Experimentally, depending on the situation, pick up coils embracing the sample or voltage leads attached to it provide a signal proportional to $\Delta\phi/\Delta t$, hence yield information on $\Delta\phi/\Delta H_a$ since $\Delta H_a/\Delta t$ can readily be measured simultaneously. We note that the voltage leads arrangement requires rapid variations of the magnetic flux to produce an adequate signal since, in a sense, the circuit can be regarded as a single turn pick up coil. Voltages leads, however, are required to monitor, (i) steady state flux flow voltages and (ii) changes in the azimuthal flux permeating a long solid cylinder.

Once $\Delta\phi/\Delta H_a$ versus H_a is known, it is a straightforward matter to generate the locus of ϕ (or $\langle B \rangle$) vs. H_a. In our work, an operational amplifier performs the integration of the instantaneous signal due to $\Delta\phi/\Delta t$ while the intensive variable H_a (or I) is simultaneously monitored. Using an X-Y recorder we can consequently plot $\phi(H)$ continuously versus H. Experimentally, it is often more convenient to monitor $\mu_o\langle M \rangle = \langle B \rangle - \mu_o H$ vs. H instead of $\langle B \rangle$ vs. H. This change is accomplished by using a bucking coil to perform the subtraction of the instantaneous signal

of $(\mu_o HA)/dt$ from that due to $\Delta\phi/\Delta t$. We find however that it is easier to discuss the physical content of the investigations in terms of ϕ or $\langle B \rangle$ vs. H rather than $\langle M \rangle$ vs. H.

The area under any portion of the H vs. $\langle B \rangle$ curve measures the energy, averaged over the volume of the specimen, which is flowing into the sample when H is increasing in magnitude and the energy flowing out of the sample when H is decreasing in magnitude since $\Delta W = H_a \Delta\langle B \rangle$. This is illustrated in Fig. 1.1. The area enclosed by the closed locus of $\langle B \rangle$ vs. H therefore measures the net energy flow, hence the energy dissipated (converted into heat). When the flux response function, locus of $\langle B \rangle$ vs. H and the resulting enclosed area are independent of the rate of change or frequency, viscous drag plays no role and the energy loss is attributed entirely to hysteresis effects. The closed curve can then be denoted the hysteresis curve. Sequences of B profiles with H increasing and decreasing are also depicted in Fig. 1.2. In these displays the vertical boundaries at x = 0 and x = X/2 (or r = R and r = 0) indicate one surface and the midplane of an infinite slab (the surface and centreline of an infinite cylinder). We also take $\vec{B}$ and $\vec{H}$ to be directed along the vertical.

1.5 DISTRIBUTION OF ENERGY DISSIPATION

The local rate of energy dissipation and its time average per cycle is also of special interest. In particular, this information is important in assessing the stability of a material against flux jumps. These catastrophic events are triggered when the local energy dissipation is excessive thereby causing a large and sometimes runaway rise

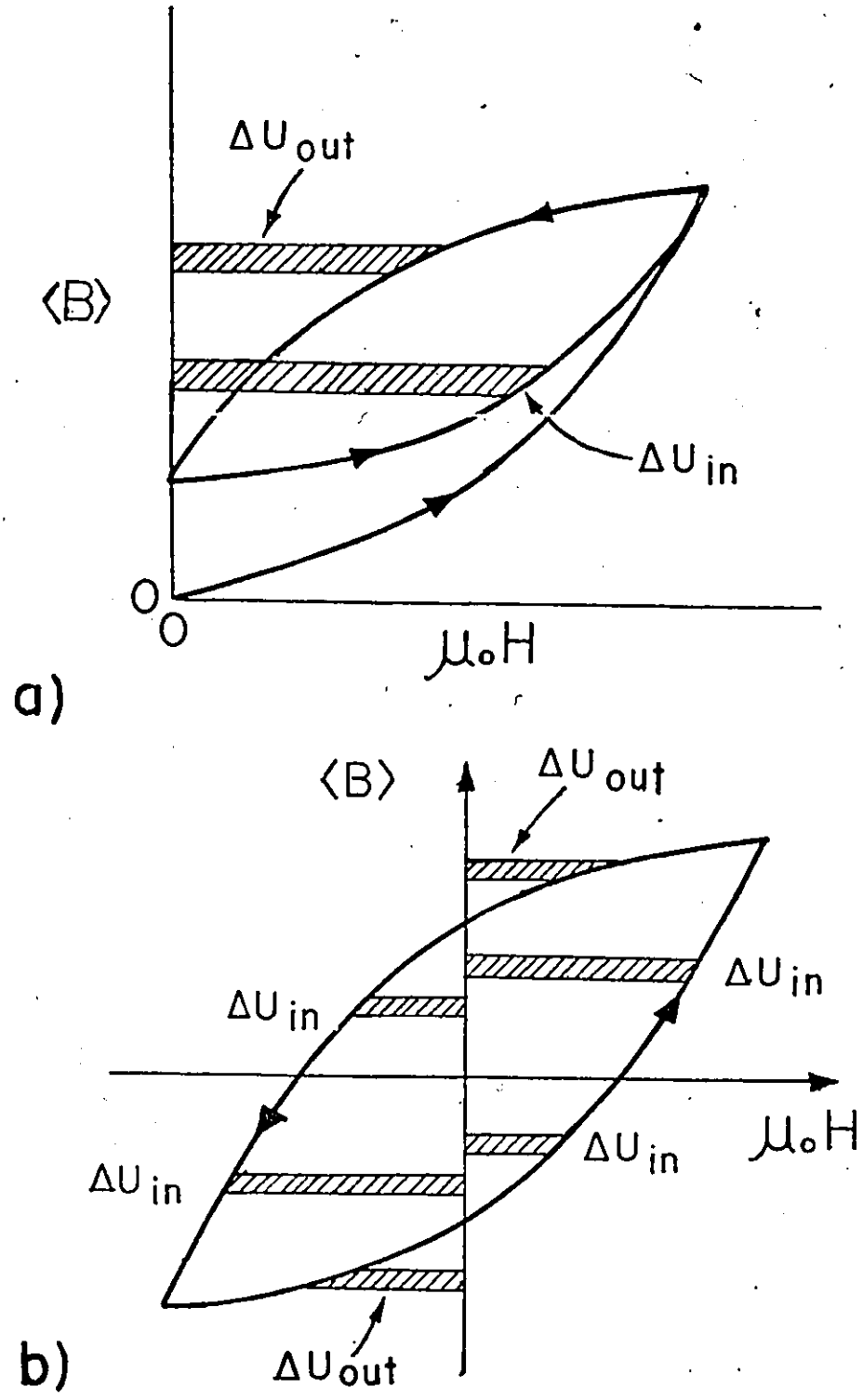

FIG. 1.1. Schematic display of increments of energy flow into (ΔU_{in}) and out (ΔU_{out}) of a sample during half-wave (a) and full-wave (b) hysteresis cycles.

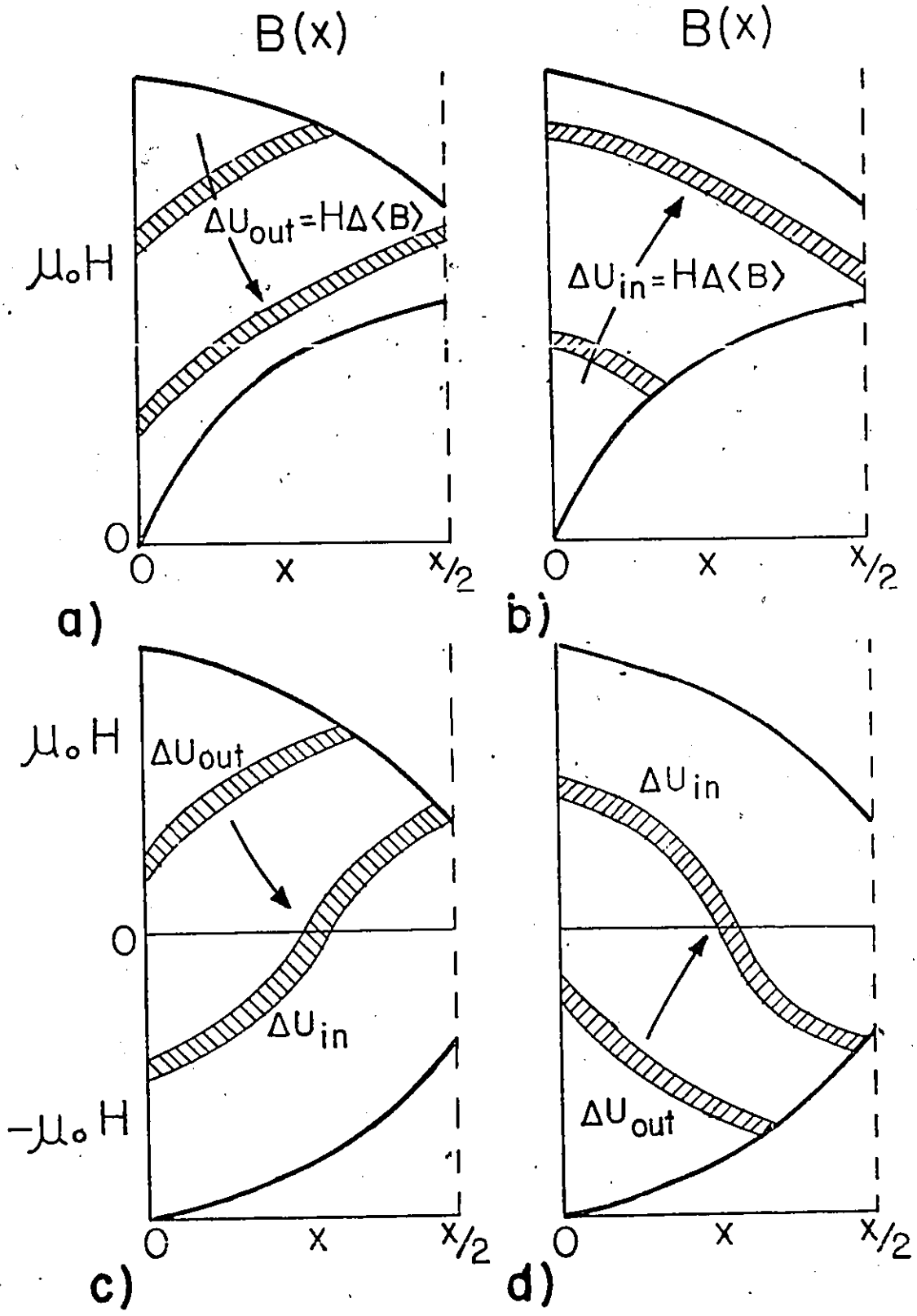

FIG. 1.2. Evolution of B profiles and rate of energy flow during the sweep of the applied magnetic field H for half-wave and full-wave cycles.

in temperature. Further, the partial or complete collapse of the superconducting state can propagate throughout the volume of the sample. For these reasons these occurrences are called flux avalanches.

Wischmeyer and Urban (17-18) have calculated energy dissipation profiles for a hollow tube in the context where $H(x) = B(x)/\mu_o$ and $H_a = B_{si}/\mu_o$, hence they ignored the role of equilibrium diamagnetism and surface barriers. In each of these computations a specific analytic expression was introduced to describe $J_c(B)$. In these studies, by neglecting (i) the existence of $H_{eq}(B)$ at the interface where flux annihilation occurs and (ii) the presence of any surface barrier(s), two major contributions to local energy dissipation have been ignored. Clem has examined the evolution of the energy dissipation distribution and the various contributions to the total energy loss, in a systematic and thorough manner taking all of the pertinent quantities into account. In the following paragraphs we outline some salient features emerging from his careful theoretical scrutiny.

To explore the local energy production, we return to Poynting's vector, $\vec{S} = \vec{E} \times \vec{H}$, and exploit the divergence theorem to convert the surface integral into a volume integral, namely

$$\int (\vec{E} \times \vec{H}).d\vec{A} = \int \nabla.(\vec{E} \times \vec{H})dv. \tag{1.4}$$

Making use of a vector identity for the divergence of a vector product leads to

$$- \int (\vec{E} \times \vec{H}).d\vec{A} = \int (\vec{E}.\ \nabla \times \vec{H})\ dv - \int (\vec{H}.\ \nabla \times \vec{E})dv \tag{1.5}$$

Introducing Maxwell's equation $\nabla \times \vec{H} = \vec{J}$ and Faraday's equation $\nabla \times \vec{E} = -\partial\vec{B}/\partial t$ we obtain

$$\frac{\Delta W}{\Delta t} = \vec{E}.\vec{J} + \vec{H}.\frac{\partial \vec{B}}{\partial t} \tag{1.6}$$

for the local rate of energy conversion and

$$\Delta W = \int_{t_1}^{t_2} dt \int (\vec{E}.\vec{J}) \frac{dv}{V} + \int_{t_1}^{t_2} dt \int \vec{H}.\frac{\partial \vec{B}}{\partial t} \frac{dv}{V} \tag{1.7}$$

for the spatial average of energy change during an arbitrary time interval $\Delta t = t_2 - t_1$. When $t_2 - t_1 = T$ corresponds to the duration (the period) of a complete cycle of $H_a(T)$, equation (1.7) is a variant of equation (1.1) and yields the net energy dissipation (heat production) per unit volume and per cycle, hence hysteretic losses when $\vec{E}$, $\vec{J}$, $\vec{H}$, and $\frac{\partial \vec{B}}{\partial t}$, therefore $\Delta W/\Delta t$ are rate (frequency) independent.

In type II superconductors, whether reversible or irreversible, the second term in equation (1.7) yields no net local contribution to energy dissipation during a complete cycle since $H_{eq}(B)$ is single-valued (reversible). In insulating ferromagnetic materials, this term is responsible for the energy dissipation since here, H is not a single-valued function of B.

To simplify the rest of our discussion of this topic, we focus on planar geometry and consider an infinite slab of thickness 2X with the midplane located at x = 0. We take H and B along the z axis, hence $\vec{E}$ and $\vec{J}$ along y and drop the axial subscripts and vector arrows. In this context the integral form of Faraday's equation $\int \vec{E}.d\vec{\ell} = d\phi/dt$

leads to

$$E(x) = \frac{d\phi(x)}{Y\, dt} \tag{1.8}$$

where $\phi(x)$ is the flux threading an area xY between the midplane and the boundary at x.

A reversible (Abrikosov or Meissner) current, I_A, in equilibrium with B_{si} flows at the surface in a sheath of the order of a penetration depth thick. This current always flows in a diamagnetic sense (shielding against flux entry). The electric field, E_s, in the corresponding surface volume reverses direction, however, depending on whether B_{si}, hence the flux threading the sample, is increasing or decreasing. Consequently,

$$\int_{t_1}^{t_1+T} E_s\, I_A\, dt = 0 \tag{1.9}$$

because the sum of positive $E_s\, I_A\, dt$ during half of the cycle is cancelled by the equal sum of negative $E_s\, I_A\, dt$ during the other half. We note that the screening current $I_A = Z \int j_A\, dx$ is connected to the local (microscopic) magnetic induction $\vec{b}$ or internal magnetic field $\vec{h} = \vec{b}/\mu_o$ in the penetration-depth region via $\nabla \times \vec{b} = \mu_o \vec{j}_A$ or $\nabla \times \vec{h} = \vec{j}_A$ rather than to the quasi-macroscopic quantity $\vec{H}$ in equilibrium with the flux line density $\vec{B}$.

In contrast, the irreversible currents I_b' and I_b'' associated with the surface barriers against flux entry and exit always flow in

the same direction as the surface electric field E_s. This can be seen by noting that (i) I_b' flows in a diamagnetic sense (shielding against flux entry) when B_{si}, hence ϕ, are increasing in magnitude, whereas (ii) I_b'', flows in a paramagnetic (flux retaining) sense when B_{si} is decreasing in magnitude.

On one side of an interface where the flux distribution reverses polarity, $H_{eq}(+B) = H_{cl}$ and on the other side $H_{eq}(-B) = -H_{cl}$. The region Δx_i, of the order of a few penetration depths, straddling this interface (the plane where B traverses zero), is therefore filled with a macroscopic current $I_i = 2H_{cl}$ per unit length z. Consideration of the corresponding sequences of B and H profiles shows that; (i) the current I_i always flows in the same sense as the electric field E_i which is generated at the interface and (ii) $\Delta\phi_i/\Delta t = E_i Y$ corresponds to the rate of annihilation of vortices of one polarity. Consequently, in the volume $\Delta v_i = YZ\Delta x_i$ where flux annihilation takes place, the rate of energy dissipation (heat production) can be written

$$(1.10) \qquad (\vec{E}.\vec{J})\ YZ\Delta x_i = E_i I_i Y = 2 H_{cl} \frac{\Delta\phi_i}{\Delta t}$$

Urban and Wischmeyer (17, 18) by ignoring the reversible magnetization, hence taking $H = B/\mu_o$, effectively distribute the flux annihilation energy over a volume of thickness $\Delta x_i'$ where B varies from $+B_{cl}$ through zero to $-B_{cl}$. The dimension $\Delta x_i'$ is at least several penetration depths and therefore much greater than Δx_i.

The instantaneous temperature profile and, consequently, the time and spatial evolution of the local energy dissipation can, in principle, be monitored by inserting an array of minuscule thermocouples in small holes drilled in the sample. As with attempts to monitor the B profile directly, the spatial resolution and the sensitivity which can be achieved by these techniques are, however, disappointing. Also, as with the local measurements of the flux configurations, it is difficult to ascertain the perturbation introduced by the hole on the energy dissipation in its vicinity.

1.6 TOTAL ENERGY DISSIPATION

Thermometric techniques have also been used to obtain information on energy dissipation averaged over the sample volume and over time. This has been accomplished by monitoring; (i) the increase in the rate of evaporation of the liquid helium in which the specimen is immersed or (ii) the rise in temperature of the specimen assembly (precautions having been taken to ensure temperature uniformity). The thermometric approach has merit in circumstances where an electromagnetic method of detection (a wattmeter) provides data difficult of interpretation. For instance, the designer or user of a superconducting magnet may be interested in knowing the total energy dissipated when the device is ramped from zero to a preset value. Here measurements of the current in phase with the applied voltage determine the total energy input. The fraction of this energy which is stored must be determined separately and may be difficult to calculate.

The (electromagnetic) wattmeter is a most useful device for providing data on energy dissipation averaged over the sample and per cycle as a function of amplitude, frequency, bias field, temperature etc (139, 140). This apparatus is designed to detect and integrate over time, hence per cycle, the product of the flux response function ($\Delta\phi/\Delta t$ or voltage V) in phase with the sinusoidal intensive (driving) variable H(t) or I(t). This device or approach however has an important shortcoming. It does not record and provide the user with the very meaningful fine-grained information, namely $\Delta\phi/\Delta H_a$ vs. H_a, which it actually detects and processes during its operation.

In our work, the energy dissipated per cycle is an end result of detailed measurements which contain considerable information regarding the evolution of the spatial average of the distribution of the flux density in the specimen. As indicated earlier, we monitor the flux threading the sample (or $\langle B \rangle$ or $\langle M \rangle$) continuously, starting with specified initial conditions, as an applied magnetic field is initially varied and subsequently cycled between chosen limits. In the regime where $\vec{J}$ adopts a component along $\vec{B}$, we monitor the variation of the flux permeating the sample along two appropriate orthogonal directions. Graphical or planimeter integration of the area enclosed by the locus of $\langle B \rangle$ along the direction of the component of the applied magnetic field which is varying yields the hysteresis losses per cycle. All of these data, the detailed locus of the magnetic moment, as $\vec{H}_a$ is varied and the energy dissipated per cycle (the hysteretic "surface") are the raw materials which we analyse to obtain insight into the detailed behaviour of the configurations of the magnetic induction inside the specimen.

In this manner we establish contact with the basic interactions and processes which come into play while gathering data of technological interest.

1.7 DIFFERENT CYCLES

In many applications, the cycle of interest is where H_a is periodically swept from zero to a specified value and returned to zero. This cycle can conveniently be described by the expression

$$H_a = h_o (1 + \cos \omega t) \tag{1.11}$$

although the specific form of the time dependence is immaterial in our work (triangular, rectangular, irregular, etc.). The important quantities here are the amplitude h_o and the bias field, $H_o = h_o$ in the present example. We will refer to this category of cycles as the half-wave case, in analogy with pulse generators.

In other circumstances, the cycle of interest is where H_a changes direction, swinging between symmetric positive and negative limits. This applied cycle can conveniently be written

$$H_a = h_o \cos \omega t \tag{1.12}$$

We will refer to this situation as the full-wave case, again in analogy with pulse generators. We have already noted that the reversal of polarity brings the interesting phenomenon of flux annihilation into the picture. Further, as we shall see in some detail in Chapter 6, the

nature of the surface step will play an important role in dictating the shape of the hysteresis curve as H_a swings through zero. The full-wave and half-wave situations therefore present fundamental differences.

It is evident from inspection of equations (1.11) and (1.12), that the two special cases just described constitute particular instances of a wide spectrum of possible cycles. The general case, always in the context that the sinusoidal form for the time dependence has no special merit, can be expressed by

$$H_a = H_o + h_o \cos \omega t \tag{1.13}$$

The simple expressions just listed focus on the relative magnitude of the bias field H_o and of the amplitude h_o. In order to examine the spectrum of possible situations realistically and systematically, suitable scales for measuring H_o and h_o need to be introduced. For the ideal type II superconductor (no bulk pinning and no surface barrier) the appropriate reference quantities are H_{c1} and H_{c2}. In irreversible type II superconductors where both bulk pinning and surface barriers to flux entry (I_b') and exit (I_b'') come into the picture, the useful and important measuring sticks are, (i) $I_{bT} = I_b' + I_b''$, the sum of the magnitude of the two barriers and (ii) ΔB^*_{si}. The latter denotes the magnitude of the change in the internal magnetic induction at the surface which causes the front of a disturbance in the B profile to penetrate to the midplane (infinite slab) or centreline (infinite cylinder). We note that ΔB^*_{si} is material dependent in the sense that the bulk pinning strength and the size (thickness of the slab or radius of the cylinder) enter in its determination. Further since J_c decreases

with B, for a given specimen, ΔB^*_{si} will vary as the bias field changes.

Exploiting a phase sensitive detector and spectrum analyser, the harmonic content of the magnetic response of the specimen in and out of phase with a pure sinusoidal driving signal can be investigated. The coefficients of the in and out of phase components of the fundamental correspond to the magnitude of the real and imaginary permeability. These quantities can be studied as a function of the amplitude and frequency of the input signal, of the bias field and temperature. The results are compared with predictions constructed using various forms for $I_b(B)$, $H_{eq}(B)$ and $J_c(B)$. This approach requiring sophisticated apparatus and demanding special experimental precautions, however, produces no fundamentally new data and is basically equivalent to the method we have exploited. It may be convenient, for purposes of analysis, to exploit sinusoidal time dependences. Further, the framework, nomenclature and operations involved in this approach have the merit of being familiar to most physicists.

1.8 FOCUS OF THE THESIS

A. Valley of the Losses (Collinear regime)

Clem (3) in a systematic theoretical investigation of the dependence of hysteretic losses on collinear amplitudes and bias field, predicted a novel and significant behaviour. He found that for a fixed amplitude $h_o < \Delta B^*_{si}/\mu_o$, the losses W can traverse a deep valley as the bias field H_o increases from zero. We call this feature, the Clem valley, for obvious reasons. He explored various choices and combinations of $J_c(B)$, $H_{eq}(B)$, $I'_b(B)$ and $I''_b(B)$ which cause this phenomenon to occur. This survey revealed that for certain circumstances, the bias field H_o, where the minimum in the valley appears, bears a simple relationship to the amplitude.

The experimental discovery of the predicted effect was first

reported by Thompson et al. (40) who investigated a thin walled cylinder of Nb_3Ge. Subsequently, Kovachev (34) explored the temperature dependence of this minimum in strips of Nb_3Sn and extracted information on the variation of the surface barrier with temperature from his observations. Ciszek et al. (23, 24) have also recently explored this minimum. Upon receiving a preprint of Clem's paper containing the prediction of this effect and Thompson's et al's report of its discovery, we undertook a search and study of the phenomenon in a VTi ribbon whose behaviour we were investigating in another context. Because this specimen exhibits some anisotropy, we pursued the measurements with the collinear H_o and h_o directed along the length (z-axis) and along the width (y-axis) of the ribbon. Our data, presented in chapter 5, show that a pronounced valley occurs in this material for both orientations.

Various other investigations of the magnetic behaviour of this sample indicate that bulk pinning plays a dominant role and that the surface barrier(s) and $H_{eq}(B)$ make negligible contributions to the magnetic response, even in the low field regime. Further, this auxiliary work shows that when $B < B_{c2}$, the B profiles in this sample can be satisfactorily described by the simple prescription,

$$\frac{dB}{dx} = \pm \frac{\alpha_{1/2}}{B^{1/2}} \tag{1.14}$$

We refer to this as the Yasukochi approximation (123). Using this simple expression together with the boundary condition $B_{si} = \mu_o H_a$, which implies that $I'_b = I''_b = 0$ and $\mu_o H(x) = B(x)$, hysteretic curves and losses can readily be computed.

In view of the good correspondence between these calculations and our observations, we deemed it worthwhile to explore computationally, the character of the Clem valley, generated by other basic forms for dB/dx (or dB/dr), always here in the crude but simple framework where

$B_{si} = \mu_o H_a$ and $B(x) = \mu_o H(x)$. These limiting or extremal formulae are the Kim-Anderson approximation

$$\frac{dB}{dx} = \pm \frac{\alpha_o}{B} \tag{1.15}$$

and a suitably modified Bean-London approximation

$$\frac{dB}{dx} = \pm \alpha_1 (1 - \frac{B}{B_{c2}}) \tag{1.16}$$

We pursue these calculations for both infinite slab and cylinder geometry and examine the dependence of $H_{o\ min}$, the bias field H_o where the minimum occurs, on the amplitude h_o. We also extend all of these calculations to the range of amplitudes h_o exceeding $\Delta B^*_{si}/\mu_o$. We call the situation where $h_o = \Delta B^*_{si}/\mu_o$, the saturation (full penetration) case. Hence we denote the instances where $h_o < \Delta B^*_{si}/\mu_o$ as below saturation and those where $h_o > \Delta B^*_{si}/\mu_o$ as above or beyond saturation.

B. Barrier Effects

The dependence of hysteresis losses on the height of the surface barrier has been examined theoretically by Sekula and Barrett (16) and by Fournet and Mailfert in 1970 (6). Both groups exploited the Bean-London approximation (J_c = constant), took $\mu_o H = B$, hence ignored equilibrium diamagnetism and considered infinite slab geometry. The former stipulated a barrier independent of B against flux entry and no barrier against flux exit. We call this picture, the asymmetric barrier model. They examined the half-wave case (see eqn. 1.11). Fournet and

Mailfert also stipulated a barrier independent of B against flux entry and a barrier of the same height as the former opposing flux exit. We refer to this picture as the symmetric barrier mode. Fournet and Mailfert focused on the full-wave case (see eqn. 1.12). Both groups limited their analysis to the situation where $h_o < B^*_{si}/\mu_o$, hence to below full penetration (below saturation). These calculations yield identical results. This feature is expected from careful qualitative considerations. Further the calculations show, as intuitively anticipated, that the hysteresis losses, (i) decrease as the ratio of the barrier height to the amplitude increases, and (ii) vanish when the barrier no longer allows flux to enter the specimen.

Measurements by Bussière and collaborators (76-78, 81) and others on materials exhibiting a strong surface barrier show a precipitous decline in A.C. losses as the amplitude diminishes to a threshold value. This threshold constitutes a signature of the surface barrier. Further, the dependence of the A.C. losses on amplitude is well reproduced by formulae akin to that developed by the authors just mentioned. This agreement may have created a climate where it is taken for granted that large barriers must lead to lower losses. Bussière and Clem (22) have, however, intimated that under certain circumstances an increase in hysteretic losses may arise although the barrier is made <u>higher</u>.

We undertook a systematic computational study of this problem. Focusing on both the full-wave and half-wave cases we examined the predictions for both the infinite slab and the infinite cylinder geometries. We explored the behaviour expected using the Bean-London approximation, $j_c \equiv$ constant, exploited by Fournet and Mailfert and

Sekula and Barrett. For completeness however we also pursued the calculations using the Kim-Anderson approximation, $j_c = \alpha_o/B$. These two expressions, represent radically different descriptions of bulk pinning and span a wide range of possible situations. For simplicity in these calculations, we took the barriers to entry and exit of flux to be independent of B as H_a sweeps between the limiting values. In order to assess the importance of different types of barrier situations we examined both the symmetric and asymmetric configurations described above. Finally we considered the regime of amplitudes lying below and beyond full penetration (saturation).

The results of this extensive investigation are presented in chapter 6. The crucial feature which emerges from this scrutiny and survey is that in numerous instances, an increase in the surface barrier will give rise to an appreciable increase in hysteretic losses. This feature has important bearing on applications. A qualitative understanding of this phenomenon can be obtained by realising, as noted by Clem in his 1979 lectures (4), that the losses depend on both, (i) the quantity of flux moved in and out during each cycle and (ii) the magnitude of the deviation between <B> and $\mu_o H_a$ during the cycle.

C. Model of Non Rotating Vortices

The major part of our research on hysteretic losses has been directed to the relatively unexplored and poorly understood regime where $\vec{j}$ has a component along $\vec{B}$ (noncollinear situation). In this study we have focused on planar geometry (ribbons), because of the simplicity of this situation and also in order to complement the earlier and on going

investigations of this problem in our laboratory, namely, the work of Gauthier (67, 68) on solid cylinders (wires), Boyer (47-49) on rotating disks and Fillion (62) on hollow tubes. Our hope is that the choice of different geometries as well as samples will make it possible to identify and document all of the basic aspects of the behaviour encountered in this novel regime. The results achieved to date by our group support the merits of this multipronged approach.

A simple picture has been put forward and partly developed by Campbell and Evetts (141) in their monograph to account for the configurations of flux encountered in the nonparallel (noncollinear) regime. They propose that the sheets of flux lines as they are made to progress into the specimen retain the orientation they had when created at the surface. The stark simplicity of this idea endows it with considerable appeal. We note also that flux cutting is ignored or obviated by the exploitation of this concept. Careful qualitative considerations, however, reveal that the concept is flawed. Firstly it leads to unphysical discontinuous changes at H_{c2}. More importantly, in our view, application of the concept leads to serious boundary conditions problems or surface mismatches between $\mu_o \vec{H}_a$ and $\vec{B}_{si}$ when the nonparallel flux lines are caused to move out of the specimen.

In chapter 3 we pursue in considerable detail the consequences of this postulate that vortices migrate without rotation. To reduce the picture to its essentials we only take bulk pinning into account. We examine the quantitative predictions for three basic approximations for bulk pinning and also for the special case where pinning is zero (force free situation). The results of these calculations are presented and

compared with extensive data obtained on a ribbon of VTi immersed in a static longitudinal magnetic field when a magnetic field perpendicular to the former and directed along the broad faces is impressed. We examine the evolution of the longitudinal and transverse components of the magnetic induction threading the sample starting with four basic categories of initial unidirectional flux profiles. The comparison shows that the data progressively diverges from the predictions of the model regardless of the form of the bulk pinning introduced in the calculations. We conclude that by forbidding changes in flux orientation, such as would be produced by the mechanism of flux cutting, the model gradually fails to correctly describe the observed behaviour. The concept, however, provides a useful approximate account of the evolution of the flux configurations during the initial portion of the sweep of the applied field. In some applications, the range over which the predictions are valid can be significant.

D. Noncollinear Regime and a New Valley in the Losses

In chapter 4, the principal chapter, in our view, of this thesis both in volume and import, we present an extensive series of measurements of magnetic behaviour and hysteretic losses in ribbons of VTi and Nb in the regime where $\vec{j}$ has a component along $\vec{B}$. This work constitutes a major extension of the earlier investigations of Timms and LeBlanc (142) and of Lachaine (143, 144) on ribbon samples.

To simplify the physics and the analysis we let the ribbon become superconducting in a chosen bias magnetic field which may be tilted with respect to the length of the ribbon. The component of the applied

magnetic field along the length of the ribbon, $H_{//}$, is always maintained constant while the transverse component, $H_{\perp}$, directed along the broad faces is increased and cycled between chosen limits. In the spirit of equation (1.13) we write for the transverse component

$$H_{\perp} = H_{\perp i} + h_{\perp} \cos \omega t \tag{1.17}$$

We have investigated the magnetic response and measured the hysteretic losses as a function of, (i) the amplitude $h_{\perp}$, (ii) the bias field component $H_{\perp i}$ and (iii) the magnitude of $H_{//}$. We stress that two quantities are monitored simultaneously and continuously as $H_{\perp}$ varies. These are the average magnetic induction $\langle B_y \rangle$ along $H_{\perp}$ and $\langle B_z \rangle$ along $H_{//}$. A crucial feature to bear in mind is that $\langle B_z \rangle$ varies although $H_{//}$ is fixed. In particular, a very pronounced valley in the hysteretic losses for a fixed $h_{\perp}$ as a function of $H_{//}$ is observed. This feature is analogous too but more dramatic than the Clem valley. The changes in this valley brought about by the bias field $H_{\perp i}$ have also been documented.

The specimens we have studied exhibit anisotropic magnetic response. The magnetization curve measured along the length of the ribbon sample differs by a few and even several percent from that along the width. Further the demagnetization factor along the width of the ribbons, although small, is not negligible. To obtain some insight on the role of the anisotropy and end effects on the phenomena under scrutiny we have repeated many of the measurements with $H_{\perp}$ maintained stationary (instead of $H_{//}$) and with $H_{//}$ (instead of $H_{\perp}$) as the

variable component. This is equivalent to repeating the investigation after rotating the ribbon through 90^{o}.

Our analysis of this vast assortment of data is empirical. We retain only the contribution of bulk pinning to the phenomena in order to simplify the picture. In other words we take, consistent with our observations, that the surface barriers are negligible and ignore the reversible or equilibrium diamagnetism. The latter neglect is warranted when $H_{//}$ is appreciably larger than H_{c1}. We continue, however, to ignore this feature even when $|\vec{B}(x)| \lesssim \mu_o H_{c1}$.

To interpret our results we pursue the framework put forward and explored by our group to account for the noncollinear regime. This viewpoint assumes that the configurations which nonparallel sheets of flux lines adopt under driving forces where $\vec{j}$ has a component along $\vec{B}$ corresponds to critical states of density and orientation of the magnetic induction $\vec{B}(x)$. It is fairly straightforward matter to identify a simple analytic function for the bulk pinning which generates B profiles and consequently magnetization curves adequately corresponding to that observed in the standard collinear regime. We then postulate that the B dependence of the critical gradients of flux density is unaffected by the spatial variation of the direction of the vortices. The problem then becomes one of obtaining a "good" formula by judicious trial and error to describe the B dependence of the critical angle gradient. Our approach to this problem is described in chapter 4. After considerable computational effort we arrived at a simple expression which successfully accounted for a vast assortment of data on a VTi ribbon. In particular, the interesting valley exhibited by the hysteretic losses at fixed

amplitude vs. $H_{//}$ and the effect of the bias field H_{li} on this feature, are remarkably well described. We then applied this formula to the analysis of extensive measurements on a Nb sample. We find that this formula again yields encouraging agreement with our rich collection of data on this specimen. These successes may provide incentive and direction for future theoretical attacks on the complicated but important problem of flux line interactions and processes operating (flux line cutting) in the noncollinear regime. Recent theoretical investigations by Clem and other workers (B) have elucidated basic aspects of this formidable problem in the limit where bulk pinning is zero.

CHAPTER 2

DESCRIPTION OF SAMPLES AND EXPERIMENTAL PROCEDURE

2.1 INTRODUCTION

In this thesis, the results of measurements of the axial and transverse components of the magnetization and of hysteresis losses in ribbons of type II superconductors are presented in the situation where the currents are generated by induction. Another alternative would be to feed a transport current to the sample through leads connected to an external power supply. However, joule heating at the contacts causes problems. In particular this leads to nonuniform temperatures in the sample and possibly, currents limited locally at the contacts. Even if these difficulties are surmounted by maintaining the "waist" of the sample above the temperature of the ends, presumably the weakest cross section will determine the critical current. Further, in some materials the critical current is extremely high and beyond the capacity of readily available current supplies. In the present work, it was therefore chosen to introduce persistent currents, flowing along the ribbon, by induction. This is done by applying (or reducing) a magnetic field $H_\perp$ directed perpendicular to the axis of the ribbon and along its wide face. The ribbon may be visualized as consisting of two halves (infinite slabs) separated by the midplane parallel to the two wide faces. The magnitude of the total induced current in either half must now be deduced from the magnitude of the transverse magnetic moment $\mu_o \langle M_\perp \rangle$ instead of being read directly with an ammeter. We also chose to introduce currents flowing around the axis of the ribbon by induction. This is done by applying

(or reducing) a magnetic field $H_{//}$ directed along the axis of the ribbon. Since the width of the ribbon is large compared to its thickness, the ribbon can again be regarded as equivalent to two infinite slabs separated by a midplane and carrying "conduction" currents flowing in opposite directions in each half and perpendicular to the axis of the ribbon.

2.2 DESCRIPTION OF SAMPLES

1- $V_{0.24}Ti_{0.76}$

The sample was cut with a wire saw from an arc-melted ingot of high purity VTi (obtained from Materials Research Corporation) and was mounted without any chemical or heat treatment after cutting. The ribbon was 3.6 cm long, 0.51 cm wide and 0.15 cm thick.

2- Nb

The samples were cut from a Niobium sheet of metal, (obtained from Kawecki Berylco Industries) and unannealed after final rolling. It consists of a stack of six identical ribbons electrically insulated by mylar spacers, as shown in Fig. 2.1-A. Each sample is a single rectangular piece of ribbon, 3.63 cm long, 0.555 cm wide and 0.025 cm thick.

2.3 EXPERIMENTAL PROCEDURE

A non-inductive bifilar heater coil is wound directly on the sample which permits us to erase previous magnetic history by raising the temperature of the sample above T_c before the start of a measurement. Care was taken to wind this heater uniformly to ensure temperature homo-

geneity along the length of the sample. An insulated #38 manganin wire supplied by Wilbur B. Driver Co. was used. The sample-heater assembly was covered with epoxy and fits tightly inside a "slot" at the centre of the transverse pick up coil, just like a cassette fits in the slot of a cassette recorder, see Fig. 2.2. Using this set up the number of turns on the transverse pick up coil was increased by a factor of more than ten compared to the awkward arrangement exploited by Lachaine who placed his sample inside a coffin which was inserted in a cylinder on whose sides the transverse pick up coil was wound: Extra care was taken to prevent any possible movement or rotation of the sample with respect to the applied magnetic field. Vacuum grease in the slot surrounds the sample, and fills the slight voids between the walls and the sample. At low temperatures the frozen grease prevents motion of the specimen.

Two orthogonal superconducting coils made of multifilamentary NbTi wire provide separately and independently the longitudinal and the transverse magnetic field. The axial magnetic field $H_{//}$ is supplied by a long solenoid which is positioned inside and rigidly clamped to a rectangular coil which produces the transverse magnetic field $H_{\perp}$.

We monitor continuously the magnetization of the sample using two orthogonal pick up coils, one measuring the magnetization $\mu_o \langle M_{//} \rangle$ along the axis of the ribbon and the other $\mu_o \langle M_{\perp} \rangle$ along the width of the specimen. Following standard practice, each pick up coil is connected in series opposition to a bucking coil which senses the corresponding applied magnetic field but does not "see" the sample. A schematic of the sample and pick up coils is shown in Fig. 2.1. Each balanced pick

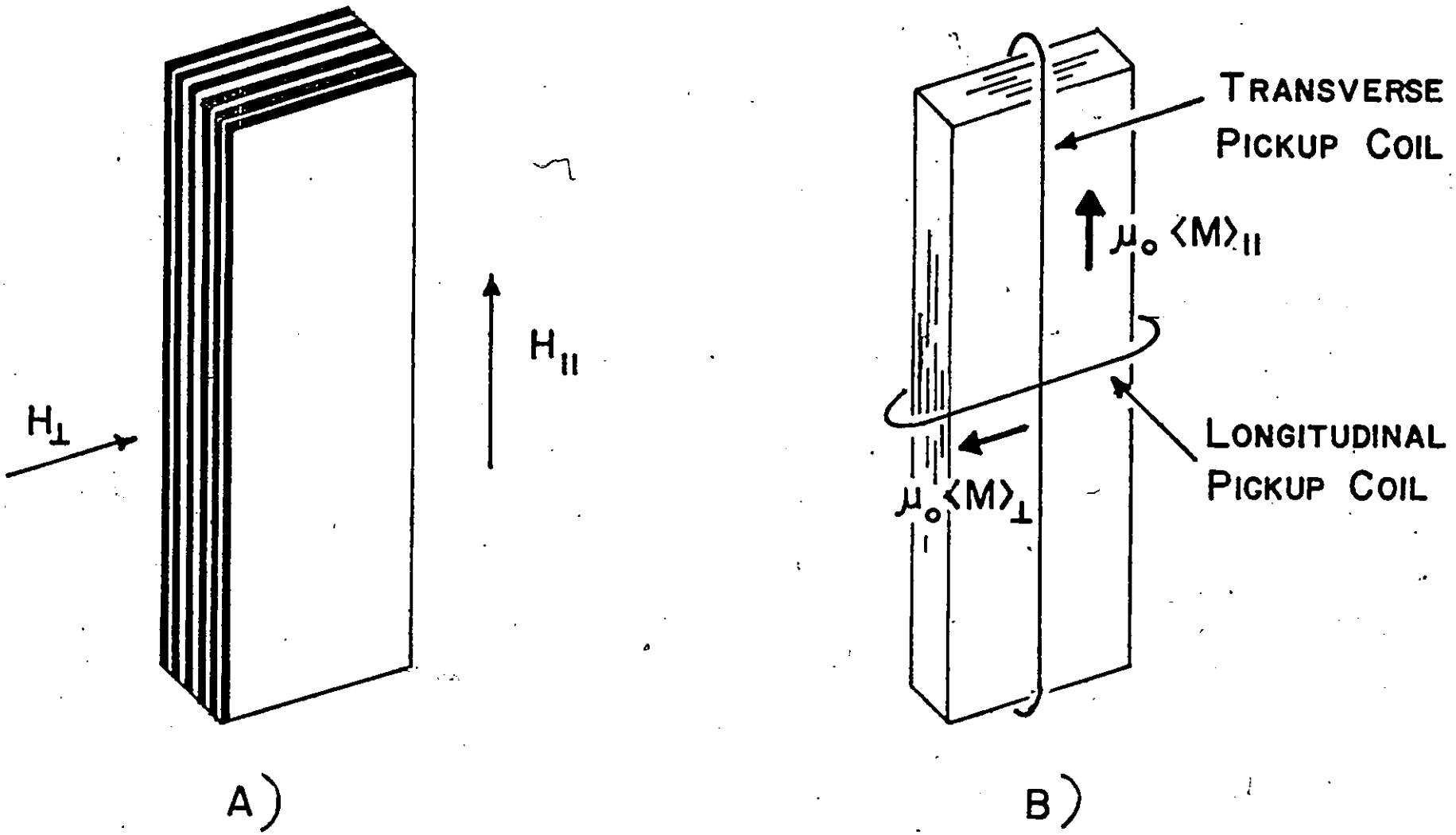

FIG. 2.1. Schematic of sample A) and pick up coil B) arrangement.

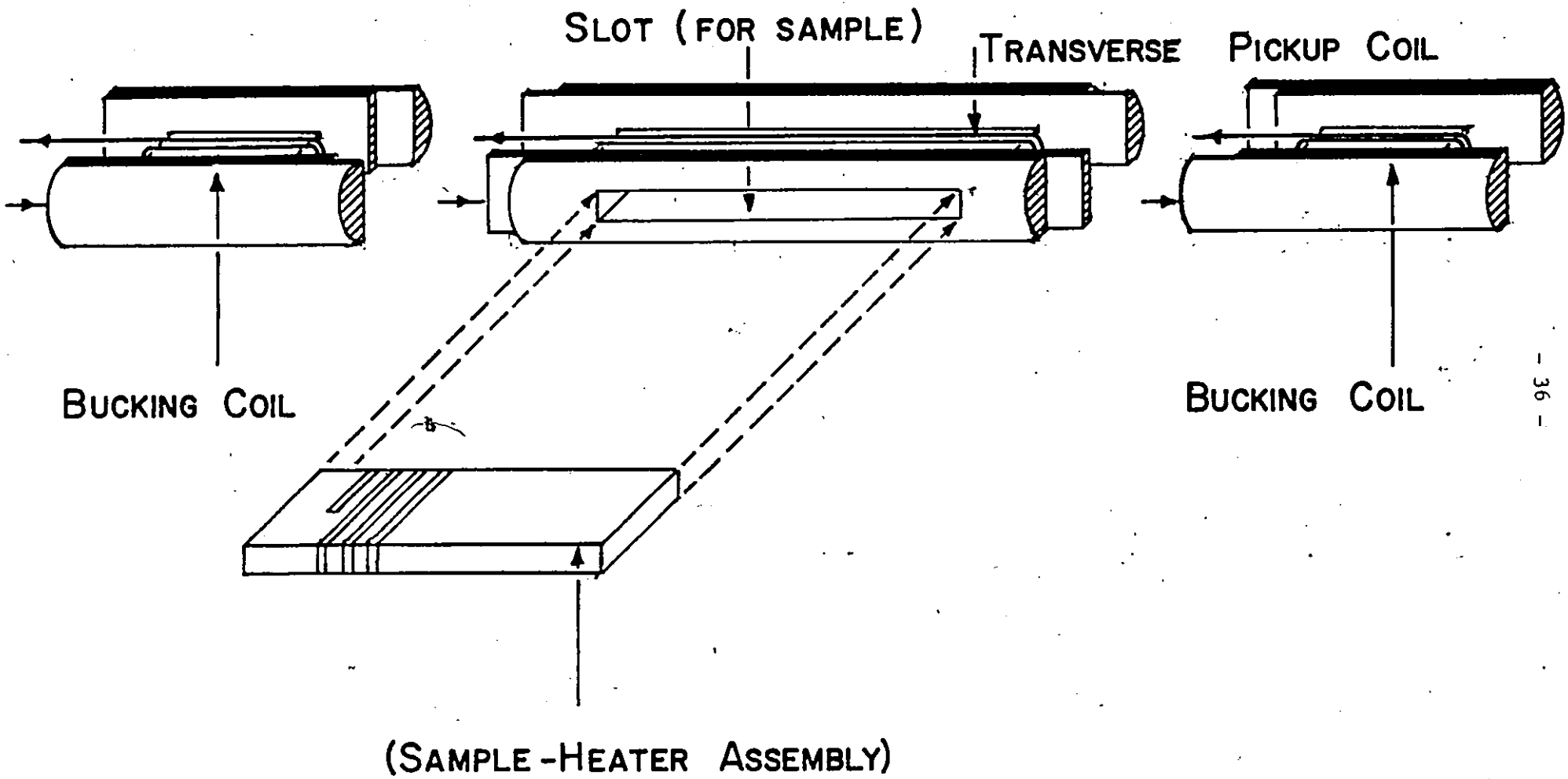

FIG. 2.2. Schematic of sample-heater-transverse pick up coil assembly.

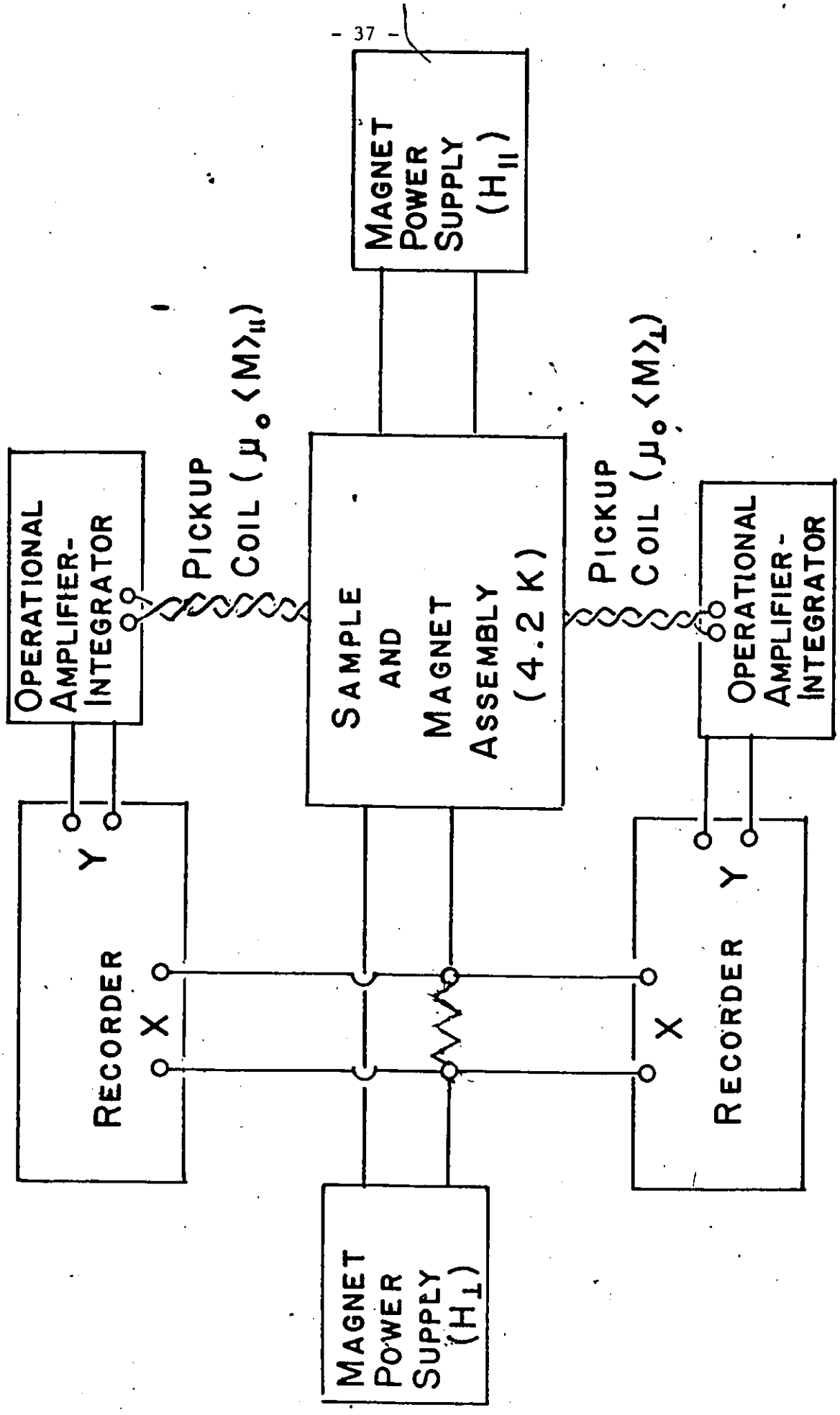

FIG. 2.3. Schematic of measurement set-up.

up coil feeds an operational amplifier-integrator (PAR Model 215) which drives the Y axis of an X-Y recorder. The X axis of the recorders are driven by a signal proportional to the transverse field $H_{\perp}$ or to the longitudinal field $H_{//}$ according to the situation under study. We separately monitor the longitudinal and the transverse components of the magnetization of the sample continuously and simultaneously using two X-Y recorders, as the transverse field $H_{\perp}$ or the longitudinal field $H_{//}$ is varied slowly over the desired ranges. A schematic of the experimental set up is shown in Fig. 2.3. Following standard procedure, the magnetization curves are calibrated on the assumption that negligible flux enters the virgin specimen during the initial rise of the applied magnetic field in the low field range below H_{c1} (perfect diamagnetism). The magnetic field at which the magnetization ceases to be linear is taken as H_{c1}.

2.4 TYPICAL MEASUREMENTS

A- Simple magnetization curve

The sample is cooled below T_c (becomes superconducting) in the absence of a magnetic field (except for the earth's magnetic field). Then the applied axial magnetic field (or the transverse field) is increased. The corresponding signal from the pick up coil is monitored continuously as the applied axial field (or transverse field) is varied. Then the sample is heated to above T_c to erase traces of this magnetic history and the measurement is repeated with the sample in the normal state. This is necessary to determine the background signal due to slight unbalance of the bucking coil, and nonlinear dependence of the

applied field on the generating current, etc.

B- The four categories of initial magnetic states envisaged are the following,

i) nonmagnetic: the sample becomes superconducting in the presence of a magnetic field ($H_{//}$ or $H_{\perp}$) then a magnetic field orthogonal to the first ($H_{\perp}$ or $H_{//}$) is applied.

ii) diamagnetic: the sample becomes superconducting in zero field (earth's field) then the longitudinal (or transverse) magnetic field is increased to the chosen value.

iii) paramagnetic: the sample becomes superconducting in $H_{//}$(or $H_{\perp}$) $\geq$ H_{c2} or from a high value if H_{c2} is excessive. $H_{//}$(or $H_{\perp}$) is then lowered to a selected value of the same polarity.

iv) hybrid: the sample becomes superconducting in $H_{//}$ (or $H_{\perp}$) $\geq H_{c2}$ or from a high value if H_{c2} is excessive. $H_{//}$(or $H_{\perp}$) is then lowered to a selected value of the opposite polarity.

C- Hysteresis Measurements: Types of Measurements, Precautions and Procedures.

We have measured hysteresis losses in two basically different regimes, denoted collinear and noncollinear. The initial applied magnetic field, $\vec{H}_i$, and the maximum superimposed magnetic field increment, $\Delta\vec{H}$ have the same orientation in the collinear regime whereas they are tilted with respect to each other in the noncollinear case. The situation where $\Delta\vec{H}$ and $\vec{H}_i$ are orthogonal constitutes a specially interesting case of the noncollinear regime. In our work, $\Delta\vec{H}$ is always directed either along

the length of the ribbon ($\Delta H_{//}$) or perpendicular to the length and parallel to the flat faces ($\Delta H_{\perp}$). Also, in our work, in the collinear regime, $\vec{H}_i$ is chosen either parallel ($H_{//}$) or transverse ($H_{\perp}$). Representative instances of these two regimes are sketched on the next page.

For each regime we have investigated the response of the specimens over a large span of H_i and a wide range of ΔH. Two particular cases of the collinear regime are of special interest and are denoted full-wave and half-wave. In the former $H_i = 0$, in the latter $H_i = \Delta H$. These two situations have been examined quite extensively by previous workers and lend themselves more readily to analytic treatment and exposition. Analogs of these two cases are encountered in the non-collinear regime and are sketched in Fig. 2.4(ii) (a) and (b).

The approach we adopt, of specifying an initial applied magnetic field $\vec{H}_i$ and regarding $\pm \Delta\vec{H}$ as a vector added symmetrically to this reference vector, may appear to be just a matter of convenience. It can be argued that only the extremal vectors are required and significant. Indeed in the analysis of the hysteresis curves, the initial conditions play no role and only the external B profiles and the progression between these enter into the picture. An alternative representation of the non-collinear regime is shown in Fig. 2.4 (iii). Measurements by J. R. Cave in our laboratory and some published data show , however, that in practice, the results depend, although perhaps not markedly, on previous history hence on the choice of $\vec{H}_i$. For this reason in our work we always specify the set of initial conditions, i.e., the previous temperature-magnetic field history since the onset of the superconducting state. In our

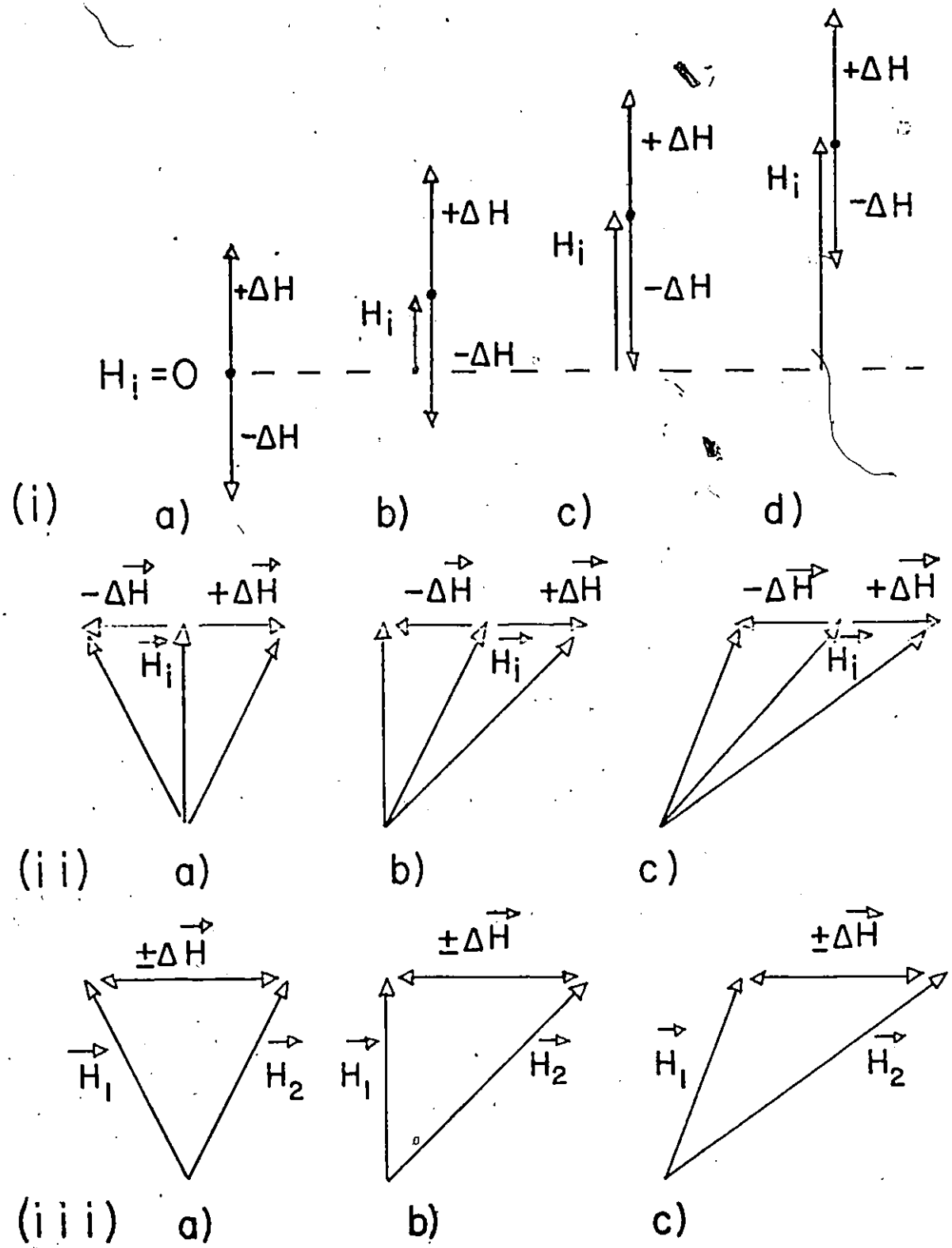

FIG. 2.4 Schematic representations of various categories of cycles of $\vec{H} + \Delta\vec{H}$ where (i) $\vec{j}$ is perpendicular to $\vec{B}$ and (ii) and (iii) $\vec{j}$ has a component along $\vec{B}$.

investigation of hysteresis losses we choose to always let the sample cool from T_c to 4.2 K in the selected $\vec{H}_i$. and varied $\pm\Delta\vec{H}$ symmetrically about this "bias" vector, proceeding first to $\vec{H}_i + \Delta\vec{H}$ then to $\vec{H}_i - \Delta\vec{H}$.

It is now well established that a superconducting coil generates a magnetic field H which is a nonlinear and hysteretic function of I, the current fed into the superconducting coil. This contrasts with normal metal (eg. copper) coils where H is a linear and single valued function of I, hence can be written H = CI, where C is a geometric factor. The problem of hysteresis is less severe when the superconducting coil is wound with multifilamentary wire rather than with tape. Further both a large ratio of length to outer diameter and a small ratio of outer to inner diameter tend to reduce the hysteresis. The reason for this is that the hysteresis arises from persistent closed currents induced to circulate in the body of the winding. As a consequence, the hysteresis increases and eventually "saturates" as the sweep in H increases.

The hysteresis of our long and relatively thin wire wound solenoid, in isolation, is not significant in most of our measurements. The rectangular coil, however, although wire wound, exhibits, as expected because of its geometry, more hysteresis. The problem of hysteresis becomes more acute when the rectangular coil embraces the solenoid orthogonally as in our arrangement. Here the hysteresis curve of H vs I of one coil is affected not only by the presence of the material of the other coil but also be the magnetic field generated by its companion and the magnetic history of the latter.

Ideally then, in view of these features, we should monitor $H_{//}$ and $H_{\perp}$ at the position of the sample with suitable "detectors".

The severe problems and difficulties this solution represents compel us to rely on the currents $I_{//}$ and $I_{\perp}$ fed to the two coils separately to provide the measure of $H_{//}$ and $H_{\perp}$. We are well aware however that neither $I_{//}$ nor $I_{\perp}$ are exact and single-valued functions of $H_{//}$ and $H_{\perp}$. To minimize the consequences of this approach we have exploited a procedure which, we found, ensures reproducibility of the data and reduces contributions or distortions arising from the hysteresis of the varying applied magnetic fields.

We describe this procedure by focussing on a specific situation. Consider Fig. 2.4 (ii) (c). $\vec{H}_i$ is produced by first applying the parallel component and then the transverse component. This order of application is retained throughout a given investigation. Next $H_{\perp}$ is raised to the selected upper limit $H_{\perp} + \Delta H_{\perp}$ and subsequently cycled repeatedly between that limit and the lower limit $H_{\perp} - \Delta H_{\perp}$. This cycling establishes the locus of the hysteresis which the superconducting coils traverse. Now we proceed to the determination of the raw data for the response of the sample to this identical field cycle. This determination always requires two parts. In one part, (i) the sample is maintained normal and in the other, (ii) the sample is in the superconducting state (at 4.2 K) having become superconducting in $\vec{H}_i$. The order of these measurements is immaterial but it is crucial that the sense and the limits of the variation of the applied field selected earlier by preserved throughout all the cycles. The signals from the pick up coils versus the current generating the varying component of $\vec{H}$ ($\Delta\vec{H}_{\perp}$ in the present case) are recorded in (i) and (ii). The "background" curve, (i), is substracted from the response curve, (ii), and the resultant tracing constitutes

the final data which we display on convenient scales in this thesis.

CHAPTER 3

MODEL OF NON ROTATING VORTICES

3.1 INTRODUCTION

Type II superconductors exhibit a variety of interesting behaviour when a transport current I is made to flow along the length of a specimen immersed in a magnetic field $H_{//}$ directed along the longitudinal axis of the sample. In particular, (i) the capacity of wires and ribbons to carry a lossless current I_c is appreciably augmented (C), (ii) hysteresis losses at low frequencies are substantially diminished (A(iii)) and (iii) the magnetic induction along $H_{//}$ varies as I is changed even though $H_{//}$ is maintained stationary(67,68,73,142-145).

Campbell and Evetts (141) have correctly stressed that an understanding of these phenomena should be developed from considerations of the movement of quantized flux vortices since the behaviour of these entities and their interaction with each other and with the metallic lattice ultimately dictate the evolution of the macroscopic configurations of the magnetic induction and the distribution of the current. A basic and simple situation of practical interest is that of a long, wide ribbon immersed in a magnetic field directed along its length. The initial density of flux lines threading the ribbon parallel to its length may be uniform or may vary with depth. A conduction current is now caused to flow along the length of the ribbon either by induction or through leads attached to the ends. For purposes of analysis the ribbon is visualized as a segment of an infinite slab. Campbell and Evetts in their monograph (141) have put forward and explored the

interesting postulate that the sheets of vortices already permeating the slab and those subsequently nucleated at the surface, as the current is impressed, retain their orientation as they are made to migrate inside the specimen.

In this thesis, we focus on infinite slab geometry and examine in detail the consequences of this assumption. Campbell and Evetts (141) have already developed some general aspects of this approach and pursued a few specific cases. Yamafuji et al. (75) have explored the special situation where the pinning behaviour is of the Bean-London (2, 13) type.

The concept that vortices migrate inside an infinite slab without undergoing rotation is attractive for its simplicity and appears very plausible at first glance. Further, it is in many instances, readily amenable to analytic treatment. We will show however that upon closer scrutiny this picture leads to behaviour not in accord with observations when pursued over extensive ranges and generates unphysical results in a variety of fundamental situations and in the limit of H_{c2}. Nevertheless an examination of the predictions of the model is of interest and provides a basis for estimating the extent of rotation of flux sheets occurring in real cases.

First we develop basic formulae to describe the evolution of the average components of the magnetic induction and the velocity of the vortices as the external field varies in intensity and direction. We believe that our development is simpler and our formulation physically more transparent than that found in the literature. We also present several new and useful relationships. We apply the general expressions to a comparative study of the behaviour ensuing from this model when there is no pinning,

hence force free configurations occur, and when a variety of pinning functions of the form $F_p = \alpha_n B^n$ operate, where n = 0, ½ and 1. These choices span a wide spectrum of the dependence of the pinning force density on the magnetic induction (B). The predictions also compared with observations for the simple situation frequently encountered in practice where $B_{//}$, the longitudinal component of the magnetic induction at the surface is maintained stationary as the transverse component $B_{\perp}$ is increased from zero. We examine the behaviour which arises for a variety of initial configurations of the longitudinal magnetic induction in the slab, namely (i) nonmagnetic or uniform, (ii) diamagnetic, (iii) paramagnetic and (iv) coexisting diamagnetic and paramagnetic or hybrid.

Further, we develop general expressions for mapping out the sequences of $B_y(x)$ and $B_z(x)$, the spatial distribution or profiles of the components of the magnetic induction. We apply these formulae to the special situation where $B_{//}$ is kept fixed and F_p is of the simple form given above. We explore the spatial variation of the angle subtended by the electric field $\vec{E}$ and the current density $\vec{J}$ as $\vec{B}$ varies with $B_{//}$ stationary. We also examine the behaviour for the critical transport current I_c vs. $H_{//}$ predicted by this model. Finally, we discuss some features of the problem when magnetic flux varying in orientation with depth is made to exit from the slab under the constraint that no rotation of the vortices takes place as they migrate outwards.

3.2 COMMENT ON THE PHYSICAL CONTEXT

We consider an infinite slab of thickness x = 2a. Experimentally this geometry can be approximated by using a long, wide ribbon. The wide surfaces of the ribbon (the surfaces of the infinite slab) are located at x = 0 and x = 2a. An externally applied magnetic field $H_{//}$ is directed along the length of the ribbon which we take as the z-axis. We visualize for simplicity, that $H_{//}$ is held stationary. Initially, flux lines thread the infinite slab along the z direction only. Depending on the previous magnetic history in the superconducting state, the density of flux lines may be uniform across the thickness of the slab or vary with depth. In all instances we visualize that the density of the magnetic induction $\vec{B}$ is uniform along the y and z-axis and varies with x only. Now the external magnetic field $\vec{H}_s$ along the surfaces of the slab is made to increase in strength and vary in orientation by the introduction of a component $H_\perp$ growing from zero and directed along the y-axis. As this occurs, sheets of flux lines are generated at the surfaces and penetrate into the slab. Two special cases for the origin of $H_\perp$ are of interest.

$H_\perp$ appears because a conduction current I per unit width along the y-axis is fed into the slab via leads attached to the ends at $z = \pm \infty$ and connected to an external current source. This conduction current per unit width can be written $I = \int_0^{2a} J_z(x)\, dx$ where $J_z(x)$ is the current density along the z-axis and the transverse magnetic field generated at the surfaces and outside of the infinite slab by this conduction current is $H_\perp = \pm I/2$. The y component of the magnetic induction then satisfies the condition $B_y(x) = -B_y(2a-x)$. This condition

requires that the only source of the y directed external magnetic field is the current I.

Alternatively, a uniform magnetic field $H_\perp$ may be externally applied along the y-axis. The infinite slab is then visualized as consisting of two halves divided by a midplane at x = a. A persistent current I per unit width is inductively generated by the application of $H_\perp$ and flows in opposite senses along the z-axis in each half of the infinite slab where $I = \int_0^a J_z(x)\,dx$. The "return" paths for this "circulating" current are situated at $z = \pm \infty$. The B_y profiles in the two halves are mirror images across the midplane and satisfy the condition $B_y(x) = B_y(2a-x)$.

Both of these arrangements have been exploited experimentally (66, 68, 142-144) and are complementary. The experimental results we present in this thesis have been obtained using the latter (generation by induction) approach.

The total magnetic field at the surfaces of the slab is given by

$$H_s = (H_{//}^2 + H_\perp^2)^{1/2} \tag{3.1}$$

regardless of which of the two techniques just described is used for generating $H_\perp$. It is convenient in the calculations and in the sketches to consider only one half of the infinite slab. We choose to focus on the half lying between the surface at x = 0 and the midplane located at x = a. The configurations of the magnetic induction

$$\vec{B}(x) = \hat{y}\, B_y(x) + \hat{z}\, B_z(x) \tag{3.2}$$

which are encountered as $H_\perp$ increases are then independent of the mode of production of the latter.

3.3 GENERAL FORMULATION OF THE MODEL

The crucial and basic assumptions we make are that planes of vortices as they advance (or retreat), (i) maintain their orientation of nucleation and (ii) are conserved. In the present context, conservation of vortices means that "spontaneous" creation or disappearance inside the superconductor is forbidden. The concept of conservation, however, allows for the process of mutual annihilation of oppositely directed adjacent vortex sheets. The changes of the components of the magnetic induction in a sheet of infinitesimal thickness Δx is then governed by two equations of continuity

$$\frac{\partial}{\partial x}(B_y v) = -\frac{\partial B_y}{\partial t} \tag{3.3}$$

$$\frac{\partial}{\partial x}(B_z v) = -\frac{\partial B_z}{\partial t} \tag{3.4}$$

which follow from the separate conservation of flux along the y and z directions respectively. These two differential equations are coupled through the spatially varying velocity of migration $\vec{v} = \hat{x}\, v_x(x)$ of the vortex planes moving in the x direction only. They express the constraints that the number and the orientation of flux lines are conserved inside the superconductor after nucleation. For brevity, we write v without the subscript throughout this chapter.

Since $B = \sqrt{B_y^2 + B_z^2}$, where $B_y = B_y(x,t)$ and $B_z = B_z(x,t)$

then $$B_y \frac{\partial B_y}{\partial x} + B_z \frac{\partial B_z}{\partial x} = B \frac{\partial B}{\partial x}$$

and $$B_y \frac{\partial B_y}{\partial t} + B_z \frac{\partial B_z}{\partial t} = B \frac{\partial B}{\partial t}$$

Consequently equations (3.3) and (3.4) can be combined to yield the relationship

$$\frac{\partial}{\partial x} (Bv) = -\frac{\partial B}{\partial t} \tag{3.5}$$

which is an "equation of continuity" for the density $N = B/\phi_o$ of the flux lines, where ϕ_o is the flux quantum. Equation (3.5) however only contains the requirement that flux does not vanish (except by mutual annihilation) inside the superconductor and does not forbid rotation of the flux lines.

The rate of increase of the average components of the magnetic induction can be obtained by integrating equations (3.3) and (3.4) over the half thickness a.

In all of the situations which we examine, v = 0 at the mid-plane by symmetry considerations. Integration of equations (3.3), (3.4) and (3.5) over space from x to a then leads to

$$v(x)\, B_y = \int_x^a \frac{\partial B_y}{\partial t}\, dx' \tag{3.6a}$$

$$v(x)\, B_z = \int_x^a \frac{\partial B_z}{\partial t}\, dx' \tag{3.7a}$$

$$v(x)\, B = \int_x^a \frac{\partial B}{\partial t}\, dx' \tag{3.8a}$$

We will find it convenient to introduce the following notation

$$\langle B_y \rangle_x = \frac{1}{a-x} \int_x^a B_y dx', \quad \langle B_z \rangle_x = \frac{1}{a-x} \int_x^a B_z dx'$$

$$\langle B \rangle_x = \frac{1}{a-x} \int_x^a B dx' \quad .$$

$$\langle B_y \rangle = \frac{1}{a} \int_o^a B_y dx', \quad \langle B_z \rangle = \frac{1}{a} \int_o^a B_z dx',$$

$$\langle B \rangle = \frac{1}{a} \int_o^a B dx'$$

Equations (3.6a) and (3.7a) can also be obtained "more formally" in the following manner. Writing the Maxwell-Faraday equation $\nabla \times \vec{E} = -\partial B/\partial t$ for infinite slab geometry and integrating over space yields

$$(3.9) \qquad E_y(x) = \int_x^a \frac{\partial B_z}{\partial t} dx' \quad \text{and} \quad E_z(x) = -\int_x^a \frac{\partial B_y}{\partial t} dx'$$

since $E_y(a) = 0$ and $E_z(a) = 0$ by symmetry. Next, using the Lorentz equation

$$(3.10) \qquad \vec{E} = -\vec{v} \times \vec{B}$$

where,

$$\vec{v} = \hat{x}\, v_x(x) \quad \text{and}$$

the negative sign appears because the flux lines are moving with respect to the metallic lattice. The absence of the components $v_y(x)$ and $v_z(x)$ in $\vec{v}$ follows from the requirement that the vortices do not change orientation as they migrate. Equating components from equation (3.10) with

the corresponding components from equation (3.9) leads to equations (3.6a) and (3.7a).

Using equation (3.8a) to eliminate v(x) in equations (3.6a) and (3.7a) leads to

$$(3.11a)\quad \frac{d}{dt}\langle B_y\rangle_x = \frac{B_y}{B}\frac{d}{dt}\langle B\rangle_x$$

and

$$(3.12a)\quad \frac{d}{dt}\langle B_z\rangle_x = \frac{B_z}{B}\frac{d}{dt}\langle B\rangle_x$$

Focussing on the surface, equations (3.6a), (3.7a), (3.8a), (3.11a) and (3.12a) can be written

$$(3.6b)\quad v_s B_\perp = a\frac{d}{dt}\langle \vec{B}_y\rangle$$

$$(3.7b)\quad v_s B_{//} = a\frac{d}{dt}\langle B_z\rangle$$

$$(3.8b)\quad v_s B_s = a\frac{d}{dt}\langle B\rangle$$

$$(3.11b)\quad \frac{d}{dt}\langle B_y\rangle = \frac{B_\perp}{B_s}\frac{d}{dt}\langle B\rangle$$

$$(3.12b)\quad \frac{d}{dt}\langle B_z\rangle = \frac{B_{//}}{B_s}\frac{d}{dt}\langle B\rangle$$

where v_s denotes the instantaneous velocity of entry of the flux lines at the surface and we use the notation $B_s = B(0)$, $B_\perp = B_y(0)$ and $B_{//} = B_z(0)$ to denote the magnetic induction and its components at (but inside) the surface of the superconducting slab. Equilibrium diamagnetism and the surface barrier to flux entry or exit will determine the relationship between these quantities and the external magnetic field H_s and its components $H_\perp$ and $H_{//}$. We can set these complications aside

and develop the consequences of the basic postulates of the model by focussing on what occurs inside the specimen as $\vec{B}_s = \hat{y}\, B_\perp + \hat{z}\, B_{//}$ is made to vary. This is the approach which we adopt.

Integrating the above equations over time, we obtain

$$(3.13) \qquad \langle B_y \rangle - \langle B_y \rangle_i = \frac{1}{a} \int_o^t v_s\, B_\perp\, dt'$$

$$(3.14) \qquad \langle B_z \rangle - \langle B_z \rangle_i = \frac{1}{a} \int_o^t v_s\, B_{//}\, dt'$$

$$(3.15) \qquad \langle B \rangle - \langle B \rangle_i = \frac{1}{a} \int_o^t v_s\, B_s\, dt'$$

$$(3.16) \qquad \langle B_y \rangle - \langle B_y \rangle_i = \frac{1}{a} \int_o^t dt' \frac{B_\perp}{B_s} \int_o^a \frac{\partial B}{\partial t}\, dx$$

$$(3.17) \qquad \langle B_z \rangle - \langle B_z \rangle_i = \frac{1}{a} \int_o^t dt' \frac{B_{//}}{B_s} \int_o^a \frac{\partial B}{\partial t}\, dx$$

The previous magnetic history of the specimen (prior to time $t = 0$) dictates the initial configuration of the magnetic induction $\vec{B}_i(x)$ and determines the spatial averages $\langle B_y \rangle_i$, $\langle B_z \rangle_i$ and $\langle B \rangle_i$ of the initial $B_y(x)$, $B_z(x)$ and $B(x)$ profiles. We shall examine in some detail how the initial B profile affects the evolution of $\langle B_y \rangle$ and $\langle B_z \rangle$ by influencing v_s (or equivalently $d\langle B \rangle/dt$).

Equations (3.13), (3.14), (3.16) and (3.17) are general expressions describing the evolution of $\langle B_y \rangle$ and $\langle B_z \rangle$ with time under the constraints that vortices are conserved and maintain their orientation of creation as they migrate. Equation (3.15) only contains the restriction that flux lines are conserved after creation and allows them to rotate inside the superconductor. These expressions apply whether both or either $B_\perp$ and $B_{//}$ are varying with time and are independent of their rate of variation. When vortices are entering the slab, θ_c, the

angle of creation of the new vortices can be written $\theta_c = \tan^{-1} B_\perp/B_{//}$ and is prescribed by the direction of the magnetic induction $\vec{B}_s$ at but inside the surface. The variations of θ_c and B_s with time are independent quantities and can, in principle, be chosen by the external agent (the experimentalist). In situations, however, where vortices are exiting from the slab, the angle of departure or disappearance of vortices as they arrive at the surface, $\theta_d = \tan^{-1} B_\perp/B_{//}$ is dictated by the existing flux configuration. Consequently, now, only the variation of B_s with time can be chosen by the external agent and θ_d becomes a function of B_s generated during the creation of the vortices. This important feature has been ignored in the literature and severely limits the application of the model in cyclic situations (eg. A.C. losses). We develop some aspects of this problem in a later section. For completeness we also note at this juncture that the model cannot describe situations where $\vec{B}_s$ is made to rotate (or oscillate) at constant magnitude (48, 146).

If the sweep of the magnitude of $\vec{B}_s$ is sufficiently slow, viscous effects can be neglected and the sequence of B profiles can be visualized as a succession of quasi-static critical state configurations. Then the instantaneous B profiles and their spatial averages are independent of dB_s/dt and "follow" B_s only. Equations (3.16) and (3.17) can be written

$$(3.18) \qquad \langle B_y \rangle - \langle B_y \rangle_i = \int_{B_{si}}^{B_s} \frac{B_\perp}{B'_s} \, d\langle B \rangle$$

and

$$(3.19) \qquad \langle B_z \rangle - \langle B_z \rangle_i = \int_{B_{si}}^{B_s} \frac{B_{//}}{B'_s} \, d\langle B \rangle$$

where <B> will henceforth be viewed as a quasi-static critical state function of the time varying magnetic induction B_s'. Here the prime indicates a dummy variable and B_{si} denotes the initial value of B_s'.

We note from inspection of equations (3.16) through (3.19) that the orientation of the vortices inside the slab need not be determined in order to map out the evolution of $\langle B_y \rangle$ and $\langle B_z \rangle$ when $\vec{B}_s$ is increasing in magnitude while changing direction. This considerably simplifies our work since the solution of the problem then hinges solely on a knowledge of the sequences of B profiles. According to prevailing views these profiles can be established by exploiting the critical state concept.

3.4 VELOCITY DISTRIBUTION OF THE VORTICES

The velocity distribution of the vortices can be obtained by solving equation (3.8) which is the integral form of the equation of continuity (equation (3.5)). Useful and interesting expressions for v(x) can be readily obtained in the limit where viscous effects can be ignored. Under these circumstances, the critical state equation can be written

$$(3.20) \qquad B \frac{dB}{dx} = \pm F_p(B)$$

where

$$(3.21) \qquad F_p(B) = \frac{f_p(B)}{dH/dB}$$

is a pinning function characterizing the specimen and the equilibrium diamagnetic permeability $\mu = B/H(B)$ gives rise to the term in the

denominator in equation (3.21).

Differentiating equation (3.20) with respect to B_s and noting that $B = B(x, B_s)$ leads to

$$(3.22) \qquad \frac{\partial}{\partial x}\left(\frac{\partial B}{\partial B_s}\right) + \frac{1}{B}\left(\frac{\partial B}{\partial x} \mp \frac{\partial F_p}{\partial B}\right)\left(\frac{\partial B}{\partial B_s}\right) = 0$$

since $$\frac{\partial}{\partial B_s}\left(\frac{\partial B}{\partial x}\right) = \frac{\partial}{\partial x}\left(\frac{\partial B}{\partial B_s}\right)$$

Recalling that differential equations of the form

$$(3.23) \qquad \frac{dy}{dx} + P(x)\, y = Q(x)$$

have solutions of the form

$$(3.24) \qquad y = \left(\int Q(x)dx\; e^{\int P dx} + C\right) e^{-\int P dx}$$

and letting

$$y = \frac{\partial B}{\partial B_s}, \quad P(x) = \frac{1}{B}\left(\frac{\partial B}{\partial x} \mp \frac{\partial F_p}{\partial B}\right), \quad Q(x) = 0$$

we obtain

$$\frac{\partial B}{\partial B_s} = \frac{CF_p}{B}$$

where we have made use of

$$\int \frac{1}{B}\frac{\partial B}{\partial x}\,dx = \int \frac{dB}{B} = \ell n B \qquad \text{and}$$

$$\pm\int \frac{1}{B}\left(\frac{\partial F_p}{\partial B}\right)dx = \pm\int \frac{1}{B}\,\frac{\partial F_p}{(\partial B/\partial x)} = \pm\int \frac{dF_p}{(\mp F_p)} = -\ell n F_p$$

In the preceding manipulations, we have repeatedly made use of

the consideration that $B = B(x, B_s)$ and $F_p(B) = F_p(B(x, B_s))$.

At the surfaces $\frac{\partial B}{\partial B_s} = 1$ hence $C = B_s/F_p(B_s)$ and finally

$$(3.25) \qquad \frac{\partial B}{\partial B_s} = \frac{F_p(B)}{B} \quad \frac{B_s}{F_p(B_s)}$$

Since $B(x)$ depends on time only through B_s, then

$$\frac{\partial B}{\partial t} = \frac{\partial B}{\partial B_s} \frac{dB_s}{dt} \quad \text{and}$$

$$(3.26a) \qquad \frac{\partial B}{\partial t} = \left(\frac{dB_s}{dt}\right) \frac{B_s}{F_p(B_s)} \frac{F_p(B)}{B}$$

and

$$(3.26b) \qquad \frac{\partial B}{\partial t} = \pm \left(\frac{dB_s}{dt}\right) \frac{B_s}{F_p(B_s)} \left(\frac{\partial B}{\partial x}\right)$$

which apply to the region where the B profile is changing with time.

Equation (3.25) can be visualized and developed less formally as follows. The critical-state equation leads to solutions sketched in Figure 3.1 where the vertical dashed lines represent the midplane and a surface of the slab. Any critical configuration can be traced by fixing the position of these boundaries relative to the master curve of $B(x)$. Referring to Figure 3.1, the critical state equation leads to

$$\Delta B' = f(x')\Delta x' \qquad \text{and} \qquad \Delta B'' = f(x'')\Delta x''$$

where $f(x) = F_p(B(x))/B(x)$. Let Δx_o represent a shift of origin and take $\Delta x' = \Delta x'' = \Delta x_o$,

then

$$\frac{\Delta B'}{\Delta B''} = \frac{f(x')}{f(x'')} = \frac{dB}{dB_s} = \frac{\partial B}{\partial B_s}$$

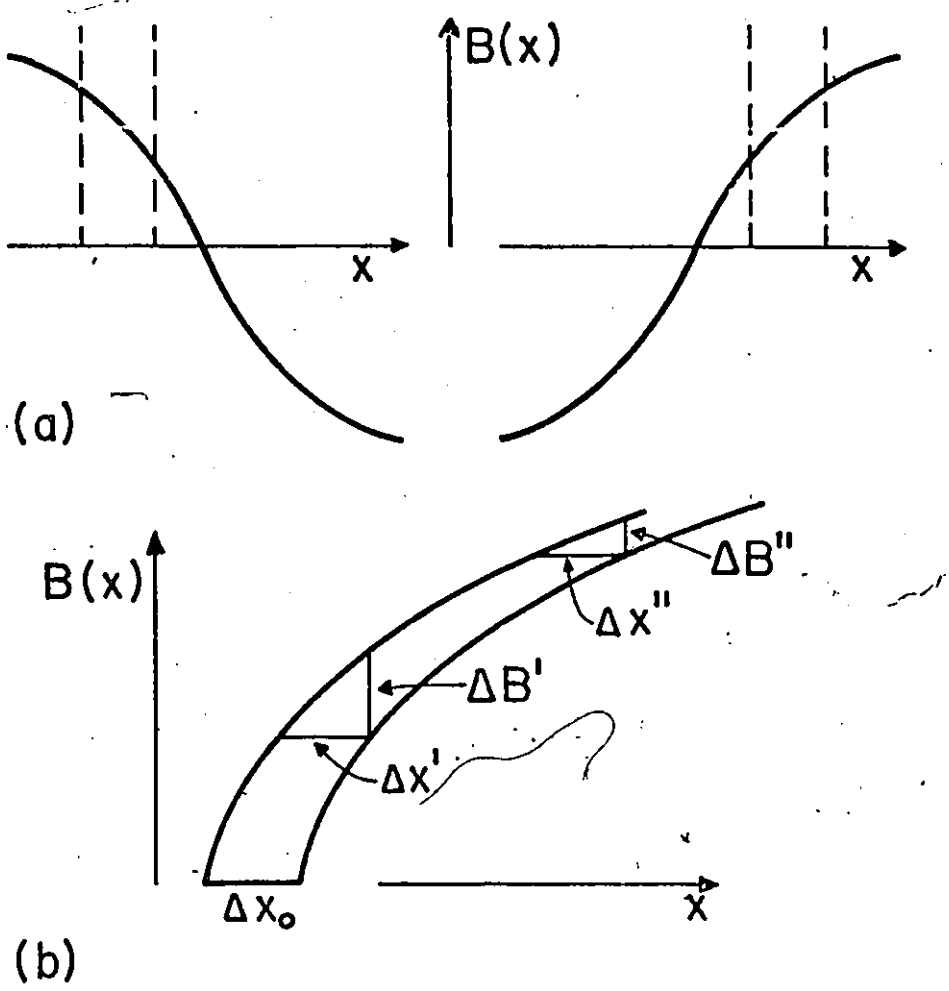

FIG. 3.1. a) Sketch illustrates that any critical state profile can be obtained by drawing the pertinent $B(x) = \pm F_p(B(x))/(dB/dx)$ curve then placing the surfaces of the infinite slab to satisfy, the boundary condition B_s and positioning the midplane at an appropriate distance a from the surface.

b) Two identical B(x) vs. x curves are drawn shifted horizontally with respect to each other, hence $\Delta x_o = \Delta x' = \Delta x''$. Therefore $\Delta B'/\Delta B'' = (F_p(B')/B')/(F_p(B'')/B'') = \partial B/\partial B_s$ if $\Delta B_s = \Delta B''$.

where we identify "ΔB" with ΔB_s. In other words, an increment in B_s is equivalent to a shift of the origin of B(x) with respect to the boundaries of the slab.

Introducing equation (3.26b) into equation (3.8) and integrating from x to x_i leads to

$$(3.27a) \quad v(x) = \pm \left(\frac{dB_s}{dt}\right) \frac{B_s}{F_p(B_s)} \left\{ \frac{B(x) - B(x_i)}{B(x)} \right\}$$

and

$$(3.27b) \quad v_s = \pm \left(\frac{dB_s}{dt}\right) \frac{1}{F_p(B_s)} \left\{ B_s - B(x_i) \right\}$$

where x_i is the depth of penetration of the time varying B profile. At x_i the front of the advancing B disturbance generated by the sweep of B_s intersects the previously existing B profile, hence the progress of x_i and the growth of $B(x_i)$ depend on the initial flux configuration. Inspection of equations (3.27a) and (3.27b) reveals the interesting result that, regardless of the particular B dependence of the pinning, $v(x) = v_s$ if $B(x_i) = 0$.

We will use the expression, saturation, to denote the instance where x_i attains the midplane of the slab. Let B_s^* denote the magnitude of the magnetic induction at but inside the surface when this occurs. Consequently we need to define two ranges for the variation of B_s, (i) before saturation, $B_{si} < B_s \leq B_s^*$ and (ii) after saturation, $B_s > B_s^*$. After saturation, the time varying B(x) profile spans the entire slab as the sweep of B_s (upwards or downwards) continues, B(a), the magnetic induction at the midplane is then independent of previous

history and becomes a function of B_s. We proceed in the context that $F_p(B)$ is known from experimental or theoretical considerations. The quantities x_i, $B(x)$, $B(x_i)$ and $B(a)$ can then, in principle, be obtained from the critical state equation (equation (3.20)) taking the initial configuration into account.

Introducing equations (3.27a) and (3.27b) into equations (3.13), (3.14) and (3.15) leads to

$$(3.28)\quad \langle B_y \rangle - \langle B_y \rangle_i = \pm \frac{1}{a} \int_{B_{si}}^{B_s^*} \frac{B_\perp}{F_p(B_s)} (B_s - B(x_i))\, dB_s$$

$$\pm \frac{1}{a} \int_{B_s^*}^{B_s} \frac{B_\perp}{F_p(B_s)} (B_s - B(a))\, dB_s$$

$$(3.29)\quad \langle B_z \rangle - \langle B_z \rangle_i = \pm \frac{1}{a} \int_{B_{si}}^{B_s^*} \frac{B_{//}}{F_p(B_s)} (B_s - B(x_i))\, dB_s$$

$$\pm \frac{1}{a} \int_{B_s^*}^{B_s} \frac{B_{//}}{F_p(B_s)} (B_s - B(a))\, dB_s$$

$$(3.30)\quad \langle B \rangle - \langle B \rangle_i = \pm \frac{1}{a} \int_{B_{si}}^{B_s^*} \frac{B_s}{F_p(B_s)} (B_s - B(x_i))\, dB_s$$

$$\pm \frac{1}{a} \int_{B_s^*}^{B_s} \frac{B_s}{F_p(B_s)} (B_s - B(a))\, dB_s$$

which apply when B_s varies beyond B_s^*. For situations where B_s does not attain B_s^*, the second integral on the right-hand side does not appear and the upper limit of the first integral in equations (3.28), (3.29) and (3.30) is B_s instead of B_s^*. These three formulae constitute alternative and very useful forms of equations (3.13) through (3.17) but apply only when viscous effects can be ignored. We stress that all of the expressions we have developed so far apply whether $\vec{B}_s$ changes direction or not as its magnitude increases or decreases.

3.5 HYSTERESIS LOSSES: STANDARD SITUATION

Equations (3.27a) and (3.27b) for the velocity distribution of the vortex sheets provides a very useful starting point for calculations of energy dissipation configurations and hysteresis losses in the standard situation where $\vec{B}_s$ oscillates in magnitude only about a fixed initial value B_{si}. We take $\vec{B}_s$ to be directed along the z-axis and ignore subscripts except where pertinent. Introducing equation (3.27a) into equation (3.10) yields for the electric field

$$(3.31) \qquad E_y(x) = \pm \left(\frac{dB_s}{dt}\right) \frac{B_s}{F(B_s)} \left(B(x) - B(x_i)\right)$$

Alternatively, this result follows from introducing equation (3.26b) into equation (3.9) and integrating.

Using Poynting's theorem, $\vec{S} = \vec{E} \times \vec{H}$, the rate of energy flow through a unit area in the y-z plane can be written

$$(3.32) \qquad S(x) = \pm \left(\frac{dB_s}{dt}\right) \frac{B_s}{F(B_s)} \left(B(x) - B(x_i)\right) H_z(x)$$

The rate of energy dissipation per unit volume $dP/dt = \vec{E}.\vec{j}$ becomes

$$(3.33) \qquad \frac{dP(x)}{dt} = \pm \left(\frac{dB_s}{dt}\right) \frac{B_{se}}{F(B_s)} \left(B(x) - B(x_i)\right) \frac{dH}{dx}$$

where we have made use of Maxwell's equation $\nabla \times \vec{H} = \vec{j}$.

Clem (3) has developed expressions analogous to equations (3.31), (3.32) and (3.33) using a different but equivalent approach.

To exploit these expressions we need to specify the equilibrium diamagnetism relation between B and H and the dependence of the surface barrier on B increasing or decreasing. Finally integrations over a period must be performed to yield the net energy dissipation per cycle and hysteresis losses. Clem (3) has pursued this formidable task for a large variety of basic cases.

3.6 EVOLUTION OF $\langle B_y \rangle$ AND $\langle B_z \rangle$

We now examine the effect of different modes of pinning including the absence of pinning (the force free limit) and also the role played by various initial configurations of the magnetic flux on the evolution of $\langle B_y \rangle$ and $\langle B_z \rangle$ in the context that flux lines do not rotate as they are made to migrate into the slab. In this exercise we have focussed on four "basic" pinning behaviours, namely, three of the form $F_p = \alpha_n B^n$ where n = 1, ½ and 0 and the force free case where $F_p = 0$ since $\alpha_n = 0$. The pinning functions with n = 1, ½, and 0 are enshrined in the literature and are associated historically with Bean-London (2, 13), Yasukochi et al.(123) and Kim et al.(119) respectively. These simple expressions span a broad spectrum of the dependence of pinning

on B. When necessary, the existence of an upper bulk critical field B_{c2} can be taken into account by exploiting more complicated formulae of the form $\alpha_n B^n f(B/B_{c2})$ where $f(B/B_{c2})$ are monotonically decreasing functions of B/B_{c2}. These complications, however, generally make numerical solutions necessary.

Integration of equation (3.20) with $F_p = \alpha_n B^n$ yields

$$B(x) = B_s \pm B_* \frac{x}{a} \tag{3.34a}$$

$$B(x) = (B_s^{3/2} \pm B_*^{3/2} \frac{x}{a})^{2/3} \tag{3.34b}$$

$$B(x) = (B_s^{2} \pm B_*^{2} \frac{x}{a})^{1/2} \tag{3.34c}$$

for n = 1, ½ and 0 where $B_* = \alpha_1 a$, $(3\alpha_{1/2} a/2)^{2/3}$ and $(2\alpha_0 a)^{1/2}$ respectively and $B_s^* = B_*$ when $B_{si} = 0$. The negative (positive) sign is used when B_s is increasing (decreasing). These expressions apply in the range $0 \leq x \leq x_i \leq a$. In the range $x_i \leq x \leq a$ expressions similar to the above determine the B profile but the previous magnetic history must be taken into account in specifying the boundary conditions.

We now confine our attention to the special situation where B_s is made to increase from $B_{si} = B_{//}$ with $B_{//}$ stationary.

For the force free case $B(x) = B_s$ throughout the thickness of the slab. Consequently, $d\langle B\rangle/dB_s = 1$ and integration of equations (3.18) and (3.19) leads to

$$\langle B_y \rangle = B_\perp - B_{//} \cos^{-1} \frac{B_{//}}{B_s} \tag{3.35}$$

$$\langle B_z \rangle - B_{//} = B_{//} \ell n \left(\frac{B_s}{B_{//}}\right) \tag{3.36}$$

The initial magnetic configuration or state is established by the magnetic and thermal history of the specimen in the superconducting state prior to the time t = 0 where the variation of $\vec{B}_s$ from $\vec{B}_{si}$ starts. We consider four categories of initial states which are of special interest. These are shown schematically in Figure 3.2. Let H_i' denote the external magnetic field present when the slab cools from T_c to T_f and H_i its intensity at time t = 0 when the initial state has been established. We take H_i' and H_i to be collinear and directed along the z-axis. For ease in visualizing the initial B profiles we ignore equilibrium diamagnetism and surface barriers. Consequently we introduce the boundary conditions.

(3.37) $\quad B_{si} = \mu_o H_i \quad$ and $\quad B_{si}' = \mu_o H_i'$

where $\quad \mu_o = 4\pi\ 10^{-7}$ Tm/A.

The four categories of initial magnetic states we envisage are the following:

1) Nonmagnetic; The applied field is not changed after cooling from T_c to T_f. Then $H_i = H_i'$ and $B_i(x) = B_i'(x) = \mu_o H_i = \mu_o H_i'$

2) Diamagnetic; $H_i > H_i' \geq 0$ hence $B_i(x) \geq B_i' \geq 0$.

3) Paramagnetic; $H_i' \leq H_{c2}$ and $0 \leq H_i < H_i'$ hence $0 \leq B(x) \leq B_i'$

4) Hybrid; $H_i' \leq H_{c2}$ and $0 < H_i < H_*$ is directed opposite to H_i'. The crucial feature of this state is that the B profile changes polarity at some depth $0 < x_o < a$. H_* is the applied field starting with $H_i = 0$ which causes the advancing flux gradient to penetrate to the midplane of the slab.

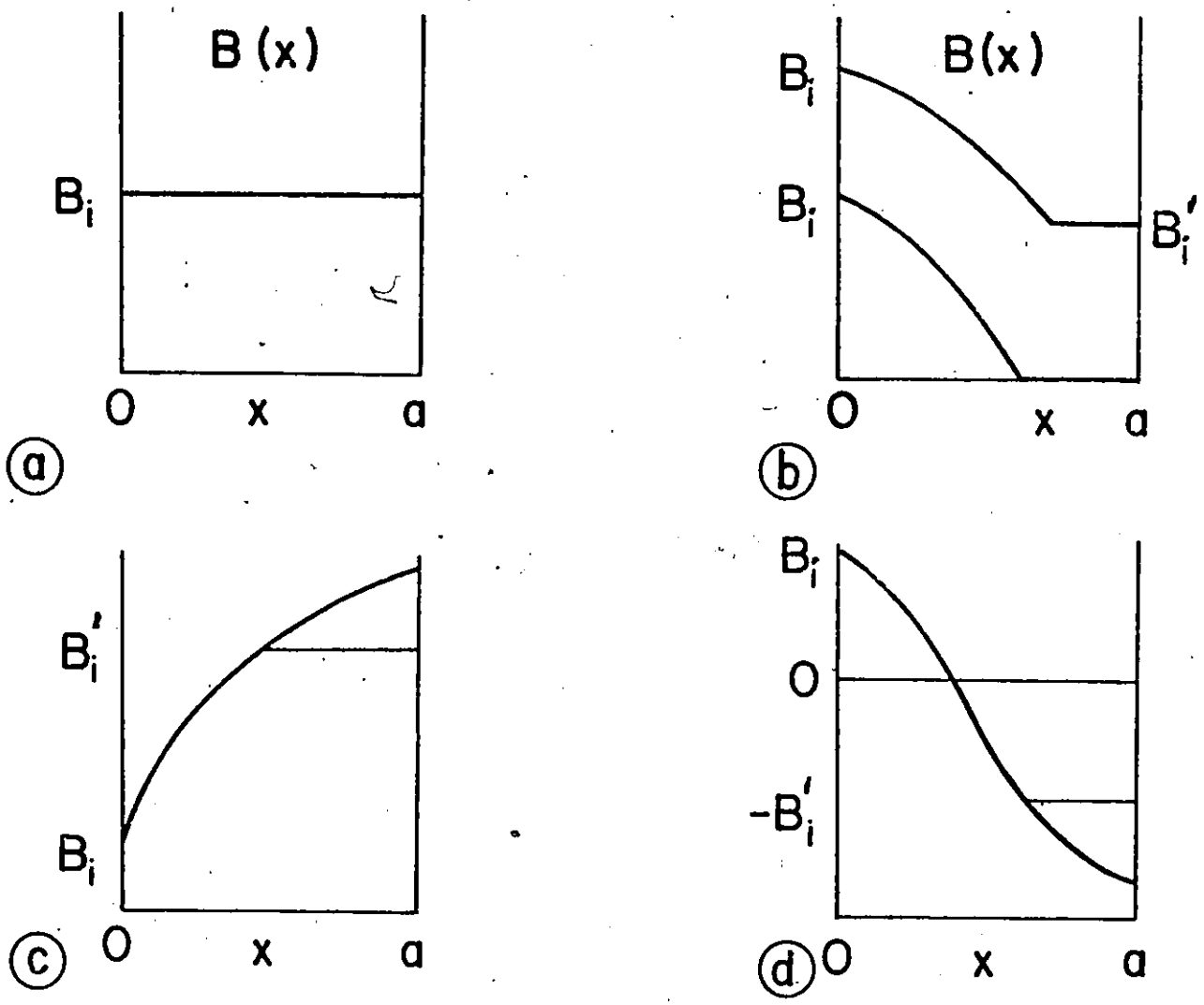

FIG. 3.2 Schematic of initial configurations of magnetic induction.

a) Nonmagnetic, $B(x) = B_i$.

b) Diamagnetic, applied field initially raised to B_i from 0 or from $B_i' \neq 0$.

c) Paramagnetic, applied field decreased to B_i from B_i' or from a field much larger than B_i'.

d) Hybrid, applied field swept to B_i through zero from $-B_i'$ or from a much larger (negative) field. See inserts to Fig. 3.10, 3.14, 3.18 and 3.23 for variation of $H_{//}$ and $H_{\perp}$ in superconducting state.

a) Influence of Pinning

In Figures 3.3 and 3.4 we compare the evolution of $\langle B_y \rangle$ and $\langle B_z \rangle$ as B_s increases from $B_{//}$ (kept fixed) for the four pinning modes listed above and with the slab initially in the nonmagnetic state. The curves are normalized to B_* and we have chosen $B_{//} = B_*$ as a convenient illustrative case. We note that the curves of $\langle B_y \rangle$ and $\langle B_z \rangle$ move away from the horizontal axis in the sequence n = 1, ½ and 0. The force free curve is uppermost in Figure 3.3 and intersects the n = 0 and ½ curves.

For some simple forms of F_p, equations (3.28) and (3.29) can be readily integrated analytically and we present a collection of such results in appendix II. Some of the expressions have already been obtained by Campbell and Evetts (141) and Yamafuji et al.(75). Calculations exploiting these analytic expressions have been performed to provide a check on the computer program we have developed to obtain $\langle B_y \rangle$ and $\langle B_z \rangle$ numerically from equations (3.28) and (3.29) for arbitrary forms of F_p.

When the evolution of $\langle B_y \rangle$ and $\langle B_z \rangle$ is displayed versus $B_\perp$ instead of B_s, the relative position of the curves remains unchanged and their main features are not substantially modified. This can readily be seen by rewriting equations (3.11b) and (3.12b) as follows for comparison

$$(3.11c) \quad \frac{d\langle B_y \rangle}{d B_s} = \frac{B_\perp}{B_s} \frac{d\langle B \rangle}{d B_s}, \quad \frac{d\langle B_y \rangle}{d B_\perp} = \left(\frac{B_\perp}{B_s}\right)^2 \frac{d\langle B \rangle}{d B_s}$$

$$(3.12c) \quad \frac{d\langle B_z \rangle}{d B_s} = \frac{B_{//}}{B_s} \frac{d\langle B \rangle}{d B_s}, \quad \frac{d\langle B_z \rangle}{d B_\perp} = \left(\frac{B_\perp}{B_s}\right)\left(\frac{B_{//}}{B_s}\right) \frac{d\langle B \rangle}{d B_s}$$

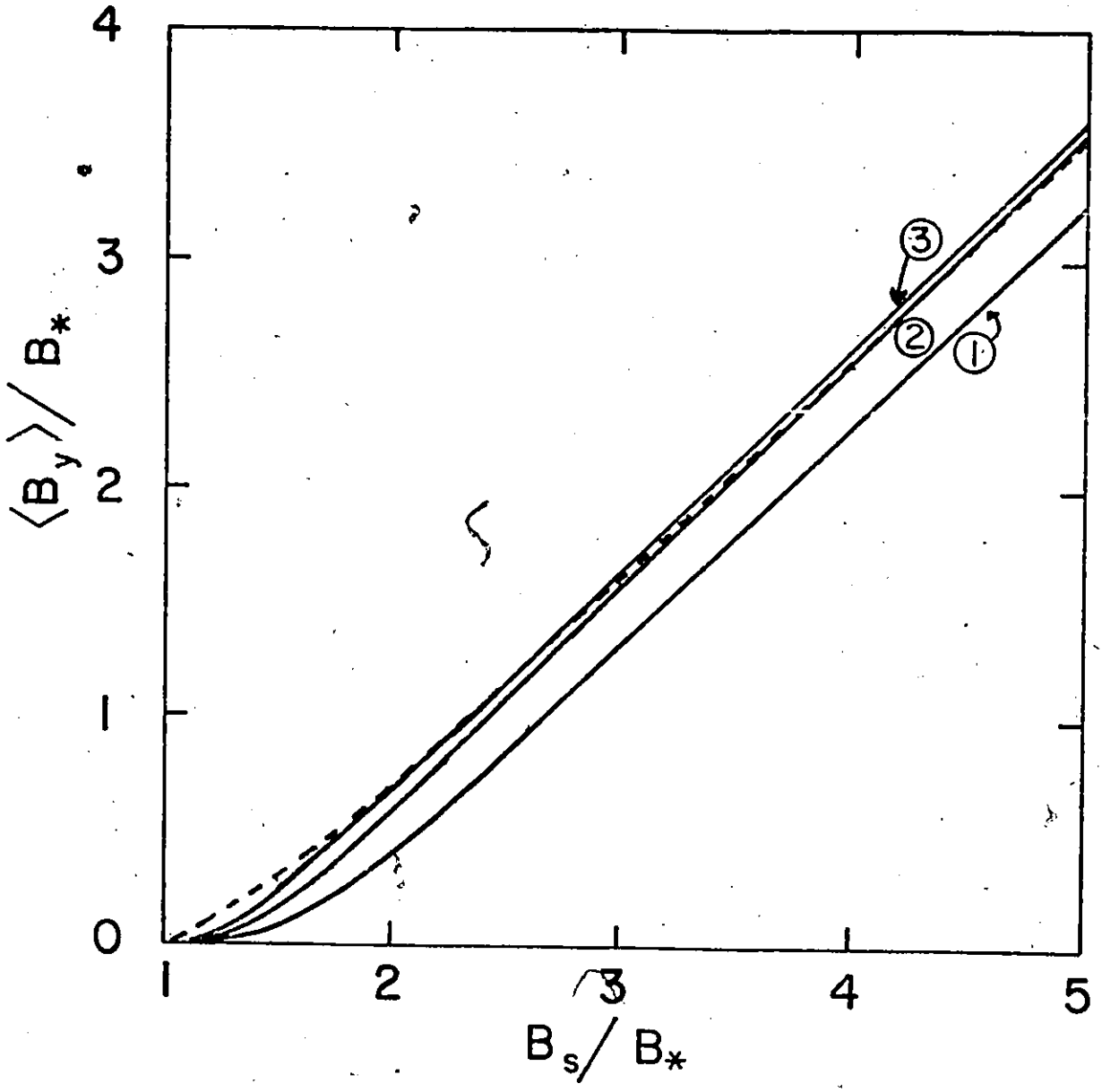

FIG. 3.3 Growth of $\langle B_y \rangle / B_*$ vs. B_s / B_* at constant $B_{//} / B_* = 1.0$ with n = 1 (curve 1), n = 1/2 (curve 2) and n = 0 (curve 3) in $F_p = \alpha_n B^n$. Dashed curve shows force free ($\alpha = 0$) case.

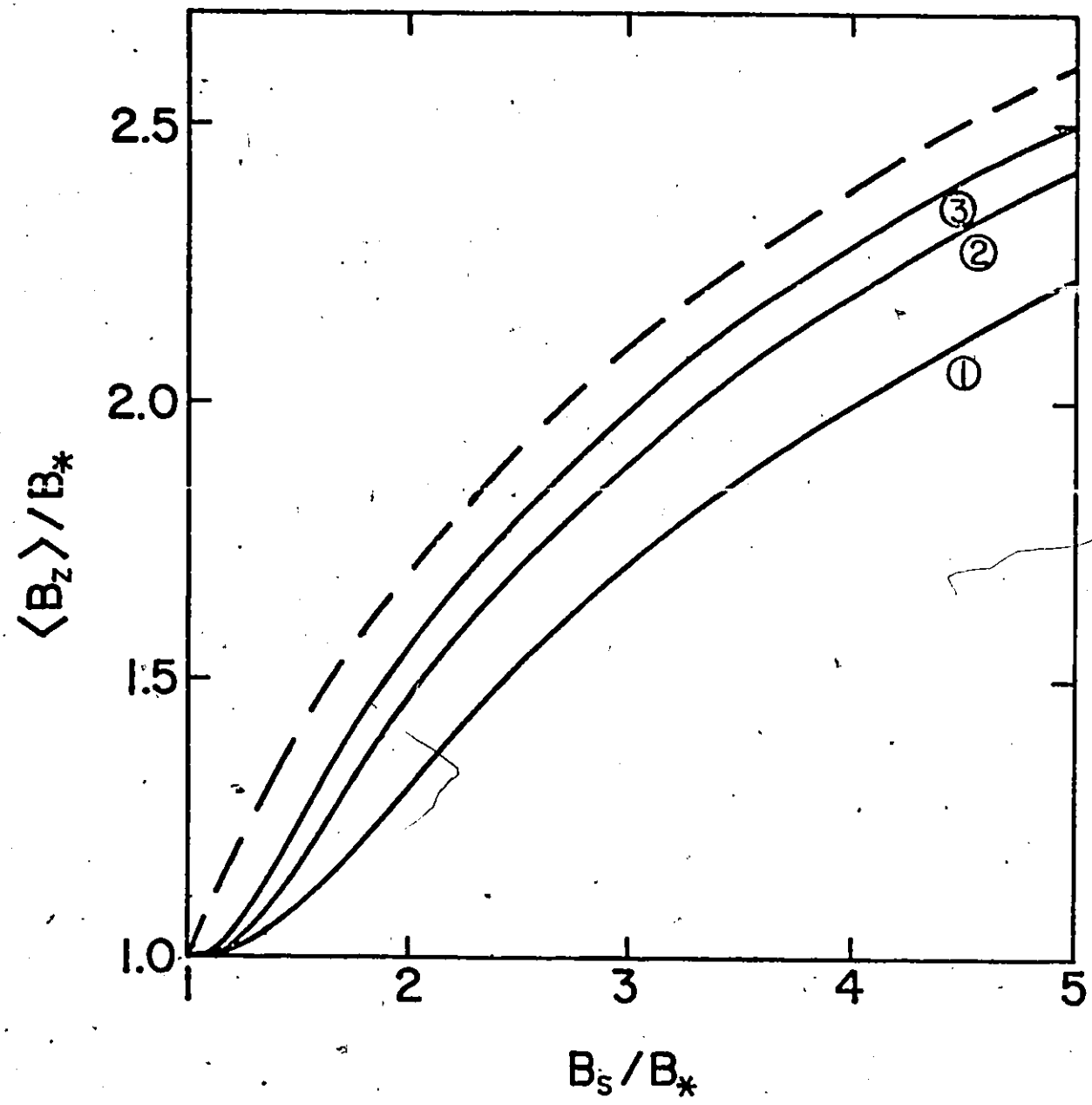

FIG. 3.4 Growth of $\langle B_z \rangle / B_*$ vs. B_s/B_* at constant $B_{//}/B_* = 1.0$ with n = 1 (curve 1), n = ½ (curve 2) and n = 0 (curve 3) in $F_p = \alpha_n B^n$. Curve 4 (dashed) shows force free ($\alpha = 0$) case.

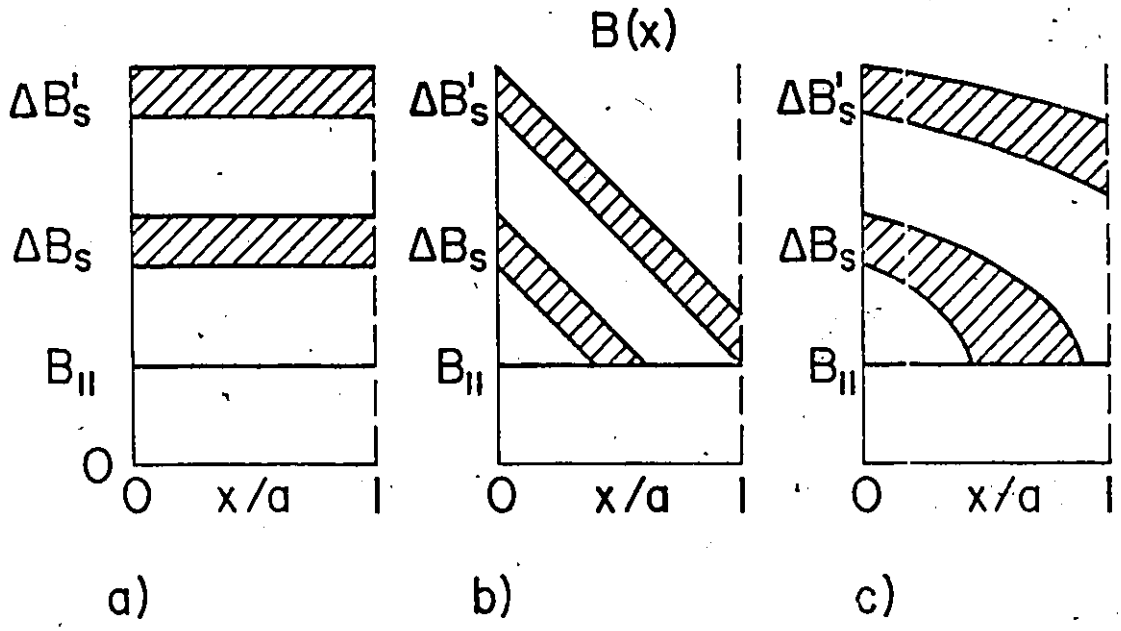

FIG. 3.5 Schematic comparing increment of flux, hence $d\langle B\rangle/dB_s$ for, (a) force free case, (b) Bean-London approximation and (c) Kim approximation.

Here, the expressions on the right apply only when $B_{//}$ is stationary since then $dB_s/dB_\perp = B_\perp/B_s$.

Exploiting numerical or analytic solutions of equation (3.20) to obtain $d\langle B\rangle/dB_s$ we can of course also follow the evolution of $\langle B_y\rangle$ and $\langle B_z\rangle$ by integrating equations (3.11c) and (3.12c) analytically or numerically. We find the latter equations particularly useful in visualizing the behaviour of $\langle B_y\rangle$ and $\langle B_z\rangle$ and in understanding the influence of pinning on this behaviour. This insight can be obtained without performing tedious calculations but by considering sequences of B profiles as sketched in Figure 3.5. In this exercise it is also helpful to examine the expressions for $d\langle B\rangle/dB_s$ which can be readily derived for simple forms of F_p and are presented in appendix I. We note the following pertinent features which emerge from these considerations and account for the relative position of the various curves in Figures 3.3 and 3.4. (i) In the force free case, $d\langle B\rangle/dB_s = 1$ for all values of B_s. (ii) In the Bean-London approximation $d\langle B\rangle/dB_s < 1$ and rises linearly to unity as B_s increases to the saturation value. After saturation, $d\langle B\rangle/dB_s = 1$. (iii) When $0 \leq n < 1$, the B profiles are convex upwards, $d\langle B\rangle/dB_s < 1$ during the initial stages of the approach to saturation and is then greater than for the Bean-London approximation. After saturation $d\langle B\rangle/dB_s \gtrsim 1$.

The rate of growth of $\langle B_y\rangle$ and $\langle B_z\rangle$ after saturation and in the high field range is seen to be insensitive to the presence and mode of pinning. The relative shifts in the various curves arise mainly during the approach to saturation and it is in this limited range that pinning plays a significant role. In view of these predictions, we can

verify whether rotation of vortex sheets occurs during their compression and establish the extent of rotation which occurs by comparing predictions with observations taken for sweeps of B_s well beyond B_s^* at constant $B_{//}$. It is accordingly of interest to pursue the evolution of $\langle B_y \rangle$ and $\langle B_z \rangle$ up to B_{c2}.

We stress that the continuous increase of $\langle B_z \rangle$ in Figure 3.4 is not a consequence of the choices made for F_p which, in effect, takes B_{c2} as infinite. In Figures 3.6 and 3.7 we present curves calculated using equations (3.28) and (3.29) where we have taken $F_p = \alpha B(1 - B/B_{c2})^2$ and chosen $B_{c2} = 4.0\ B_*$ where $B_* = \alpha a$. In these two Figures we display $\langle M_\perp \rangle = (\langle B_y \rangle - B_\perp)/\mu_o$ and $\langle M_{//} \rangle = (\langle B_z \rangle - B_{//})/\mu_o$ versus $H_\perp = B_\perp/\mu_o$ for various stationary values of $B_{//}/B_{c2}$. Again we take the initial state as nonmagnetic. We note that both $\langle M_\perp \rangle$ and $\langle M_{//} \rangle$ are appreciable at $(H_\perp^2 + H_{//}^2)^{1/2} = H_{c2}$ when $H_{//}/H_{c2} \neq 0$ and that $\langle M_\perp \rangle$ increases with $H_{//}/H_{c2}$. The curves displayed in Figures 3.6 and 3.7, except that where $H_{//} = 0$, are not sensitive to the choice of $\alpha_n B^n f(B/B_{c2})$. To illustrate this last feature, we display in Figures 3.8 and 3.9 families of curves of $\langle M_\perp \rangle$ and $\langle M_{//} \rangle$ versus $H_\perp$ calculated with $F_p = \alpha(1 - B/B_{c2})^2$ where $B_{c2} = 4.3\ B_*$ and $B_* = (2\alpha a)^{1/2}$. Inspection shows that the curves in Figures 3.8 and 3.9 nearly overlap the corresponding curves of Figures 3.6 and 3.7. These features are intrinsic to the model of non rotating vortex sheets.

The continuous growth of $\langle B_z \rangle$ with B_s (or $B_\perp$), until B_{c2} is attained, occurs because every vortex added to the slab increases the z component of the magnetic induction. Since the vortices already permeating the specimen, maintain their orientation and are conserved,

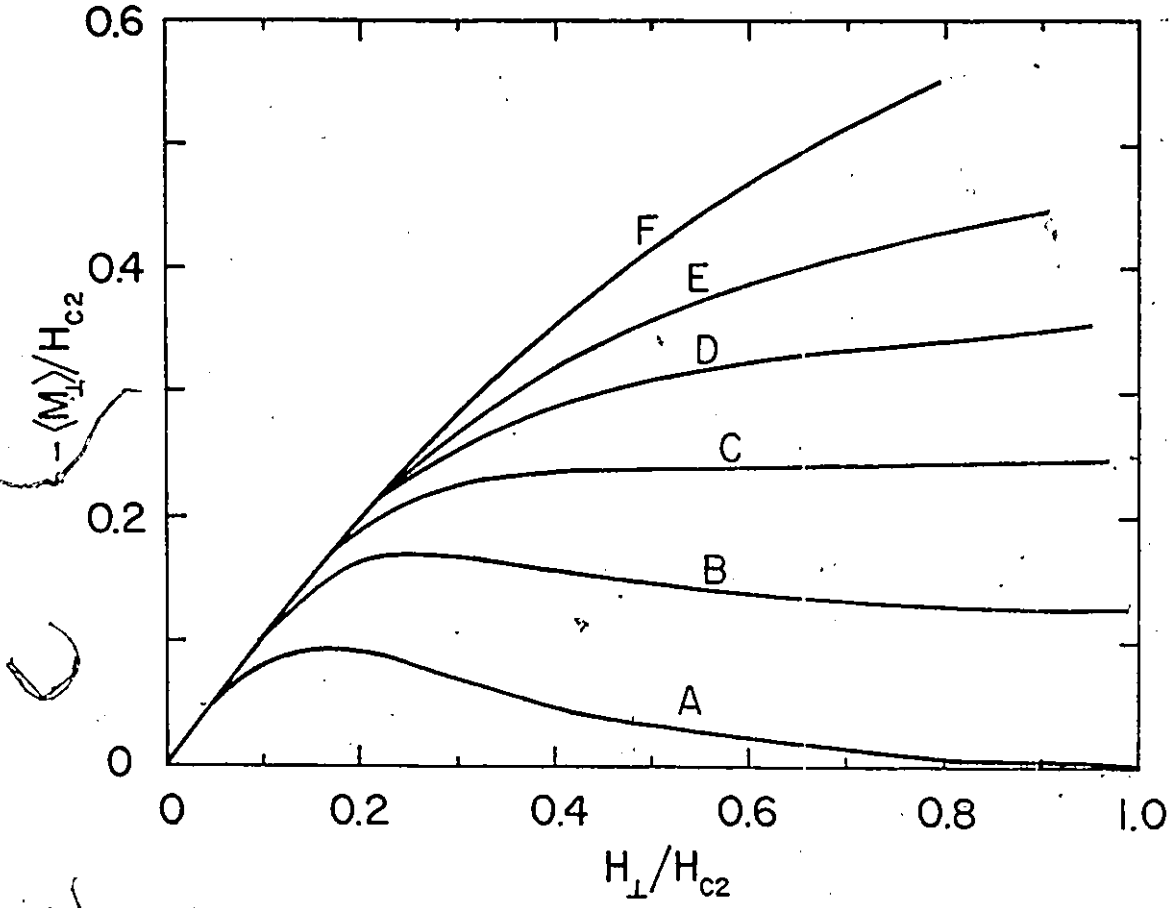

FIG. 3.6 $\langle M_\perp \rangle / H_{c2}$ vs. $H_\perp / H_{c2}$ calculated with $F_p = \alpha B(1 - (B/B_{c2}))^2$ $B_{c2} = 4.0\ B_*$ and $B_* = \alpha a$. Nonmagnetic initial state and $H_{//}/H_{c2}$ stationary at 0.0, 0.1, 0.2, 0.3, 0.4 and 0.6 for curves A, B, C, D, E and F respectively.

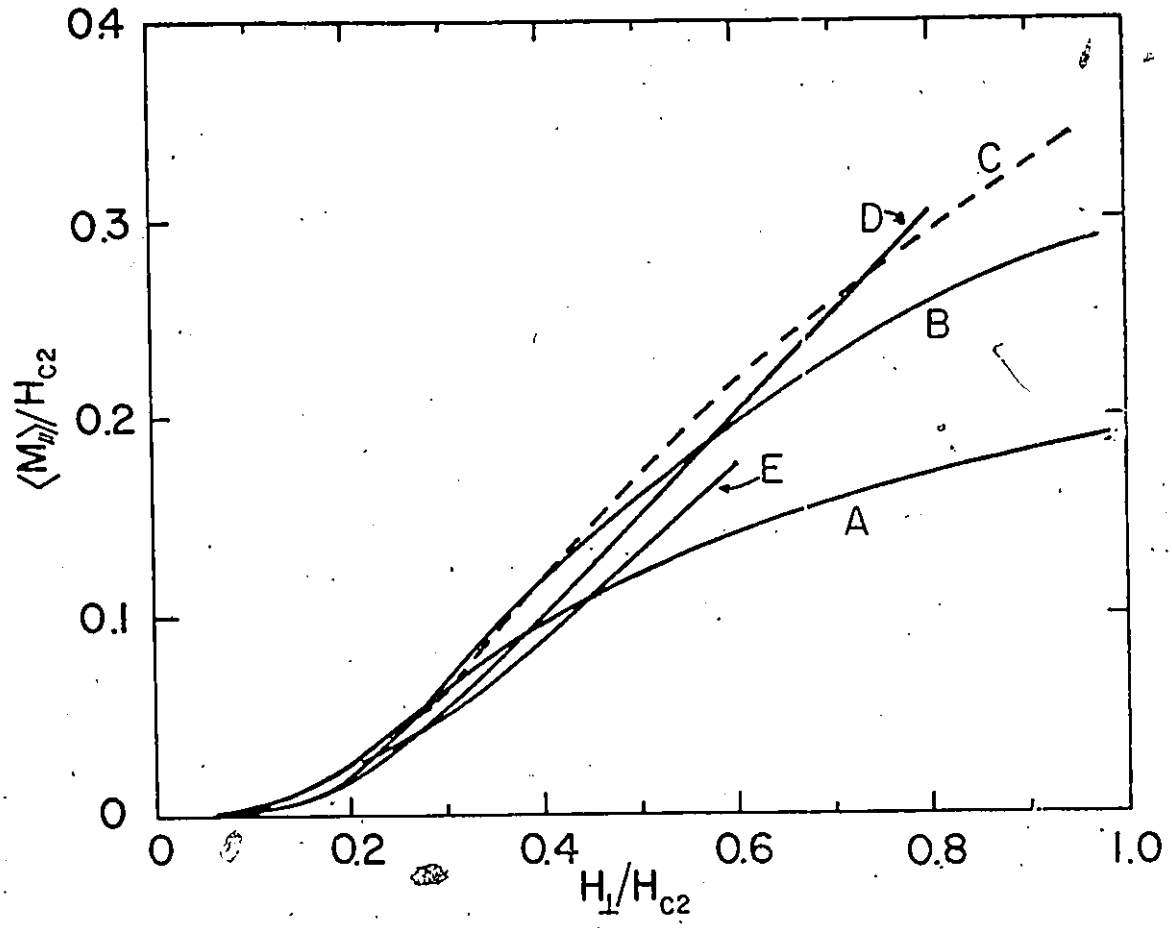

FIG. 3.7 $\langle M_{//} \rangle / H_{c2}$ vs. $H_\perp / H_{c2}$ calculated with F_p, B_{c2} and B_* as in Fig. 3.6. Nonmagnetic initial state and $H_{//}/H_{c2}$ stationary at 0.1, 0.2, 0.3, 0.6 and 0.8 for curves A, B, C, D and E respectively.

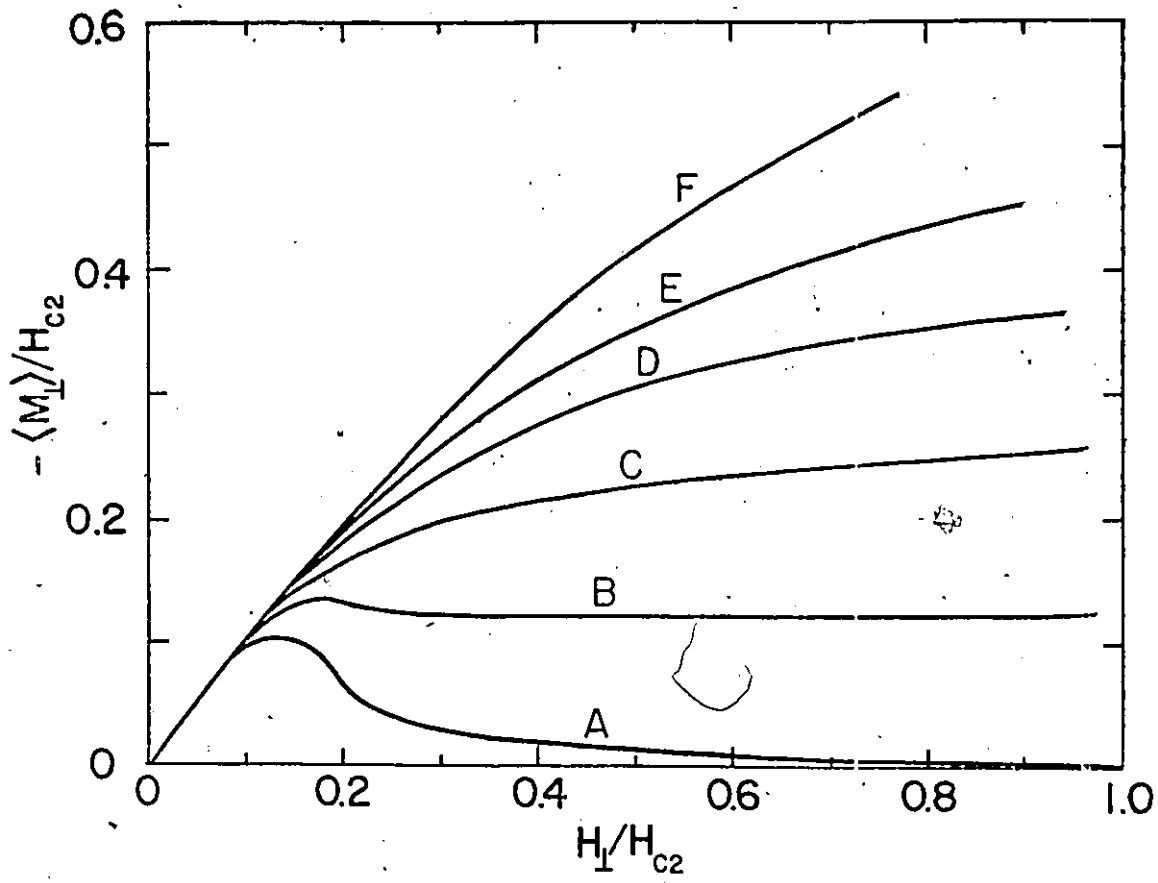

FIG. 3.8 $\langle M_\perp \rangle / H_{c2}$ vs. $H_\perp / H_{c2}$ calculated with $F_p = \alpha(1 - (B/B_{c2}))^2$ where $B_{c2} = 4.3\, B_*$ and $B_* = (2\alpha a)^{\frac{1}{2}}$. Nonmagnetic initial state and $H_{//}/H_{c2}$ stationary at 0.0, 0.1, 0.2, 0.3, 0.4 and 0.6 for curves A, B, C, D, E and F respectively. Compare with Fig. 3.6.

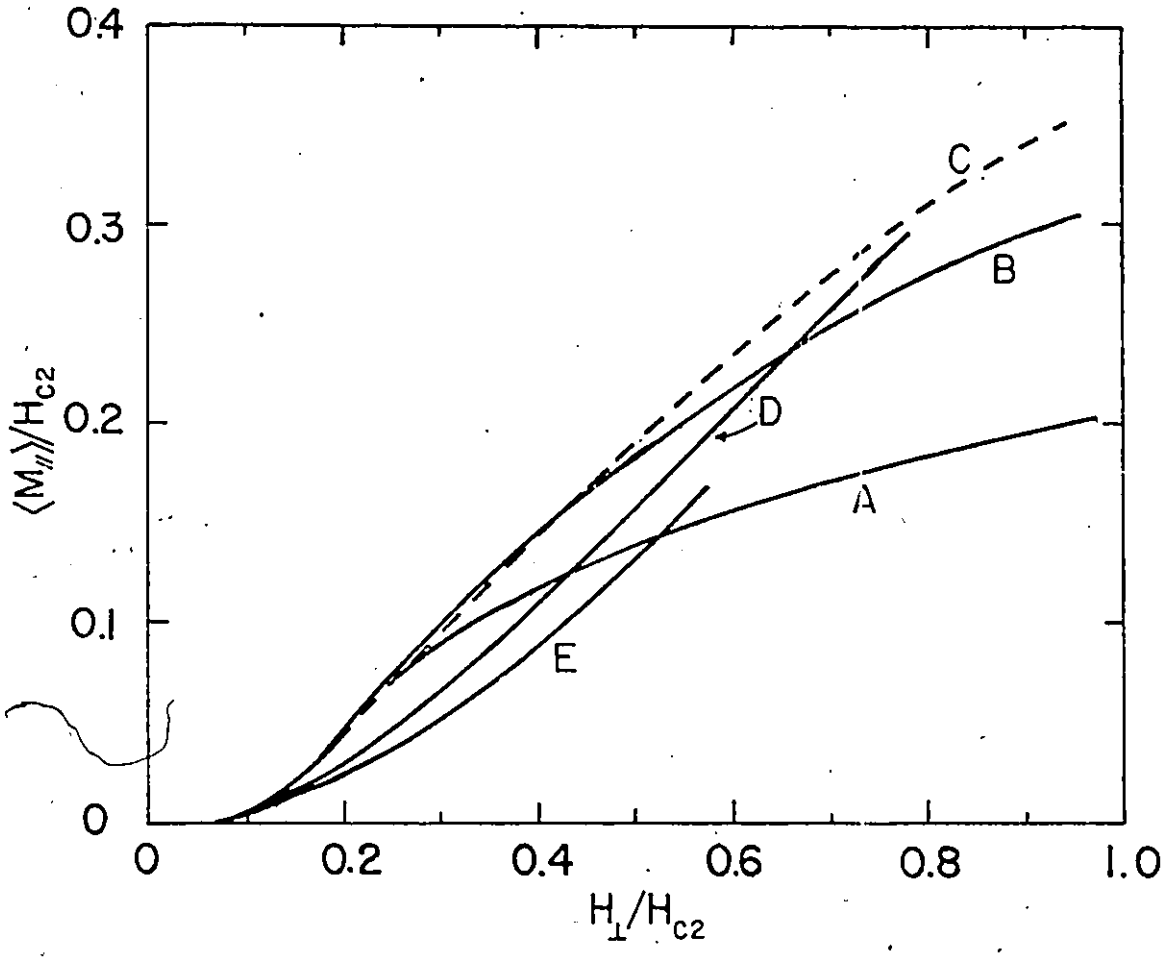

FIG. 3.9 $\langle M_{//} \rangle / H_{c2}$ vs. $H_{\perp}/H_{c2}$ calculated with F_p, B_{c2} and B_* as in Fig. 3.8. Nonmagnetic initial state and $H_{//}/H_{c2}$ stationary at 0.1, 0.2, 0.3, 0.6 and 0.8 for curves A, B, C, D and E respectively. Compare with Fig. 3.7.

there is no mechanism in this model whereby $\langle B_z \rangle$ can reach a plateau or decrease. Inexorably then the model leads to the unphysical existence of a large $\langle B_z \rangle >> B_{//}$ at B_{c2}. The magnetic moment associated with this "excess" component of magnetic induction must disappear discontinuously when the superconducting state is quenched at B_{c2}.

The model also intrinsically leads to the unrealistic result that $\langle B_y \rangle < B_\perp$ at $B_s = B_{c2}$, regardless of the choice of F_p, when $\langle B_z \rangle_i \neq 0$ and $\vec{B}_s$ changes direction as it increases in magnitude. This arises because the B_y profile cannot then penetrate to the midplane but can advance only to a maximum depth

$$\frac{x_{max}}{a} = \frac{B_{c2} - \langle B_z \rangle_i}{B_{c2}} < 1$$

since a central core region of half thickness $a - x_{max}$ must exist to accommodate the vortices initially threading the slab along the z-axis before $B_\perp$ is applied. Again we note that the magnetic moment associated with this "deficit" of magnetic induction must vanish abruptly when the superconducting state is destroyed at B_{c2}.

Experimentally, $\langle M_\perp \rangle$ and $\langle M_{//} \rangle$ after traversing a peak are observed to approach zero asymptotically as H_s approaches H_{c2} (142).

b) Role of Initial Flux Configurations

We examine the evolution of $\langle B_y \rangle$ and $\langle B_z \rangle$ ensuing with the slab in each of the four initial states enumerated earlier in this section. We again confine our attention to the situation where $B_{//}$ is maintained stationary as $B_\perp$ is increased from zero. B_s is swept from various $B_{//}$ to values well beyond B_s^* but low compared with B_{c2}.

It is convenient to display the locus of the components of the magnetization; $\langle M_{\perp} \rangle$ and $\langle M_{//} \rangle$, rather than the magnetic induction, versus $B_{\perp}$. The theoretical curves we present were all calculated using $F_p = \alpha_{\frac{1}{2}} B^{\frac{1}{2}}$ since among the four pinning modes we have explored, this simple form generates the best correspondence with our data and we have taken $B_* = (3\ \alpha_{\frac{1}{2}} a/2)^{2/3}$.

For each initial configuration we present a corresponding family of experimental curves. The experimental data were obtained by continuously monitoring $\langle B_y \rangle$ and $\langle B_z \rangle$ with orthogonal pick up coils embracing a ribbon of $V_{0.24}Ti_{0.76}$ at 4.2 K and each separately feeding an electronic amplifier-integrator which drive the Y axes of an X - Y_1 Y_2 recorder. A signal proportional to $H_{\perp}$ drives the X axis. The experimental arrangement and procedure have been described in chapter 2. H_{c2} at 4.2 K is $\approx$ 4 T . Since H_{c2} for the specimen is appreciably larger than the maximum H_s attained in the measurements we can ignore the existence of H_{c2} in the calculated curves which we present.

i) Nonmagnetic Initial State

Corresponding families of experimental and calculated curves for $\langle M_{\perp} \rangle$ and $\langle M_{//} \rangle$ vs $H_{\perp}$ with the specimen initially in the nonmagnetic state (uniform $B_z = \mu_o H_{//}$) for several values of $H_{//}$ can be compared by inspection of Figures 3.10 through 3.13. The initial growth of the magnetic moments versus $H_{\perp}$ and the rise in the sequence of the curves with $H_{//}$ when $H_{//}$ is small are well reproduced. When $H_{//} \neq 0$, however, the calculated curves continue to grow with $H_{\perp}$

whereas the experimental curves decline after traversing a peak. The latter feature is an indication that the planes of vortices threading the specimen undergo rotation or bending.

ii) Diamagnetic Initial State.

Corresponding families of experimental and calculated curves with the slab initially in the diamagnetic (flux shielding) state can be compared from inspection of Figures 3.14 through 3.17. The rate of quenching of the initial diamagnetic moment and the subsequent growth of a paramagnetic moment along $H_{//}$ is satisfactorily reproduced by the model. As in the nonmagnetic case, the calculated curves continue to rise with $H_{\perp}$ whereas the data curves reach a summit and decline.

iii) Paramagnetic Initial State.

Corresponding families of experimental and calculated curves with the slab initially in the paramagnetic (flux retaining) state can be compared from inspection of Figures 3.18 through 3.21. Again only the initial portions of the experimental curves are reproduced by the model.

The "extreme" case when $H_{//}$ is absolutely zero deserves special comment since the model of non rotating vortex sheets then generates a special situation. Vortex sheets of trapped flux directed along the z-axis are being compressed in the region $x_o \leq x \leq x_i$ as shown schematically in Figure 3.22. The magnetic moment along the z-axis remains constant as $H_{\perp}$ is applied. The region $0 \leq x \leq x_o$ is penetrated by sheets of vortices oriented purely along the y-axis

and created by the application of $H_{\perp}$. The physical picture demanded by the model in this idealized limit is one where the orientation of adjacent sheets of flux lines changes abruptly by 90^{o} at x_o. The "discontinuities" in the B_z and B_y profiles imply that adjacent sheets of persistent currents also change direction abruptly by 90^{o} at x_o. In the model, these discontinuities are smeared out over the macroscopic region $0 \leq x \leq x_o$ provided that $H_{//}$, although very small, is not absolutely zero. In the latter case, $\langle M_{//} \rangle$, according to the model, must increase slightly as $H_{\perp}$ is applied since flux lines with a small component along the z-axis are being created. Under these circumstances we observe (see Figure 3.21) that $\langle M_{//} \rangle$ initially traverses a region where it is slowly diminishing and then decreases rapidly. It is interesting to note that when $H_{//} \neq 0$, the experimental curves do rise initially as $H_{\perp}$ is applied. Subsequently however $\langle M_{//} \rangle$ and $\langle M_{\perp} \rangle$ decline with $H_{\perp}$ suggesting that the flux lines rotate or bend inside the specimen.

iv) Hybrid Initial State.

Corresponding families of experimental and calculated curves with the slab initially in the hybrid or composite (flux shielding and flux retaining) state can be compared from inspection of Figures 3.23 through 3.26. Clearly, the agreement is quite poor.

For the hybrid initial state, novel circumstances are encountered in the application of the model which require special attention. To fix ideas we consider that the slab became superconducting in $H_{//i}$ directed along the negative z-axis. This field

was then reduced in intensity to zero and then increased in strength to $H_{//}$ directed along the positive z direction thereby generating the $B_z(x) = B(x)$ profiles shown schematically in Figures 3.27(a) and 3.27(c). Two cases can occur: (i) the positive flux exceeds the negative flux and (ii) vice versa. The treatment of the first case is straightforward. As $H_\perp$ is impressed, the positively directed flux lines gradually annihilate all of the initial negative flux. The residual positive flux is then compressed in the region $x_o \leq x \leq a$ as sketched in Figure 3.27(b). The evolution of the $B(x)$ and $B_z(x)$ profiles for case (ii) is more complicated. At some juncture during the application of $H_\perp$, the initial positive flux is completely annihilated by a fraction of the negative flux. Subsequently, the residual negative flux is compressed, in a critical state, in a central region $x_o \leq x \leq a$. The crucial differences between the two cases is the sequence of configurations of the $B(x) = B_z(x)$ profile encountered in this central region after flux annihilation has been completed. In applying the model we visualize that flux lines must be perfectly antiparallel for mutual annihilation to take place. Consequently, we assume that flux lines created during the application of $H_\perp$ cannot annihilate with the adjacent planes of residual negatively directed flux lines. The sequence of B and B_z profiles imposed by these idealized requirements are sketched in Figure 3.27(d). Consequently, for case (ii) the sequence of B profiles sketched in Figure 3.27(d) must be taken into account in evaluating $d\langle B\rangle/dB_s$ when equations (11c) and (12c) are exploited.

In the idealized model, in case (ii), as compression takes

place, the B_z profile at x_o changes direction by 180^o less an infinitesimal amount and the residual negative flux persists until H_s attains H_{c2}. In the real situation we expect that the flux lines to the left of x_o, although not exactly antiparallel to those on the right of x_o, will continue to annihilate with the latter until these negatively directed sheets of flux lines have been completely annihilated. A comparison of curves A in Figures 3.25 and 3.26 suggests that this indeed takes place.

Finally we stress that the continuous rise exhibited by the calculated curves presented in this section is a direct consequence of the model itself. This feature then cannot be made to disappear by exploiting pinning functions which decrease to zero as B increases to B_{c2}. Agreement with observations must therefore be sought in setting aside the basic postulate of non rotation of the flux lines.

3.7 SEQUENCES OF $B_y(x)$ AND $B_z(x)$ PROFILES

The evolution of $\langle B_y \rangle$ and $\langle B_z \rangle$ as $\vec{B}_s$ changes direction while increasing in strength can, as we have seen, be followed without a knowledge of the sequence of the $B_y(x)$ and $B_z(x)$ profiles. It is, however, of considerable interest to determine the detailed configurations of these B_y and B_z profiles. Also, this information is necessary in order to calculate the behaviour of $\langle B_y \rangle$ and $\langle B_z \rangle$ for situations where $\vec{B}_s$ undergoes cyclical variations.

The condition that the flux lines maintain their orientation as they migrate and experience compression (or decompression) can be written

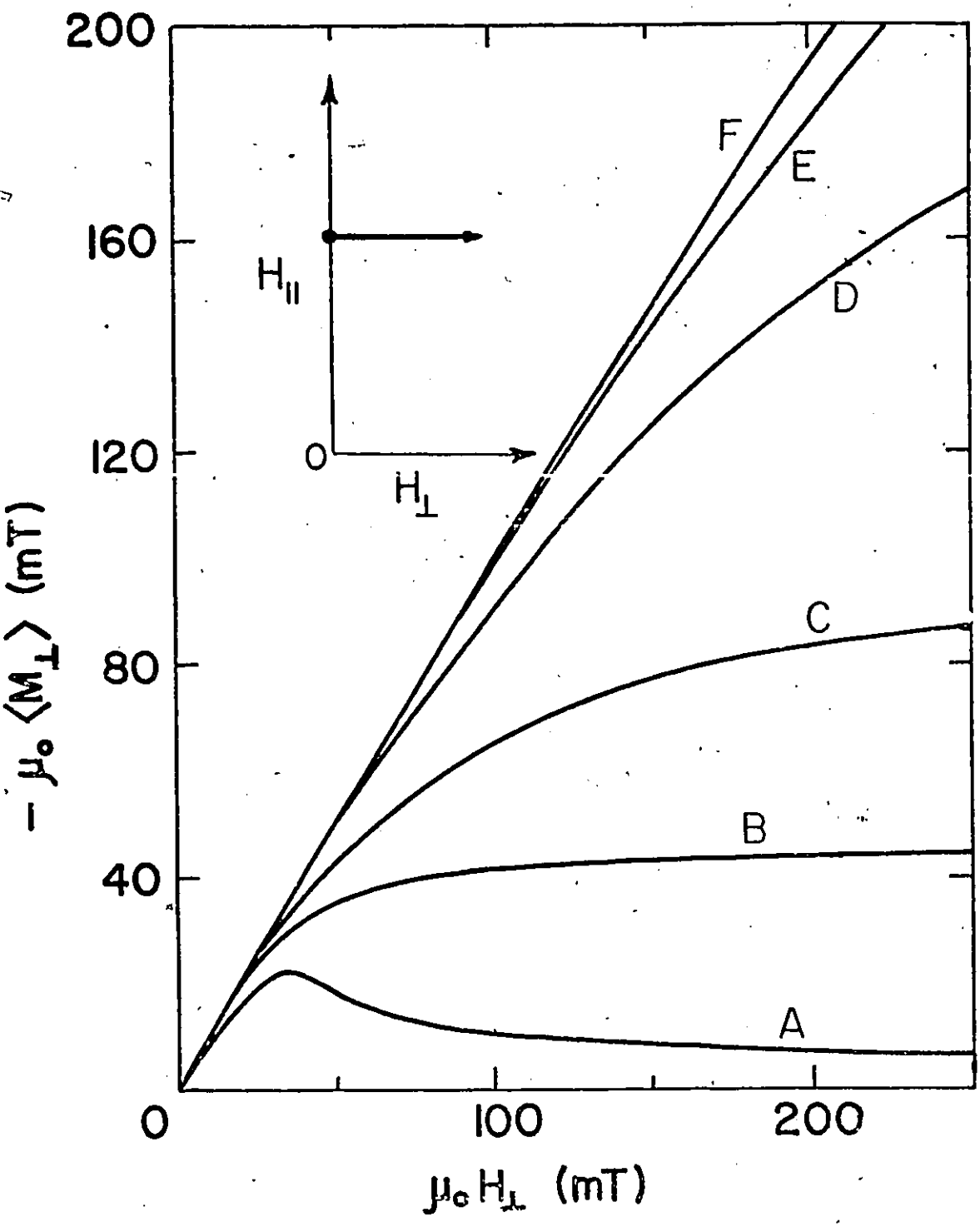

FIG. 3.10 $\langle M_\perp \rangle$ vs. $H_\perp$ calculated with $F_p = \alpha B^{\frac{1}{2}}$ where $B_* = (3\,\alpha a/2)^{2/3}$ is chosen as 50 mT. Initial state is nonmagnetic. $H_{//}$ stationary at 0, 36, 72, 180, 360 and 540 mT for curves A, B, C, D, E and F respectively. Inset shows variation of $H_{//}$ (none) and $H_\perp$ in superconducting state.

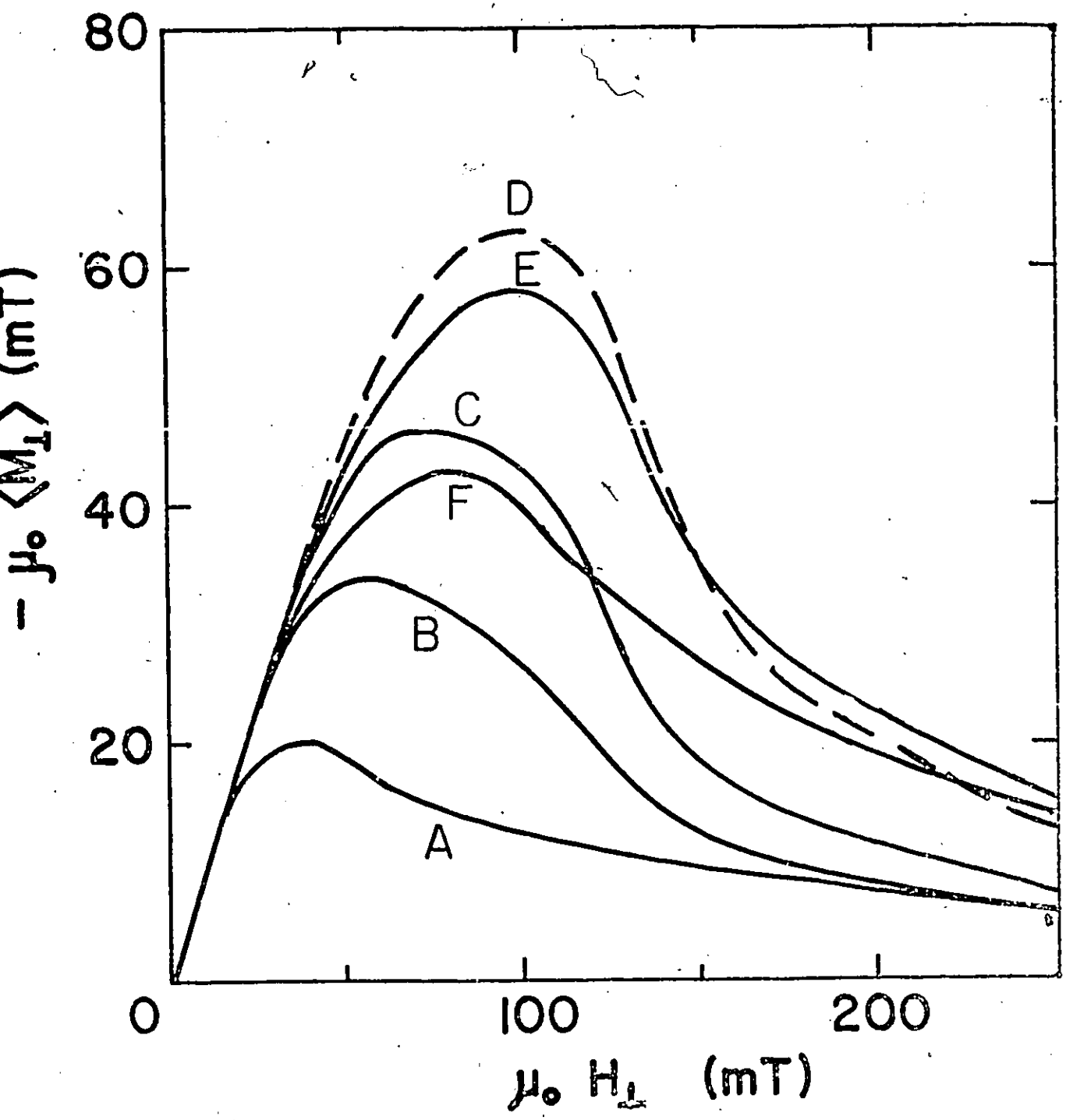

FIG. 3.11 $\langle M_\perp \rangle$ vs. $H_\perp$ measured for VTi ribbon at 4.2 K. Initial state is nonmagnetic. $H_{//}$ as in Fig. 3.10.

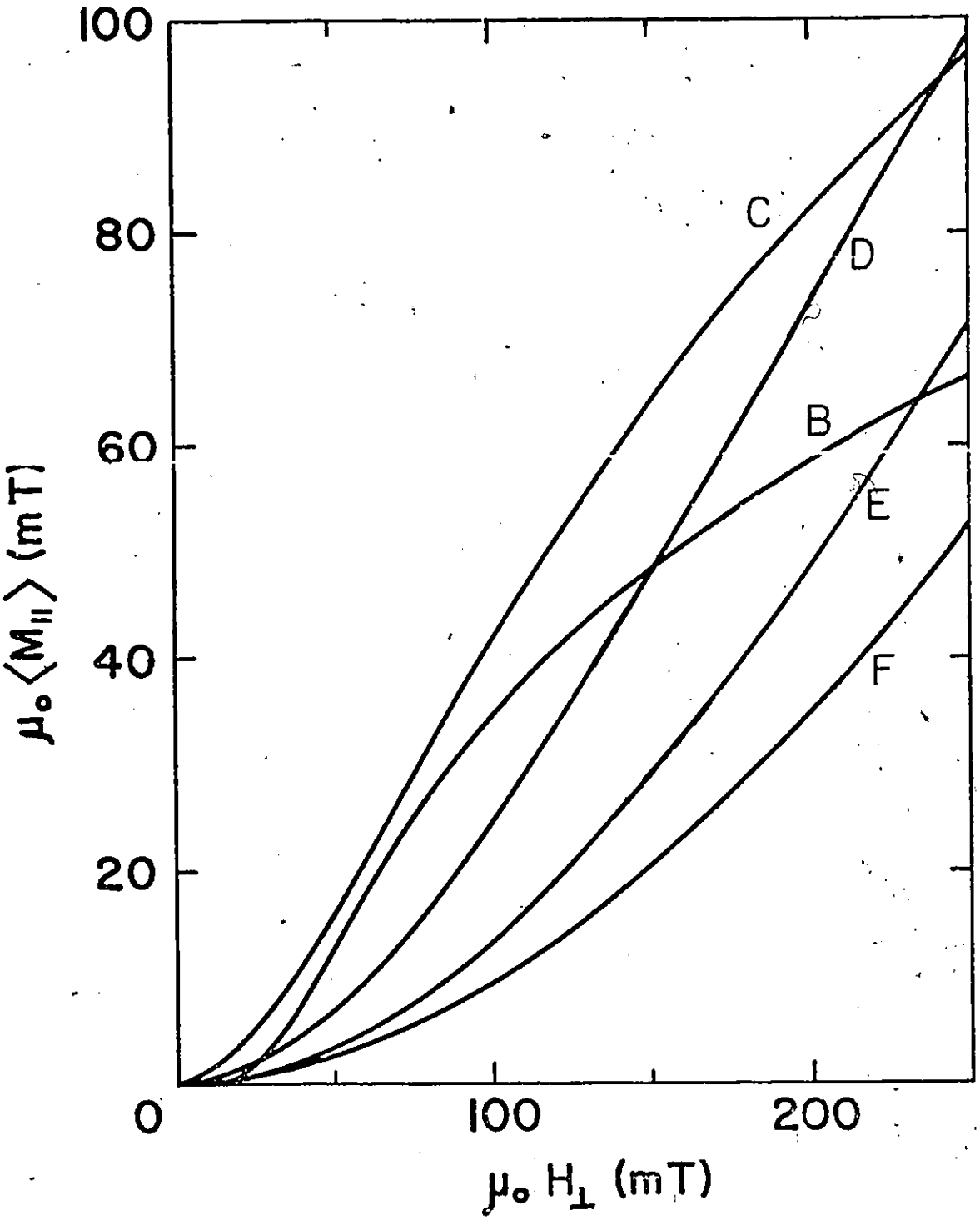

FIG. 3.12 $\langle M_{//} \rangle$ vs. $H_\perp$ calculated with F_p and B_* as in Fig. 3.10. Initial state is nonmagnetic. $H_{//}$ as in Fig. 3.10 $\langle M_{//} \rangle = 0$ when $H_{//} = 0$.

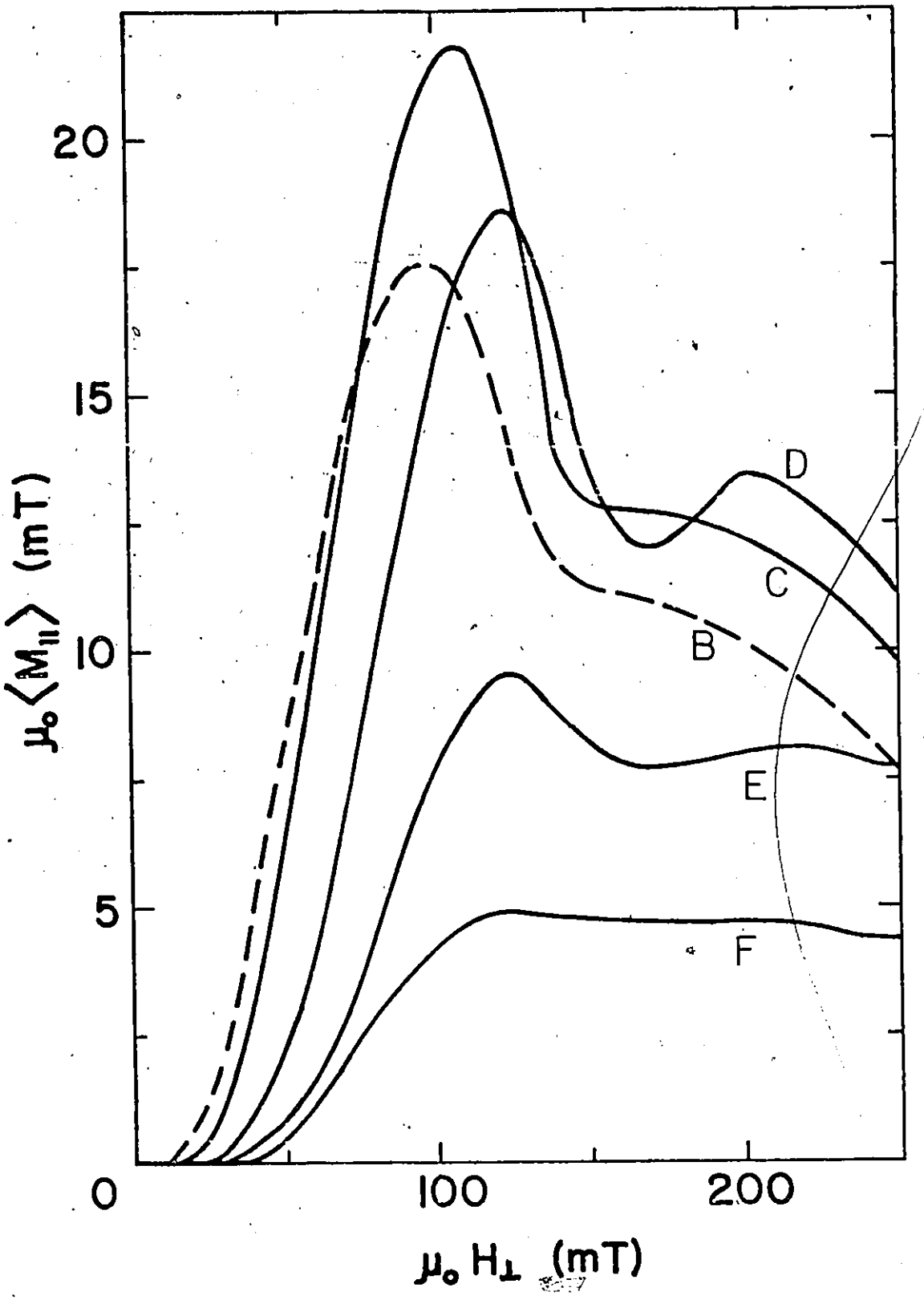

FIG. 3.13 $\langle M_{//} \rangle$ vs. $H_\perp$ measured for VTi ribbon at 4.2 K. Initial state is nonmagnetic. $H_{//}$ as in Fig. 3.10. $\langle M_{//} \rangle \approx 0$ when $H_{//} = 0$.

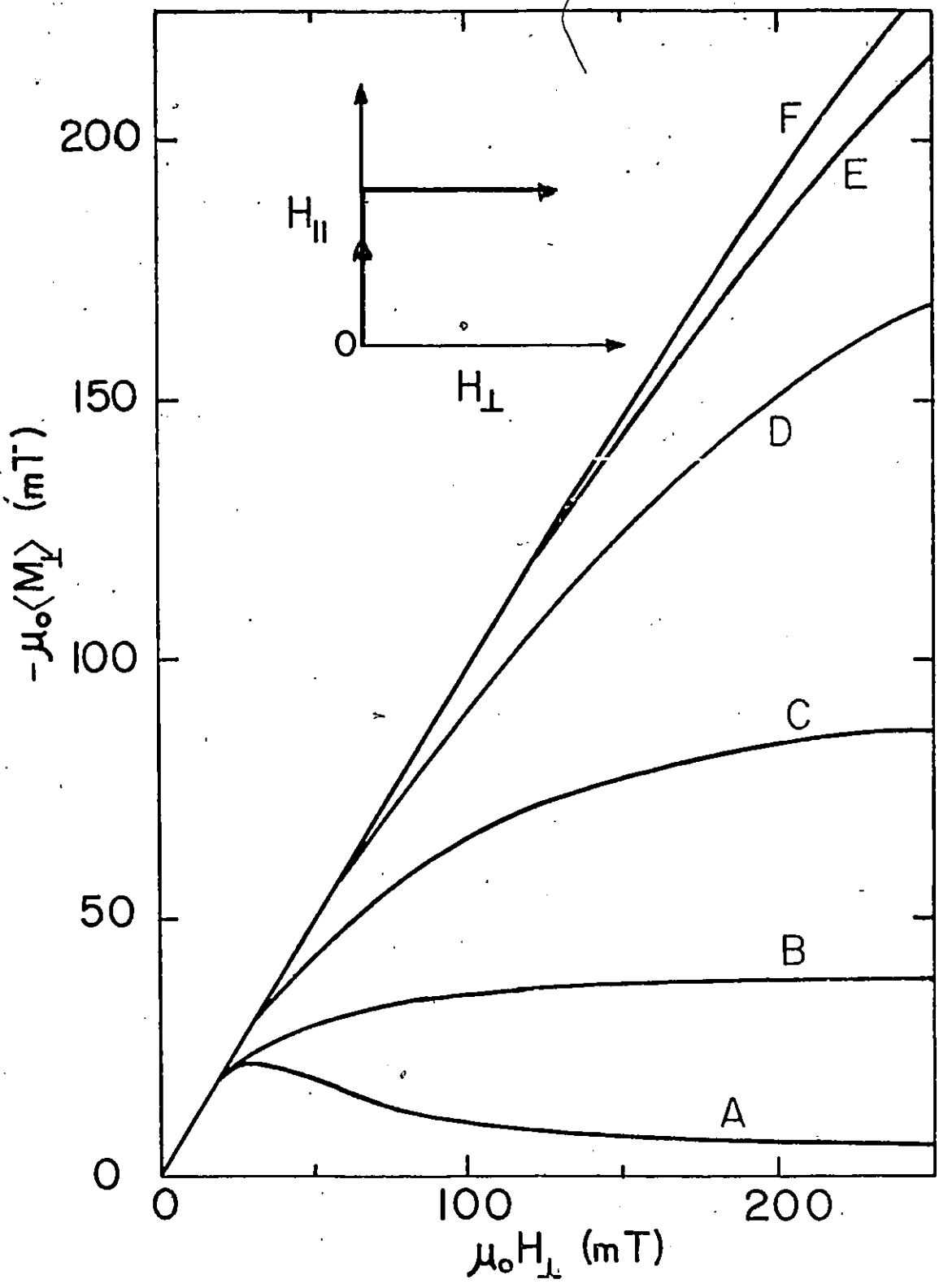

FIG. 3.14 $\langle M_\perp \rangle$ vs. $H_\perp$ calculated with F_p and B_* as in Fig. 3.10. Initial state is diamagnetic. $H_{//}$ as in Fig. 3.10. Inset shows variation of $H_{//}$ and $H_\perp$ in superconducting state.

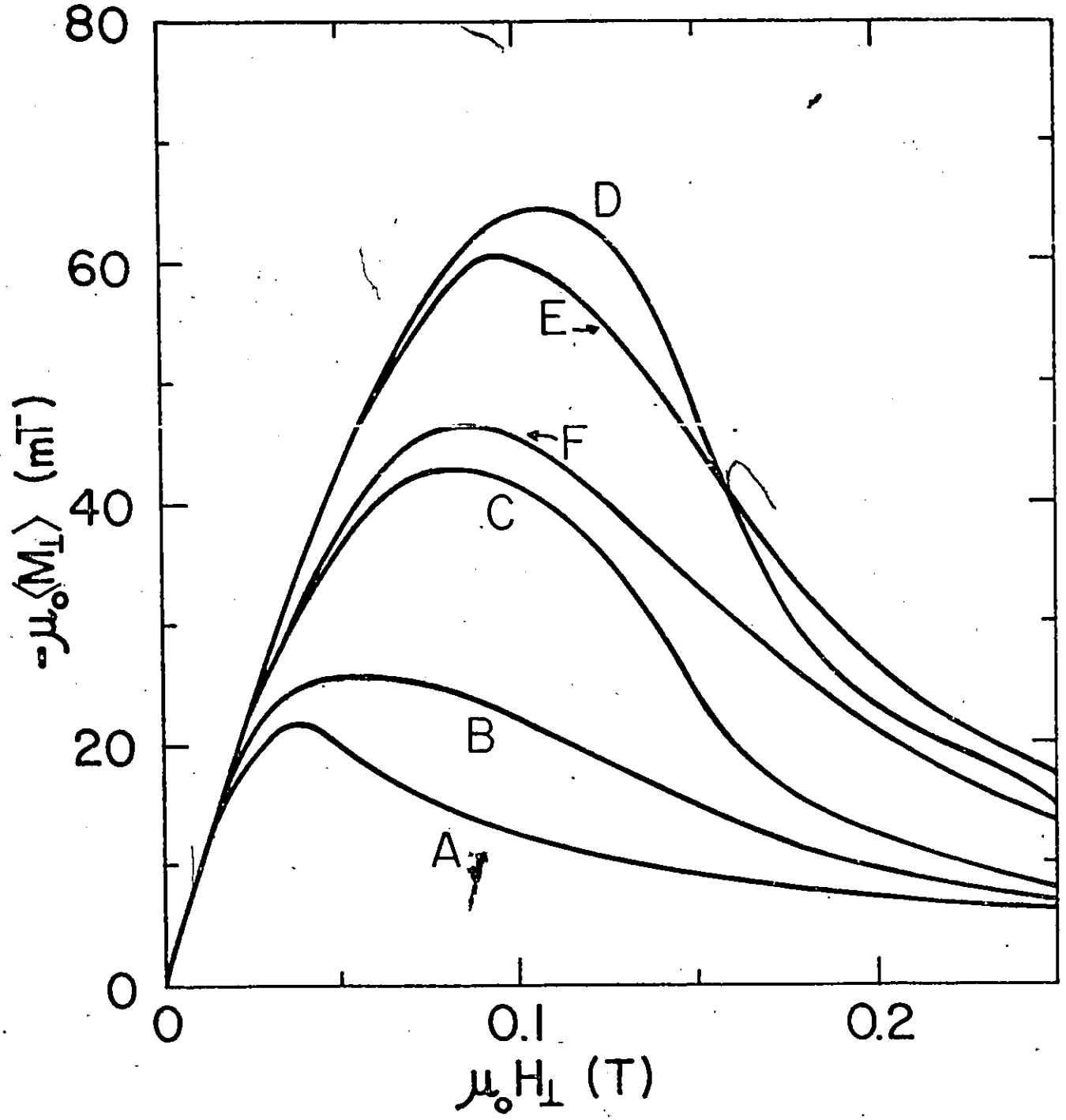

FIG. 3.15 $\langle M_\perp \rangle$ vs. $H_\perp$ measured for VTi ribbon at 4.2 K. Initial state is diamagnetic. $H_{//}$ as in Fig. 3.10.

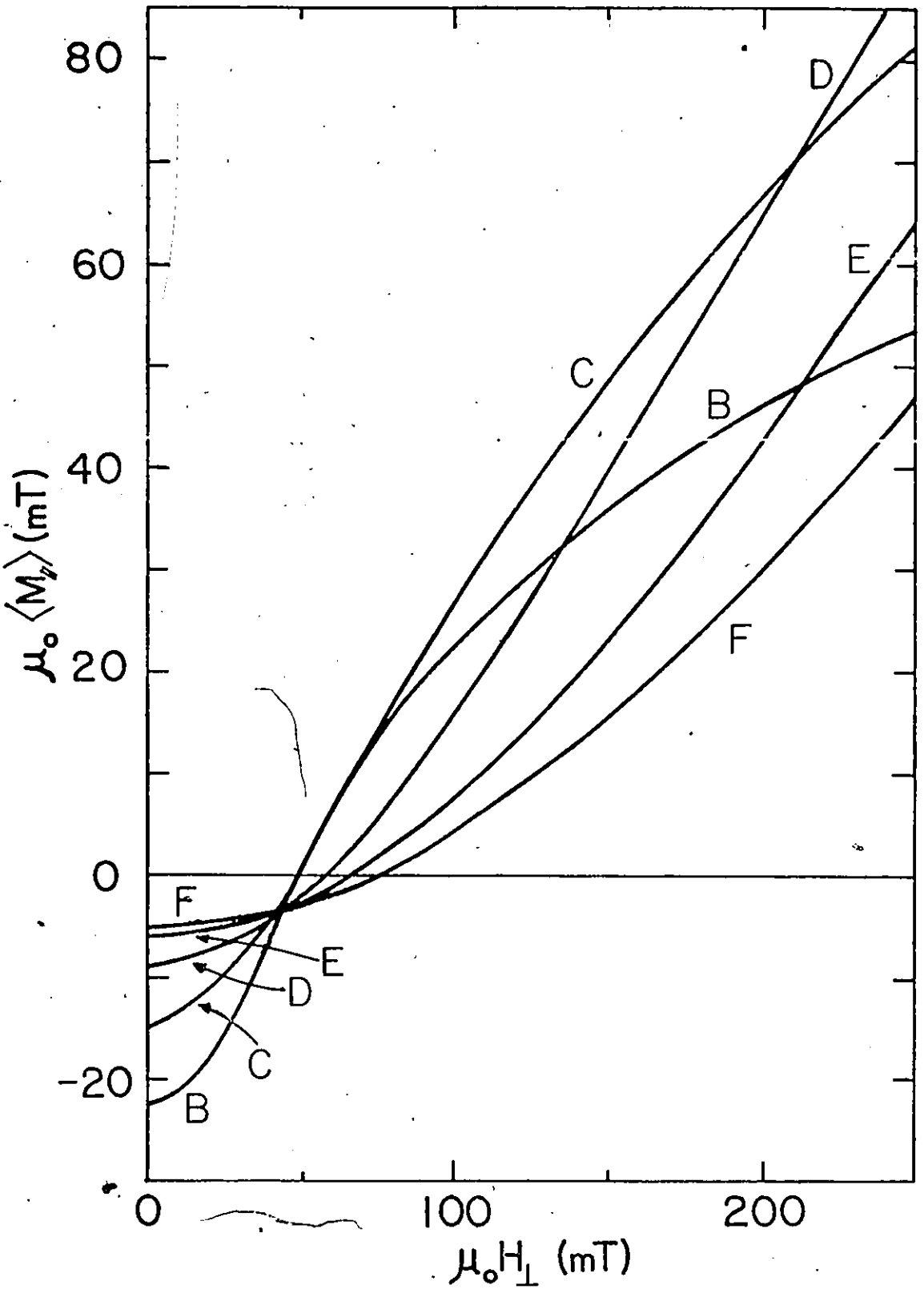

FIG. 3.16 $\langle M_{//} \rangle$ vs. $H_\perp$ calculated with F_p and B_* as in Fig. 3.10. Initial state is diamagnetic. $H_{//}$ as in Fig. 3.10. $\langle M_{//} \rangle = 0$ when $H_{//} = H_i = 0$.

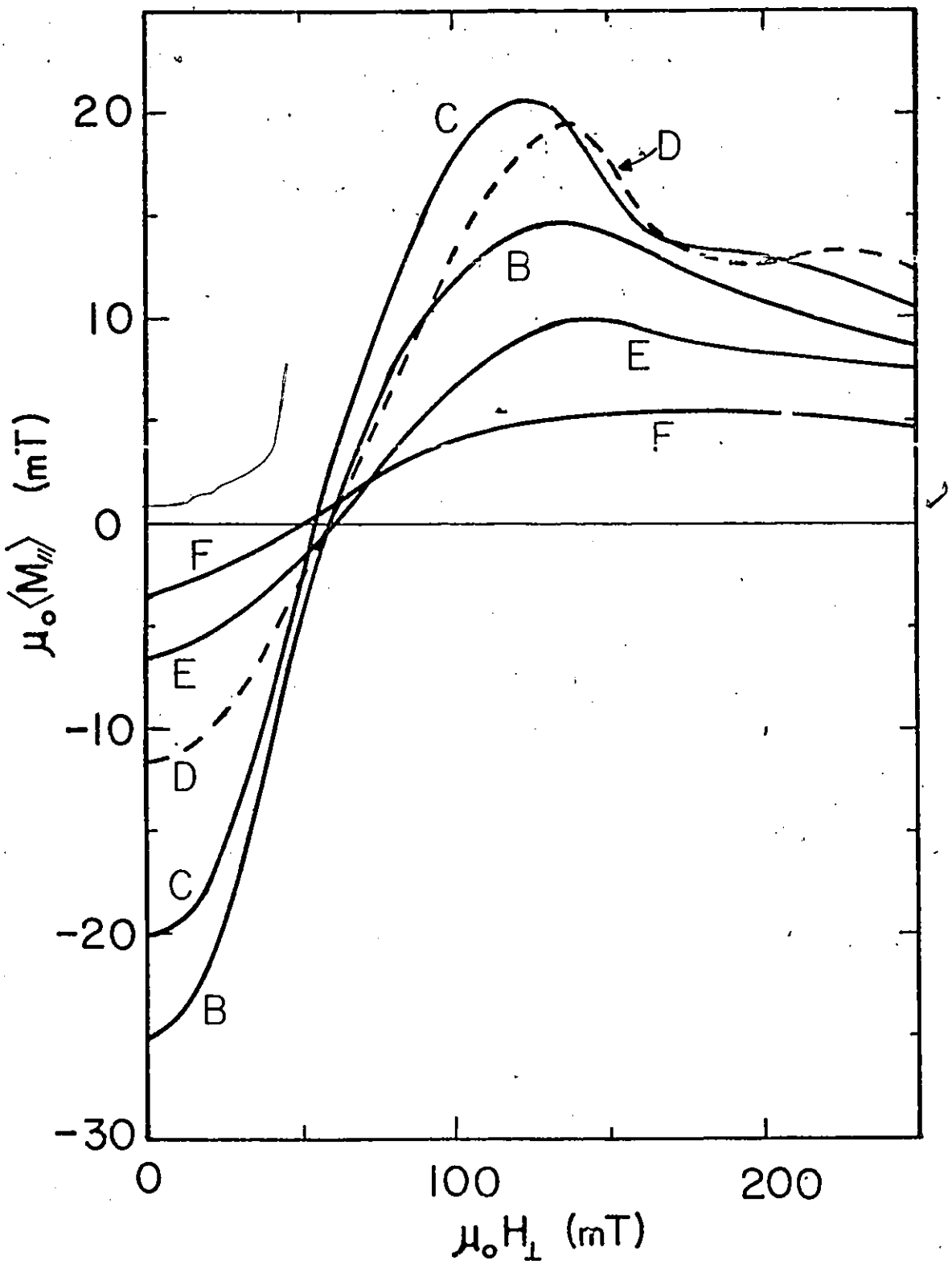

FIG. 3.17 $\langle M_{//}\rangle$ vs. $H_\perp$ measured for VTi ribbon at 4.2 K. Initial state is diamagnetic. $H_{//}$ as in Fig. 3.10. $\langle M_{//}\rangle \approx 0$ when $H_{//} = H_i = 0$.

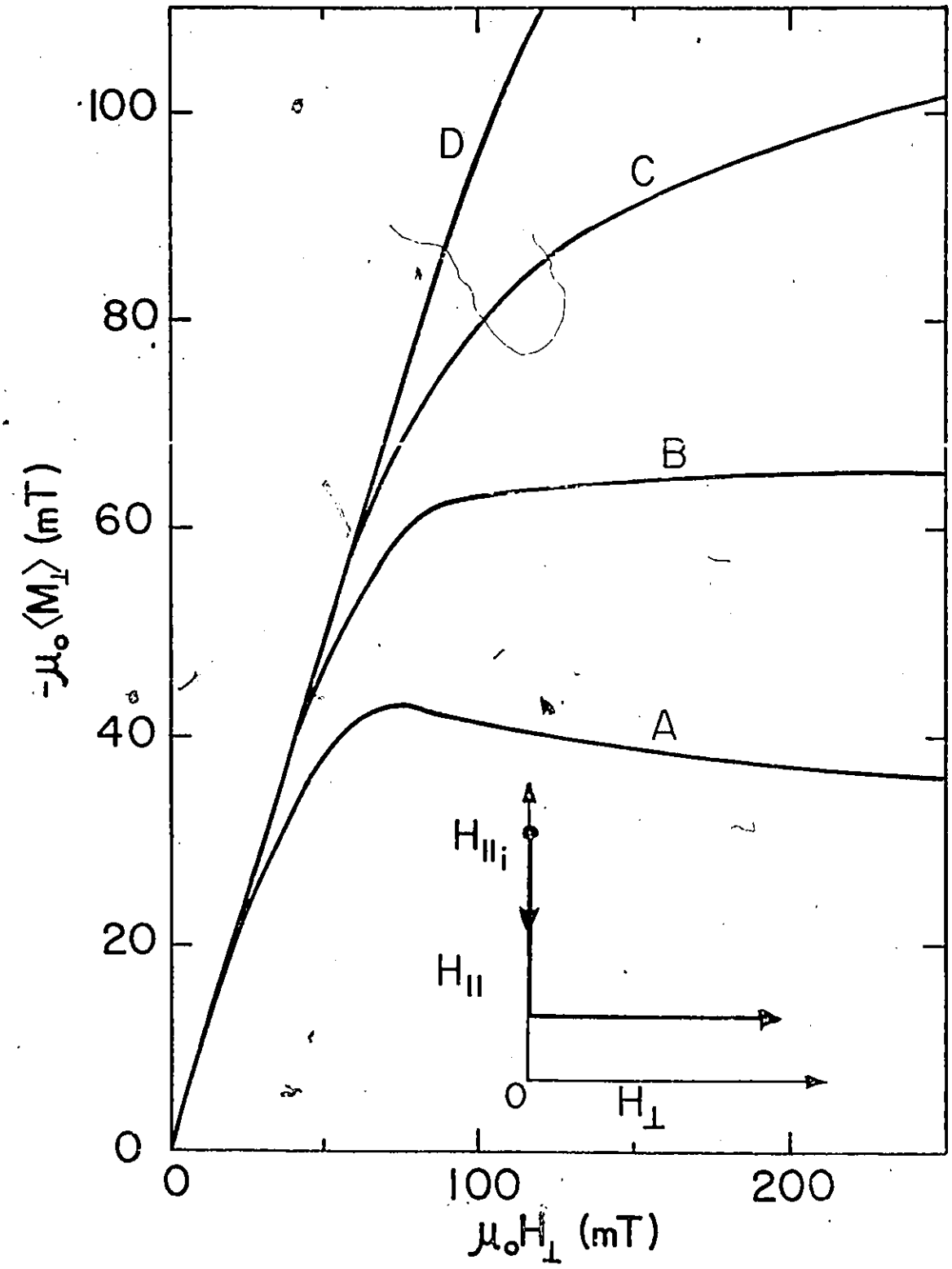

FIG. 3.18 $\langle M_\perp \rangle$ vs. $H_\perp$ calculated with F_p and B_* as in Fig. 3.10. Initial state is paramagnetic. $H_{//}$ as in Fig. 3.10. Inset shows variation of $H_{//}$ and $H_\perp$ in superconducting state.

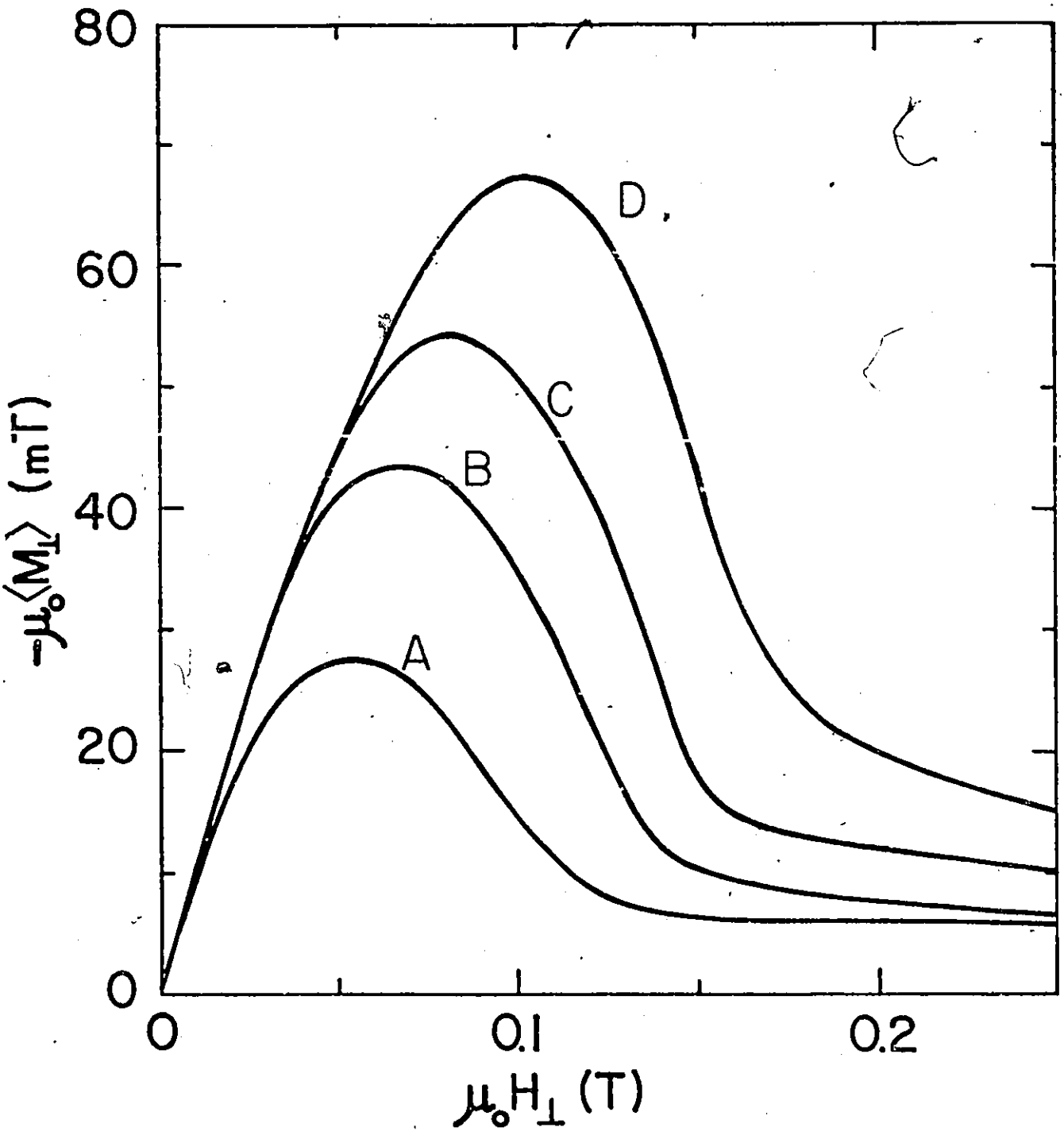

FIG. 3.19 $\langle M_\perp \rangle$ vs. $H_\perp$ measured for VTi ribbon at 4.2 K. Initial state is paramagnetic. $H_{//}$ as in Fig. 3.10. Sample becomes superconducting with $H_{//i}$ = 400 mT.

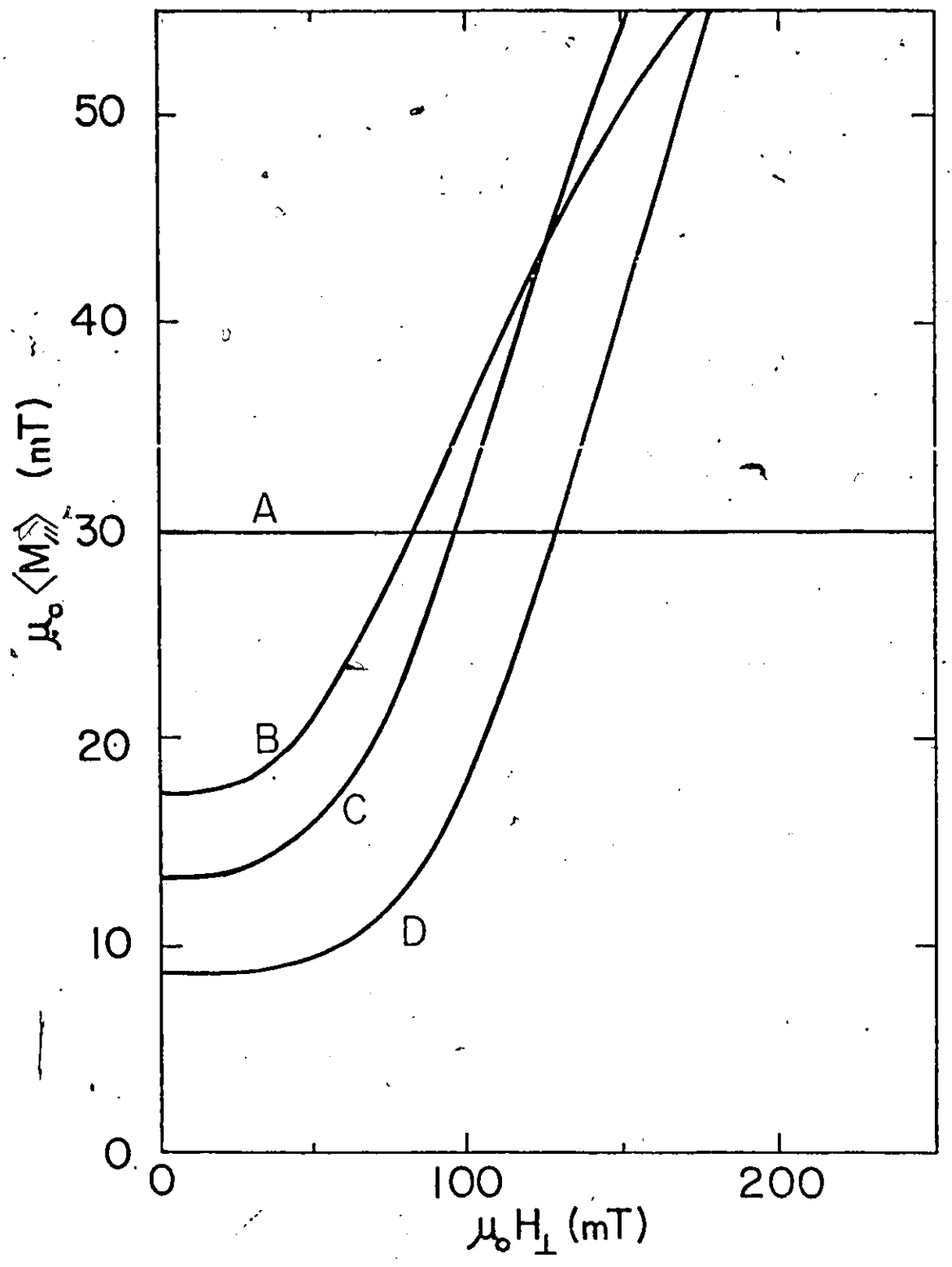

FIG. 3.20 $\langle M_{//} \rangle$ vs. $\hat{n}_\perp$ calculated with F_p and B_* as in Fig. 3.10. Initial state is paramagnetic. $H_{//}$ as in Fig. 3.10.

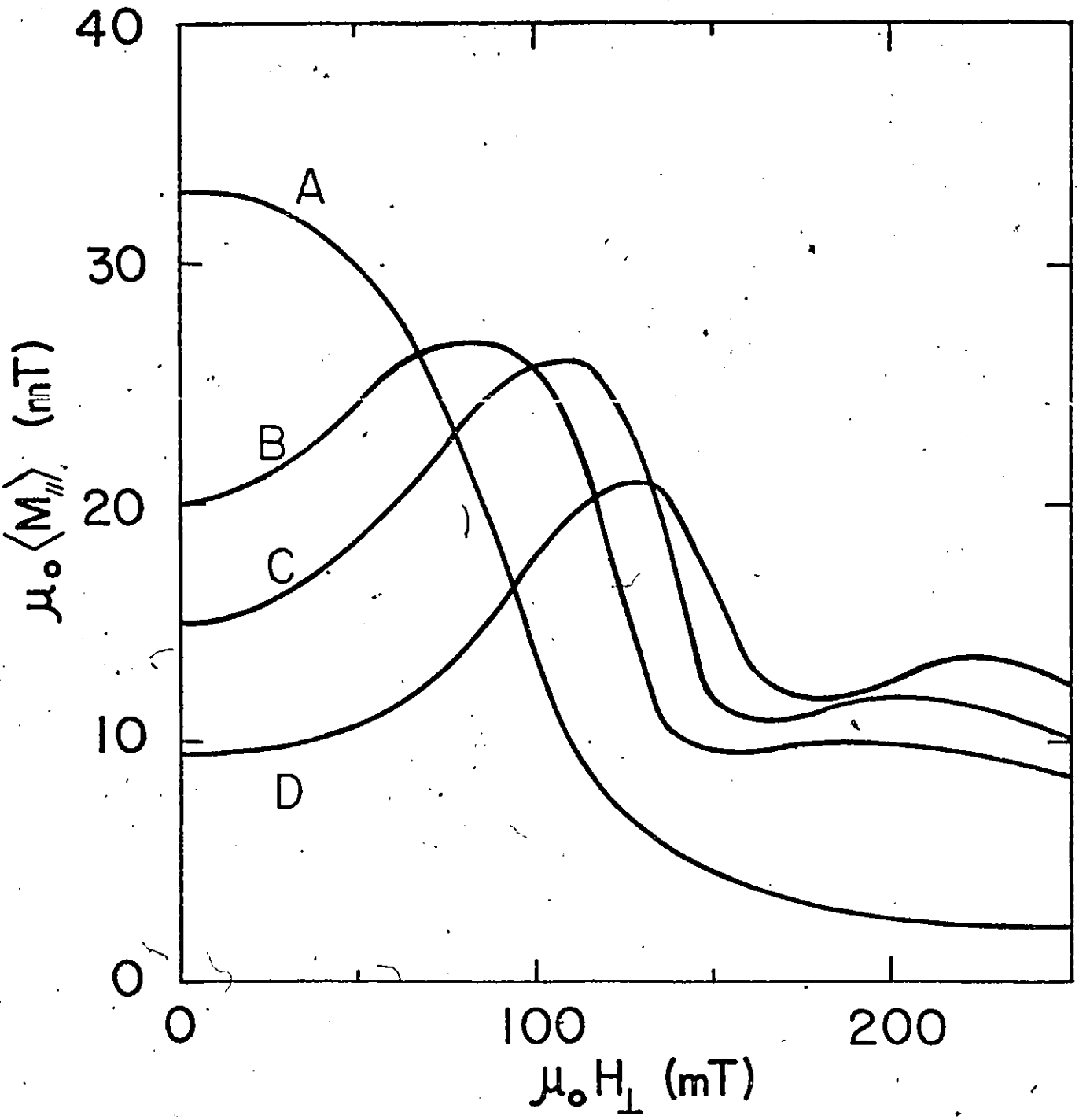

FIG. 3.21 $\langle M_{//} \rangle$ vs. $H_\perp$ measured for VTi ribbon at 4.2 K. Initial state is paramagnetic. $H_{//}$ as in Fig. 3.10. Sample becomes superconducting with $H_{//i}$ = 400 mT.

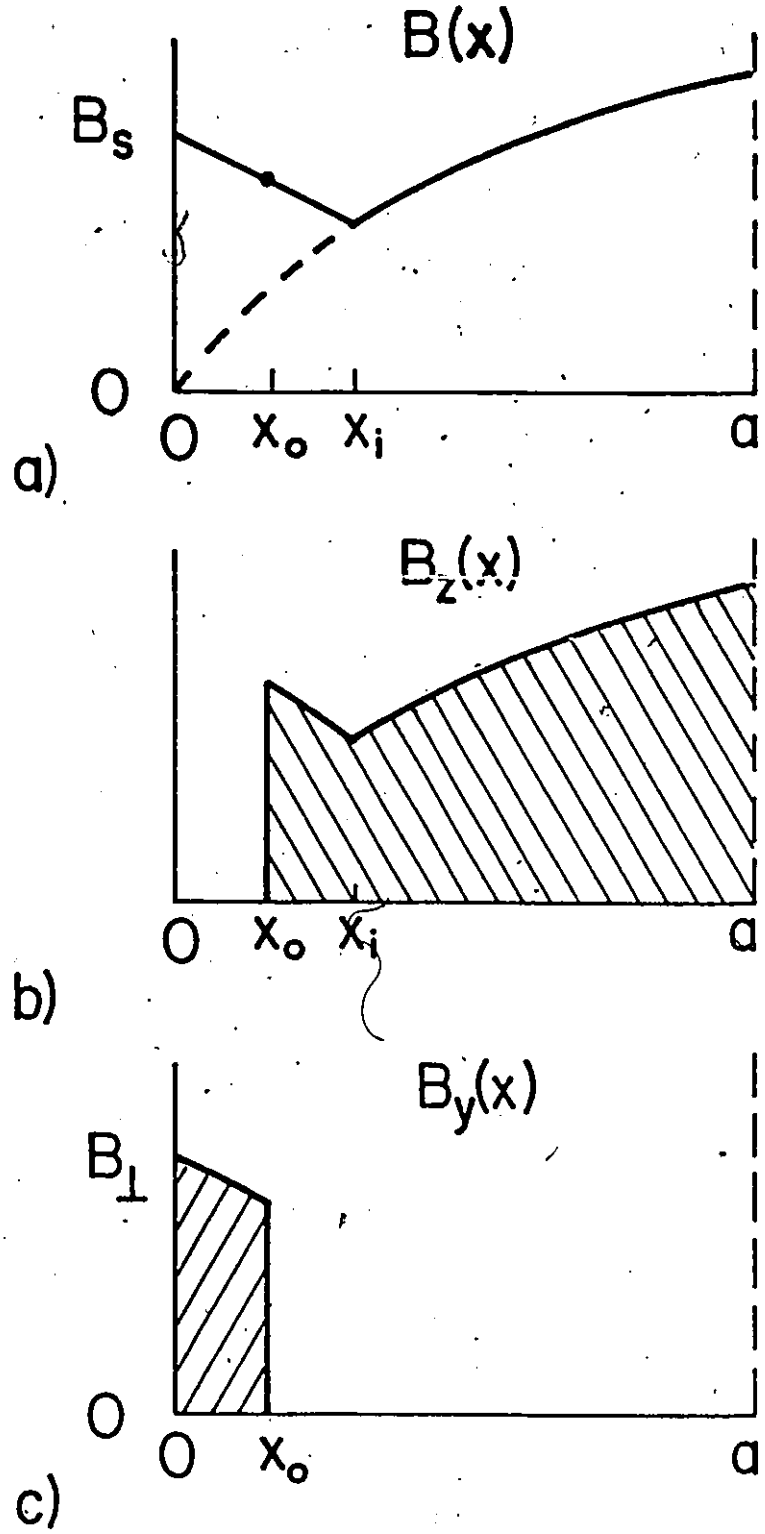

FIG. 3.22 Schematic of B, B_z and B_y profiles as $B_\perp$ is applied from zero to infinite slab in paramagnetic initial state where $B_{//} = 0$. Note discontinuity in B_z and B_y profiles at x_o required by model of non rotating vortices.

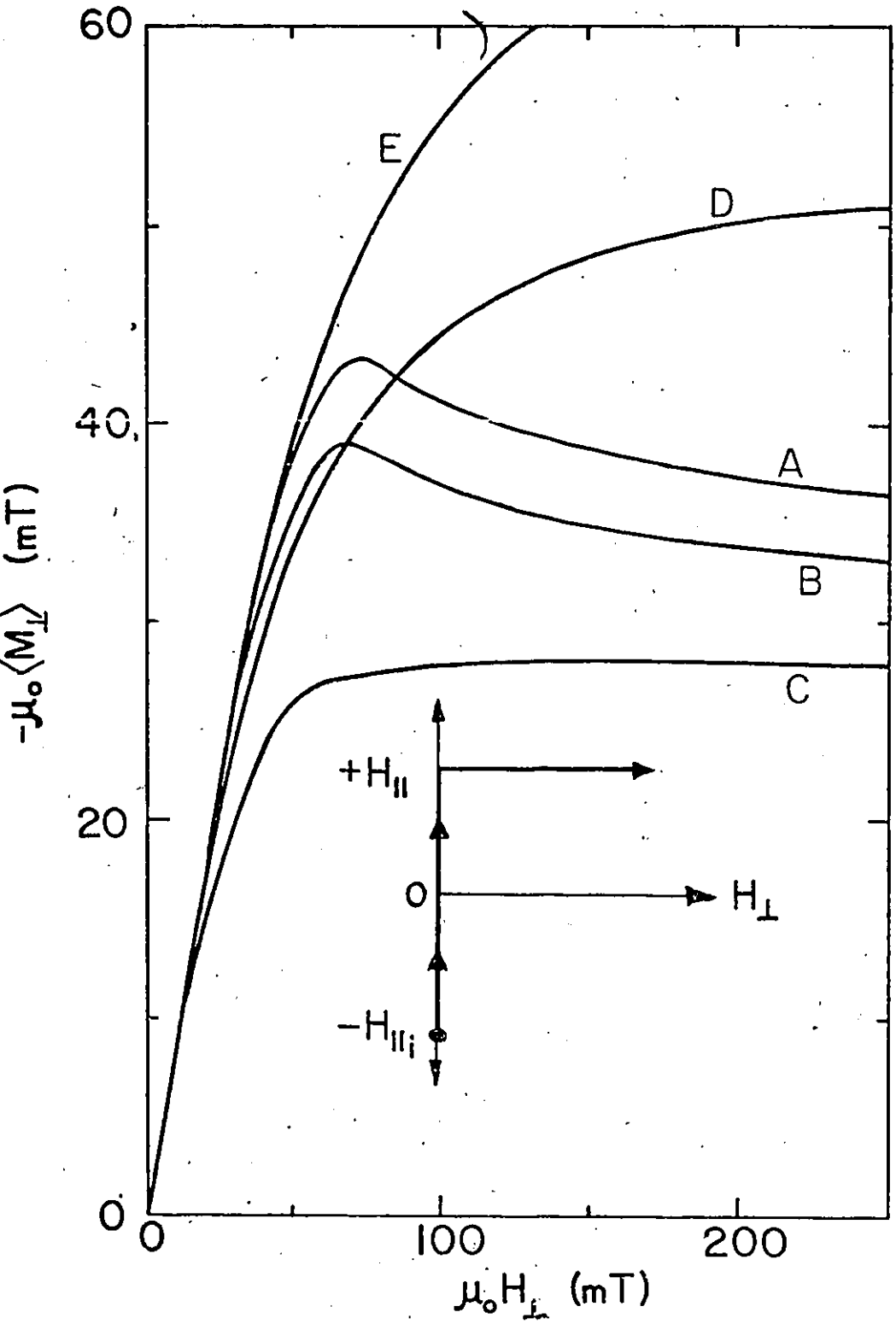

FIG. 3.23 $\overline{\langle M_\perp \rangle}$ vs. $H_\perp$ calculated with F_p and B_* as in Fig. 3.10. Initial state is hybrid. $H_{//}$ stationary at 0, 11, 28, 45 and 56 mT for curves, A, B, C, D and E respectively. Inset shows variation of $H_{//}$ and $H_\perp$ in superconducting state.

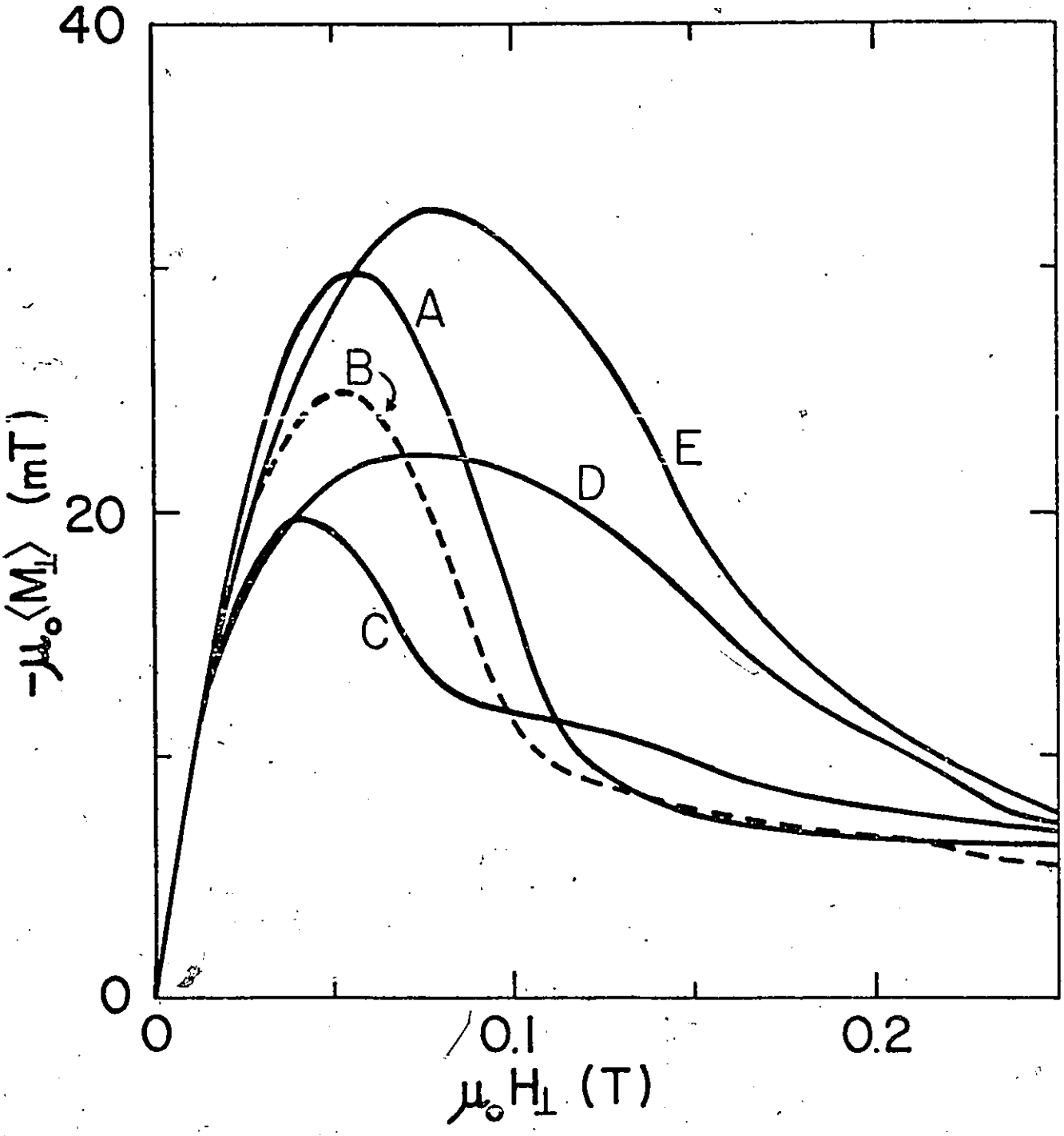

FIG. 3.24 $\langle M_\perp \rangle$ vs. $H_\perp$ measured for VTi ribbon at 4.2 K. Initial state is hybrid. $H_{//}$ as in Fig. 3.23. Sample becomes superconducting with $H_{//i} = -400$ mT.

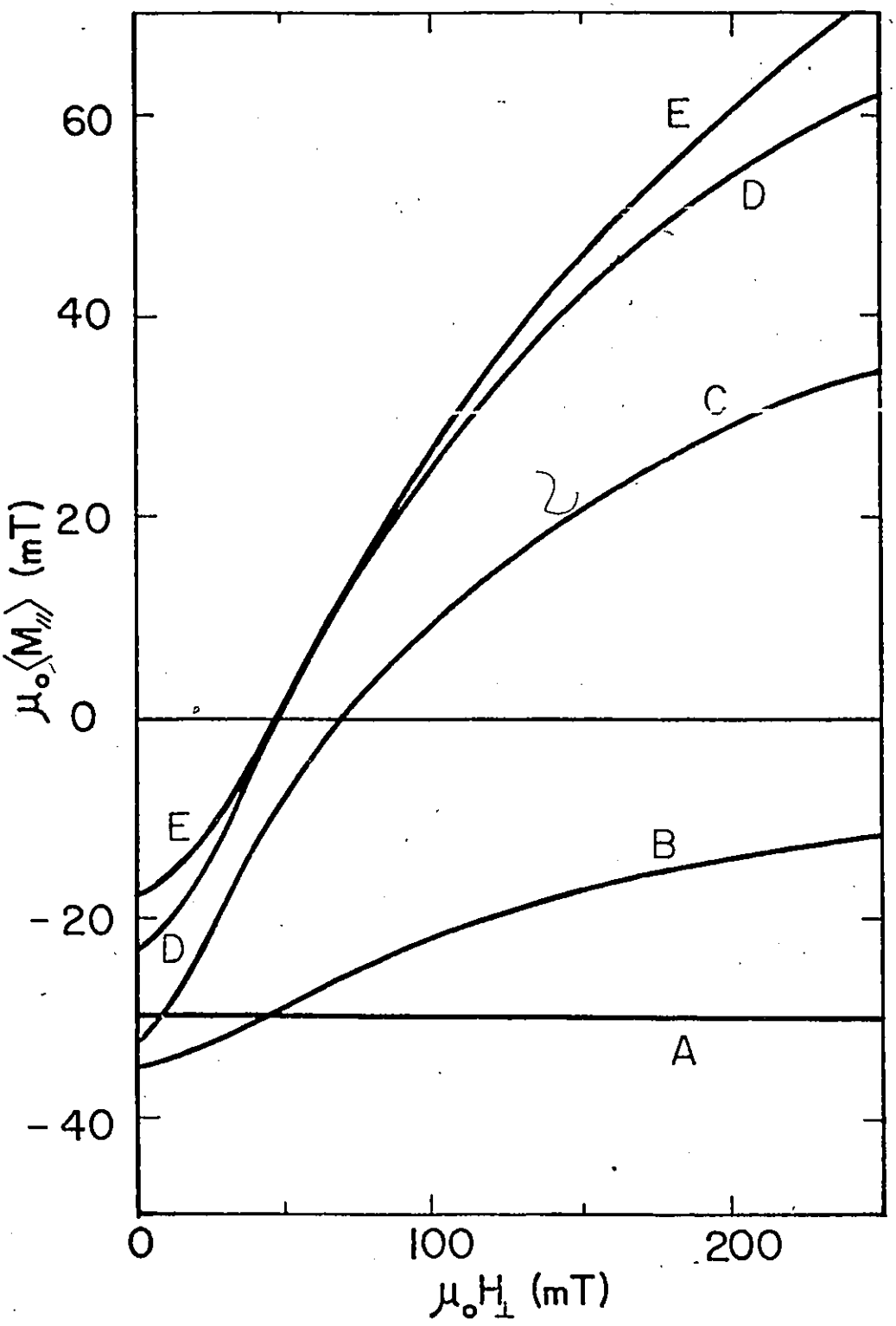

FIG. 3.25 $\langle M_{//} \rangle$ vs. $H_\perp$ calculated with F_p and B_* as in Fig. 3.10. Initial state is hybrid. $H_{//}$ as in Fig. 3.23.

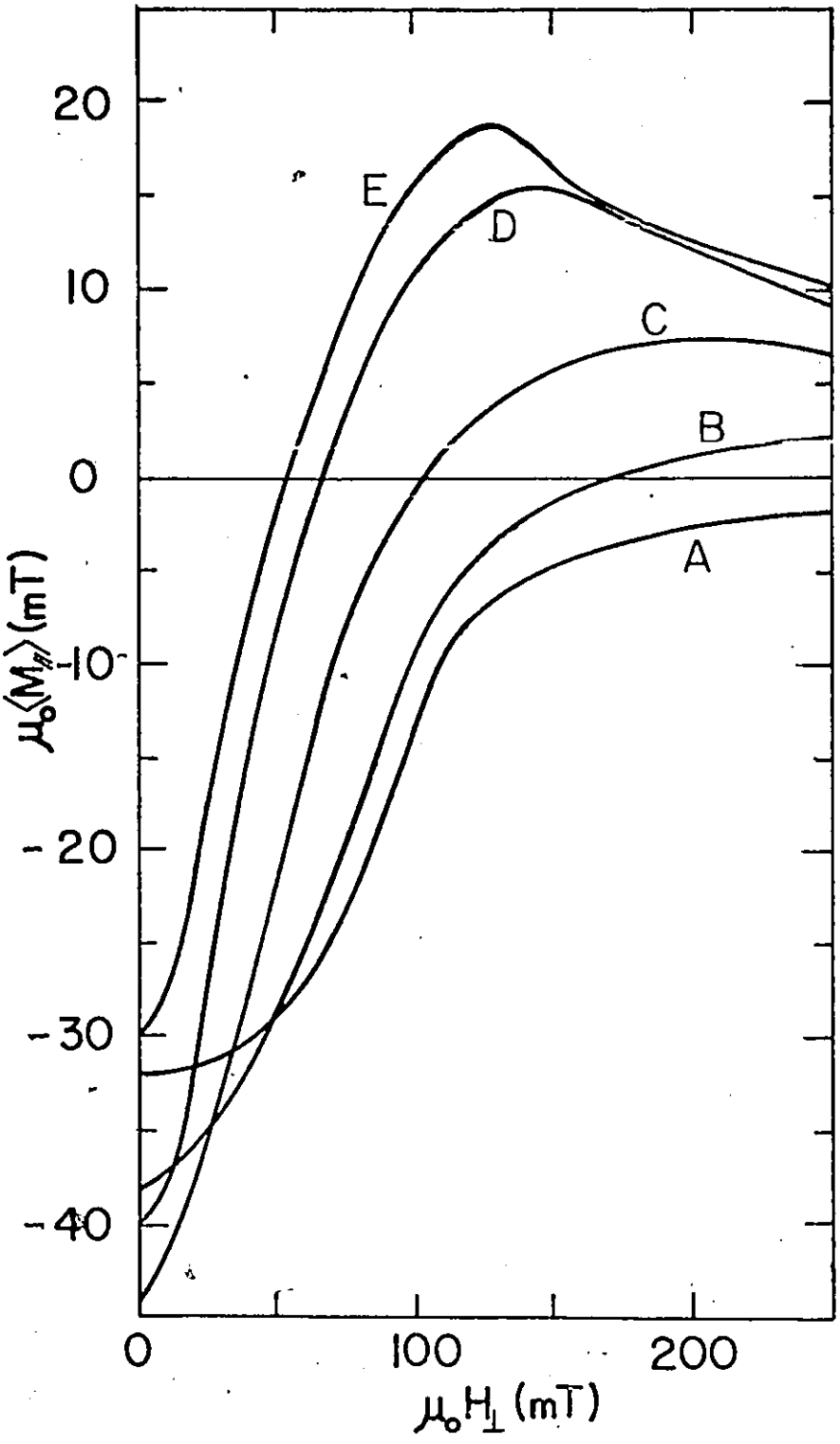

FIG. 3.26 $\langle M_{//}\rangle$ vs. $H_\perp$ measured for VTi ribbon at 4.2 K. Initial state is hybrid. $H_{//}$ as in Fig. 3.23. Sample becomes superconducting with $H_{//i}$ = -400 mT.

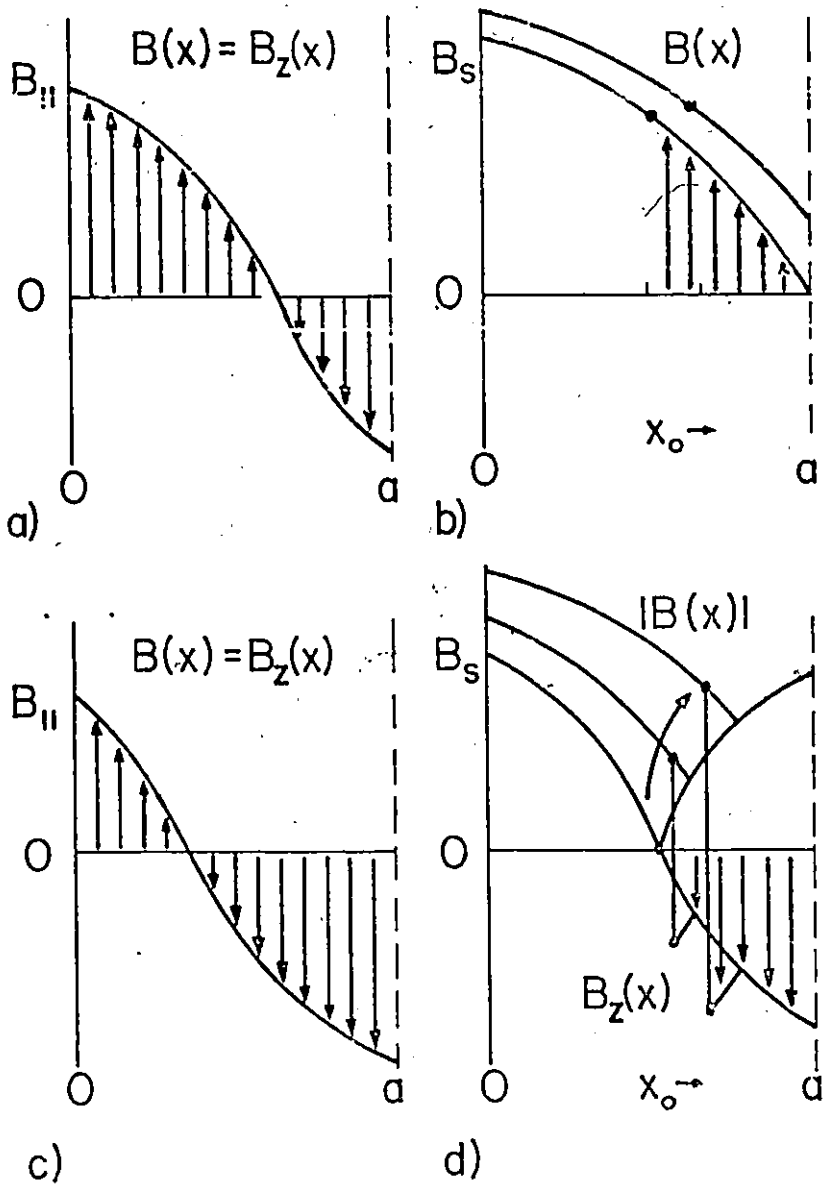

FIG. 3.27 Schematic of sequences of B and B_z profiles as B_s is increased with $B_{//}$ stationary with slab initially in a hybrid magnetic state. Two possibilities are sketched in (a) and (c). In (b) and (d) the process of mutual annihilation of flux lines has been completed. Subsequently, flux lines from the initial configuration which have survived annihilation are compressed between x_o and a. In (c), $B_z(x)$ is continuous since the surviving flux lines point parallel to $B_{//}$. In (d), however, $B_z(x)$ is discontinuous at x_o since the surviving flux lines are oriented antiparallel to $B_{//}$.

$$(3.38)\qquad \frac{B_y(x,B_s)}{B(x,B_s)} = \frac{B_y'(x',B_s')}{B'(x',B_s')}\ ,\quad \frac{B_z(x,B_s)}{B(x,B_s)} = \frac{B_z'(x',B_s')}{B'(x',B_s')}$$

Let B_c denote the magnitude of the magnetic induction at the surface and $B_{//c}$ and $B_{\perp c}$ its components at the time t' for the creation of a plane of vortices located at x at a later time t when the magnetic induction at the surface is B_s. Then equation (3.38) reads

$$(3.39)\qquad \frac{B_y(x,B_s)}{B(x,B_s)} = \frac{B_{\perp c}}{B_c}\ ,\qquad \frac{B_z(x,B_s)}{B(x,B_s)} = \frac{B_{//c}}{B_c}$$

since $B'(0,B_c) \equiv B_c$, $B_y'(0,B_c) \equiv B_{\perp c}$ and $B_z'(0,B_c) \equiv B_{//c}$

Let $\theta(x)$ denote the direction of the flux lines

$$(3.40)\qquad \theta(x) = \cos^{-1}\frac{B_z}{B} = \sin^{-1}\frac{B_y}{B} = \tan^{-1}\frac{B_y}{B_z}$$

To determine the present location, or equivalently, the density, of a sheet of flux lines created at an earlier time t', when the magnetic induction at the surface had a magnitude B_c and an orientation θ_c, we proceed as follows. The change in density of a sheet of flux lines as it migrates is given by the total derivative

$$(3.41)\qquad dB = \left(\frac{\partial B}{\partial x}\right) dx + \left(\frac{\partial B}{\partial B_s}\right) dB_s$$

where the infinitesimal displacement of the sheet $dx = v(x)\ dt$. Exploiting the expressions for v(x) derived earlier (equation (3.27)) and introducing the critical state relation, $B(\partial B/\partial x) = \pm F_p$, equation (3.41) becomes

$$(3.42)\qquad BdB = -F_p(B)\frac{B_s}{F_p(B_s)}\,dB_s + F_p(B)\frac{B_s B(x_i)}{F_p(B_s)B}\,dB_s + B\left(\frac{\partial B}{\partial B_s}\right) dB_s$$

Using equation (3.25) to rewrite the last term, equation (3.42) simplifies to

$$\frac{B^2 dB}{F_p(B)} = \frac{B_s B(x_i) dB_s}{F_p(B_s)} \tag{3.43}$$

To follow the "trajectory" of a sheet of flux lines as it advances into the slab after creation at the surface we need to solve the integral form of equation (3.43), namely

$$\int_{B_c}^{B} \frac{B^2 dB}{F_p(B)} = \int_{B_c}^{B_s^*} \frac{B_s B(x_i) dB_s}{F_p(B_s)} + \int_{B_s^*}^{B_s} \frac{B_s B(a) dB_s}{F_p(B_s)} \tag{3.44a}$$

which applied for vortices created when $B_c < B_s^*$ but where B_s is raised beyond B_s^*. When B_s is not raised to the saturation value, the second integral on the right-hand side does not appear and the upper limit of the first integral is B_s instead of B_s^*. Equation (3.44) provides a relationship between $B(x,B_s)$ and B_c. The components $B_y(x,B_s)$ and $B_z(x,B_s)$ can then be determined from equation (3.39). The initial magnetic state influences the evolution of the B_y and B_z profiles through $B(x_i)$.

Again we confine our attention to the situation where $B_{//}$ is maintained constant as $B_\perp$ is impressed from zero, hence $B_{//c} = B_{//}$ and $B_{\perp c} = (B_c^2 - B_{//}^2)^{\frac{1}{2}}$.

For the force free case where $dB = dB_s$ we trace the path of the flux lines by introducing $v = (a-x)dB_s/B_s dt$, which follows from equation (3.8a), into the displacement $dx = vdt$ and integrating

$$\int_0^x \frac{dx}{a-x} = \int_{B_c}^{B_s} \frac{dB_s}{B_s}$$

which yields $B_c = (a-x)\, B_s/a$. This result also follows directly from flux conservation since the flux threading the slab when $B = B_c$ is compressed inside the region of width $2(a-x)$ when $B = B_s$. Introducing B_c into equation (3.39) we obtain

$$(3.45) \quad B_y(x) = \frac{\{B_s^2(1 - \frac{x}{a})^2 - B_{//}^2\}^{1/2}}{1 - \frac{x}{a}}, \quad B_z(x) = \frac{B_{//}}{1 - \frac{x}{a}}$$

which apply for the range $0 \le x \le x_o$ where $x_o/a = 1 - (B_{//}/B_s)$. For the region $x_o \le x \le a$, $B_z(x) = B_s$. These results have already been derived by Campbell and Evetts (141).

As we have noted earlier, for the diamagnetic initial state when $B(x_i) = 0$, hence before saturation, $v(x)$ is uniform and given by $v(x) = (dB_s/dt)\, B_s/F_p(B_s)$ according to equation (3.27). Since the vortices all travel at the same instantaneous velocity, they then experience no change in density as they advance. Thus $B(x,B_s) = B_c$ because the density of the flux lines is not altered during their migration since creation. This result also follows from equation (3.43) where $dB = B - B_c = 0$ when $B(x_i) = 0$. Under these circumstances, equation (3.39) yields

$$(3.46) \quad B_y(x) = (B^2(x) - B_{//}^2)^{1/2}, \quad B_z(x) = B_{//}$$

over the range $0 \le x \le x_o$ and $B_z(x) = B(x)$ from $x_o \le x \le x_i$ where x_o is determined by $B(x_o,B_s) = B_{//}$. This simple sequence of profiles is sketched in Figure 3.28.

We now focus attention on the nonmagnetic initial state where $B_i(x) = B_{//}$ and develop analytic expressions where $F_p = \alpha_n B^n$

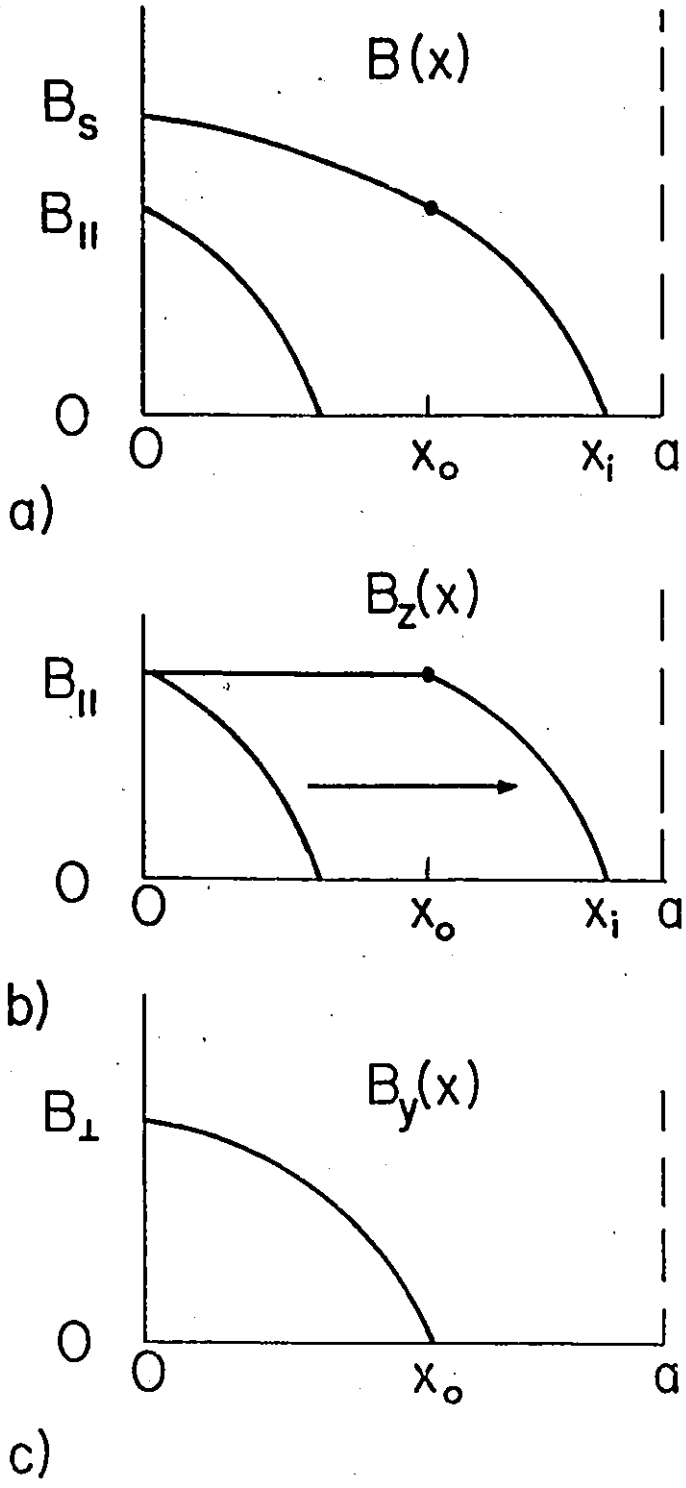

FIG. 3.28 Shows schematically evolution of B, B_z and B_y profiles as $B_\perp$ is increased from 0 with $B_{//}$ stationary for diamagnetic initial state where $B(x) = 0$ for $x_i \leq x \leq a$. $B_z(x) = B_{//}$ for $0 \leq x \leq x_o$ since flux lines advance at a spatially uniform velocity under these circumstances. Consequently, flux lines retain the density as well as the orientation of creation during migration until x_i attains midplane.

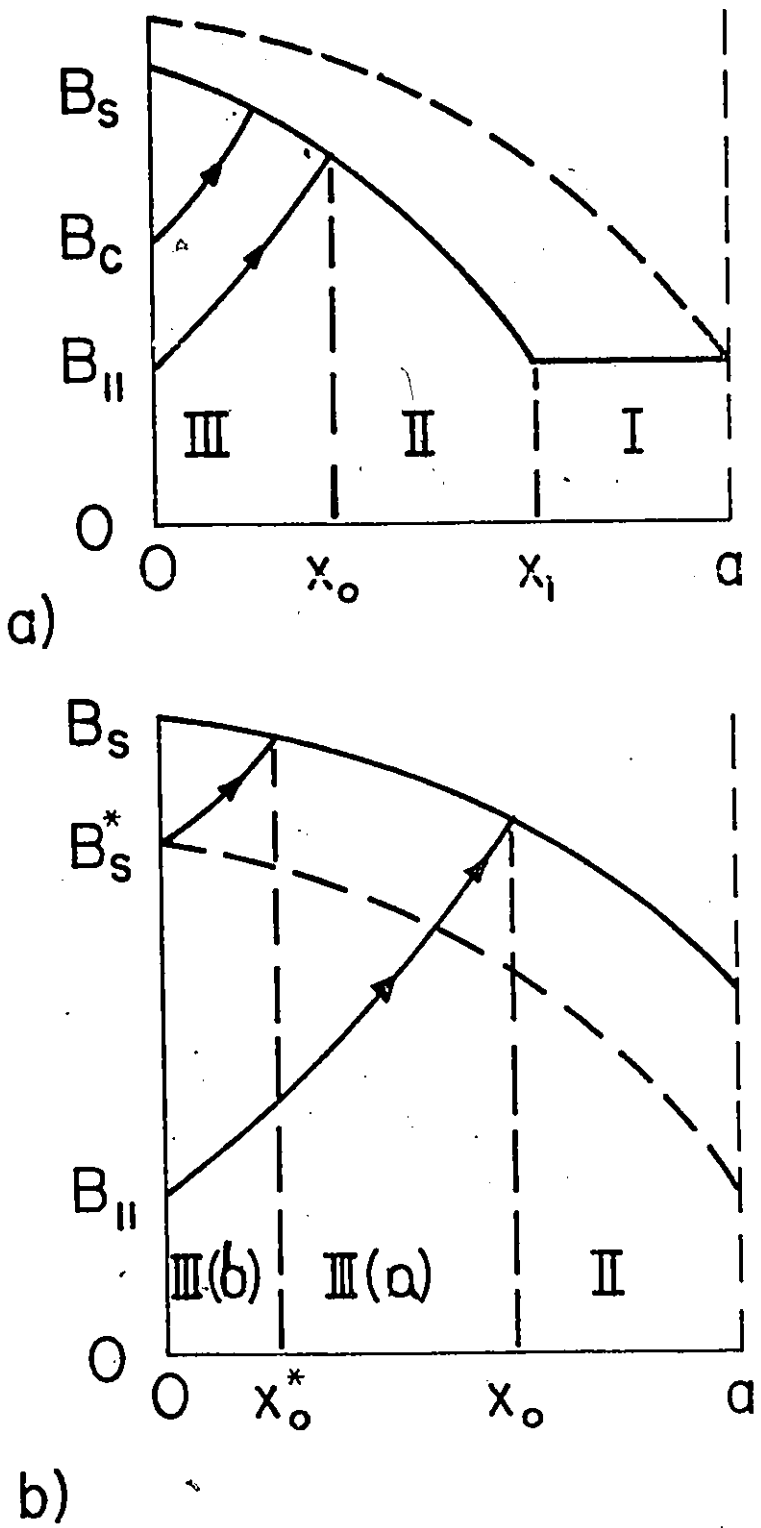

FIG. 3.29 Shows schematically the change of density of flux lines as they advance in the slab a) before and b) after saturation is attained starting with a nonmagnetic initial state where B_s increases with $B_{//}$ stationary.

with n = 1, ½ and 0. We consider the sequences of profiles before and after saturation separately.

a) Before Saturation: $B_{//} \leq B_s \leq B_s^*$ and $B(x_i) = B_{//}$

In tracing the B, B_z and B_y profiles we can identify three regions in the slab as shown schematically in Figure 3.29.

Region I spanning the width $x_i \leq x \leq a$ contains the vortices originally threading the slab whose density is yet undisturbed by the entry of flux lines. The width of this region shrinks to zero as x_i, the front of the disturbance in the B profile, advances to the midplane as B_s increases to B_s^* and saturation occurs. The boundary x_i follows from the condition $B(x_i) = B_{//}$. In the Bean-London approximation we find

$$\frac{x_i}{a} = \frac{B_s - B_{//}}{B_*} \tag{3.47}$$

Region II, occupying the space between x_o and x_i, contains the vortices which initially were threading the space between $0 \leq x \leq x_i$ at $B_{si} = B_{//}$ and are now compressed in a critical state configuration. Since the vortices maintain their orientation during compression, $B_z(x) = B(x)$. The location of the x_o boundary as a function of B_s can be obtained by solving the integral equation

$$\int_{x_o}^{x_i} B(x)dx = B_{//}x_i \tag{3.48a}$$

Alternatively, x_o can be determined by taking $B_c = B_{//}$ as the limit of integration in equation (3.44a). In the Bean-London approximation we find

$$(3.49) \qquad \frac{x_o}{a} = \frac{B_s}{B_*} - \frac{(B_{//}(2B_s - B_{//}))^{\frac{1}{2}}}{B_*}$$

Region III spanning $0 \leq x \leq x_o$ contains the vortices nucleated during the sweep of B_s from $B_{//}$. Introducing the appropriate pinning function into equation (3.44a), noting that $B(x_i) = B_{//}$ for the nonmagnetic initial state and integrating yields

$$(3.50a) \qquad B^2 = B_c^2 + 2B_{//}(B_s - B_c)$$

$$(3.50b) \qquad B^{5/2} = B_c^{5/2} + \frac{5}{3} B_{//} (B_s^{3/2} - B_c^{3/2})$$

$$(3.50c) \qquad B^3 = B_c^3 + \frac{3}{2} B_{//} (B_s^2 - B_c^2)$$

where n = 1, ½ and 0 for equation (3.50) a, b and c respectively. The B_y and B_z profiles are determined by introducing B_c calculated from these expressions into equation (3.39). For instance equation (3.50a) leads to

$$(3.51) \qquad B_c = B_{//} + \{ (B_s - B_{//})^2 - 2B_s B_* (\frac{x}{a}) + B_*^2 (\frac{x}{a})^2 \}^{\frac{1}{2}}$$

which yields equation (3.49) when $B_c = B_{//}$.

(b) After Saturation: $B_s > B_s^*$

Again we identify three regions although region I has vanished. We refer the reader to Figure 3.29(b).

All of the vortices originally permeating the slab are now compressed in a critical state in region II which spans the width $x_o \leq x \leq a$. The boundary x_o is a function of B_s and can be obtained by solving the integral equation

$$(3.48b) \qquad \int_{x_o}^{a} B(x)dx = B_{//}a$$

Alternatively x_o can be obtained by taking $B_c = B_{//}$ as the limit of integration in equation (3.44a). In the Bean-London approximation we find

$$(3.52) \qquad \frac{x_o}{a} = \frac{B_s}{B_*} - \left\{\left(\frac{B_s}{B_*}\right)^2 - 2\left(\frac{B_s - B_{//}}{B_*}\right) + 1\right\}^{\frac{1}{2}}$$

Region III(a) spans the width $x_o^* \leq x \leq x_o$ and contains all the vortices created during the sweep of B_s from $B_{//}$ to B_s^*. The first integral on the right-hand side of equation (3.44a) describes the trajectory of these vortices as B_s increased to B_s^*. The second integral describes their subsequent advance as B_s progresses beyond B_s^*. Introducing the appropriate pinning function into equation (3.44a), again noting that $B(x_i) = B_{//}$ for the nonmagnetic initial state and integrating we obtain

$$(3.53a) \qquad B^2 = B_c^2 + 2B_{//}(B_s^* - B_c) + \left\{ (B_s - B_*)^2 - B_{//}^2 \right\}$$

$$(3.53b) \qquad B^{5/2} = B_c^{5/2} + \frac{5}{3} B_{//}(B_s^{*3/2} - B_c^{3/2}) + \left\{(B_s^{3/2} - B_*^{3/2})^{5/3} - B_{//}^{5/2}\right\}$$

$$(3.53c) \qquad B^3 = B_c^3 + \frac{3}{2} B_{//}(B_s^{*2} - B_c^2) + \left\{(B_s^2 - B_*^2)^{3/2} - B_{//}^3\right\}$$

for n = 1, ½ and 0 respectively and we have made use of equation (3.34) for B(a). Equation (3.53a) can readily be solved and leads to

$$(3.54) \qquad B_c = B_{//} + \left\{2B_* (B_s - B_{//}) - B_*^2 - 2B_s B_* \left(\frac{x}{a}\right) + B_*^2 \left(\frac{x}{a}\right)^2\right\}^{\frac{1}{2}}$$

where we have made use of $B_s^* = B_{//} + B_*$ which follows from equation (3.34a). Letting $B_c = B_{//}$ in equation (3.54) leads to equation (3.52).

Region III(b) adjacent to the surface and spanning the width $0 \leq x \leq x_o^*$ contains the vortices created since B_s attained B_s^*.

Their trajectory is described by the expression

$$(3.44b) \qquad \int_{B_c}^{B} \frac{B^2 dB}{F_p(B)} = \int_{B_c}^{B_s} \frac{B_s B(a) dB_s}{F_p(B_s)}$$

which yields

$$(3.55a) \qquad B^2 = B_c^2 + (B_s - B_*)^2 - (B_c - B_*)^2$$

$$(3.55b) \qquad B^{5/2} = B_c^{5/2} + (B_s^{3/2} - B_*^{3/2})^{5/3} - (B_c^{3/2} - B_*^{3/2})^{5/3}$$

$$(3.55c) \qquad B^3 = B_c^3 + (B_s^2 - B_*^2)^{3/2} - (B_c^2 - B_*^2)^{3/2}$$

for n = 1, ½ and 0 respectively. The interface between regions III(a) and III(b) is obtained by letting $B_c = B_s^*$ in equation (3.44b) (hence in equation (3.55)). For the Bean-London approximation, (equation (3.55a)), we find

$$(3.56) \qquad B_c = B_s\left(1 - \frac{x}{a}\right) + \frac{B_*}{2}\left(\frac{x}{a}\right)^2$$

which leads to

$$(3.57) \qquad \frac{x_o^*}{a} = \frac{B_s}{B_*} - \left\{\left(\frac{B_s}{B_*}\right)^2 - 2\,\frac{(B_s - B_{//})}{B_*} + 2\right\}^{1/2}$$

when we let $B_c = B_s^*$ where $B_s^* = B_{//} + B_*$.

In Figure 3.30 we present a sequence of B_z and B_y profiles for the force free case and for the Bean-London approximation starting from the nonmagnetic state. The curves are normalized to $B_{//}$ and we have chosen $B_{//} = B_*$ for illustration.

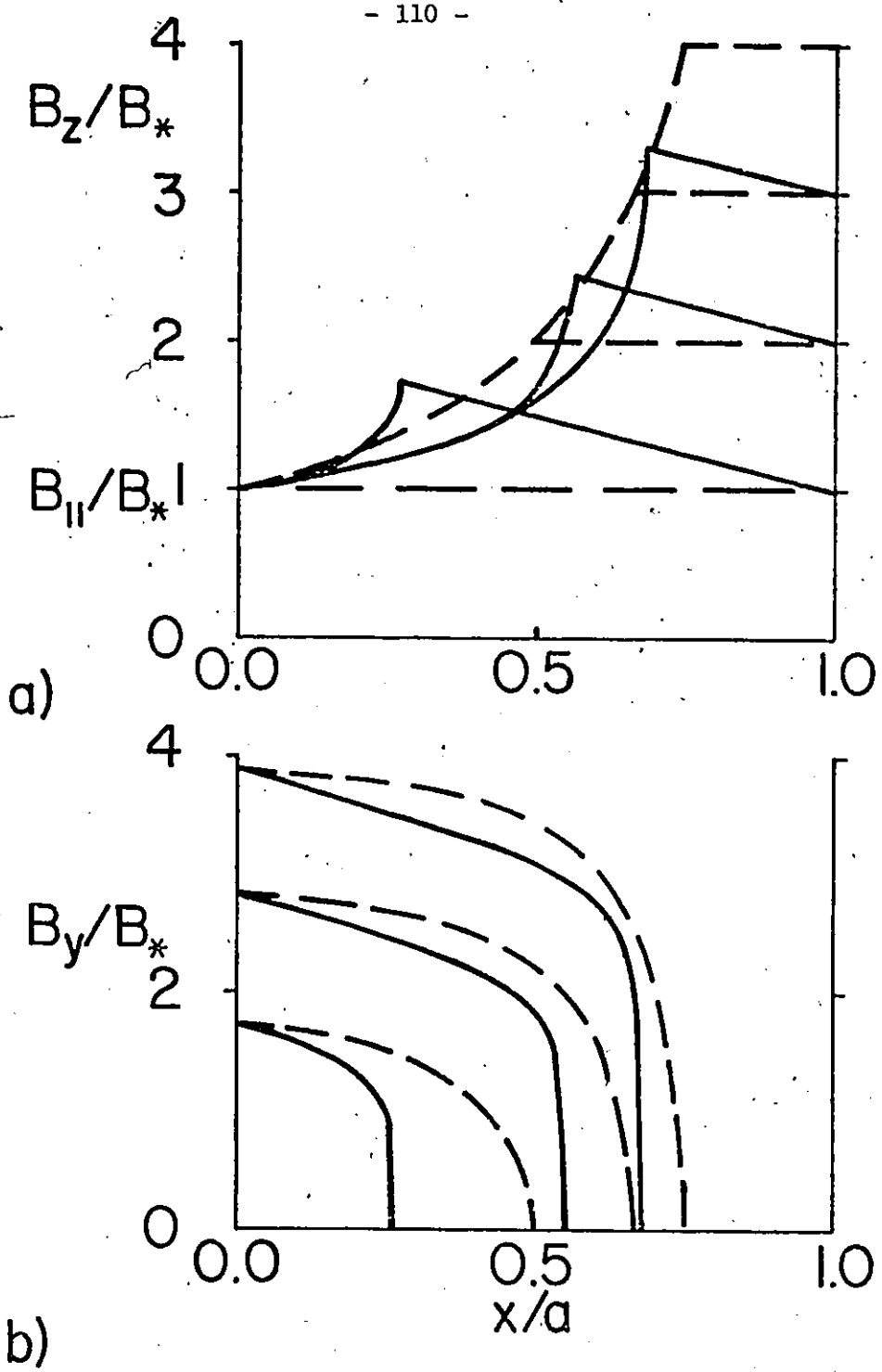

FIG. 3.30 Illustrates evolution of B_z and B_y profiles as $B_\perp$ increases from zero with $B_{//}$ stationary and taken equal to B_*. $B_s/B_* = 2,3$ and 4 as $B_z(x)$ rises and $B_y(x)$ advances. Dashed and solid curves are calculated for force free case and with Bean-London approximation ($F_p = \alpha B$) respectively.

3.8 DIRECTION OF $\vec{E}$ WITH RESPECT TO $\vec{J}$

It is of interest to determine

$$\psi = \sin^{-1} \frac{\vec{E} \times \vec{J}}{\hat{x}\, E\, J} = \cos^{-1} \frac{\vec{E} \cdot \vec{J}}{EJ} \tag{3.58}$$

the angle subtended by the electric field $\vec{E}$, generated by the penetration of the flux lines into the slab and the persistent current density $\vec{J}$. Introducing equations (3.11a) and (3.12a) into equation (3.9) yields

$$E_y = (a-x) \frac{B_z}{B} \frac{d}{dt} \langle B \rangle_x, \quad E_z = -(a-x) \frac{B_y}{B} \frac{d}{dt} \langle B \rangle_x \tag{3.59}$$

According to the concept of equilibrium diamagnetism (assuming isotropy)

$$\frac{\partial H_y}{\partial B_y} = \frac{\partial H_z}{\partial B_z} = \frac{\partial H}{\partial B} \tag{3.60}$$

The components of the current density from Maxwell's equation $\nabla \times \vec{H} = \vec{J}$ can therefore be written, for infinite slab geometry,

$$J_y = - \frac{\partial H}{\partial B} \frac{\partial B_z}{\partial x}, \qquad J_z = \frac{\partial H}{\partial B} \frac{\partial B_y}{\partial x} \tag{3.61}$$

Exploiting equations (3.59) and (3.61) we write

$$E_y J_z - E_z J_y = \frac{(a-x)}{B} \left(\frac{\partial H}{\partial B}\right) \frac{d}{dt} \langle B \rangle_x \left\{ B_z \frac{\partial B_y}{\partial x} - B_y \frac{\partial B_z}{\partial x} \right\} \tag{3.62}$$

In region II (see Figure 3.29) where flux lines, initially threading the slab at some arbitrary uniform orientation $\theta(x) = \theta_i$, are now undergoing compression, we find that

$$B_z \frac{\partial B_y}{\partial x} - B_y \frac{\partial B_z}{\partial x} = 0 \tag{3.63}$$

since here $B_y(x)/B_z(x) = \tan^{-1} \theta(x) = \tan^{-1} \theta_i$, an arbitrary constant. Consequently $\vec{E} \times \vec{J} = 0$ and $\psi = 0$, hence the electric field lies parallel to the current density, as expected.

Using equations (3.59) and (3.61) we write $\vec{E}.\vec{J}$ as

$$(3.64) \qquad E_y J_y + E_z J_z = - \left(\frac{a-x}{B}\right) \left(\frac{\partial H}{\partial B}\right) \frac{d}{dt} \langle B \rangle_x \left\{B_y \frac{\partial B_y}{\partial x} + B_z \frac{\partial B_z}{\partial x}\right\}$$

In the force free situation, $B_y \, \partial B_y/\partial x + B_z \, \partial B_z/\partial x = 0$ since $\vec{j} \times \vec{B} = 0$. Consequently $\vec{E}.\vec{J} = 0$ and the electric field is orthogonal to the current density, as required, since there is no energy dissipation.

In hysteretic materials, in the region $0 \leq x \leq x_o$, the slope of B_z is positive (negative) when the slope of B_y is negative (positive). Consequently, $B_z \, (\partial B_y/\partial x) - B_y \, (\partial B_z/\partial x) \neq 0$ hence $\sin \psi \neq 0$. Therefore, $\vec{E}$ cannot lie along $\vec{J}$ in the volume where the flux lines are not unidirectional as they are created and advance into the slab. We stress that this result is independent of the choice of pinning function. In his analysis of rotational hysteresis, Bean (146), examines a quasi steady state where flux lines rotate in phase with $\vec{B}_s$ which rotates with constant magnitude. He presents solutions which satisfy the condition $\psi = 0$, in contrast with the situation which prevails in the model we pursue in this thesis. Our analysis indicates that the requirement $\psi = 0$ is incompatible with the postulate that the planes of vortices do not rotate as they advance into the slab.

For the special situation where $B_{//}$ is maintained constant as $B_{\perp}$ is impressed, differentiation of equation (3.39) leads to

$$(3.65)\qquad \frac{\partial B_y}{\partial x} = \frac{(B_c^2 - B_{//}^2)^{\frac{1}{2}}}{B_c}\,\frac{\partial B}{\partial x} + \left(\frac{B_{//}}{B_c}\right)^2 \frac{B}{(B_c^2 - B_{//}^2)^{\frac{1}{2}}}\,\frac{\partial B_c}{\partial x}$$

and

$$(3.66)\qquad \frac{\partial B_z}{\partial x} = \frac{B_{//}}{B_c}\,\frac{\partial B}{\partial x} - \frac{B_{//}B}{B_c^2}\,\frac{\partial B_c}{\partial x}$$

Introducing these results into equations (3.61), (3.62) and (3.58) we obtain

$$(3.67)\qquad \sin\psi = \frac{B_{//}B}{B_c(B_c^2 - B_{//}^2)^{\frac{1}{2}}}\;\frac{\partial B_c/\partial x}{\left\{\left(\frac{\partial B_z}{\partial x}\right)^2 + \left(\frac{\partial B_y}{\partial x}\right)^2\right\}^{\frac{1}{2}}}$$

Again we note that $\psi(x) \neq 0$ when $B_{//} \neq 0$. The computation of $\psi(x)$ is evidently a formidable task. Using equation (3.45) in equation (3.67) we can verify that $\sin\psi = -1$ for the force free configuration.

3.9 REMOVAL OF FLUX AND CYCLIC BEHAVIOUR

When $\vec{B}_s$, the magnetic induction at the surface increases in magnitude as its direction θ_s changes, the two variables B_s and θ_s are independent. Among the multitude of possible concomitant variations of B_s and θ_s we have focussed on the special situation where $B_\perp$ is raised from zero with $B_{//}$ stationary. When, however, $\vec{B}_s$ decreases in magnitude, its orientation becomes a function of B_s and this relationship is dictated by $\vec{B}_{max}(x)$, the configuration of the magnetic induction existing in the slab when the down sweep of B_s starts.

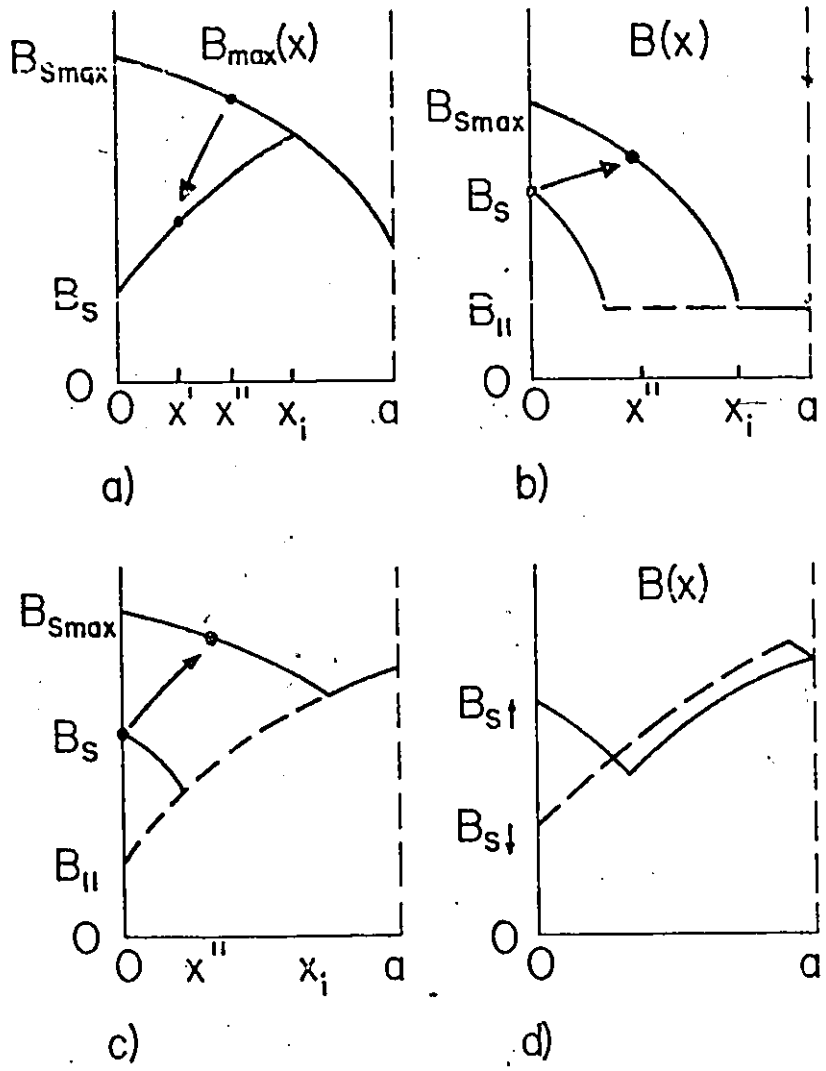

FIG. 3.31 Sketches of the evolution of various B(x) profiles to aid in visualizing the meaning and relationship of various quantities employed in section 3.9 of the text in the framework of flux conservation.

a) Vortices located at x'' on the $B_{max}(x)$ profile are found at x' after decrease of B_S from B_{Smax}.

b) Nonmagnetic initial state. Vortices created at x = 0 have advanced to x'' (indicated by dot) when B_S attains B_{Smax}.

c) Paramagnetic initial state. Vortices created at x = 0 have advanced to x'' (indicated by dot) when B_S attains B_{Smax}.

d) With $B_{//}$ stationary B_S is increasing (solid curve) until saturation profile (not shown) is established. Subsequently B_S is decreased. By flux conservation, when area under dashed profile equals that under solid profile, vortices which entered at flux density $B_{S\uparrow}$ must exit at flux density $B_{S\downarrow}$. The postulate that vortices do not rotate during migration then requires that at exit, $B_z(0) = B_{//} B_{S\downarrow}/B_{S\uparrow}$.

Now, the dependence of θ_s on B_s (hence of $B_\perp$ and $B_{//}$ on B_s) must first be unravelled before equations (3.16) and (3.17) (or the equivalent equations (3.28) and (3.29)), which describe the evolution of $\langle B_y \rangle$ and $\langle B_z \rangle$, can be exploited.

Throughout this study, the critical state equation (equation (3.20)) enables us to map out the sequences of B(x) profiles as B_s is swept up, swept down or varied cyclically, starting from any imaginable initial configuration. To determine the concomitant evolution of $\theta(x, B_s)$ during the down sweep of B_s we can continue to exploit equation (3.43) in the integral form

$$(3.68) \qquad \int_{B_{max}(x'')}^{B(x',B_s)} \frac{B^2 dB}{F_p(B)} = \int_{B_{smax}}^{B_s^*} \frac{B_s B(x_i) dB_s}{F_p(B_s)} + \int_{B_s^*}^{B_s} \frac{B_s B(a) dB_s}{F_p(B_s)}$$

where $0 < B_s < B_{smax}$. See Figure 3.31(a) for aid in visualizing the symbols. In situations where x_i does not penetrate to the midplane, the second integral on the right-hand side does not appear and B_s replaces B_s^* as the upper limit on the first integral. B_s^* again denotes the magnetic induction at the surface when x_i reaches the midplane during the down sweep of B_s. Equation (3.68) provides a relationship between x' and x". It enables us to determine the depth x" on the $B_{max}(x)$ profile from which a sheet of vortices has originated and is now located at x' when the magnetic induction at the surface is B_s. The components of the magnetic induction at x' on the $B(x,B_s)$ profile can then be determined from the postulate of conservation of orientation during migration, which can be written

$$(3.69a)\qquad \frac{B_y(x',B_s)}{B(x',B_s)} = \frac{B_{ymax}(x'')}{B_{max}(x'')}\ , \qquad \frac{B_z(x',B_s)}{B(x',B_s)} = \frac{B_{zmax}(x'')}{B_{max}(x'')}$$

and is a variant of equation (3.38).

Focussing on the sheets of vortices as they arrive at the surface, $x' = 0$, the upper limit of the integral on the left-hand side of equation (3.68) becomes $B_s \equiv B(0,B_s)$. This special case of equation (3.68) enables us to determine from which depth x'' on the $B_{max}(x)$ profile, the plane of vortices now at the surface has originated. We then determine the orientation of B_s from equation (3.69) which can now be written

$$(3.69b)\qquad \frac{B_\perp}{B_s} = \frac{B_{ymax}(x'')}{B_{max}(x'')}\ , \qquad \frac{B_{//}}{B_s} = \frac{B_{zmax}(x'')}{B_{max}(x'')}$$

We emphasize that we cannot now prescribe that $B_{//}$ remain constant during the down sweep of B_s even if $B_{//}$ was held constant during the up sweep of B_s which established the $\vec{B}_{max}(x)$ configuration. The postulate of non rotating vortices requires that $B_{//\downarrow}/B_{s\downarrow} = B_{//\uparrow}/B_{s\uparrow}$ where we let the up and down arrows denote entry and exit quantities. In the force free case $B_{s\downarrow} = B_{s\uparrow}$ since the flux lines emerge at the same density they had at entry. In hysteretic materials, however, $B_{s\downarrow} < B_{s\uparrow}$, the density of a sheet of flux lines at exit is less than their density at entry. This can readily be seen by considering sequences of B profiles during the up sweep and subsequent down sweep in the light of flux conservation (see Figure 3.31(d)).

Having followed this procedure just outlined to extract the variation of $B_\perp$ and $B_{//}$ with B_s decreasing we can then proceed to a

calculation of the evolution of $\langle B_y \rangle$ and $\langle B_z \rangle$ using equations (3.16) and (3.17) (or (3.28) and (3.29)). We can thereby again avoid the effort required to trace in detail the sequence of the $B_y(x)$ and $B_z(x)$ profiles. In this exercise, it is only necessary to determine the detailed $\vec{B}_{max}(x)$ configuration. The latter can be obtained, without calculating the intermediate $\vec{B}(x)$ configurations during the up sweep of B_s from B_{si} to B_{smax}, by taking $B_s = B_{smax}$ for the upper limit of integration of equation (3.44) and letting the lower limit sweep the range $B_{si} \leq B_c \leq B_{smax}$.

We now outline an alternative approach for the determination of the sequences of B_y and B_z profiles during the up and down sweeps of B_s. The method is equivalent to that developed earlier and is not more nor less tedious to implement. To fix ideas we focus on the situation where B_s is decreasing from B_{smax} (see Figure 3.31(a)). From conservation of flux we can write

$$(3.70) \qquad \int_{x'}^{x_i} B(x,B_s)dx = \int_{x''}^{x_i} B_{max}(x)dx$$

which can be solved analytically or numerically to yield x' versus x" (or vice versa). This expression contains the same information as equation (3.68). The sheet of vortices located at x" when the magnetic induction at the surface was B_{smax} is now found at x' when the magnetic induction at the surface is B_s. Exploiting equation (3.69a) we then determine $B_y(x')$ and $B_z(x')$. Choosing x' = 0 in equation (3.70) we obtain the position of origin on the $B_{max}(x)$ profile of the vortices now exiting. Introducing this information

in equation (3.69b), yields $B_\perp$ and $B_{//}$ versus B_s. Thus a calculation of detailed B_y and B_z profiles can again be set aside and the evolution of $\langle B_y \rangle$ and $\langle B_z \rangle$ with B_s computed using equations (3.16) and (3.17) (or (3.28) and (3.29)).

In the Bean-London approximation, $B(x) = B_s + B_*(x/a)$ when $0 \le x \le x_i$ and $B(x) = B_{max}(x)$ when $x_i \le x \le a$ and $B_{max}(x) = B_{smax} - B_*(x/a)$ we find

$$\frac{x_i}{a} = \frac{B_{smax} - B_s}{2B_*} \tag{3.71}$$

and

$$\frac{x''}{a} = \frac{B_{smax}}{B_*} - \left\{ \frac{1}{2} \left(\frac{B_s + B_{smax}}{B_*}\right)^2 - \left(\frac{B_s}{B_*} + \frac{x'}{a}\right)^2 \right\}^{1/2} \tag{3.72}$$

In the Kim ($F_p = \alpha_0$) approximation, $B(x) = (B_s^2 + B_*^2(x/a))^{1/2}$ when $0 \le x \le x_i$, and $B(x) = B_{max}(x)$ when $x_i \le x \le a$ and $B_{max}(x) = (B_{smax}^2 - B_*^2(x/a))^{1/2}$ we find

$$\frac{x_i}{a} = \frac{B_{smax}^2 - B_s^2}{2B_*^2} \tag{3.73}$$

and

$$\frac{x''}{a} = \left(\frac{B_{smax}}{B_*}\right)^2 - \left\{ \frac{1}{\sqrt{2}} \left(\frac{B_s^2 + B_{smax}^2}{B_*}\right)^{3/2} - \left(\left(\frac{B_s}{B_*}\right)^2 + \frac{x'}{a}\right)^{3/2} \right\}^{2/3} \tag{3.74}$$

Letting $x' = 0$ in equations (3.72) and (3.74) gives the initial position of the sheet of flux line which is now exiting from the slab hence its orientation since the configuration $\vec{B}_{max}(x)$ is presumed to be known.

The $\vec{B}_{max}(x)$ configuration generated by the up sweep of $\vec{B}_s$ can also be calculated using equation (3.70) with $x' = 0$. We refer the reader to Figures 3.31(b) and 3.31(c) for sketches of B(x) profiles. Again we note that in this exercise the intermediate B_y and B_z profiles generated during the up sweep of $\vec{B}_s$ need not be computed.

By way of illustration of the behaviour we consider a cycle where $B_\perp$ oscillates between 0 and $B_{\perp max}$. Again we stipulate that $B_{//}$ is maintained stationary during the increase of $B_\perp$. When $B_\perp$ decreases from $B_{\perp max}$ to zero, $B_{//}(B_s)$, however, must be allowed to vary as dictated by the configuration of the flux inside the slab as the vortices depart. We also wish to insure that the cycle is closed. This is accomplished by starting from a saturated paramagnetic initial state (see Figure 3.31(c)). In this situation, when $B_\perp$ returns to zero and B_s returns to $B_{//}$, after their excursions to $B_{\perp max}$ and B_{smax}, the configuration of flux which is encountered corresponds to the initial one.

We adopt the Bean-London approximation and choose $B_{//} = B_*$ and let $\vec{B}_s$ sweep from $B_{//}$ to B_s^*, hence $B_s^* = 3B_{//}$, $B_{\perp max} = 2\sqrt{2}\, B_*$. The cycle traversed by $\vec{B}_s$ in the $B_{//} - B_\perp$ plane is displayed in Figure 3.32. In the force free case, $\vec{B}_s$ descending retraces the path of $\vec{B}_s$ ascending. Taking $0 \leq n \leq 1$ in $F_p = \alpha_n B^n$ and the corresponding B_* yields return paths of $\vec{B}_s$ lying between the Bean-London (n = 1) trajectory and the horizontal (force free case) and displayed upwards with decreasing n. The sequences of B_z and B_y profiles when n = 1 are displayed in Figure 3.33. During the

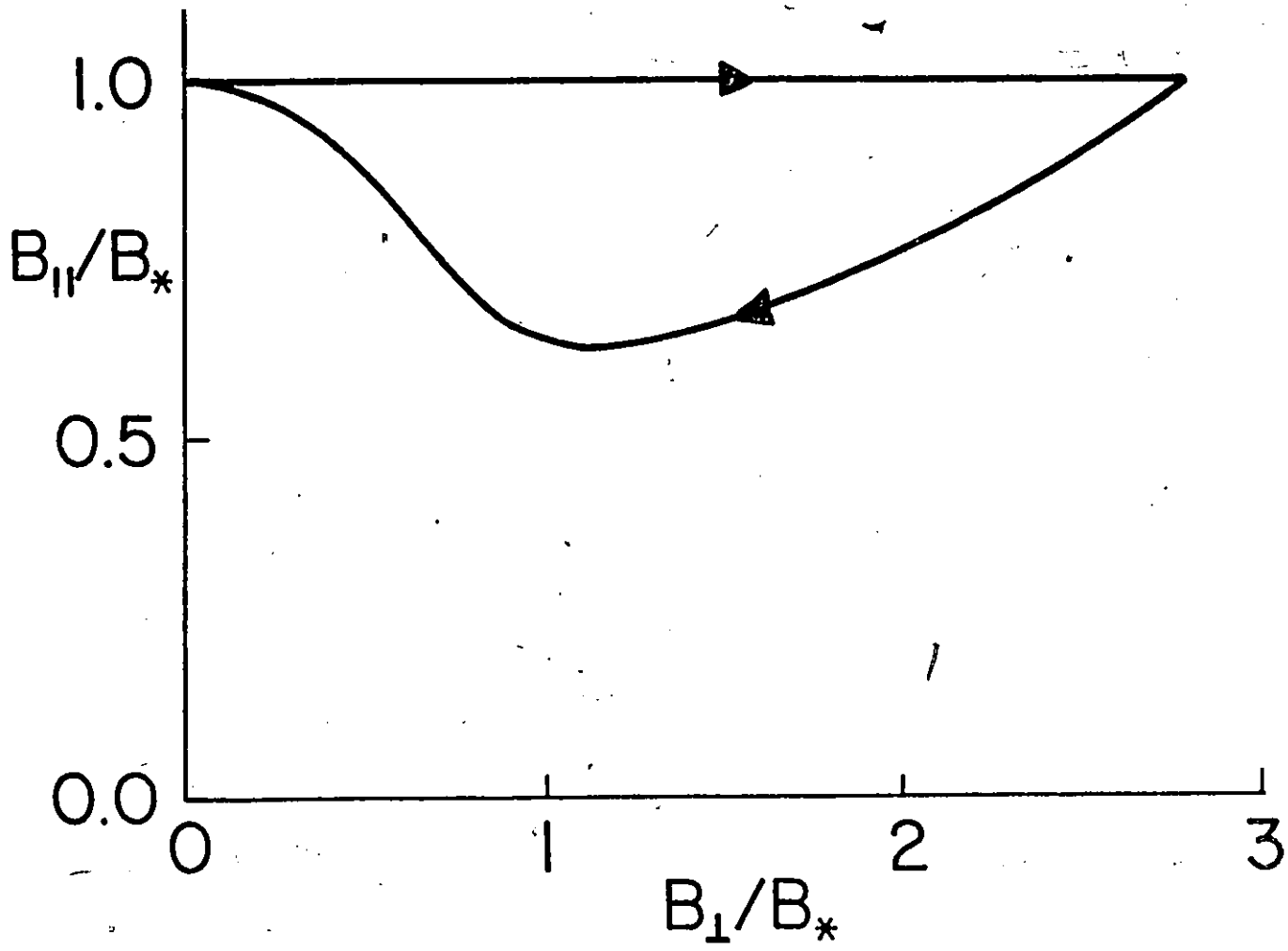

FIG. 3.32 Locus of $B_z(0)$, hence $\vec{B}_s$, in $B_{//} - B_\perp$ plane which is mandated by the model when B_s is decreased from 3 $B_{//}$ to $B_{//}$ subsequent to an increase of $B_\perp$ from 0 with $B_{//}$ stationary where the $B_z(x)$ profile was initially in a saturated paramagnetic configuration. The Bean-London approximation ($F_p = \alpha B$) is used to determine the B profiles and $B_{//}$ is chosen equal to B_*. In force free case locus of $\vec{B}_s$ during down sweep retraces that of up sweep.

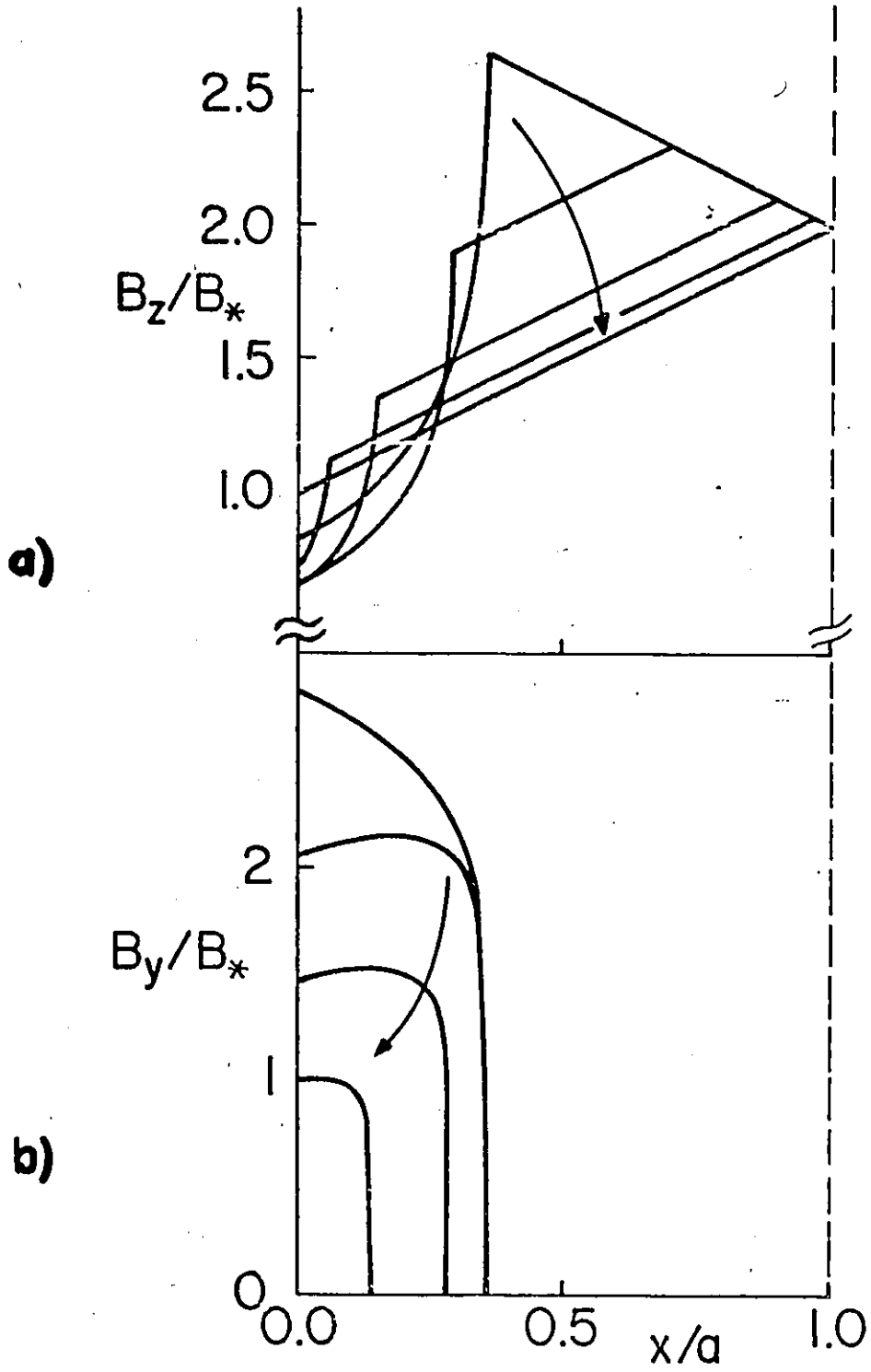

FIG. 3.33 Evolution of B_z and B_y profiles during down sweep of $\vec{B}_s$ shown in Fig. 3.32 where previous history and parameters of the calculation are indicated. In the sequence of the profiles as indicated by the arrows, $B_s/B_* = 2.4$, 1.6, 1.2, 1.06 and 1.0 for (a) and 3.0, 2.2, 1.6 and 1.2 for (b).

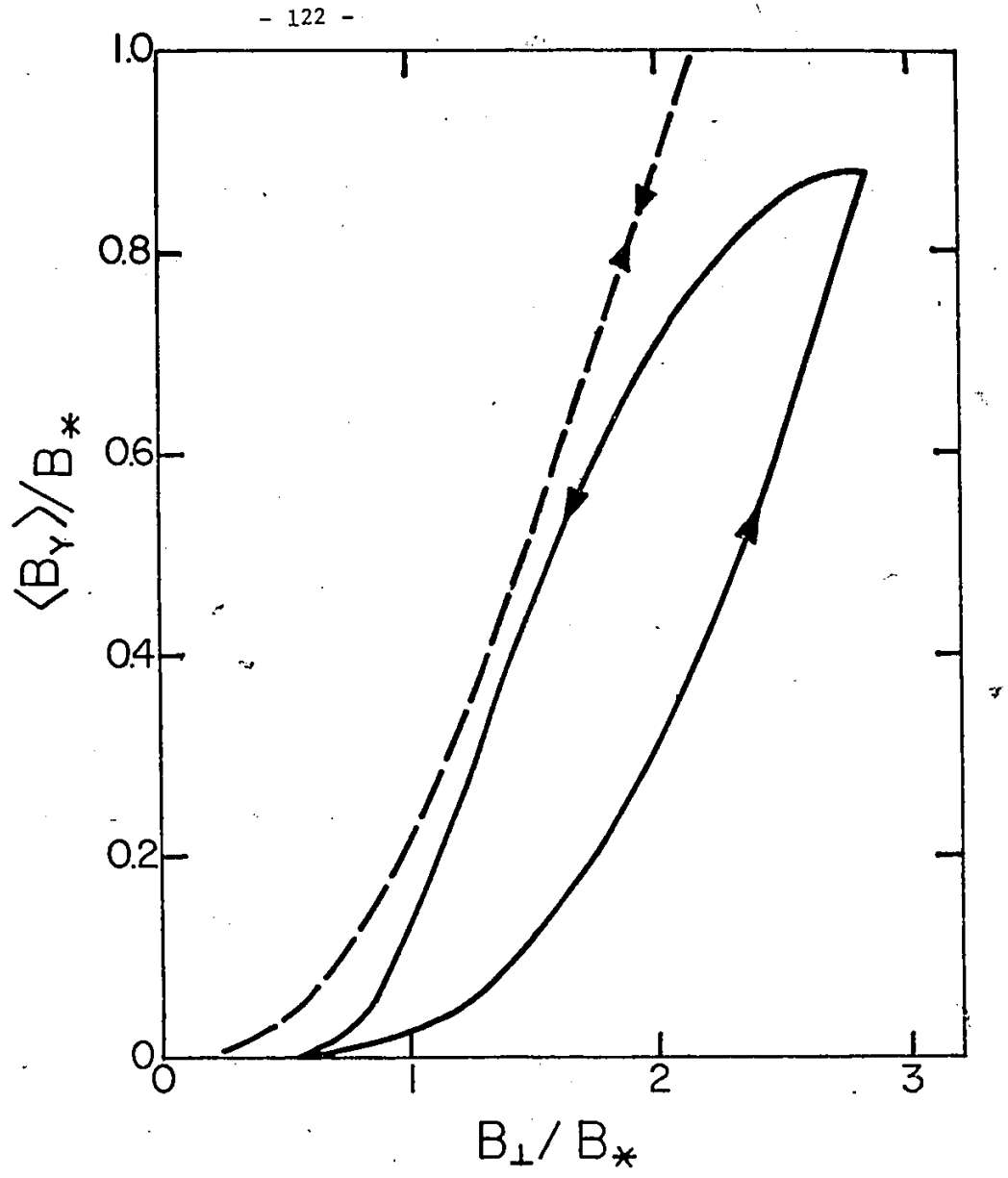

FIG. 3.34 Evolution of $\langle B_y \rangle$ profile corresponding to closed cycle shown in Fig. 3.32 where the initial state and the parameters of the calculation are indicated. Solid curve shows $\langle B_y \rangle$ vs. $B_\perp$ where $H_{//}$ is maintained constant only during up sweep of B_s. Dashed curve shows variation of $\langle B_y \rangle$ for force free case, the curve is reversible since down sweep of $\vec{B}_s$ must, in this case retrace the up sweep shown in Fig. 3.32.

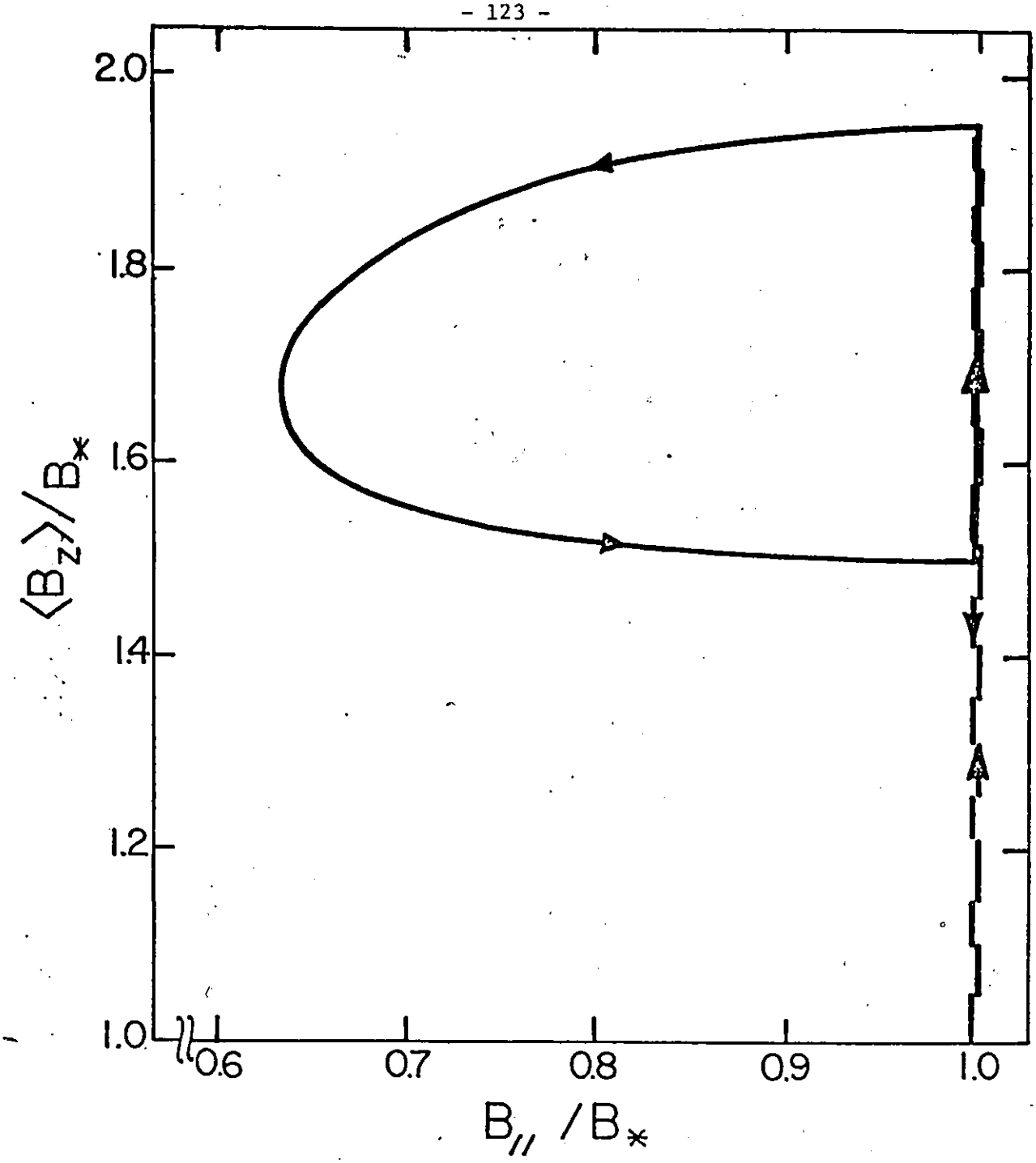

FIG. 3.35 Evolution of $\langle B_z \rangle$ profile corresponding to closed cycle shown in Fig. 3.32 where the initial state and the parameters of the calculation are indicated. Solid curve shows $\langle B_z \rangle$ vs. $B_{//}$ which is maintained constant only during up sweep of B_s. Dashed curve shows variation of $\langle B_z \rangle$ for force free case, the curve is reversible, since down sweep of B_s must, in this case, retrace the up sweep shown in Fig. 3.32, then $B_{//}$ is stationary during decrease of $B_\perp$ and $\langle B_z \rangle$ vs. $B_{//}$ traces a vertical line.

initial portion of the down sweep of $B_\perp$, the front of the B_y profile, x_o, remains stationary until $x_i = x_o$ and decompression of the initial trapped flux begins. Subsequently x_o moves outwards and the B_y profiles retreat from the slab as x_i continues its advance to the midplane. We show $\langle B_y \rangle$ versus $B_\perp$ and $\langle B_z \rangle$ versus $B_{//}$ during the cycle in Figures 3.34 and 3.35 respectively. The dissipation of energy per cycle is equal to B_*^2/μ_o times the sum of the areas enclosed by these two curves. The dashed line in Figures 3.34 and 3.35 show $\langle B_y \rangle$ vs. $B_\perp$ and $\langle B_z \rangle$ vs. $B_{//}$ for the force free case. Using $F_p = \alpha_n B^n$, the corresponding B_* and letting $\vec{B}_s$ sweep from $B_{//}$ to B_s^* generates enclosed areas which diminish as n decreases from 1 to 0.

3.10 I_c VERSUS $B_{//}$

The conduction current is taken to flow in the z direction. For initial magnetic states where $\langle B_z \rangle \neq 0$, a steady state of flux flow resistance cannot occur with non-rotating vortices since then $v = 0$ at the midplane by symmetry. Under these circumstances a bulk critical current I_c (per unit length y of slab) is attained only when $B_s = B_{c2}$ and superconductivity in the bulk is destroyed. This leads to a Silsbee-like rule

$$I_c = \frac{2}{\mu_o} \left(B_{c2}^2 - B_{//}^2\right)^{\frac{1}{2}} \tag{3.75}$$

which is not in accord with observations (66, 68). We also note that I_c is independent of the initial magnetic state. When $B_{//} = 0$ and $\langle B_z \rangle = 0$, mutual annihilation of oppositely directed vortices, at the

midplane, generating a steady state flux flow resistance can take place when $B_s \geq B_s^*$. Ignoring equilibrium diamagnetism and surface barriers, this picture leads to $I_c = 2B_s^*/\mu_o$. Consequently I_c vs. $B_{//}$ is discontinuous at $B_{//} = 0$ unless $B_s^* = B_{c2}$.

The critical currents encountered when the externally applied magnetic field has a component $H_{\perp a}$ in the y direction are also of interest (147). Under these circumstances and again ignoring equilibrium diamagnetism and surface barriers we can write

$$\frac{\vec{B}_s}{\mu_o} = \hat{y}\,(H_{\perp a} \pm \frac{I}{2}) + \hat{z}\,H_{//} \tag{3.76}$$

for the magnetic induction just inside the surfaces, where the positive sign applies to one surface of the slab and the negative to the other. The B profiles across the width of the infinite slab are no longer symmetric about the midplane when $I \neq 0$. At the surface where the negative sign applies, B_s changes direction and decreases in magnitude as $I/2 \rightarrow H_{\perp a}$. According to the critical state concept, the decrease in B_s causes an exit of some vortices at this surface. Let us now visualize that initially (at $I = 0$) the vortices threading the slab are oriented along $\vec{H} = \hat{y}H_{\perp a} + \hat{z}H_{//}$. As I is impressed the direction of the vortices does not correspond to $\vec{B}_s/\mu_o = \hat{y}(H_{\perp a} - (I/2)) + \hat{z}H_{//}$. The present model of vortices not rotating during migration now leads to a dilemma or impasse and is inapplicable to a treatment of the straightforward situation just envisaged. At the surface where $\vec{B}_s$ increases in magnitude as I is introduced, vortices are created and enter the slab, and no problem of a discontinuity arises.

3.11 CONCLUSION

We have examined in some detail, in the context of the quasi-static critical state, the consequences of the postulate that vortices migrate without rotation in infinite slabs of type II superconductors when, $\vec{B}_s$ the magnetic induction at the surface changes its direction, θ_s, as it is swept in magnitude.

For large sweeps of B_s and θ_s, the behaviour predicted by the model is insensitive to the mode of pinning and approaches the force free case. This occurs because the sequences of B profiles are nearly parallel and horizontal as B_s becomes large. The rate of entry of flux lines is then approximately proportional to ΔB_s whether pinning operates or not. Although $B_{//}$ is maintained constant the model leads to a continuous increase in $\langle B_z \rangle$ until $\vec{B}_s$ reaches B_{c2} since every vortex added to the slab has a component along the z-axis. The net flux initially threading the slab along the z direction is compressed in a core area straddling the midplane as $\vec{B}_s$ is increased. The penetration of the vortices entering the slab during the sweep of $\vec{B}_s$ is limited by the boundaries of this central core. As a consequence $\langle B_y \rangle$ also lags significantly below $B_{\perp}$ until B_s attains B_{c2} and bulk superconductivity is destroyed. These features of the model which can be appreciated intuitively appear to have been previously overlooked and are developed quantitatively. A comparison of the predictions of the model with our observations shows fair agreement during the initial portion of the increase in $\vec{B}_s$ starting from a variety of initial magnetic states. As the sweep in $\vec{B}_s$ progresses

however, the theoretical and experimental curves diverge markedly since $\langle M_z \rangle$ and $\langle M_y \rangle$ after traversing a peak are observed to decline and approach zero asymptotically whilst the calculated curves continue to rise. We are led to the conclusion that the flux lines can undergo significant rotation as they migrate into the specimen (42, 68, 144).

We have developed two different but equivalent approaches for the calculation of the evolution of the sequences of B_y and B_z profiles and their spatial averages as B_s and θ_s are varied simultaneously. In the discussion of hysteresis losses, basic and simple formulae are obtained which can be exploited in the standard situation where $\vec{B}_s$ oscillates in magnitude only without changing orientation.

Many aspects and ramifications of the model hitherto not touched upon in the literature, are developed in this thesis. In particular, we have (i) examined the behaviour prescribed by the model when (a) flux is made to exit and (b) $\vec{B}_s$ undergoes cyclical variations in magnitude and orientation, (ii) studied the direction predicted for the electric field with respect to the current density and shown that $\vec{E}$ does not lie along $\vec{J}$ in the region where the configuration of $\vec{B}$ changes direction with depth and (iii) shown that the critical currents anticipated are much larger than measured.

In summary, the simple and conceptually appealing assumption that vortices, after creation, migrate without rotation as the applied magnetic field changes magnitude and direction has been carefully pursued. In some materials (e.g., NbTi), the model leads to a satisfactory description of the data obtained with $\mu_o H_{//}$ stationary and spanning a range extending up to $\approx$ 1T with up sweeps of $\mu_o H_{\perp}$ also up to

$\approx$ 1T (144). The agreement in those circumstances is misleading in our view, because in that sample, B_*, the macroscopic penetration depth, is also very large and $\approx$ 0.8T. The present investigation, where the ranges of $\mu_o H_{//}$ and $\mu_o H_{\perp}$ extend to several B_*, indicates strongly that the basic postulate of non rotation during migration ultimately leads to poor agreement with observations and cannot be seriously retained. The detailed picture which emerges from our scrutiny of this concept should provide useful background and insight for the development of an acceptable model. The process of flux cutting (B) may very well play a role in the reorientation of the sheets of flux lines as they migrate.

CHAPTER 4

HYSTERESIS LOSSES AND MAGNETIC PHENOMENA IN NONCOLLINEAR REGIMES

4.1 INTRODUCTION

Hysteresis losses in situations where an oscillating magnetic field $\vec{h}_o(t)$ is collinear with a stationary bias magnetic field $\vec{H}_{bias}$ applied along the surfaces of a ribbon or cylindrical sample of a type II superconductor have been extensively investigated both experimentally and theoretically. In a major survey and synthesis of our present understanding of hysteresis losses in the collinear regime, Clem (3) predicted that, in some samples, these losses, $W(h_o, H_{bias})$, would trace a valley when the measurements are performed and displayed as a function of the bias field H_{bias} for particular chosen amplitudes h_o. This feature, of import for applications, has already been reported and investigated by several workers (23, 34, 40). In the next chapter we address the contribution of bulk pinning to this phenomenon. The losses, both predicted and observed, at the bottom of the valley, $W(h_o, H_{bias})_{min}$, still constitute, however, a significant fraction of the losses occurring at its left hand summit (at zero bias, $W(h_o, 0)$). In other words, the depth of the valley is not impressive.

In this chapter we investigate hysteresis losses in situations where $\vec{h}_o(t)$ is orthogonal to $\vec{H}_{bias}$. In this configuration we find that the losses, $W(\vec{h}_o, \vec{H}_{bias})$ again traverse a valley when examined as a function of H_{bias} for various chosen amplitudes. The valley now, however, can be appreciably more spectacular than in the collinear regime. This

feature is of technological interest. Further the origin of this deep valley appears to involve a physical process which does not occur in the collinear arrangement, namely, flux cutting.

A valley in $W(\vec{h}_o, \vec{H}_{bias})$ where $\vec{h}_o$ and $\vec{H}_{bias}$, directed along the broad surfaces of the sample, are orthogonal or tilted with respect to each other, (this is denoted the noncollinear regime) was first observed by Lachaine in ribbon samples of NbTi and VTi. In his measurements, the "left side" of the valley was mapped out but only the base of the right slope was explored experimentally. His analysis reproduced the dramatic decline in the losses from zero bias to the floor of the valley and predicted a continuation of the rise and the formation of a right slope beyond the observed base. In this chapter we extend his measurements on the VTi specimen and trace out the entire valley in detail. Further we show that the right slope rises to a broad plateau which then descends towards zero ("sea level") as H_{bias} increases towards H_{c2}. Pursuing the trailblazing exploration of Lachaine further, we examine the evolution of the shape of the valley and the broad peak when $\vec{H}_{bias}$ has a component, $H_{b\perp}$ along the oscillating field $\vec{h}_o$. It is convenient to plot W versus $H_{//}$, the component of $\vec{H}_{bias}$ which is orthogonal to $\vec{h}_o$. These plots show that the valley shifts to the right and fills in (becomes shallower) as $H_{b\perp}$ is increased. We have also investigated the behaviour of hysteresis losses in the noncollinear regime for a Nb ribbon. Here $H_{//}$ and $H_{b\perp} + h_o$ scan the entire range from 0 to H_{c2}.

Clem has pointed out a basic difference between the collinear and noncollinear regimes. In the former (assuming material isotropy),

the current density j is perpendicular to the magnetic induction $\vec{B}$ everywhere in the sample. Here $\vec{j}$ and $\vec{B}$ are viewed as quasi-microscopic averages over cross sections encompassing a few vortices. In the latter regime, regions occur where $\vec{j}$ has a component along $\vec{B}$. Indeed the entire sample may be occupied by such regions. Further, an extreme case can be envisaged such that $\vec{j}$ lies along $\vec{B}$ wherever $\vec{j}$ exists. This arrangement is known as a force free configuration. In regions where $\vec{j}$ has a component along $\vec{B}$, the direction, $\hat{\theta}$, of neighbouring sheets of flux line varies spatially. To account for our observations we adopt the double critical state formulation first put forward by Lachaine and successfully exploited by him and other workers in our laboratory to reproduce extensive data for a variety of geometries and situations where the noncollinear regime prevails. According to this approach, configurations of non parallel sheets of flux lines in hysteretic type II superconductors are dictated by two critical state prescriptions, one for dB/dx, the gradient in the density of the magnetic flux (B profile) and another for $d\theta/dx$ the spatial variation of the orientation of the flux lines (θ profile). Lachaine, Gauthier and Boyer have pursued various analogous expressions for $d\theta/dx$. We have found that their formulae do not yield a good description of our data. Consequently we devoted a major effort to a methodical search for a simple analytic function for $d\theta/dx$ which yields an optimum fit to our extensive results.

We then examine the detailed evolution of the spatial average of the magnetic induction threading the ribbon specimen along its length, $\langle B_z \rangle$, and along its width, $\langle B_y \rangle$, as the external applied field is cycled with the longitudinal component, $H_{//}$, kept fixed. We also compare the

rich variety of intricate curves encountered with that generated by the double critical state model using our final formula.

4.2 OUTLINE OF THE EXPERIMENTAL RESULTS

Extensive measurements were performed on a ribbon of VTi and also on a ribbon of Nb. The dimensions of these samples are given in table 4.1.

Table 4.1

Sample	$\alpha_{1/2}$ ($T^{3/2}/m$)	B_{c2} (T)	B_* (T)	Thickness (m)	Width (m)
VTi	10	4.0	0.05	1.5×10^{-3}	5.1×10^{-3}
Nb	1.8×10^{3}	0.4	0.24 T	0.25×10^{-3}	5.5×10^{-3}

In Fig. 4.1 we display, W, the hysteresis losses per cycle per unit volume, measured on the VTi specimen at a chosen amplitude h_o = 0.05 T as a function of the stationary longitudinal magnetic field $H_{//}$. This amplitude was chosen after an exploratory scan of hysteresis losses. The choice was guided by the following observations from this survey. Although deeper valleys occur with decreasing amplitude, the small signals make measurements difficult and lead to greater scatter and uncertainty in the data. With increasing amplitudes the bottom of the valleys shifts to higher $H_{//}$ and the valleys fill in. Indeed upon further increases in amplitude, W versus $H_{//}$ exhibits a rise which becomes steeper and a peak whose summit becomes higher and shifts to

the right. Selections from our data illustrating this sequence of behaviour are presented in Fig. 4.5a. The time varying transverse magnetic field can be written

$$H_1(t) = H_{b1} + h_o\, f(t) \tag{4.1}$$

where H_{b1} is a transverse static bias magnetic field and f(t) varies smoothly between plus and minus one. The special cases where $H_{b1} = 0$ and $H_{b1} = h_o$ are referred to as the full-wave and half-wave cases respectively. Inspection of Fig. 4.1 reveals that for the full-wave case, W versus $H_{//}$ traces a deep valley which is followed by a broad peak which is expected to continue its monotonic descent towards zero at H_{c2}. The ratio of 1 to 6 between the losses at the minimum and at $H_{//} = 0$ is comparable to that reported by Lachaine for a NbTi ribbon sample. These values are of interest for applications. The valley observed for the half-wave case is evidently shallower and its floor is shifted towards higher $H_{//}$. These modifications in the structure of the valley brought about by increasing H_{b1} from 0 to h_o were pursued by taking $H_{b1} = \frac{3}{2} h_o$, $2h_o$ and $3h_o$. These data are also displayed in Fig. 4.1. It is evident that the valley fills rapidly as H_{b1} is increased and has essentially vanished at $H_{b1} = 3h_o$.

Series of measurements were also taken with $H_{//}$ set at the minimum in the valley for the half-wave case and in the vicinity of this minimum as a function of H_{b1}. These measurements constitute vertical data cuts of Fig. 4.1 and examine the movement of the valley floor as H_{b1} is increased. One such set of data, shown in Fig. 4.5b,

exhibits, in a different perspective, a monotonic rise of the valley floor and its transformation into a peak.

We note that the data points where $H_{//} = 0$ in Fig. 4.1 represent measurements of $W(h_o, H_{bias})$ for a fixed h_o where H_{bias} and h_o are collinear. Examination of the sequence of these five data points as a function of H_{bl} shows that W initially decreases, then rises and decreases again. In other words, this subset of data also displays a valley followed by a peak. This valley was predicted by Clem and in the next chapter we examine this particular feature in detail.

Hysteresis losses observed in the Nb ribbon sample in the non-collinear regime are displayed in Fig. 4.6. In this specimen, the valley for the full-wave case is less pronounced than in the VTi sample and the peak is a dominant feature. The family of data curves show the disappearance of the valley and collapse of the peak as a bias field along h_o is increased.

The hysteresis losses are determined by measuring the area enclosed by the closed curve of $\langle B_\perp \rangle$ versus $H_\perp(t)$ which is traced on an X-Y recorder as $H_\perp(t)$ is repeatedly cycled slowly and smoothly between the chosen limits. $\langle B_\perp \rangle$ denotes the spatial average of the magnetic induction along $H_\perp$. Alternatively and equivalently the magnetization $\mu_o \langle M_\perp \rangle = \langle B_\perp \rangle - \mu_o H_\perp$ may be monitored. We refer the reader to chapter 2 for an expose of the experimental arrangement, details of procedures and precautions, method of calibration and tests of the reliability of data. Figs. 4.15, 4.17, 4.19, 4.21 and 4.23 present various sets of observed hysteresis curves.

$\langle B_{//} \rangle$, the spatial average of the magnetic induction along $H_{//}$, also evolves as $H_{\perp}$ is varied although $H_{//}$ is maintained constant. An increase in $\langle B_{//} \rangle$ during the initial application of $H_{\perp}$ with $H_{//}$ stationary is already well known and has been called the longitudinal paramagnetic effect. An analogous behaviour is also observed in wires of type II superconductors immersed in a static longitudinal magnetic field as a conduction current I, fed through the wire via leads from an external source, is impressed. Here, the azimuthal magnetic field H_{θ}, generated by I, plays the role of $H_{\perp}$ applied to the ribbon. The rich variety of behaviour of the locus of $\langle B_{//} \rangle$ as $H_{\perp}$ or I are cycled, although extensively investigated by our group, remains to be addressed in detail in the published literature. In part IV of this chapter we report on this intriguing phenomenon and Figures 4.21, 4.23 and 4.29 show selected sets of observations.

Evidently, for a ribbon specimen, one may choose to maintain $H_{\perp}$ stationary and cause $H_{//}$ to be cycled. We then write

$$H_{//}(t) = H_{b//} + h_o f(t) \tag{4.2}$$

in analogy with equation 4.1. Here $H_{b//}$ is a bias magnetic field collinear with $h_o f(t)$, which varies between $+h_o$ and $-h_o$. These measurements provide additional information and shed light on the role of anisotropy and the finite dimensions of the ribbon on the phenomena encountered.

We have investigated the hysteresis losses in our VTi and Nb ribbons in both of these two arrangements. For the Nb sample we choose to show the data where $H_{\perp}$ is stationary and $H_{//}$ is varied in Fig. 4.6.

One reason for this choice is that the occurrence of flux jumps for some ranges of $H_{//}$ and H_{b1}, cast doubt on the validity of some of the data. Focussing on one arrangement for the VTi sample and the alternative arrangement for the Nb sample also has the merit of shedding light on an important component of our formulae for analysing the phenomena, as we shall see later.

4.3 DEVELOPMENT OF THE MODEL

A. The Double Critical State Concept

In the preceding chapter we have shown that the conceptually attractive concept of the displacement without rotation of flux lines can generate an adequate description of the evolution of $\langle B_y \rangle$ and $\langle B_z \rangle$ during the initial application of $H_\perp$ in a static $H_{//}$ over a limited range. Thus the model may be exploited to describe the magnetic response during the first quarter cycle of a full-wave oscillation or during the first half-cycle of a half-wave oscillation. We have seen, however, that the model is intrinsically incapable of addressing the outward migration of the flux lines in the conditions of our measurements, and is therefore inapplicable to the description of the phenomena during periodic oscillations of $\vec{H}_s$. Consequently we seek a different approach which allows flux lines to rotate at they migrate in order to interpret our observation.

To analyze our vast assortment of observations we adopt the basic approach developed by Lachaine and successfully exploited by Gauthier, Boyer and Cave. Gauthier investigated hysteresis losses and the evolution of the longitudinal flux in wires of type II superconductors

as I is cycled below the critical current I_c with $H_{//}$ stationary. Boyer and Cave studied the evolution of the magnetic flux threading the plane of disks and hysteresis losses as rotation and oscillations of the disk are made to occur in the presence of a static magnetic field directed parallel to its flat faces and perpendicular to the axis of rotation or oscillation. In view of its conceptual simplicity we present the model in its entirety.

We consider an infinite slab, of thickness 2X, whose surfaces lie in the y-z plane and are located at x = 0 and x = 2X. In view of the symmetry of the configurations envisaged, we focus on one half of the slab occupying the space between the surface at x = 0 and the midplane at x = X. The externally applied magnetic field, $\vec{H}_s$, is directed parallel to the surfaces. The components of $\vec{H}_s$ along y and z are denoted $H_\perp$ and $H_{//}$ respectively. We visualize that $H_{//}$ is kept fixed while $H_\perp$ varies with time as described by equation 4.1.

For simplicity, we assume that the density of vortices adjacent to the surface is $B_s = \mu_o H_s$ and that $\vec{B}_s$ lies along the external magnetic field $\vec{H}_s$ as the latter changes direction. In other words, we ignore equilibrium diamagnetism and the possible existence of surface barriers to flux entry or exit. The essential model, however, is independent of these simplifications and, in principle, these features could be introduced into the basic framework if needed.

The model stipulates that (i) all gradients in the density of magnetic flux exist in a critical state and (ii) there is no dependence of the critical density gradient on the orientation configuration of the lattice of flux lines. Formally then we write

(4.3a) $$\frac{dB}{dx} = f_B(B)$$

regardless of whether the lattice of flux lines is unidirectional or spatially varying in orientation. Here $f_B(B)$ is a continuous function of B characterizing a given specimen and $B = (B_y^2 + B_z^2)^{1/2}$ with B_y and B_z the components of the magnetic flux density along y and z.

It is useful to write

(4.4) $$f_B(B) = \frac{F_p(B)}{B}$$

where $F_p(B)$ represents the pinning force density. Equation 4.3a then reads

(4.3b) $$\frac{dB}{dx} = \frac{F_p(B)}{B}$$

With this prescription, once equipped with a knowledge of $F_p(B)$ for a given material, sequences of B profiles, as B_s is caused to vary, can readily be mapped using the "classical" rules for the generation of gradients of flux density, and for the entry, exit and migration of flux lines.

The "classical" rules however, were developed and apply in the restricted framework where adjacent sheets of flux lines are parallel. Gauthier and also Boyer and LeBlanc felt compelled to infer from their observations that, in certain circumstances, diamagnetic gradients in flux density can be generated when the orientation of adjacent sheets of vortices is made to vary spatially (with depth in the present planar

geometry). Recently, Clem has examined these configurations theoretically and developed a detailed quasi-microscopic description of this behaviour from considerations of the interaction of non parallel flux lines and the ensuing flux cutting processes. For the time being we will ignore these complications and pursue the "standard" picture for the evolution of the B profiles.

Next, the model stipulates that all gradients of the θ profile exist in a critical state wherever a spatial variation of $\theta(x)$, the direction of the sheets of flux lines, is made to occur. Here

$$\theta(x) = \tan^{-1} \frac{B_y(x)}{B_z(x)} \tag{4.5}$$

The picture put forward by Lachaine is therefore referred to as a double critical state model.

At the outset we visualize that for a given isotropic material at a fixed temperature, $d\theta/dx$ should depend on the flux density only and write

$$\frac{d\theta}{dx} = f_\theta(B) \tag{4.6}$$

where $f_\theta(B)$ is a continuous function of B characterizing a given specimen. For the present we make no assumption regarding any relationship between $f_\theta(B)$ and $f_B(B)$ (Equations 4.3 and 4.6) in harmony with the data on rotating and oscillating disks of Boyer, Cave and LeBlanc. Lachaine and also Gauthier found, however, that to account for their observations, a dependence on θ had to be introduced in equation 4.6. Our efforts to

satisfactorily reproduce our data using equations 4.3 and 4.6 also proved futile. We will return to these endeavours below. As a consequence we also explored θ gradients of the form

$$\frac{d\theta}{dx} = f_\theta(B)\ F(\theta) \tag{4.7}$$

where $F(\theta)$ is a continuous function of θ.

We have developed a computer program which generates appropriate sequences of $B(x)$ and $\theta(x)$ profiles using equations 4.3 and 4.7 in tandem as B_s, the magnitude, and θ_s, the orientation, of the surface magnetic induction $\vec{B}_s$ are swept between the chosen limits (see Fig. 2.4). Some special aspects of the sequences of B profiles will be addressed later in this chapter. Arbitrary functions for $F_p(B)$, $f_\theta(B)$ and $F(\theta)$ can be introduced in the computations. The program provides us, as desired, with sequences of profiles of $B(x)$, $\theta(x)$, $B_y(x) = B(x) \sin \theta(x)$, $B_z(x) = B(x) \cos \theta(x)$. Further the program yields sequences of spatial averages, $\langle B_y \rangle$ and $\langle B_z \rangle$, also denoted $\langle B_\perp \rangle$ and $\langle B_{//} \rangle$, or equivalently, $\mu_o \langle M_{//} \rangle = \langle B_{//} \rangle - \mu_o H_{//}$ and $\mu_o \langle M_\perp \rangle = \langle B_\perp \rangle - \mu_o H_\perp$ versus $H_\perp(t)$ for selected values of stationary $H_{//}$. Finally, the program is designed to compute the area enclosed by the $\langle B_\perp \rangle$ vs $H_\perp(t)$ curves (hysteresis loops) for series of stationary $H_{//}$. In other words W, the hysteresis losses per unit volume, are computed numerically by exploiting the standard expression

$$W = \oint H_\perp \, d\langle B_\perp \rangle \tag{4.8}$$

which follows from Poynting formulation for the net energy flow into the specimen when $H_{//}$ is taken to be stationary. Figures 4.4 and 4.9 show the families of curves for hysteresis losses in the VTi and Nb ribbons generated using equations 4.3 and 4.7. The correspondence with the appropriate data is, in our view, quite impressive.

We now turn to our approach for the determination of $F_p(B)$, $f_\theta(B)$ and eventually, out of necessity, $F(\theta)$. For computational convenience and esthetic reasons we seek simple analytic expressions. We ascribe no special or profound physical meaning to the various choices that are made during the search and to the final selection that ensues. Various phenomenological considerations have played a role in our pursuit of this goal and we will outline those aspects which may have some merit. Basically, our methodology is empirical. We scrutinize the wealth of data we have accumulated for clues and proceed by trial and error. In this tedious enterprise, however, we are aided by the wealth of information contained in the pertinent literature and a background of experience in such exercises which provide some helpful guidelines.

Chronologically, we first address $F_p(B)$ in "isolation". We focus on our observations of full-wave and half-wave hysteresis curves of various amplitudes when $H_{//} = 0$, hence the rich panoply of magnetic behaviour of the specimen in the classical regime where $\vec{j}$ is perpendicular to $\vec{B}$, and obtain a simple expression which satisfactorily describes these data. This effort leads us to the formula

$$F_p = \alpha_{1/2} B^{1/2} \left(1 - \frac{B}{B_{c2}}\right)^2 \tag{4.9}$$

Hence equation 4.3 in our work reads,

$$B \frac{dB}{dx} = \alpha_{1/2} B^{1/2} \left(1 - \frac{B}{B_{c2}}\right)^2 \tag{4.10}$$

in both the VTi and the Nb ribbons. In our view, it is mainly a coincidence that the same $F_p(B)$ appears adequate to generate the "standard" magnetic response of these two samples of different materials. The parameters $\alpha_{1/2}$ and B_{c2} used in the calculations are listed in table 4.1. The success achieved by our choice can be judged by comparing Fig. 4.25 with 4.26 and inspection of Fig. 4.10. In our view, the correspondence between calculations and observations is good for the VTi ribbon. The "fit" in the case of the Nb sample leaves much to be desired. In the latter instance, however, we do not expect a simple formula for F_p to yield a good description of the relevant data. In this material, the neglect of the surface step, hence equilibrium diamagnetism and the surface barrier(s), is not justified and the magnetic behaviour cannot correctly be ascribed mainly to bulk pinning. Other investigations pursued in our laboratory of other samples cut from this Nb sheet show that the surface step indeed makes an appreciable contribution to the magnetic response.

B. The Electrodynamic Model, $B_z(x) = \mu_o H_{//}$

Before we undertake the quest for explicit formulae for $f_\theta(B)$ and $F(\theta)$ and as background for this endeavour, it is useful to explore a plausible description of the noncollinear regime which we

denote the electrodynamic model.

The well established critical state idea that, the Lorentz driving force density $\vec{F}_L = \vec{j} \times \vec{B}$ is in equilibrium with the pinning force density $\vec{F}_p(B)$, combined with Maxwell's equation, $\nabla \times \vec{H} = \vec{j}$, in the planar geometry we are considering, lead to

$$B_y \frac{dB_y}{dx} + B_z \frac{dB_z}{dx} = \pm F_p(B) \tag{4.11}$$

in the context where $B(x) = \mu_o H(x)$, which ignores equilibrium diamagnetism. In the latter context, after allowing an isotropic slab to become superconducting in a static applied magnetic field, $H_{bias} = \hat{y} H_{b\perp} + \hat{z} H_{//}$, we expect

$$B_y(x) = \mu_o H_{b\perp} \quad \text{and} \quad B_z(x) = \mu_o H_{//} \text{ to prevail.} \tag{4.12}$$

Next $H_\perp$ is made to vary while $H_{//}$ is kept constant. In the light of Faraday's law of induction, it is not unreasonable to imagine that $B_z(x) = \mu_o H_{//}$ might remain unchanged as this occurs. Indeed, this is to be expected, if a type II superconductor is conceived to be a metal of zero resistance where, however, the current density cannot exceed a ceiling $j_c(B)$. The picture we have just put forward has already been much exploited in the literature. Equation 4.11 then simplifies to

$$B_y \frac{dB_y}{dx} = \pm F_p(B) \tag{4.13}$$

Fig. 4.2 shows the hysteresis losses calculated for the VTi ribbon on the basis of equation 4.12 where F_p given by equation 4.9 has been introduced. We note that here, self consistently, $\vec{j} = \hat{y}\, j_z = \hat{z}\, dB_y/\mu_o\, dx = \hat{z}\, j_c(B)$. Further, we point out that the electric fields $\vec{E}(x)$ generated at the B profiles are made to change must lie along the z-axis, hence parallel to $\vec{j}(x)$. (In other words, the angle subtended by $\vec{E}$ and $\vec{j}$ is zero). This is a consequence of Maxwell-Faraday's equation $\nabla \times \vec{E} = -\partial\vec{B}/\partial t$ which reads

$$(4.14) \qquad E_z(x) = -\frac{d}{dt}\int_x^X B_y\, dx$$

and

$$(4.15) \qquad E_y(x) = 0$$

for the chosen geometry, taking $B_z(x)$ uniform and constant. From the above, it is clear that the model is in accord with the classical single critical state idea and simply constitutes an application of this concept to a special situation. Chang, Kiggins, Timms, Gauthier and LeBlanc have already applied this model to a variety of circumstances.

From inspection of Figs. 4.2 and 4.7 we see that this model generates some salient features in semi-quantitative accord with observations. Focussing on Fig. 4.2 we note in particular, the presence of a deep valley which fills in and subsequent peaks which become less prominent as H_{bl} increases from 0 through h_o to 3/2 h_o. Also, the valley disappears when $h_o = 3\, h_o$. The model, however, produces a

full-wave curve which lies above that for the half-wave in the region of the valley. Experimentally, the opposite occurs, in this range. Further, the valleys are too flat and broad. Finally, the point of intersection of the curves E and D and the point of crossing of curve B over curves C, D and E straddle the region ($H_{//} \approx 1.8$ T) where A traverses the other curves. In the data, an inversion of all the five curves takes place in the vicinity of $H_{//} = 1$ T.

The occurrence of a valley followed by a peak in these curves of W versus $H_{//}$ can be understood qualitatively from examination of

$$B_y \frac{dB_y}{dx} = \pm\alpha_{1/2} B^{1/2} \left(1 - \frac{B}{B_{c2}}\right)^2 \tag{4.16}$$

which explicitly combines equations 4.9 and 4.13. For clarity and to fix ideas we focus on the half-wave and full-wave cases. We note that with an amplitude $h_o = 0.05$ T, and our choice for the parameter $\alpha_{1/2}$, the penetration of the B_y profile, when $H_{//} = 0$, just attains the midplane. As $H_{//}$ is initially increased, the rise of $F_p(B)$ causes the B_y profiles to become steeper. Hence, the depth of penetration of the B_y profiles decreases and recedes from the midplane. As a consequence, the amount of flux swept in and out of the slab during each cycle diminishes, causing the hysteresis losses to diminish also. This generates the left hand side of the valley. With a further increase in $H_{//}$, hence B, the pinning function $F_p(B)$ sketched in Fig. 4.11a traverses its peak and begins to decline. The decline in $F_p(B)$ causes the slope of the B_y profiles to become less steep and hence now to penetrate deeper and extend closer and closer to the midplane. The concomitant growth in the amount of flux swept in and out of the slab per cycle leads to

a rise in hysteresis losses. This traces the right hand side of the valley. Essentially then, the valley in losses is the image of the peak in $F_p(B)$ versus B.

The peak in W versus $H_{//}$ and its decline to zero as $H_{//}$ approaches H_{c2} occurs once the "effective" depth of penetration of the more and more shallow B_y profiles extends further and further "beyond" the midplane as $F_p(B)$ diminishes monotonically to zero. The reason for the concomitant decline in hysteresis losses can be appreciated from consideration of Fig. 4.11 . The shallow B_y profiles span the thickness of the slab and their slopes differ only slightly in magnitude. As a consequence, the energy entering the slab during the upsweep of B_y becomes comparable to the energy flowing out during the downsweep of B_y over a corresponding range. The net dissipation of energy therefore becomes small.

It is of interest at this point to remark that introducing the simple Kim-Anderson approximation $F_p = \alpha_o$ for the pinning function, into equation 4.13 which is a statement of the electrodynamic model, $(B_z(x) = \mu_o H_{//})$, leads to hysteresis losses, at a fixed amplitude and chosen transverse bias field, which are independent of $H_{//}$. The losses, of course, will vary with amplitude and transverse bias field. Analytic expressions for the hysteresis losses in this special case of the electrodynamic model can readily be obtained. These results are developed in appendix III.

The electrodynamic model has an important bearing on our final account of hysteresis losses and magnetic behaviour in the noncollinear regime in two respects.

. Firstly, there are basic differences in the sequences of B profiles between the full-wave and half-wave cases. We refer the reader to Fig. 4.12 which illustrates these differences and aids in understanding the reason for their occurrence. The crucial feature is that for the full-wave, after $H_{\perp}(t)$ or $\theta_s(t)$ reverse sign, the B profiles must descend from B_s to $\mu_o H_{//}$ in view of the stipulation that $B_z(x) = \mu_o H_{//}$. Here $\theta_s(t)$ indicates the orientation of the externally applied field. These considerations also apply to intermediate cases where $0 < H_{bl} < h_o$.

Secondly, the electrodynamic model carries very specific implications with respect to $\theta(x)$, the spatial variation of the direction of the magnetic induction $\vec{B}(x)$. This can be seen in the following way. By definition

$$B_z(x) = B(x) \cos \theta(x) \tag{4.17}$$

Taking the derivatives with respect to x yields

$$\frac{dB_z}{dx} = \cos \theta \frac{dB}{dx} - B \frac{d\theta}{dx} \sin \theta \tag{4.18}$$

Introducing the postulate that B_z is uniform leads to

$$\frac{d\theta}{dx} = \frac{1}{B} \frac{dB}{dx} \frac{1}{\tan \theta} \tag{4.19}$$

which leads

$$\frac{d\theta}{dx} = \pm \frac{F_P}{B^2} \frac{1}{\tan \theta} \tag{4.20}$$

when the critical state equation for the flux density (equation 4.3) is introduced.

The stipulation of a uniform B_z therefore contains explicit expressions for $f_\theta(B)$ and $F(\theta)$ in the double critical state framework, namely

$$f_\theta(B) = \frac{1}{B}\left(\frac{dB}{dx}\right) = \pm \frac{F_P}{B^2} \tag{4.21}$$

and

$$F(\theta) = \frac{1}{\tan\theta} \tag{4.22}$$

We will see that the special form for $f_\theta(B)$, equation 4.21, which emerges directly from the stipulation of a uniform and constant $B_z(x)$, will remain useful even when $B_z(x)$ varies with space and time although $H_{//}$ is fixed.

At this juncture, we wish to indicate that, computationally and conceptually, the electrodynamic model can be addressed in two ways. One can focus on equation 4.16 and develop a computer program which generates sequences of B_y profiles, curves of the spatial average of $\langle B_y \rangle$ vs $H_1(t)$ and calculates W, the area enclosed by these curves, for various stationary and uniform $B_z(x) = \mu_o H_{//}$. This constitutes a classical single critical state approach since the $\theta(x)$ profiles are not explicitly implicated in the exercise. Alternatively, all the quantities just enumerated as well as sequences of $B(x)$, $B_z(x)$ profiles

and also sequences of $\langle B_z \rangle$ can be obtained in the context of the double critical state model by exploiting equations 4.10 and 4.20 in tandem. As pointed out earlier, we have developed a general computer program for this purpose. The electrodynamic model therefore provides us with a means of verifying the latter program, since the two independent computational approaches must yield identical results at all stages in the present case.

C. Lachaine Formulation of the Double Critical State, $F(\theta) = k/\tan\theta$

Lachaine showed that a simple empirical modification to equation 4.20, namely, the introduction of an adjustable coefficient k, so that this equation reads,

$$\frac{d\theta}{dx} = \pm k \frac{F_P}{B^2} \frac{1}{\tan\theta} = \frac{k}{B}\left(\frac{dB}{dx}\right) \frac{1}{\tan\theta} \tag{4.23}$$

where $k > 1$ together with the critical state equation for the flux density (equation 4.10) generated curves in good accord with much of his observations on ribbons of NbTi and VTi. In particular, he noted that the evolution of $\langle B_z \rangle$ as $H_\perp$ is initially impressed with $H_{//}$ maintained fixed (the longitudinal paramagnetic effect) was reproduced in some detail. Also, these expressions provided an account of the expulsion of magnetic flux along $H_{//}$ kept fixed as $H_\perp$ is decreased to zero from its initial value after the sample has become superconducting in the chosen $H_{//}$ and initial $H_\perp$. The latter phenomenon is unknown in the published literature and has been referred to as the longitudinal

diamagnetic effect by Lachaine. Further, these equations led to curves of $\langle M_{//} \rangle$ and $\langle M_{\perp} \rangle$ versus $H_{\perp}$ in various fixed $H_{//}$ for full-wave and half-wave cycles which reproduced the main features of his measurements. Lachaine found that taking k = 2 and 3 in equation 4.23 lead to a good correspondence with his data on NbTi and VTi ribbons respectively. We have also calculated the predictions of equation 4.23 using k = 2 and 3 and find poor agreement with our observations of W vs. $H_{//}$.

We note that the sample of VTi investigated by Lachaine and ourselves is the same. The reason we reach different conclusions is that we examined hysteresis losses over a considerably more extensive range of $H_{//}$ and $H_{b\perp}$. Over the smaller range he explored, taking k = 3 provides an acceptable fit with the data.

To appreciate why Lachaine's choice of formulae and values for k, intrinsically yield the experimentally well established longitudinal paramagnetic and diamagnetic effects, it is useful to rewrite equation 4.18. As seen above, the stipulation that $k \neq 1$ in equation 4.23 signifies in the double critical state framework that $dB_z/dx \neq 0$. Introducing equation 4.23 into equation 4.18 leads to

$$\frac{dB_z}{dx} = -\frac{B_z}{B}\frac{dB}{dx}(k - 1) \tag{4.24}$$

We note that with $k > 1$, the gradients of B and B_z have opposite signs. Thus $\langle B_{//} \rangle$ must become larger than $\mu_o H_{//}$ (hence paramagnetic) when B_s is increased but smaller than $\mu_o H_{//}$ (hence diamagnetic) when B_s is decreased.

The latter feature, however, points to a basic "flaw" in the Lachaine formula. His data as well as all our pertinent observations reveal that $\langle B_{//} \rangle$ does not always decrease monotonically as B_s is lowered with $H_{//}$ kept fixed. Indeed the curves of $\langle B_{//} \rangle$ versus $H_{\perp}$ with constant $H_{//}$, often traverse a valley and rise as $H_{\perp}$ approaches zero. His formula for $F(\theta)$, looked at in the perspective of equation 4.24, is seen as intrinsically incapable of accounting for this reversal in the evolution of $\langle B_{//} \rangle$ during the final state of the downsweep of B_s since variations of the magnitudes of B and dB/dx cannot induce a reversal of the sign of dB_z/dx. Our main theoretical effort has been directed at rectifying this shortcoming.

It is now well known that the paramagnetic effect plays a significant role in enhancing the lossless current carrying capacity or critical current I_c of wires and ribbons of types II superconductors immersed in static longitudinal magnetic fields. This enhancement can be understood from a detailed consideration of equation 4.11 or its equivalent in cylindrical geometry. To illustrate the basic mechanism for the enhancement, it is useful to rewrite equation 4.11 in the form

$$(4.25) \quad \frac{1}{\mu_o} \frac{dB_y}{dx} = j_z = \frac{(|F_p| + |B_z| \left|\frac{dB_z}{dx}\right|)}{\mu_o |B_y|} = \frac{(|F_p| + |B_z||j_y|\mu_o)\cdot}{\mu_o |B_y|}$$

This presentation brings out the essential feature for the increase in longitudinal or transport current densities due to the paramagnetic effect. This occurs because the component of the Lorentz force density,

$j_y B_z$, associated with the paramagnetic effect aids the pinning force in balancing the $j_z B_y$ component of the Lorentz force density. Since, by definition, $I_c = Y\int_0^{2X} j_z \, dx$, an increase in I_c ensues. Here Y is a length along the width of the slab. Further consideration shows that the diamagnetic effect is basically an "image" of the paramagnetic effect and is also conveyed by equation 4.25. Both effects then lead to an enhancement in j_z and contribute to the reduction of hysteresis losses.

D. Boyer Formulation of the Double Critical State, $F(\theta) = k$

The electrodynamic model, where $F(\theta) = 1/\tan\theta$ assigns, in a natural way, a privileged status to the z-axis, the direction along which the strength of the applied magnetic field is kept fixed. This privileged status is a consequence of the stipulation that $B_z(x)$ remain constant and uniform. It is not evident, however, that this privileged status should survive in a framework where $B_z(x)$ is allowed to vary with position and time even though $H_{//}$ is maintained constant as $H_\perp$ is made to change. For this reason and also because of its analytic simplicity, we turn our attention to the form for $F(\theta)$ successfully exploited by Boyer and Fillion and also by Cave, namely,

$$F(\theta) = k \tag{4.26}$$

which assigns no mathematical preference to the z-axis. Here k is an adjustable temperature dependent parameter characterizing the specimen. We pursue this avenue aware of the fact that in the experiments of Boyer

and Cave on rotating disks, all directions in the y-z plane were equivalent (assuming material isotropy), whereas in our work, the "z" axis corresponds to a physically meaningful direction, since along this direction, the applied $\vec{H}$ is maintained constant.

Boyer, Fillion and LeBlanc explored three analogous forms for $d\theta/dx = f_\theta(B)$, namely

$$\frac{d\theta}{dx} = \pm \frac{k_n F_P(B)}{B^n} \tag{4.27}$$

with n = 0, 1 and 2. They found that the choice, $d\theta/dx = k\, F_p(B)/B = k(dB/dx)$ best reproduced their data. We have also pursued the predictions of the double critical state model using these three choices. Further, we have also examined the curves generated when n = 3/2 and 5/2. We find, in contrast to the conclusion of these workers, that among these choices, the form,

$$\frac{d\theta}{dx} = \pm \frac{k}{B^2} F_P(B) \tag{4.28}$$

leads to the best correspondence with our data for both the VTi and Nb samples. The W versus $H_{//}$ curves generated by this choice are displayed in Figures 4.3 and 4.8. In all our calculations relating to the VTi sample the parameter k was chosen to yield a fit to the experimental data at $H_{//}$ = 1 T when H_{bl} = 0 (full-wave case). In the analysis of the data for the Nb sample, we seek a parameter k which causes some of the various curves to either intersect or approach each other at $H_{//} \approx 1.8$ T.

For various chosen n we have also investigated the effect of changing the parameter k by factors of 1/2 and 2. This significantly affects the degree of divergence of the fine calculated curves, the depth and position of the valleys, the height and position of the peak(s) and, of course, the fit at $H_{//} \approx 1$ T. Since we are dealing with families of five experimental and five calculated curves, comparisons between data and theory become somewhat complicated and conclusions, perhaps subjective, since inferences rest on overall impressions. Consequently, our preference for equation 4.28 over the neighbouring choices, namely 3/2 and 5/2, must be viewed with caution. Nevertheless, settling on equation 4.28 as the final result of this exercise, we find the ensuing agreement with the corresponding data, to be less than satisfactory, although, perhaps, encouraging.

The curve of W versus $H_{//}$ for the half-wave case shows good correspondence with the experimental results. The sequence for the valleys is in accord with that observed. Although, this does not emerge from Figure 4.3 the calculated curves intersect at $H_{//} \approx 0.8$ T and reverse their vertical order beyond that point in qualitative agreement with the data. Since the calculated separation is very small however, the curves appear to overlap beyond $H_{//} \approx 0.8$ T on Figure 4.3.

Finally, as noted earlier, the locus of $\langle M_{//} \rangle$ versus $H_{\perp}$ can trace a valley when $H_{\perp}$ is diminishing in a constant $H_{//}$. This feature is associated with $f(\theta) = k$ in equation 4.28 and this source can be identified by combining equation 4.28 with equation 4.18 to read,

$$(4.29) \qquad \frac{dB_z}{dx} = -\frac{dB}{dx}\,\frac{(k\,\frac{B_y}{B_z} - 1)}{(1 + (\frac{B_y}{B_z})^2)^{1/2}}$$

where, empirically, we find $k > 1$. The pertinent aspect is that $|dB_z/dx|$ decreases as H_1, hence as B_y/B_z diminishes towards $1/k$, thereby causing the longitudinal diamagnetic effect to decline and even, in some instances, to vanish. Indeed, a weak longitudinal paramagnetic effect can arise, as B_y/B_z decreases from $1/k$ to zero. We have not observed this reversal of sign experimentally.

E. Our Proposed Formula, $F(\theta) = k/(1 + |\theta|)^2$

At this juncture, for guidance, we return to the behaviour generated by the electrodynamic model and compare those results with the data on hysteresis losses and the predictions of equation 4.23. In our view, this survey indicates the need for a function $f(\theta)$, whose "structure" lies between $F(\theta) = k > 1$ and $F(\theta) = 1/|\tan\theta|$. We recall that Gauthier, achieved good results exploiting $F(\theta) = k\cos^2\theta$ which is convex upwards for $0 < \theta < 45^\circ$ and downwards for $45^\circ < \theta < 90^\circ$. We find that this form is an improvement on the choice $F(\theta) = k$ in reproducing our results. It is, however, in our view, not quite satisfactory in this respect. We have consequently explored a variety of other choices starting with linear dependences of the form, $F(\theta) = 1 - b|\theta|$ where b is a coefficient. These calculations indicate that a function of $F(\theta)$ versus θ which is convex towards the origin is required. After several trials which we will not enumerate we picked the formula

$$F(\theta) = \frac{k}{(1 + |\theta|)^2} \tag{4.30}$$

where $\theta = \tan^{-1} B_y/B_z$ is in radians, as producing the best results among a variety of simple analytic expressions which have the desired shape and which we tried. Equation 4.7 then reads

$$\frac{d\theta}{dx} = \pm k \frac{F_P}{B^2} \frac{1}{(1 + |\theta|)^2} \tag{4.31}$$

We ascribe no special physical significance to the specific mathematical form chosen for $F(\theta)$ and assign equal merit to alternative expressions generating curves of $F(\theta)$ versus θ closely resembling the former. A rapid initial descent of $F(\theta)$ with θ and a finite value as θ approaches $\pi/2$ appear important in providing behaviour corresponding to our measurements. In contrast to $F(\theta) = k/\tan\theta$ exploited by Lachaine, which varies from infinity to zero, limits which appear excessive from the physical standpoint, our expression leads to better results partly from being finite at $\theta = 0$ and $\pi/2$.

Figures 4.4 and 4.9 show the families of W versus the stationary $H_{//}$ for different transverse bias fields $H_{b\perp}$ which we obtain using equation 4.31 together with equation 4.10 in the double critical state framework. We regard θ as the first term in an expansion of $\tan\theta$. In the computations for the full-wave case we consequently replaced θ by $\tan\theta$ in the range $0 \leq H_{//}/H_{c2} < 1/40$ or $1/2$ for the calculations pertaining to the VTi and Nb samples respectively.

Comparison of Fig. 4.4 with the corresponding data curves (Fig. 4.1) shows, in our view, a remarkable accord between the model predictions and the observations for the VTi ribbon. Consideration of Figures 4.3 and 4.4 indicates that, (i) the correct evolution in the structure of the valleys as H_{b1} is increased and (ii) the separation of the calculated curves beyond their point of intersection, are due mainly to the introduction of the factor $F(\theta) = K/(1 + |\theta|)^2$ in $d\theta/dx$.

We note that although the demagnetization factor along the length of both samples and along the width of the Nb ribbon is small, it is not negligible along the width of the VTi ribbon. Further, the two samples reveal a significant degree of material anisotropy. This anisotropy emerges from superposing the magnetization curves measured along the length, when only $H_{//}$ applied, with that measured along the width, when only $H_{\perp}$ is applied. A survey of our observations suggest that the anisotropy and the geometric factors play a not insignificant role in the measurements. These contributions, however, are difficult to quantify and remove from the raw data. We believe that in the absence of any such contributions, a function $F(\theta)$ would nevertheless be required to account for the observations. In other words, we regard the function $F(\theta)$, hence the angle θ, as not fundamentally linked to the geometry or the anisotropy of the specimen. We envisage, rather, that the direction in the y-z plane along which a component of the externally applied magnetic field is maintained stationary, (hence equivalently, the direction along which the applied magnetic field is caused to vary), thereby acquire a special status which must be taken into account by introducing a function $F(\theta)$ in the prescription for $d\theta/dx$. We therefore

view that, $\theta = 0$ in $F(\theta)$, is determined solely by the direction of the stationary component of the applied magnetic field. Presumably, if no stationary component were maintained in the experiments the formula for $d\theta/dx$ would be consequently affected. This view is consistent with the analysis of the data on the rotating and oscillating disks where all directions in the y-z plane are equivalent and, $F(\theta)$ reduces to a constant.

As a further test of our interpretation of the basis for $F(\theta)$ we display the set of data for hysteresis losses of the Nb ribbon where $H_\perp$ is kept stationary and $H_{//}$ is varied with time (Fig. 4.6). The corresponding calculated curves displayed in Fig. 4.9 were obtained in the framework that the plane $\theta = 0$ is determined by the stationary component of H_s, hence here, this plane lies along $H_\perp$ i.e. along the width of the slab. The reasons we select the Nb data for this test, is that this specimen has a very small demagnetization factor along its length and width and also exhibits less anisotropy than the VTi sample. In section IV, we also analyse data on the VTi ribbon in this framework. In our view, it is instructive that the same $F(\theta)$ can be exploited for both the VTi and Nb samples and yields good results in both instances, provided that the plane $\theta = 0$ is considered as tied to the stationary component of the applied magnetic field.

We attribute the disparities between calculations and measurements for the Nb specimen (compare Figures 4.6 and 4.9), to, (i) our neglect of reversible (Meissner) shielding currents and surface barrier(s) in the model and (ii) our choice of a crude approximation

(equation 4.9) for the bulk pinning behaviour. We also note here, although it is not germane to the validity of the model, that the presence of the Meissner currents, the operation of the surface barriers, and the small ratio of H_{c2} to H_{c1} for the Nb sample, allow little room for maneuver and exploration in the choice of h_o and the range of choices of $H_{b\perp}$. The reasons are the following. Firstly, h_o must be sufficiently large to overcome the reversible shielding current and the surface barrier opposing flux entry. For our specimen, this means $h_o \gtrsim 0.15$ T when $H_{b\perp} = 0$. Secondly, h_o should be chosen small enough so that the flux disturbance does not penetrate to the midplane when $H_{b\perp} = 0$. This criterion implies $h_o \lesssim 0.2$ T for our sample. If h_o is chosen larger than this, the ensuing W versus $H_{//}$ curves for various $H_{b\perp}$, show little structure and a disappointing sameness. As a consequence such data presents a poor challenge for testing the descriptive powers of our model.

F. Sequences of B profiles when $0 \leq H_{b\perp} < h_o$.

As noted above, in the discussion of the electrodynamic regime ($B_z(x) = \mu_o H_{//}$), there is a fundamental difference in the sequence of B profiles depending on whether the bias transverse field is smaller or greater than the amplitude ($H_{b\perp} \gtrless h_o$). For perspective and background, it is useful to examine the collinear regime and compare the behaviour in this regime when $H_\perp(t)$ does not reverse and does reverse polarity during its cyclical sweep. The former is illustrated in Fig. 4.12a) and c), the latter in Fig. 4.13a) and c). In the latter case it is also

instructive to view the sequences of the magnitude of the B profile which are displayed in Fig. 4.13b). In the noncollinear regime, this is the representation which must be considered in applying equation 4.10, since $B = (B_y^2 + B_z^2)^{1/2}$ does not change sign when B_y changes direction. In the noncollinear regime, however, it is no longer necessary that $B = 0$ at the plane where $\theta = 0$. Indeed, usually B will not be zero at $\theta = 0$. Consideration of a three dimensional sketch of the $\vec{B}$ configuration (see Fig. 4.13e) and consideration of Fig. 4.13d) and 4.13f) indicate however that $|B(x)|$ will reach a minimum at the plane $\theta(x) = 0$. In the situations we are now envisaging, this minimum, however, may be zero when $H_{//}$ is small, since $B_z(x)$ is allowed to evolve up or down, hence may decline to zero at that plane. We recall that in the electrodynamic model, the situation which occurred was $B = B_z = \mu_o H_{//}$ at $\theta(x) = 0$, since we stipulated that $B_z(x) = \mu_o H_{//}$. Removing this stipulation, allows $0 \leq B \lesssim \mu_o H_{//}$ at $\theta = 0$.

The sequences of B profiles during the cycle when $0 < H_{bl} < h_o$, hence for intermediate situations between the full-wave and half-wave cases, are slightly more complicated than that sketched in Fig. 4.13d). The detailed picture which applied can readily be traced from considerations of sequences of $|B|$ profiles in the collinear regime for cycles of corresponding limits.

The scheme we have just presented for the sequences of the B profiles in the noncollinear regime, in cases where $0 \leq H_{bl} < h_o$, leads to a smooth transition of the flux configurations in that regime to that encountered in the collinear regime as $H_{//}$ is taken to diminish and vanish.

In the collinear regime, the migration of the interface where B = 0 from the surface of the slab to its midplane, is associated with the encroachment of a slope of positively or negatively directed vortices into a territory occupied by oppositely directed vortices. At the advancing B = 0 plane, annihilation of antiparallel vortices, moving from the left and the right B profiles along critical flux density gradients, takes place. In the noncollinear regime, as pointed out by Clem, the processes involved in the migration of the plane where $\theta(x) = 0$ and a minimum in $|B|$ profile occurs, are more complex. Here it is visualized that the cutting and cross-joining of flux lines with the subsequent straightening of the segments effectively causes an annihilation or consumption of flux by eliminating opposite B_y components of adjacent nonparallel sheets of flux lines, straddling the $\theta(x) = 0$ interface.

The picture we have just developed applies in our analysis of curve A for the VTi sample and four of the family of five sets of data presented for the Nb specimen.

4.4 LOCUS OF $\langle M_{//} \rangle$ AND $\langle M_{\perp} \rangle$ DURING GYCLIC VARIATIONS OF $\vec{H}_s$

The area enclosed by the component of the magnetic moment which lies along the cyclically varying component of the externally applied magnetic field $\vec{H}_s$ is a measure of the dissipation of energy in the specimen. We have up to now focused on these final data and developed a model which accounts for these results. In order to obtain these integrated data, we monitored the locus of the appropriate component of the magnetic moment during complete cycles. Further, we

generally, also traced the evolution of the magnetic moment along the stationary component of $\vec{H}_s$ during each periodic swing. The intricate structure of these curves of $\langle M_{//} \rangle$ and $\langle M_{\perp} \rangle$ are replete with detailed qualitative and quantitative information which the model we put forward should also be able to reproduce in order to be accepted.

In this respect we are confronted by an embarrassment of riches since our investigation has many facets and spans a wide range of the several parameters or variables which enter the total picture. It is useful to enumerate these parameters:

i) The magnitude of the stationary component of $\vec{H}_s$.

ii) This component may be chosen to be directed along some arbitrary direction in the plane defined by the length and width of the ribbon specimen. For experimental ease we have chosen to let $\vec{H}$ stationary lie

   a) along the length of the ribbon and alternatively

   b) along the width of the ribbon. We have avoided the experimental complications involved in choosing intermediate orientations.

iii) The magnitude of the bias magnetic field which is directed perpendicularly to H stationary, hence collinear with the oscillating magnetic field, namely $H_{b\perp}$ if $H_{//}$ is kept fixed or $H_{b//}$ if it is $H_{\perp}$ which is maintained constant. Finally,

iv) The amplitude h_o of the oscillating component of the applied magnetic field.

We note that for each measurement where (i) through (iv) have been specified, we simultaneously monitor the locus of both $\langle M_{//} \rangle$ and $\langle M_{\perp} \rangle$.

In the measurements on hysteresis losses, we have already covered the domain where $h_o \gtrsim H_*$. In order to expand our survey into new territory we now turn our attention to the range of large amplitudes where the locus of the curves can trace very elaborate and fascinating meanderings. At these large amplitudes and with the chosen H stationary, the range of θ and B being scanned is appreciable. These measurements therefore constitute a severe test of equation 4.31. For convenience, but with the assurance that this "limited" approach covers the essential aspects, we have confined this investigation to half-wave and full-wave cycles, hence taken $H_{b\perp}$ (or $H_{b//}$) = 0 and h_o.

The odd numbered Figures in the series from Fig. 4.15 through 4.36, comprise a partial catalogue selected from an extensive compilation of observations to illustrate various salient features of the variety of behaviour encountered as the several parameters just enumerated are caused to change. The even numbered Figures in this sequence, display corresponding families of curves computed with the double critical state model using equations 4.10 and 4.31.

Figures 4.15 and 4.25 actually belong to the collinear regime since here $H_{//} = 0$ (the stationary component is the earth's magnetic field). As indicated earlier, it is these data that we exploit to obtain a suitable approximation for $F_p(B)$ for the specimen in the context of the classical single critical state approach. Figures 4.16 and 4.26 display the magnetization curves which this collinear model yields using equation 4.10 alone. It is of interest, however, to note that curves essentially identical to that presented in the latter two Figures are also obtained with our formulae for the double critical state model

in the limit where $H_{//}$ is small (say $\lesssim$ 0.1 mT), and tan θ is substituted for θ in equation 4.31. This is a striking example of the versatility of the model, since its predictions continue to be valid in the extreme limit of a vanishingly small $H_{stationary}$ where, in a sense, the non-collinear regime merges with the collinear regime.

We have adopted a side by side instead of a superimposed display of observed and calculated curves. Our reasons for this approach are twofold. Firstly, in view of the variety and intricacy of the families of measured curves there is a need to avoid cluttering the figures. Secondly, since in the calculations we ignore, for simplicity, any contributions from reversible Meissner currents and surface barriers and choose, for convenience, a simple analytic approximation to describe the bulk pinning, we do not expect the model to yield a one to one quantitative correspondence in all circumstances. We believe it is sufficient for the model to generate results whose magnitudes are approximately correct and to yield families of curves where the salient features and the trends of the various magnitudes evolve in harmony with observations as the pertinent parameters are modified.

An inspection and comparison of the corresponding families of measured and calculated curves in this compendium, provide strong support for the basic validity of the double critical state approach and the particular prescriptions we have selected (equation 4.10 and 4.31) to generate the B and θ profiles, hence the B_y and B_z, profiles. A few comments on some of the features are appropriate.

The growth in the gradients of the B_y profiles, hence in the critical current density, (i) shielding the ribbon against entry of an

increasing transverse component of the applied flux and (ii) opposing the exit of this flux as $H_\perp$ is reduced, emerges from a comparison of the magnitude of the maximum diamagnetic and paramagnetic magnetizations in Figures 4.15, 4.17 and 4.19. This growth is due to the presence of the stationary $H_{//}$, the parameter which has been changed. The quantities just mentioned are seen to increase by a factor of $\gtrsim 2$ in this set of Figures. This enhancement has already been explored in some detail by Timms and LeBlanc who analyzed their data on a NbTa ribbon using the electrodynamic model, i.e. $B_z(x) = \mu_o H_{//}$ hence $\langle M_{//} \rangle = 0$. The rise in magnitudes caused by $H_{//}$ is also evident when full-wave cycles are applied (see Figures 4.25 and 4.27).

The intricate evolution of the locus of $\langle M_{//} \rangle$ as a function of the amplitude of the time varying $H_\perp$ when a static $H_{//}$ is present, is exhibited in Figures 4.21 and 4.23 for the half-wave case. We note the changes in the sense of circulation of the curves, namely from counterclockwise at small amplitudes of $H_\perp$ to clockwise at larger amplitudes via figure eight loops at intermediate amplitudes. It is remarkable that our model duplicates this convoluted sequence of behaviour (see Fig. 4.22 and 4.24).

A rise in the longitudinal magnetic flux as $H_\perp(t)$ increases in magnitude with $H_{//}$ kept fixed (the longitudinal paramagnetic effect) and a decrease in this flux to levels below the applied magnetic flux (the longitudinal diamagnetic effect) are also evident in Figs. 4.21 and 4.23. These "effects" are the manifestation of complicated patterns of circulation adopted by the induced persistent current densities $\vec{j}(x, t)$, hence configurations of the magnetic induction $\vec{B}(x, t)$ during

the swing of the external magnetic field. All the macroscopic features of these phenomena are well reproduced by the model (see Figs. 4.22 and 4.24). Under full-wave oscillations of $H_{\perp}(t)$, the elaborate contortions of the persistent currents and magnetic fields lead to beautiful butterfly shaped curves as illustrated in Fig. 4.29 and duplicated theoretically in Fig. 4.30.

In Figures 4.31, 4.33 and 4.35, the component of the magnetic field along the width of the VTi ribbon, $H_{\perp}$, is kept fixed while it is the longitudinal component, $H_{//}$ which is time varying. As indicated earlier this 90^{o} rotated arrangement serves especially to shed light on the physical meaning of $F(\theta)$ in equation 4.31. In this set of Figures, the amplitude of the time varying field is chosen the same for a given family of curves and different stationary $H_{//}$ are selected. The families of calculated curves displayed in Figs. 4.32, 4.34 and 4.36, exhibit similar general features and trends as the measured ones. We note, however, that the numerical values for the amplitudes and stationary $H_{//}$ for the measurements and the calculations do not correspond exactly. We attribute this "shift" in the matching to anisotropy and the demagnetization factor. The essential message is nevertheless conveyed, that the $F(\theta)$ is linked to the direction of the stationary component of the externally applied magnetic field.

Finally we focus on the valley traced by the diamagnetic magnetization along the stationary component of the applied magnetic field as the time varying component is decreasing to zero after an excursion to sufficiently large magnitudes. This behaviour is witnessed

during both half-wave and full-wave cycles (see Fig. 4.21, 4.23, 4.29, 4.31, 4.33 and 4.35). It is evident from an examination of the corresponding calculated curves that our model reproduces this prominent feature (see Fig. 4.22, 4.24, 4.30, 4.32, 4.34 and 4.36). We find the rise in flux along the stationary component in circumstances where the varying field is being reduced to be a particularly intriguing phenomenon. We have already seen that Lachaine's expression for $F(\theta)$, namely $k/\tan\theta$, with $k > 1$, is intrinsically incapable of generating this rise, whereas it is produced by Boyer's choice of $F(\theta) = k > 1$ and also by our formula.

To gain insight into the origin of this phenomenon in our model, we proceed as before and introduce equation 4.31 into equation 4.18. This yields,

$$(4.32) \qquad \frac{dB_z}{dx} = -\left(\frac{dB}{dx}\right) \frac{1}{(1 + w^2)^{1/2}} \left(\frac{kw}{(1 + \theta)^2} - 1\right) = -\frac{dB}{dx} f(w)$$

where $w = B_y/B_z$. To simplify this expression we may replace θ by w, a valid approximation in the situations we are considering. We have selected $k = 13$ and 25 for the VTi and Nb samples respectively. Examination shows that $-f(w)$ traverses a valley when $w \approx 0.6$. As a consequence, the sequence of B_z profiles behaves as depicted schematically in Fig. 4.14c) thereby causing $\langle B_z \rangle$, hence $\langle M_z \rangle$, to reverse its descent and form a valley with $H_\perp(t)$ decreasing in $H_{//}$ stationary.

4.5 SUMMARY AND CONCLUSION

We have investigated the evolution of the spatial average of the magnetic induction, $\langle B_{//} \rangle$ and $\langle B_{\perp} \rangle$, along the length and width of ribbons of VTi and Nb in the presence of a stationary longitudinal magnetic field, $H_{//}$, as a time varying transverse magnetic field, $H_{\perp}(t)$, is made to undergo oscillations of various amplitudes h_o. A transverse bias magnetic field, $H_{b\perp}$, of different chosen intensities is also introduced. We frequently focus on the special cases where $H_{b\perp} = 0$ and h_o, denoted the full-wave and half-wave cycles. The magnetic response was explored over extensive ranges of $H_{//}$, $H_{b\perp}$ and h_o. The area enclosed by the hysteresis curves, $W = \oint H_{\perp} \, d\langle B_{\perp} \rangle$ was also measured. Performing a 90° rotation of the applied magnetic field, another series of measurements was carried out where $H_{\perp}$ is maintained fixed and a time varying $H_{//}$, superimposed collinearly on a bias level, $H_{b//}$, is caused to oscillate.

The lattice of flux lines encountered in the samples under the circumstances just described contains regions where adjacent planes of vortices are not parallel. These situations where the sheets of flux lines are made to vary in relative orientation with depth and time are referred to as the noncollinear regime. These configurations differ fundamentally from that occurring in the standard arrangement where a varying magnetic field is superimposed upon and collinear with a bias magnetic field. In the noncollinear regime, the interactions of the flux lines can be radically modified and flux cutting processes come into play, dictating the flux configurations which ensue.

Our observations are analyzed phenomenologically, exploiting the framework that both the gradients in the density of the flux lines and in their angular orientation exist in critical states. For simplicity, in our work, contributions from surface barriers and reversible shielding currents are neglected. The B profiles are taken to obey the classical critical state concept where the driving Lorentz force density is in equilibrium with the pinning force density $F_p(B)$. Consequently, $dB/dx = \pm F_p/B$, since we assume $B(x) = \mu_o H(x)$ and use planar geometry. Focusing on the magnetization curves in the collinear regime, a simple analytic expression for $F_p(B)$ is identified for each specimen which adequately reproduces the corresponding data. Armed with this prescription for the B profiles, an empirical search for an appropriate formula to describe the critical angle gradients, $d\theta/dx$, is undertaken. This inquiry, guided by previous work, leads us to the form, $d\theta/dx = k\ F_p/B^2(1+|\theta|)^2$. The appearance of a θ dependence in this governing equation is examined in several ways.

Firstly, by computationally exploring the behaviour when the magnetic induction along the static applied magnetic field component is taken to be uniform and constant ($B_z(x) = \mu_o H_{//}$ or $B_y(x) = \mu_o H_{\perp}$ as the case may be). This picture, called the electrodynamic model, leads naturally to the form $d\theta/dx = F_p/B^2 \tan\theta$, hence F_p/B^2 for the B dependence and $1/\tan\theta$ for the θ dependence.

In this model, the induced persistent currents flow along the electric fields, $\vec{E}(x)$, hence along the stationary component fo the applied magnetic field $\vec{H}_s$ and orthogonal to the time varying component of $\vec{H}_s$. This model consequently provides a frame of reference for

assessing the influence on the hysteresis losses of the appearance of persistent currents which flow perpendicularly to the stationary component of $\vec{H}_s$. A comparison of the full-wave curve predicted by this model with the corresponding data for the Nb sample (see Figs. 4.6 and 4.7) reveals that the occurrence of a deep valley in the locus of W can be attributed to the presence of the latter component of the current density. Let j_y denote the current density perpendicular to the stationary component of $\vec{H}_s$ and, B_z, the magnetic induction along this component of $\vec{H}_s$. We visualize that the reduction in energy dissipation occurs because the $j_y B_z$ component of the Lorentz force density, $\vec{F}_L$, predominently aids the pinning force density in opposing the other, energy dissipating, $j_z B_y$ component of the Lorentz forces. This allows $j_y(x)$ to attain larger densities than would exist if $j_z B_y$ were absent. This interplay of the components of the Lorentz force and the pinning force is also partly responsible for the enhancement of the current carrying capacity of wires and ribbons in stationary longitudinal magnetic fields, $H_{//}$. Using the electrodynamic model as a starting point or conceptual framework, several phenomena are readily seen to be intimately related, namely; (i) the longitudinal paramagnetic effect, (ii) the longitudinal diamagnetic effect (the less well known image of (i)), (iii) the enhancement of the critical current by a static $H_{//}$ and (iv) the decrease in hysteresis losses by a static $H_{//}$.

To further delineate the role of $F(\theta)$ and to evaluate its necessity, we pursued the double critical state concept, eliminating the θ dependence, hence taking $F(\theta) = k$ in equation 4.31. Under these circumstances, we find that the model yields poor agreement with our

data on hysteresis losses (see Figs. 4.1, 4.3 and 4.6, 4.8). Also, the locus of the curves of $\langle M_{//} \rangle$ and $\langle M_{\perp} \rangle$ as $\vec{H}_s$ is cycled was not satisfactorily reproduced although this choice for $F(\theta)$ generates an intriguing feature of the data, the appearance of a valley in the evolution of the magnetic induction along the static component of $\vec{H}_s$ as the time varying component is reduced to zero.

We contend that $F(\theta)$ in equation 4.31 is required because in our work, a component of $\vec{H}_s$ is maintained fixed, thereby giving physical meaning and a privileged status to $\theta = 0$, the direction along the stationary component of the applied magnetic field. Although anisotropy and demagnetization factors are seen to play a role in our data, the severe dependence on θ which we find necessary to introduce precludes associating $F(\theta)$ with these features. Further, we note that taking $\theta = 0$ to be fixed by the direction of the stationary component of $\vec{H}_s$ and using the same form for $d\theta/dx$, namely equation 4.31, we successfully account for our observations, (i) on both of the materials we have studied and (ii) for each material, for the situation where this component is made to lie along the length and also along the width of the ribbon samples. These results indicate that anisotropy and demagnetization factors are not responsible for the appearance of the θ dependence.

The spatial distribution of the angle ψ subtended by the current density $\vec{J}(x)$ and the electric field $\vec{E}(x)$ has played no role in our empirical approach. On physical grounds, this angle is required to

lie in the range $0 \leq \psi \leq \pi/2$. The appearance of ψ greater than 90^{o} would imply the existence of a source of energy in the region where this occurs. Further, the requirement that $\vec{E}(x)$ be spatially continuous has not been addressed. Preliminary computations of the sequences of $\vec{E}(x)$ and $\psi(x)$ profiles occurring with our model indicate that it does not generate unphysical configurations in the situations we have explored. These features are under extensive scrutiny and will be reported on as a continuation of our work.

Clem has recently developed a major modification or extension of our double critical state model which phenomenologically focuses on the processes involved in the establishment of the sequences of flux configurations for the general noncollinear regime. In his approach $j_{\perp}$, $j_{//}$, $E_{\perp}$ and $E_{//}$ the components of the current density and of the electric field perpendicular and parallel to $\vec{B}(x)$, are explicitly taken into account. Pursuing these considerations, Clem envisages the existence of three types of situations; (i) $\vec{E}$ is perpendicular to $\vec{B}$, $j_{\perp}$ is in a critical state and $j_{//}$ is subcritical, (ii) $\vec{E}$ is parallel or antiparallel to $\vec{B}(x)$, $j_{\perp}$ is subcritical and $j_{//}$ is in a critical state, and (iii) the angle subtended by $\vec{E}$ and $\vec{B}$ is $\neq 0$ nor $\pi/2$, $j_{\perp}$ and $j_{//}$ are in a critical state. Further $\vec{E}(x)$ must be continuous and the requirement that $0 \leq \psi \leq \pi/2$ must be met. Noting that $\mu_o j_{\perp}$ is equivalent to dB/dx and $\mu_o j_{//}$ to $Bd\theta/dx$, (i), (ii) and (iii) translated into the framework of our double critical state model signify that domains can exist where (a) dB/dx is critical but $d\theta/dx$ is subcritical, (b) $d\theta/dx$ is critical but dB/dx is subcritical and (c) both $\frac{dB}{dx}$ and $\frac{d\theta}{dx}$ are in critical states. Clearly, the model proposed by Clem permits greater flexibility

and a richer variety of B and θ profiles than our simple model which allows only configurations of category (c) or equivalently (iii). In the foregoing we ignore the "inert" regions where no changes have taken place (θ and B are uniform).

The computations required to determine the appropriate sequences of B and θ profiles exploiting Clem's proposals are necessarily considerably more complicated and time consuming than in our simple model. Nevertheless his more rigorous and fundamental framework is being pursued in the analysis of our observations. Pending the result of these elaborate computations we speculate that the agreement of the predictions of our model with our vast assortment of data suggests that our approach generates the major features of the sequences of B and θ profiles. We also conjecture that the introduction of a θ dependence in our formulae (equations 4.10 and 4.31) may prove to be a stratagem or shortcut which, in effect or indirectly, incorporates and takes into account our ignoring the occurrence of domains of types (a) and (b).

In closing we remark that the existence of deep valleys in the hysteresis losses in the noncollinear regime for full-wave and half-wave oscillations may prove useful in the technology of type II superconductors. In the light of our study of this valley we visualize that the decrease in A.C. losses reported by Taylor and by Sugahara and Kato for wires of type II superconductors in static $H_{//}$ mapped out a portion of the left-side of such valleys.

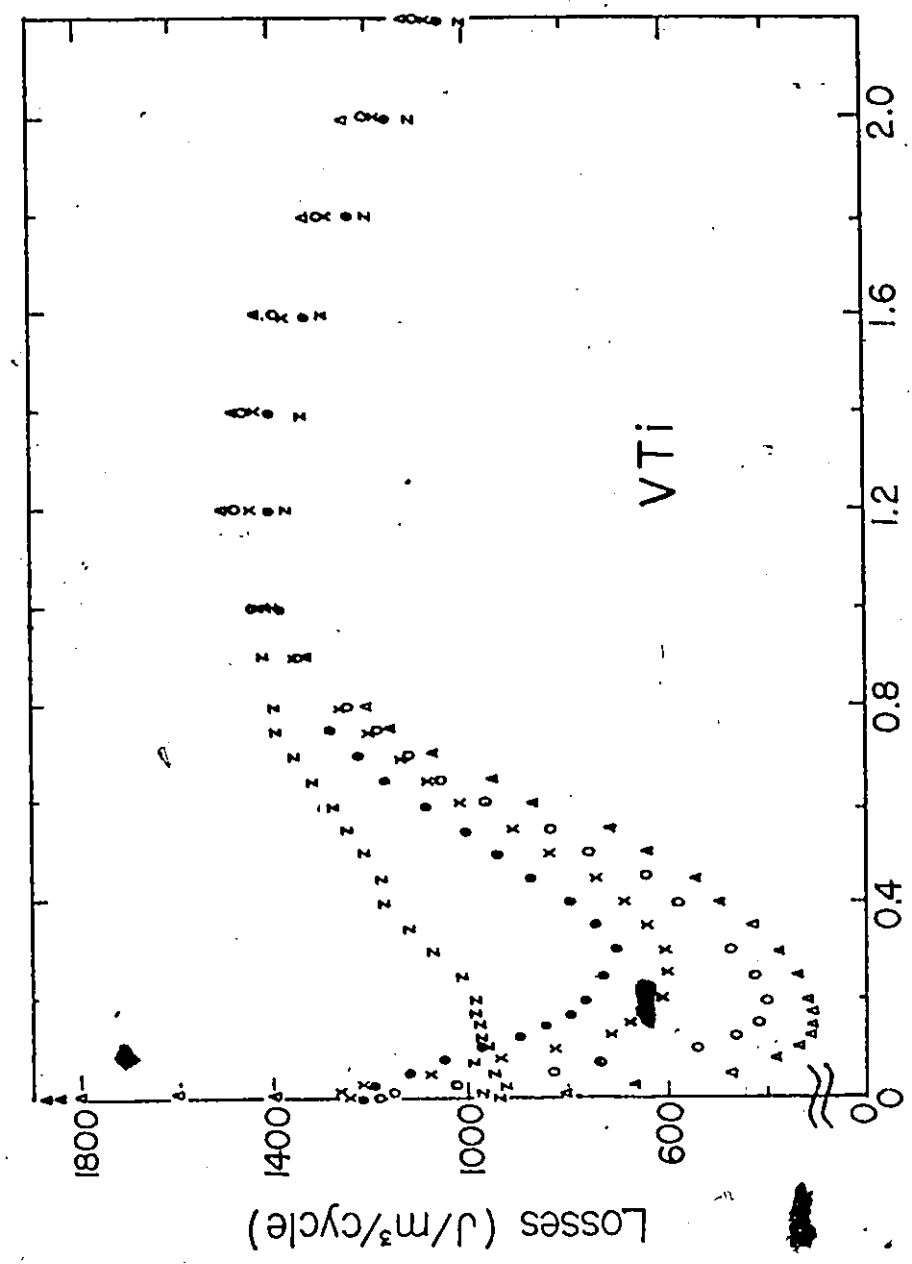

FIG. 4.1 - Hysteresis losses per cycle per unit volume, measured on the VTi specimen (at 4.2 K) at an amplitude h_o = 0.05 T as function of the stationary longitudinal magnetic field H//. The bias magnetic field (collinear with h_o) selected, $H_{b1} = 0$, h_o, 3/2 h_o, 2 h_o and 3 h_o correspond to curves (Δ), (0), (X), (●) and (Z) respectively.

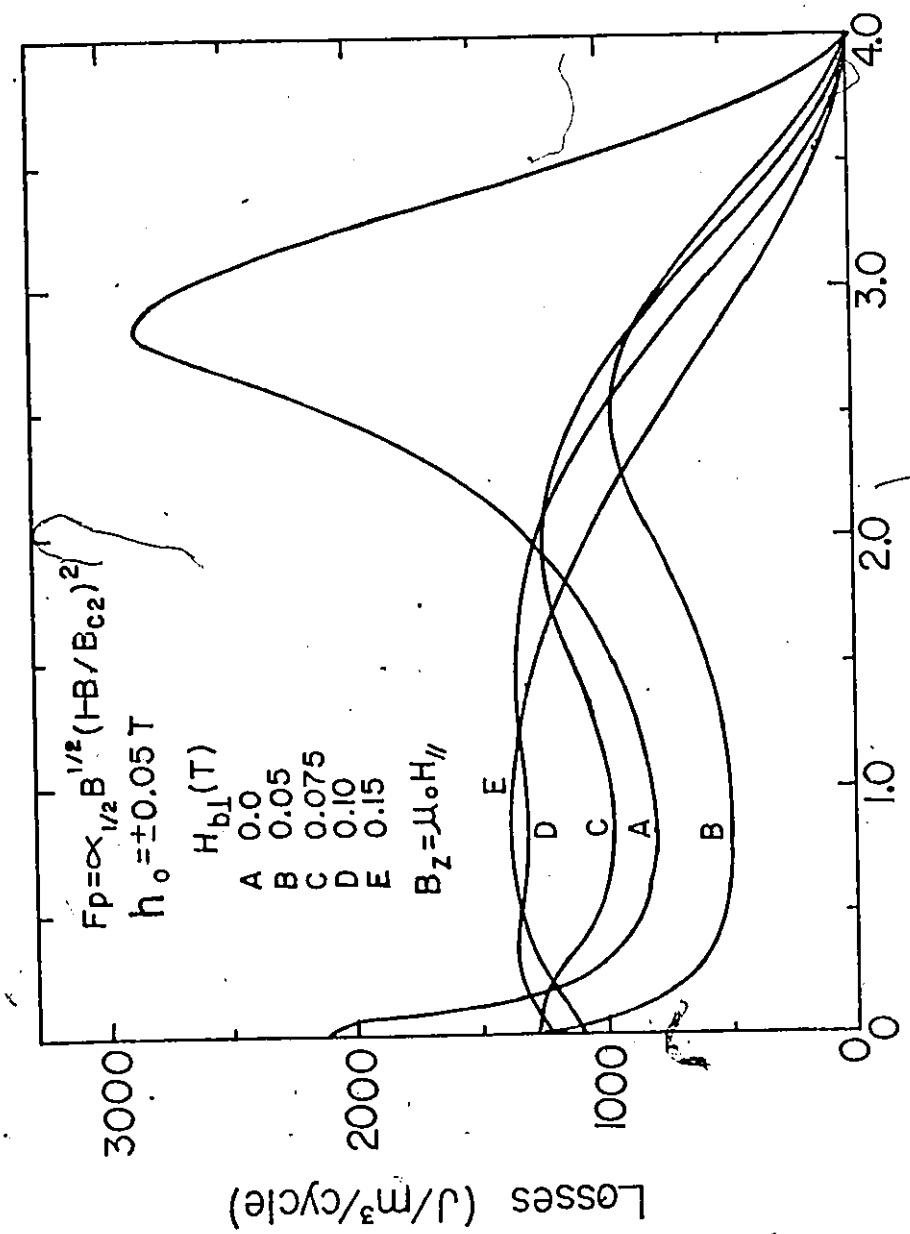

FIG. 4.2 Hysteresis losses calculated for the VTi ribbon on the basis of equation 4.12 where Fp is given by equation 4.9, as function of the stationary longitudinal magnetic field H//. The bias magnetic fields are the same as in Fig. 4.1 corresponding to curves A, B, C, D and E respectively.

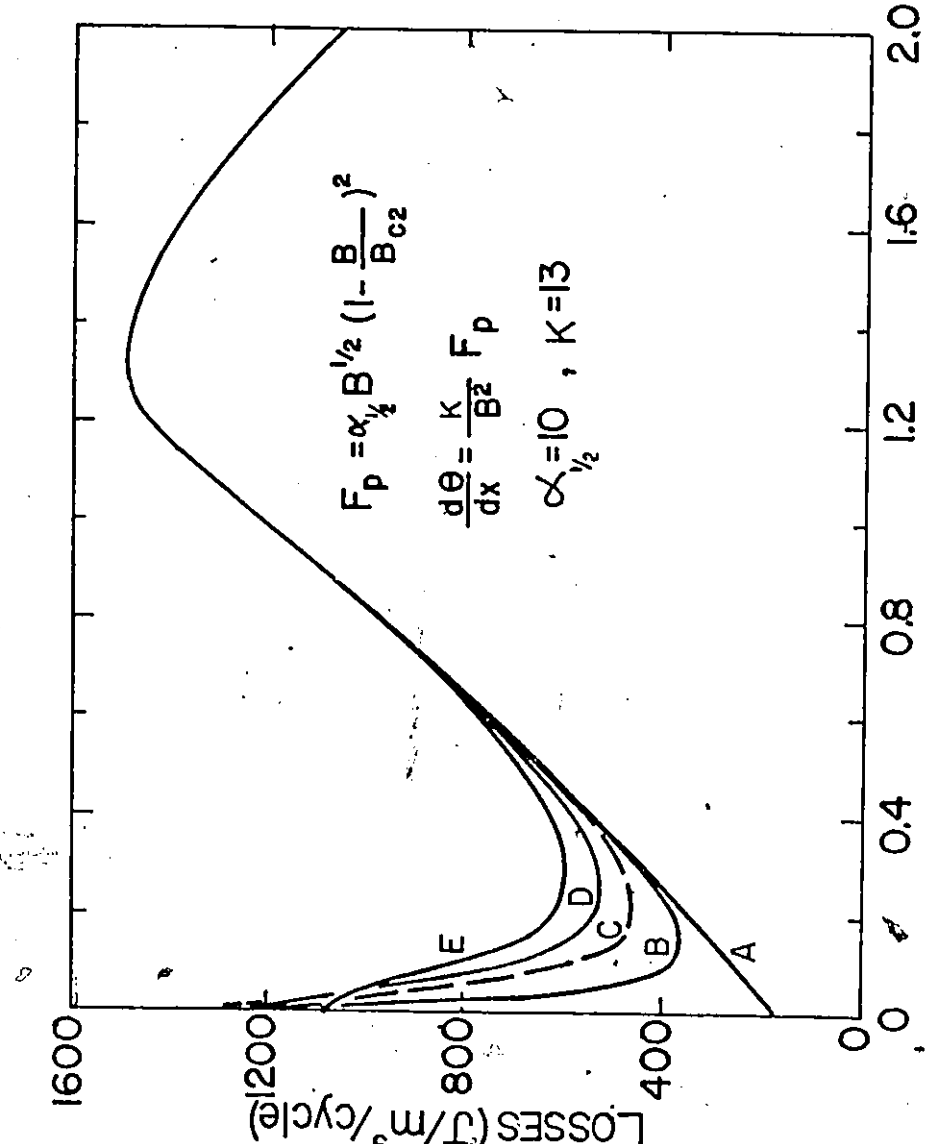

FIG. 4.3 Hysteresis losses calculated for the VTi ribbon, generated with equation 4.28 where Fp is given by equation 4.9, as function of the stationary field H// for the same bias field of Fig. 4.2.

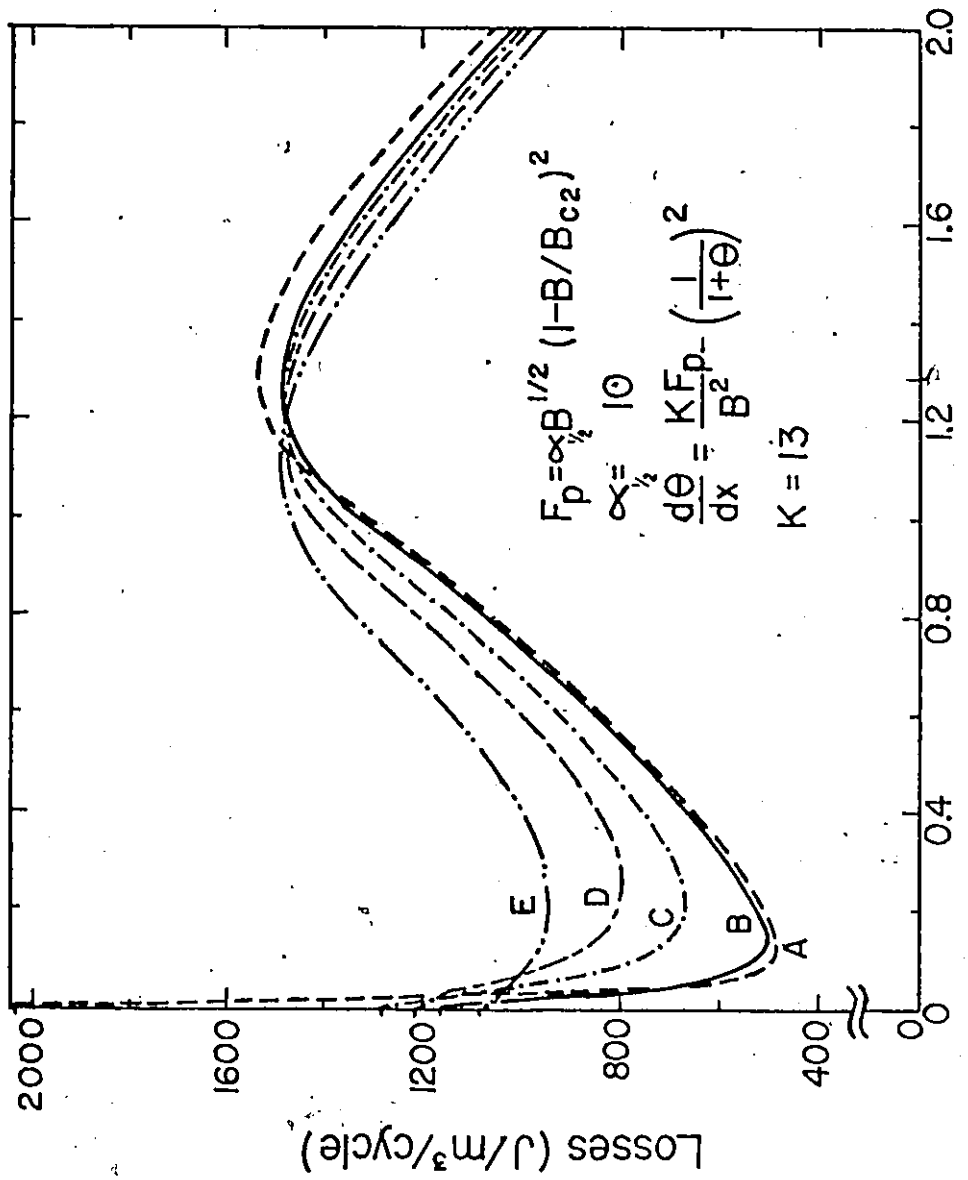

FIG. 4.4 Hysteresis losses calculated for the VTi ribbon, for different bias magnetic fields H_{b1} (same as in Fig. 4.3) using equation 4.31 together with equation 4.10 in the double critical state framework as function of the stationary magnetic $H_{//}$.

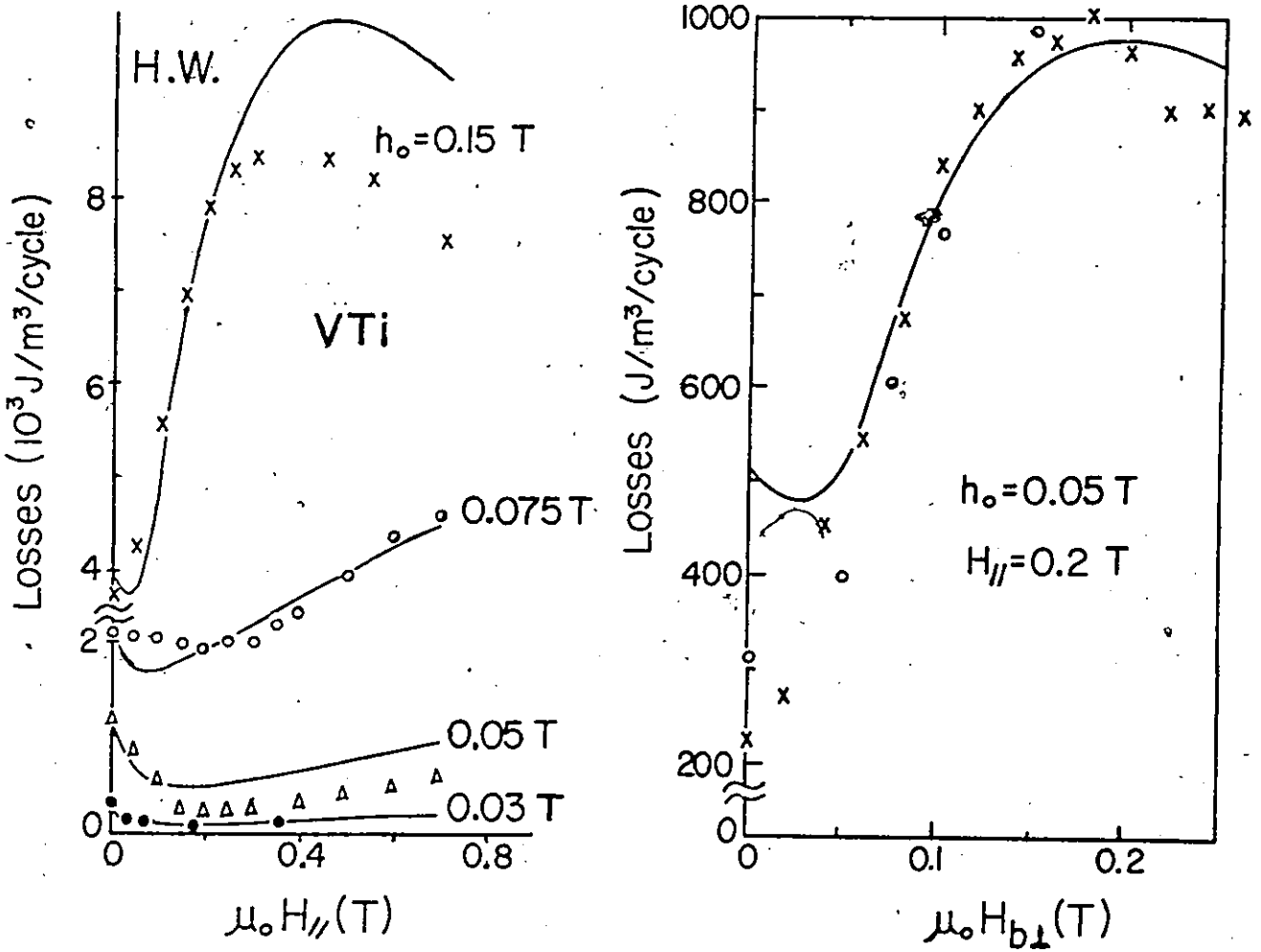

FIG. 4.5 a) Hysteresis losses as function of the stationary magnetic field (half-wave situation) for different amplitudes of oscillation h_o. Solid curves are calculated using equation 4.30 together with equation 4.10.

b) Hysteresis losses as function of the bias magnetic field $H_{b\perp}$. In fact this is a vertical cut taken at $H_{//}$ = 0.2 T, see Fig. 4.1. The solid lines are calculated curves using equations 4.10 and 4.30.

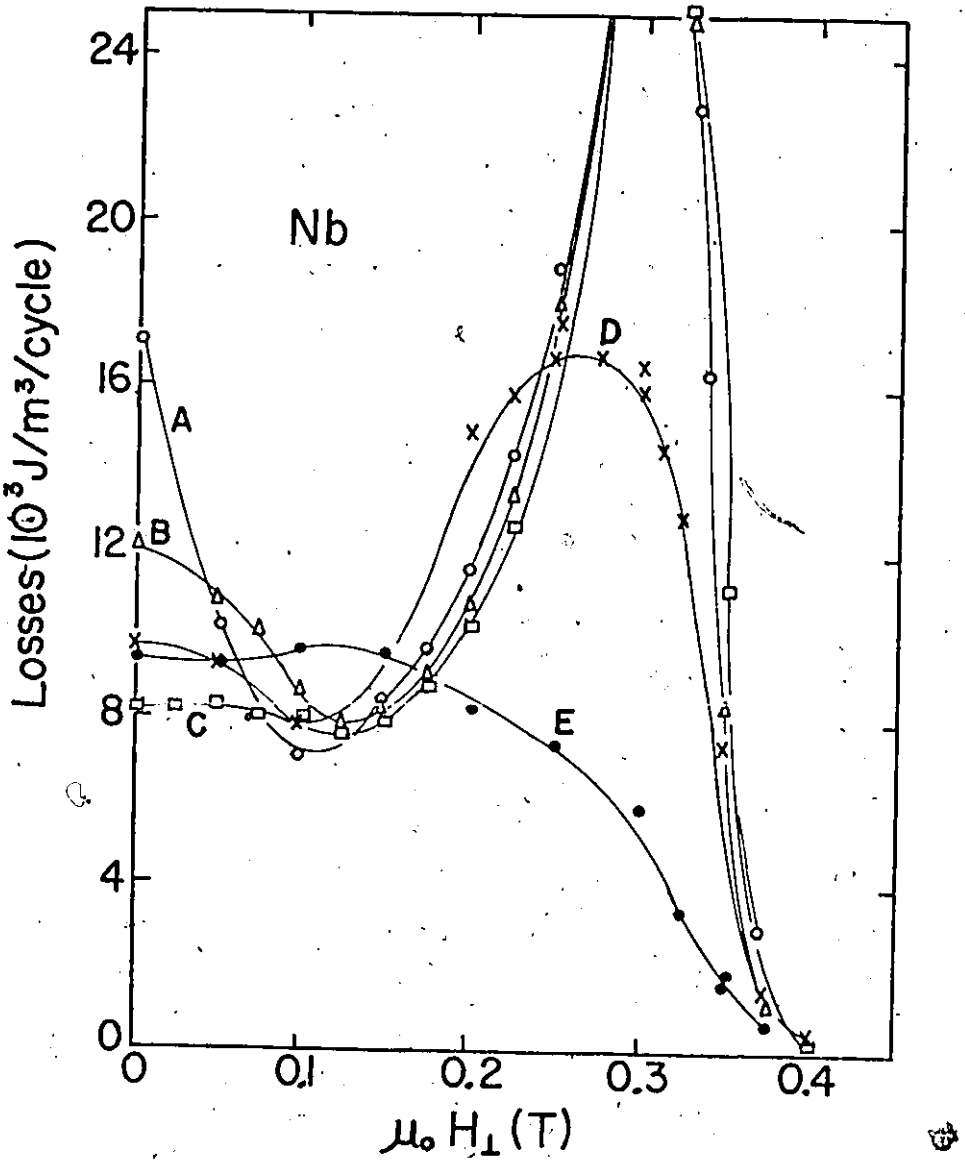

FIG. 4.6 Hysteresis losses per cycle per unit volume measured on the Nb specimen (at 4.2 K) at an amplitude h_o = 0.18 T as function of the stationary longitudinal magnetic field $H_\perp$. The bias magnetic fields (collinear with h_o) selected were, $H_{b//}$ = 0, 0.03, 0.05, 0.09 and 0.18 T for the curves A, B, C, D and E respectively.

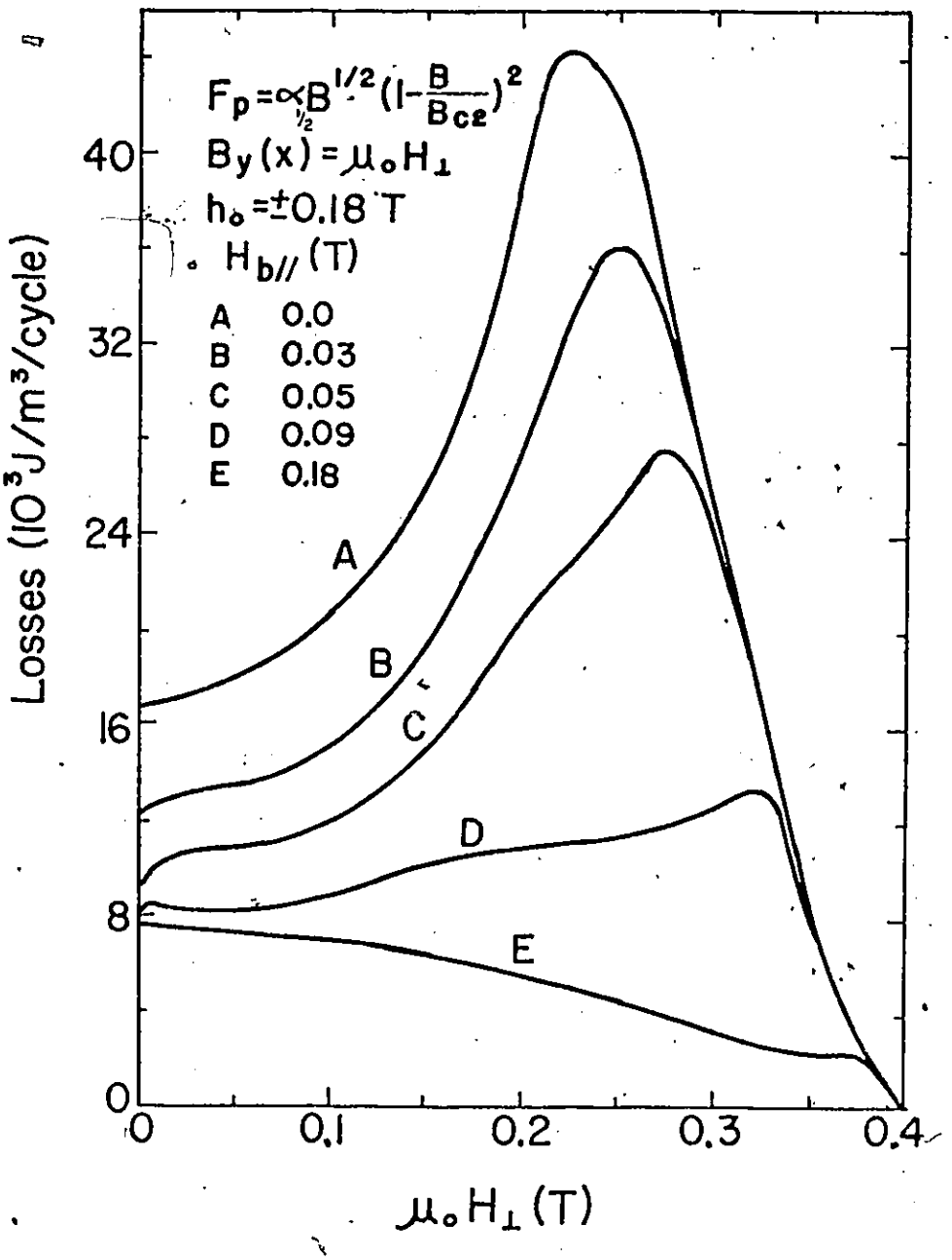

FIG. 4.7 Hysteresis losses calculated for the Nb ribbon on the basis of equation 4.12 where F_p is given by equation 4.9, as function of the stationary magnetic field $H_\perp$. The chosen bias magnetic field (collinear with h_o) $H_{b//}$ = 0, 0.03, 0.05, 0.09 and 0.18 T corresponding to curves A, B, C, D, and E respectively.

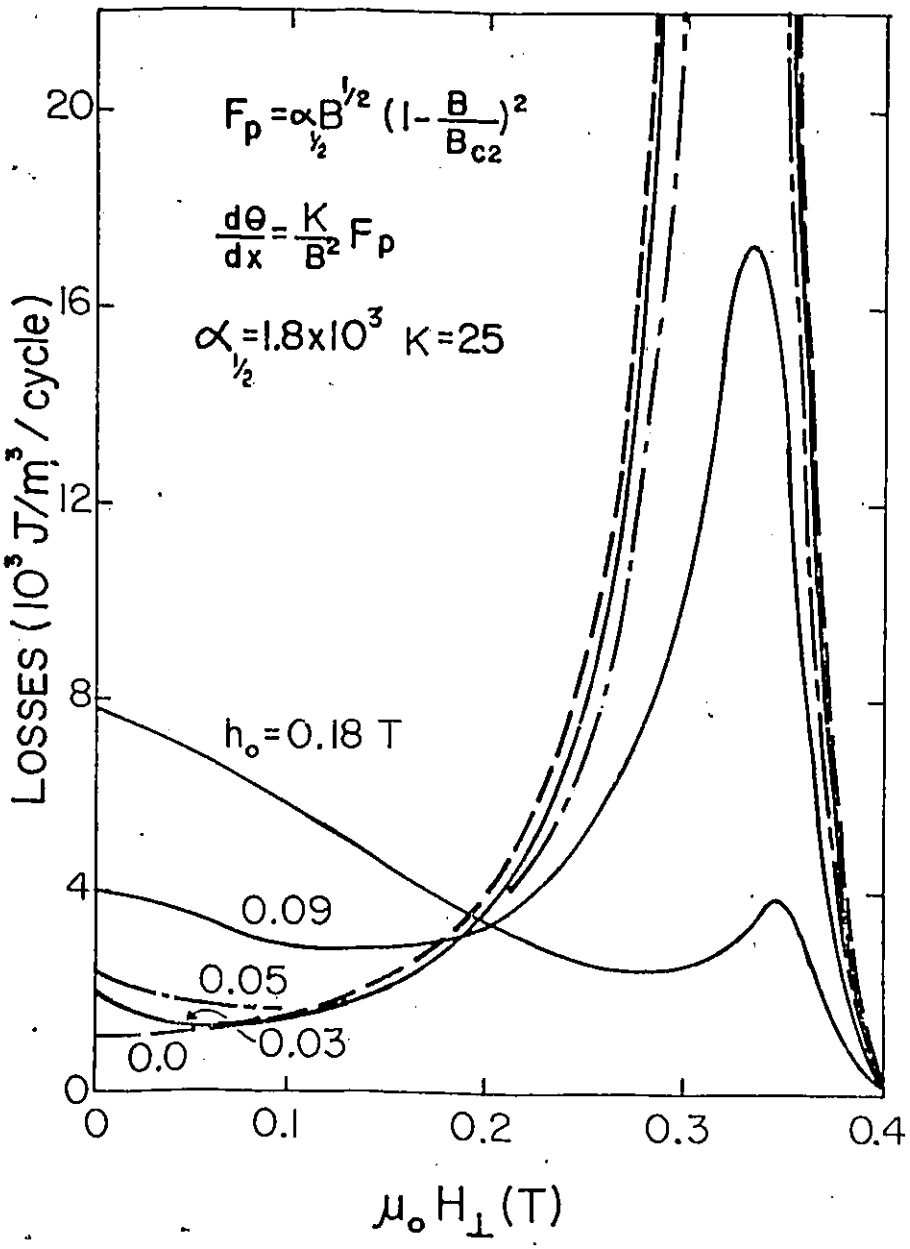

FIG. 4.8 Hysteresis losses calculated for the Nb ribbon, generated with equation 4.28 and equation 4.9 as function of the stationary field $H_\perp$ for the same bias magnetic field of Fig. 4.7

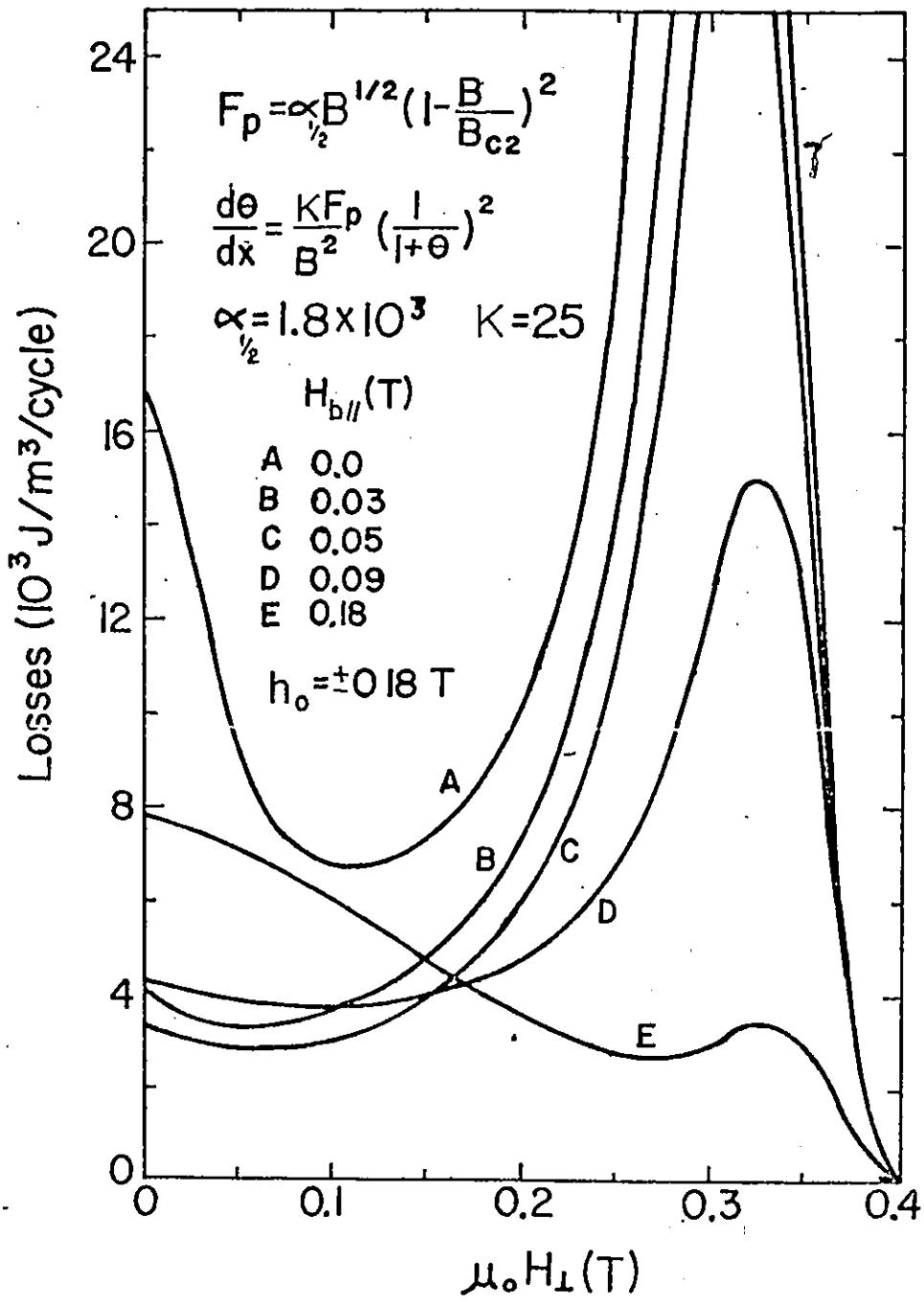

FIG. 4.9 Hysteresis losses calculated for the Nb ribbon, for different bias magnetic field $H_{b//}$ (same as in Fig. 4.7) using equation 4.31 together with equation 4.10 in the double critical state framework, as function of the stationary magnetic field $H_\perp$.

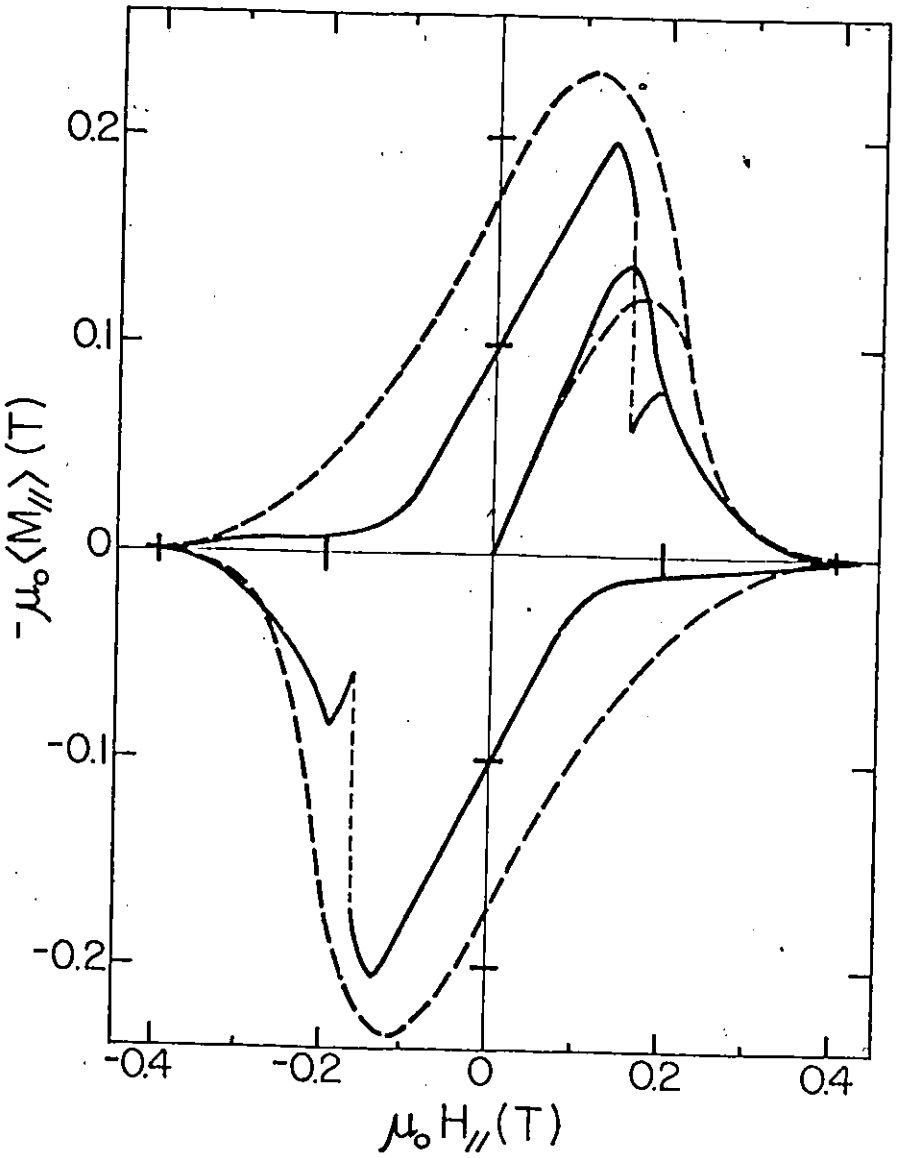

FIG. 4.10 Magnetization curve ($-\mu_o \langle M_{//} \rangle$ vs. $\mu_o H_{//}$) for the Nb specimen. The solid curve is experimental and the dashed curve is calculated using equation 4.9 with $\alpha_{1/2} = 1.8 \times 10^3$ $T^{3/2}/m$.

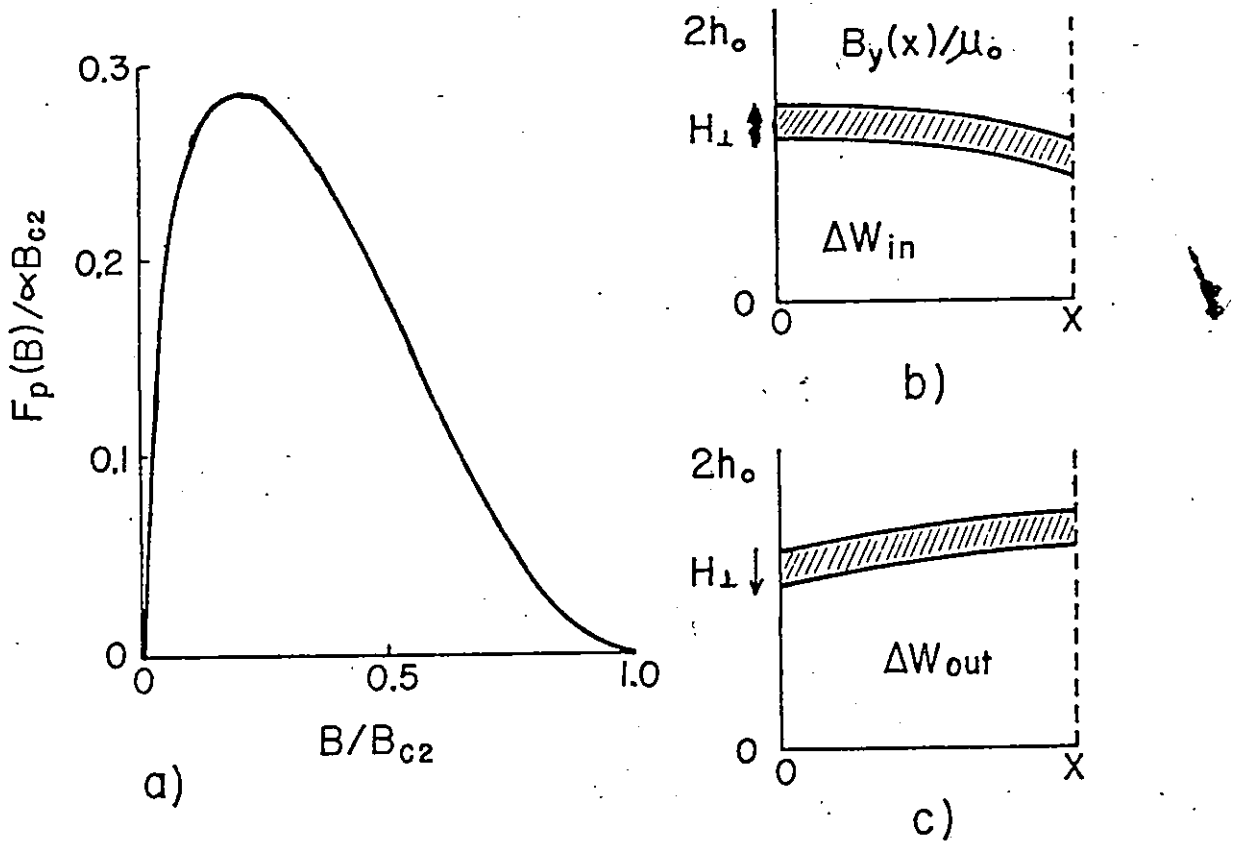

FIG. 4.11 (a) The pinning force $F_p(B)$ as function of the magnetic induction B.
(b) Schematic showing the energy entering (ΔW_{in}) the slab during the upsweep of B_y becomes comparable to
(c) the energy flowing out (ΔW_{out}) during the downsweep of B_y over a corresponding range.

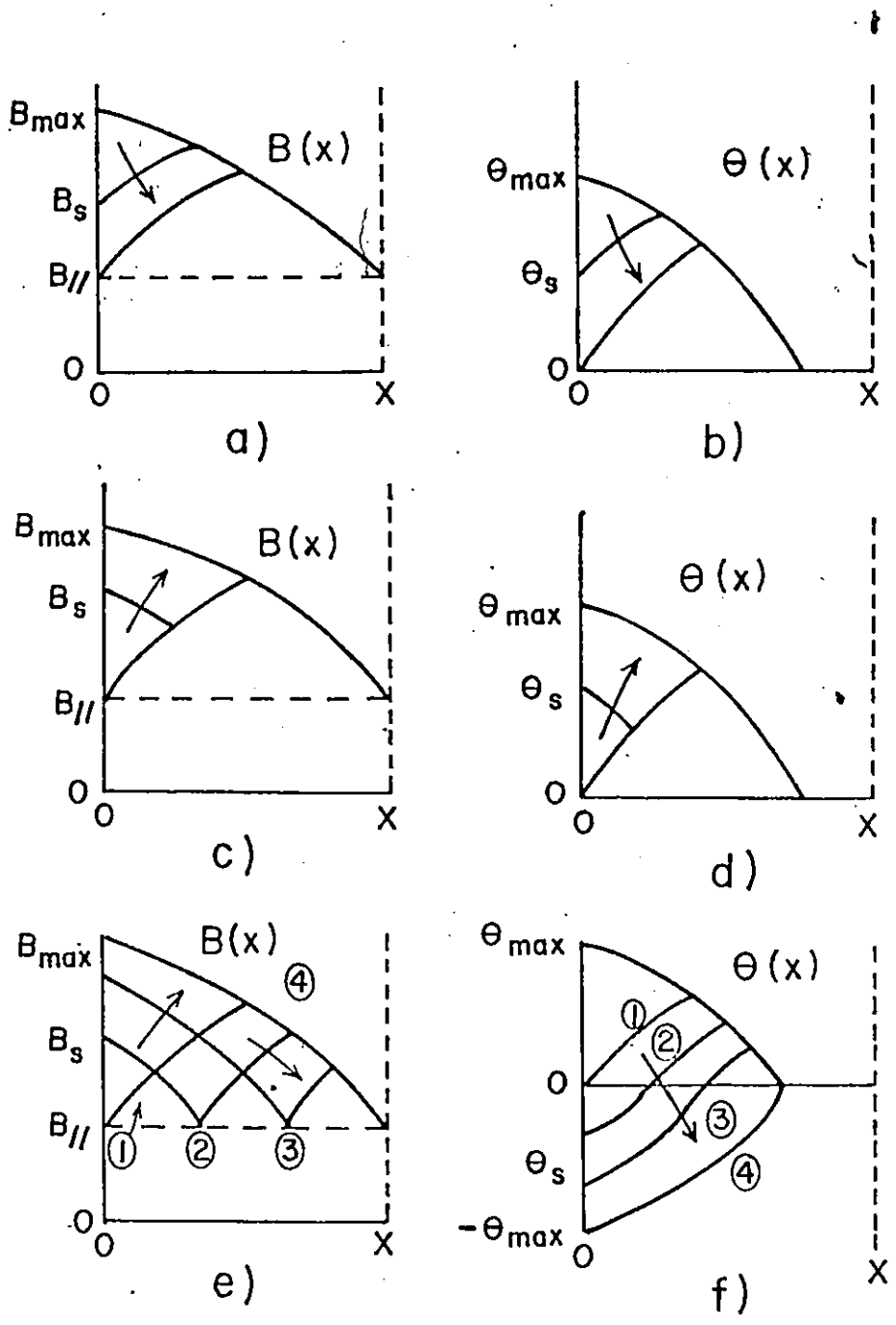

FIG. 4.12 Schematic of the basic differences in the sequences of B profiles between the full-wave and the half-wave cases in the electrodynamic model where B_z is constant. (a) Sequence of B and (b) θ profiles as B_s is decreasing and (c) B and (d) θ profiles as B_s is increasing for the half-wave case. In (e), sequence of B and (f) θ profiles for the full-wave case.

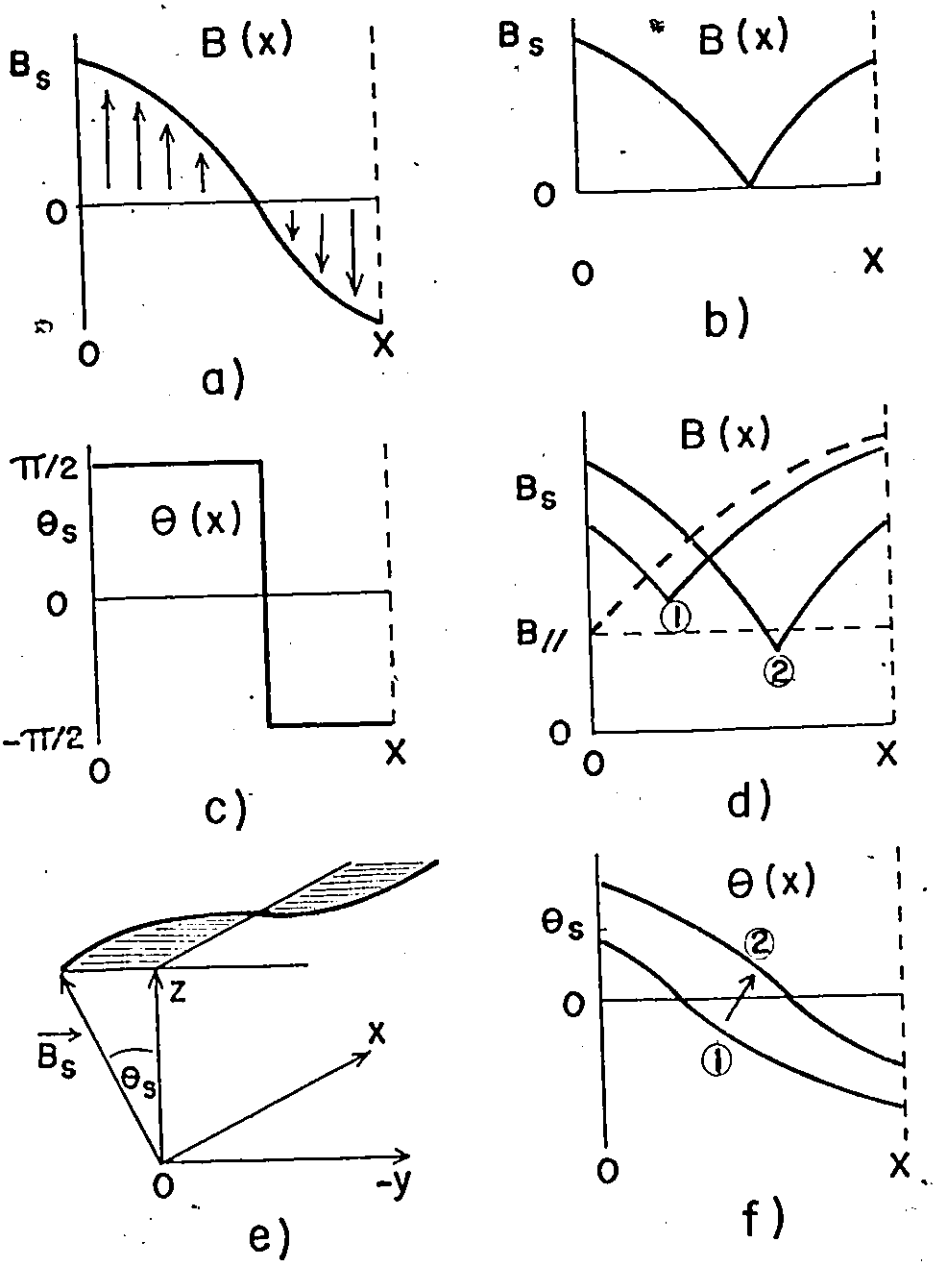

FIG. 4.13 (a) Schematic of B and (c) θ profiles for the full-wave case in the collinear regime. (b) Sequences of the magnitude of the B profile when $H_{\perp}(t)$ reverses polarity. (d) $|B(x)|$ reaching a minimum in the plane $\theta(x) \doteq 0$ and (f) the corresponding θ profiles. In (e), a three dimensional sketch of the $\vec{B}$ configuration is presented.

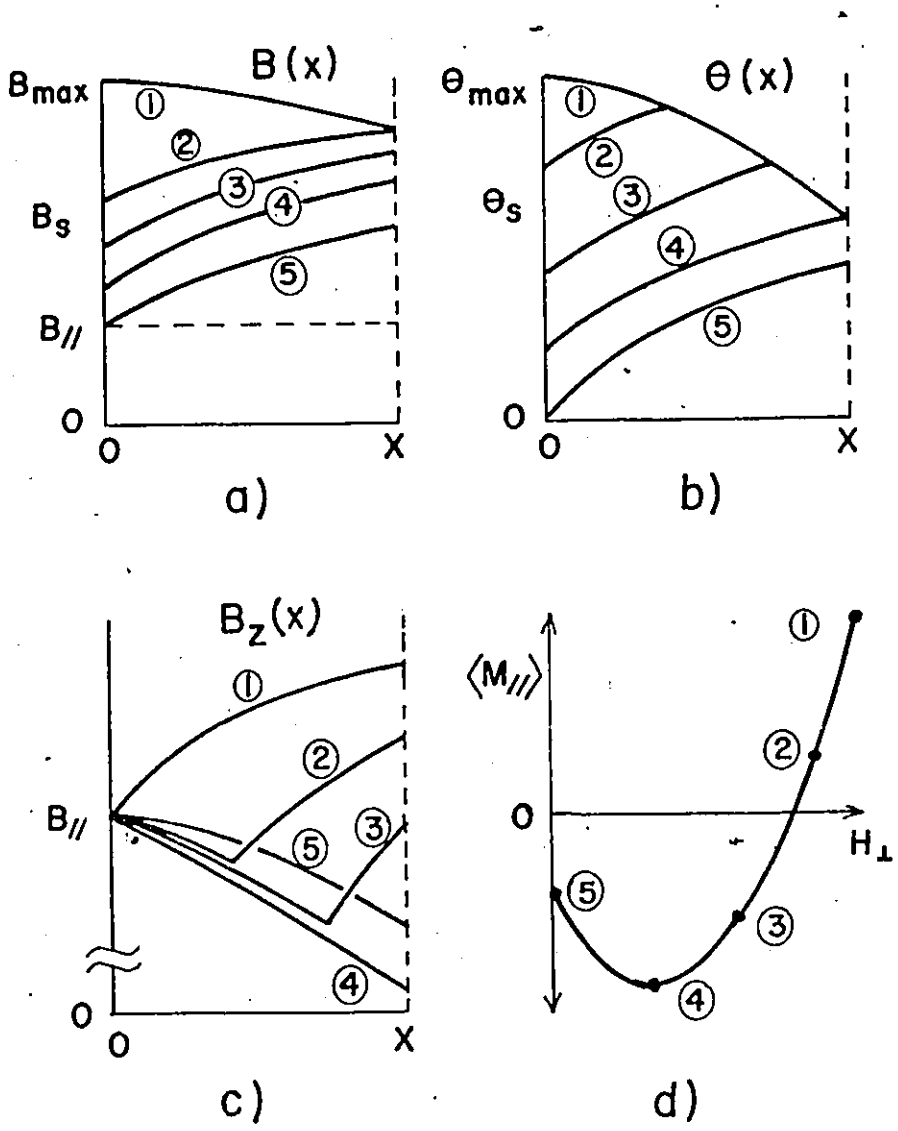

FIG. 4.14 (a) Sequence of B and (b) θ profiles as $H_\perp$ decreases while $H_{//}$ is stationary. In (c) the sequence of B_z profiles causing $\langle M_z \rangle$ to reverse its descent and form a valley (d) as $H_\perp$ decreases toward zero while $H_{//}$ is stationary.

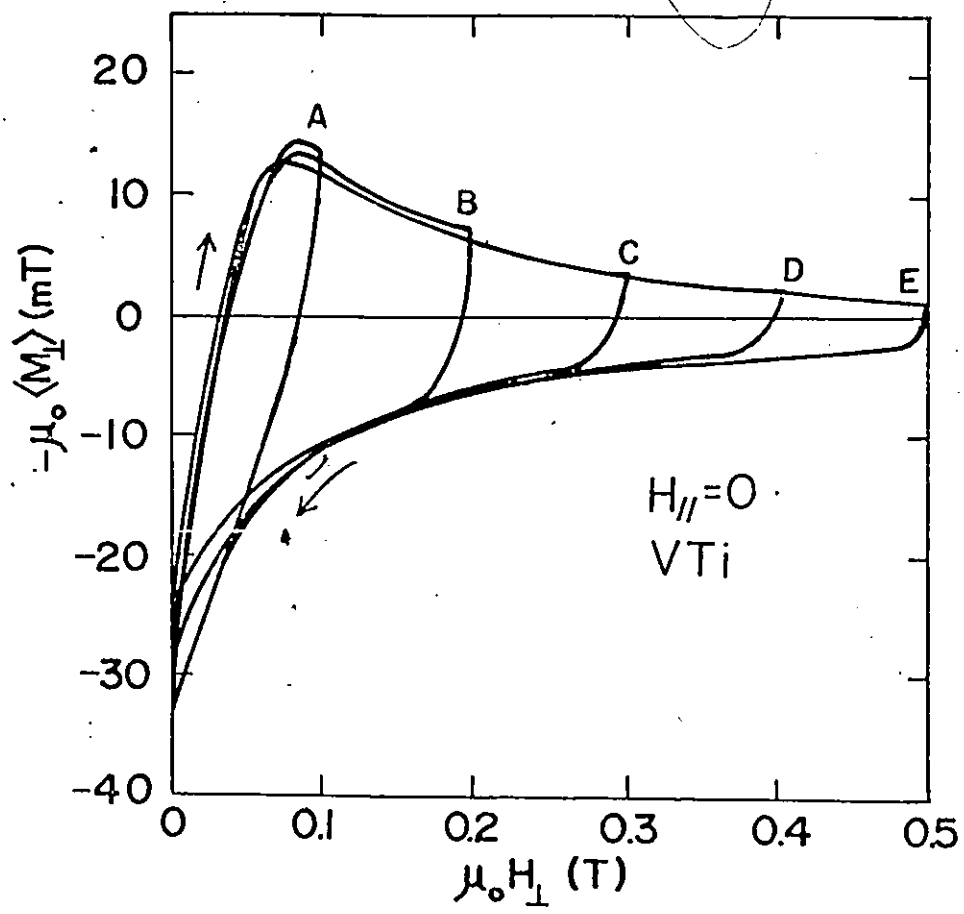

FIG. 4.15 Hysteresis curves $-\mu_o \langle M_\perp \rangle$ vs. $\mu_o H_\perp$ observed with the VTi ribbon in a stationary magnetic field $H_{//} = 0$. The various amplitudes of these half-wave cycles are: h_o = 0.05, 0.10, 0.15, 0.20 and 0.25 T for curves A, B, C, D and E respectively.

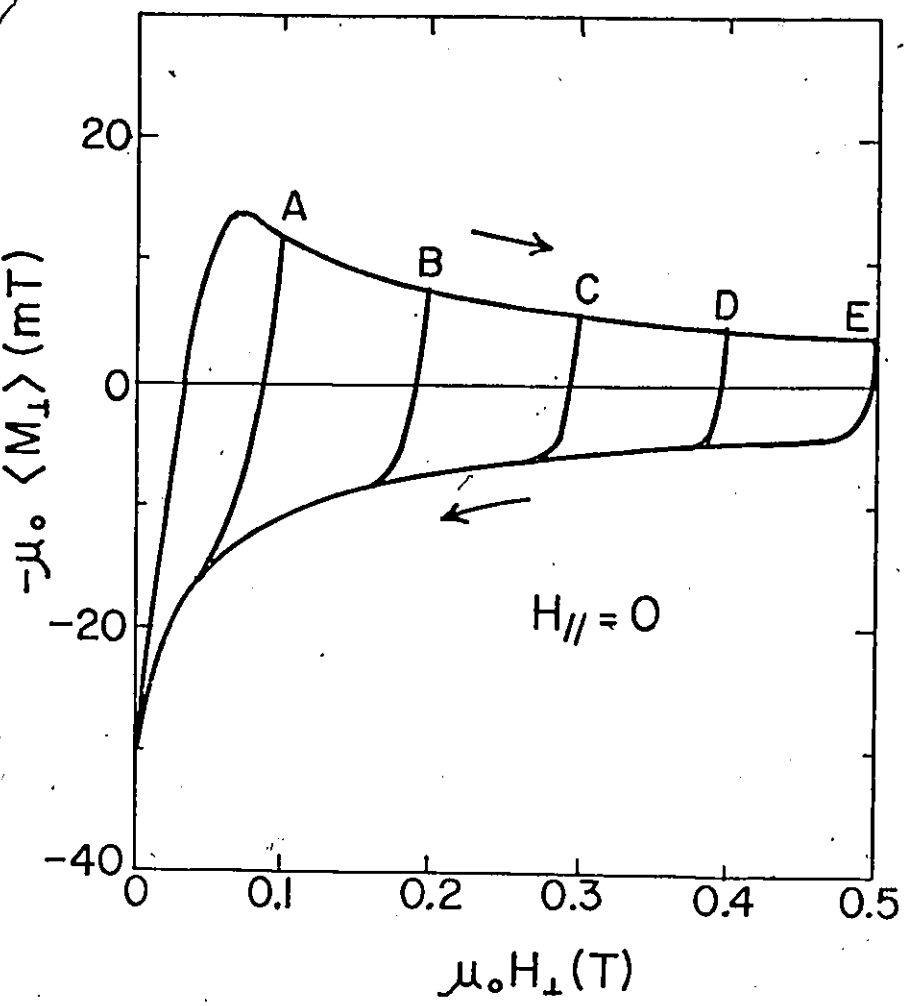

FIG. 4.16 Calculated curves computed with the double critical state model using equations 4.10 and 4.31. Compare with Fig. 4.15.

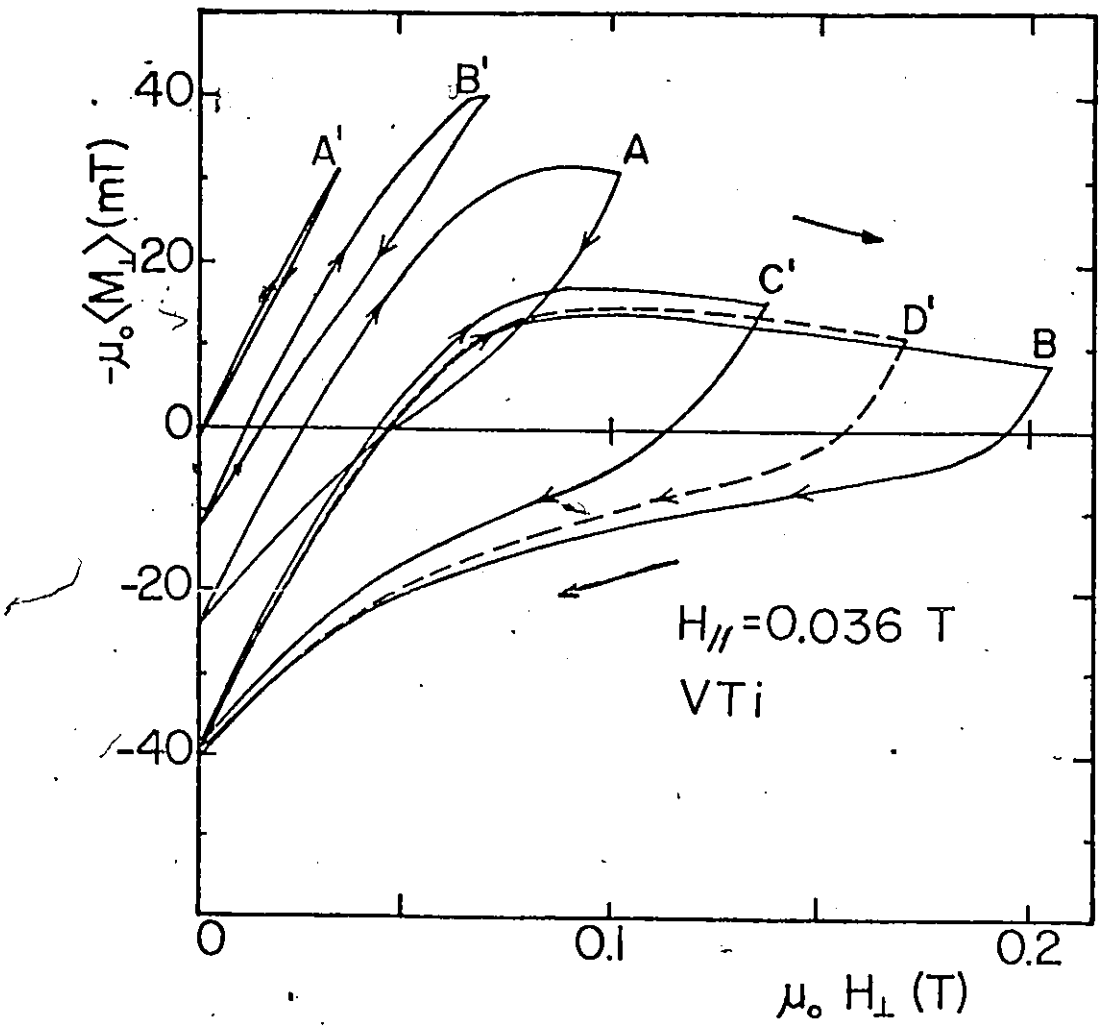

FIG. 4.17 Hysteresis curves $-\mu_o \langle M_\perp \rangle$ vs. $\mu_o H_\perp$ observed with the VTi ribbon in a stationary magnetic field $H_{//}$ = 0.036 T. The various amplitudes of these half-wave cycles are: h_o = 0.017, 0.034, 0.051, 0.068, 0.085 and 0.102 T for curves A', B', A, C', D' and B respectively.

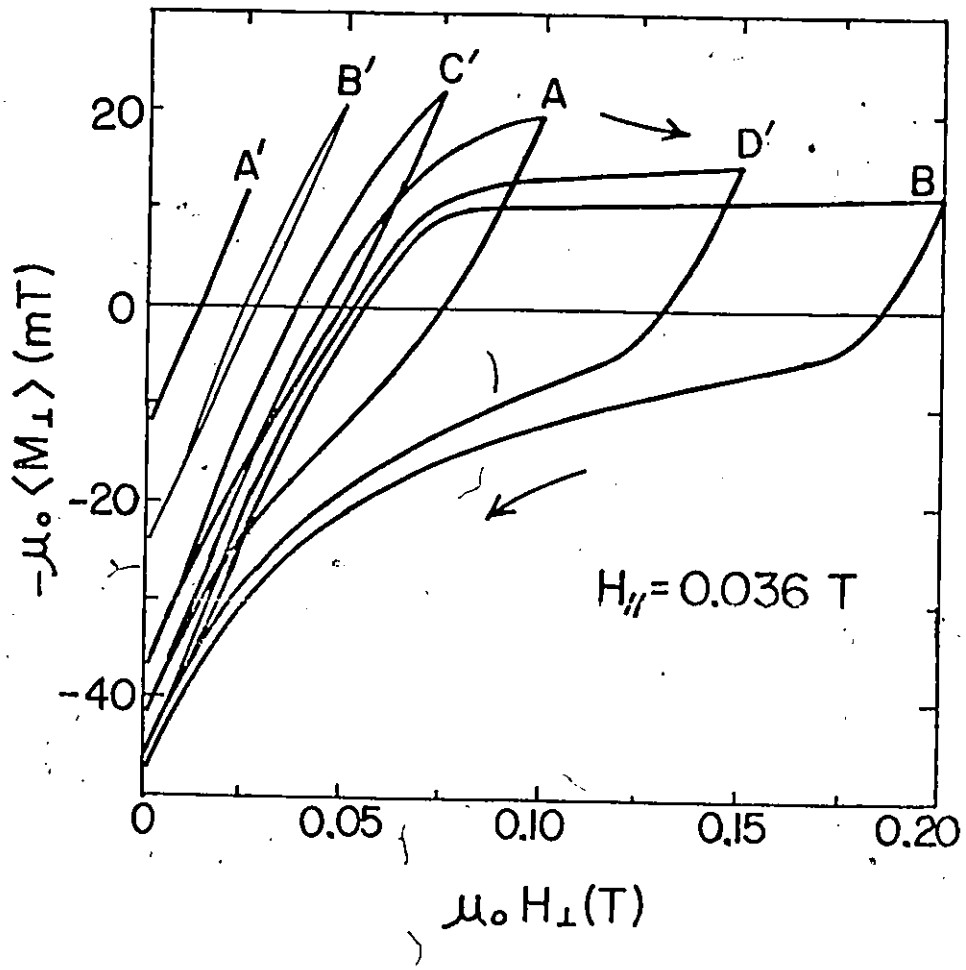

FIG. 4.18 Calculated curves computed with the double critical state model using equations 4.10 and 4.31. Compare "with care" with Fig. 4.17 because the amplitudes are not exactly in correspondence, h_o = 0.0125, 0.025, 0.0375, 0.05, 0.075 and 0.10 T for curves A', B', C', A, D' and B respectively.

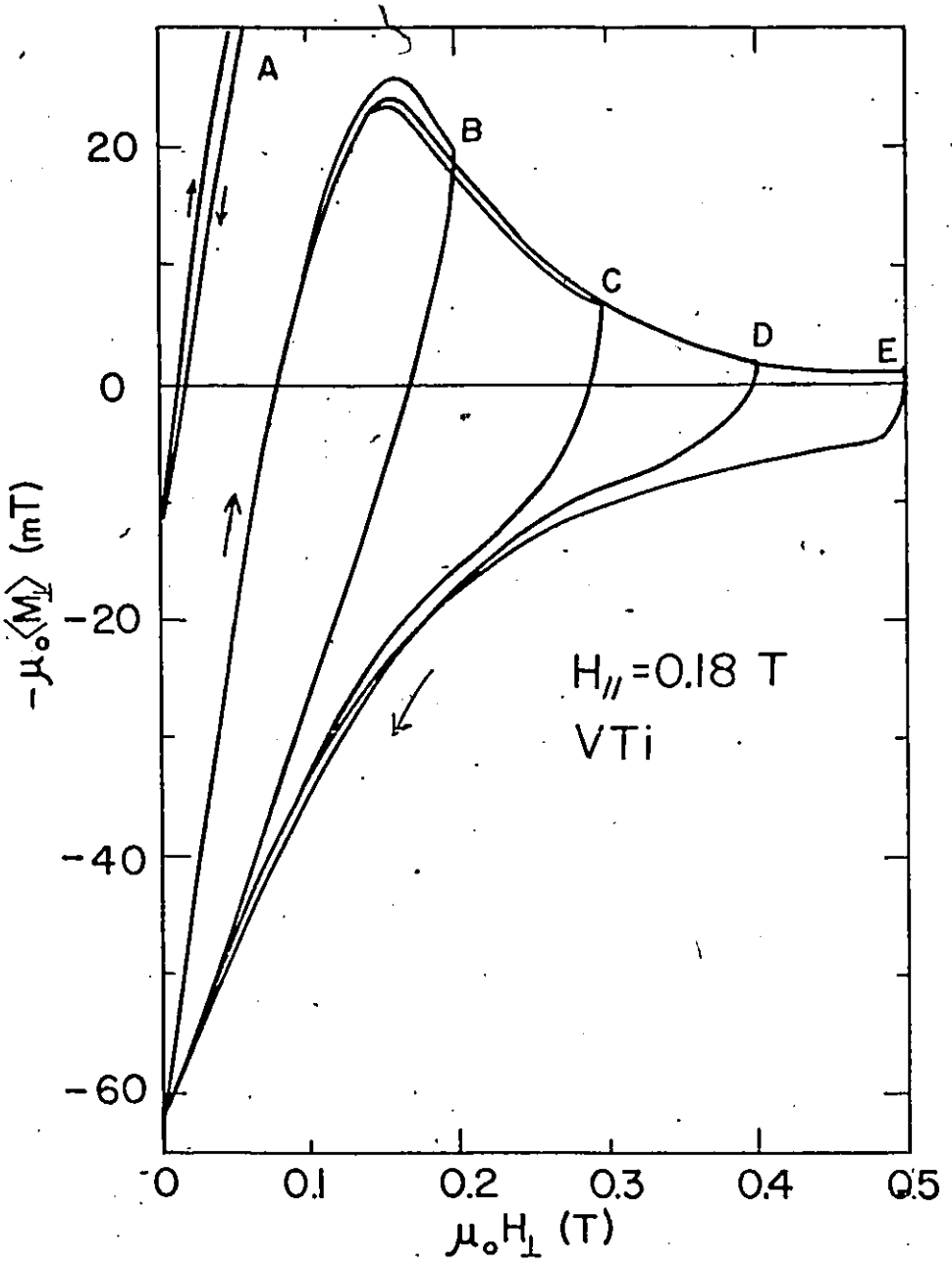

FIG. 4.19 Same as Fig. 4.15 with $H_{//}$ = 0.18 T.

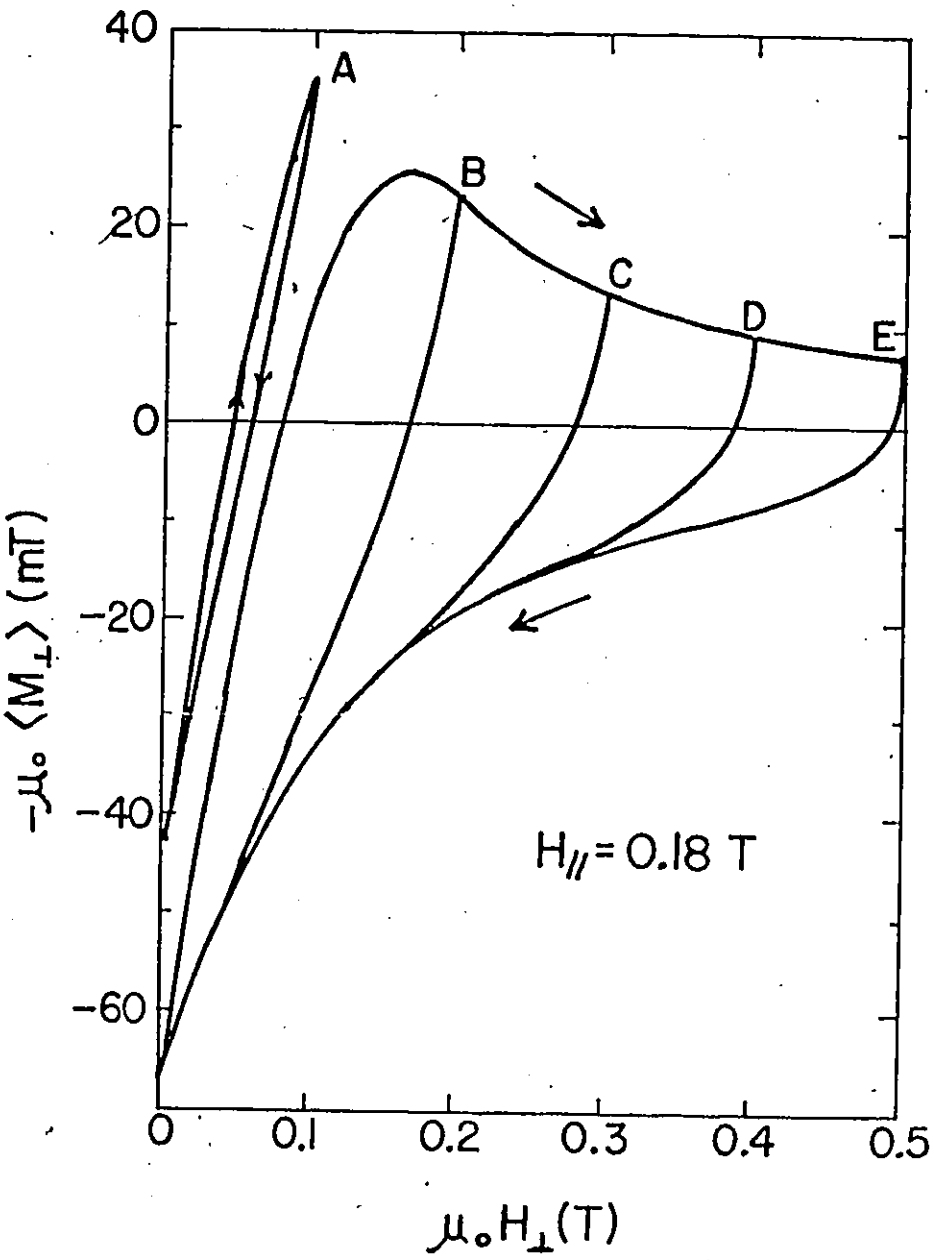

FIG. 4.20 Same as Fig. 4.16 with $H_{//} = 0.18$ T. Compare with Fig. 4.19.

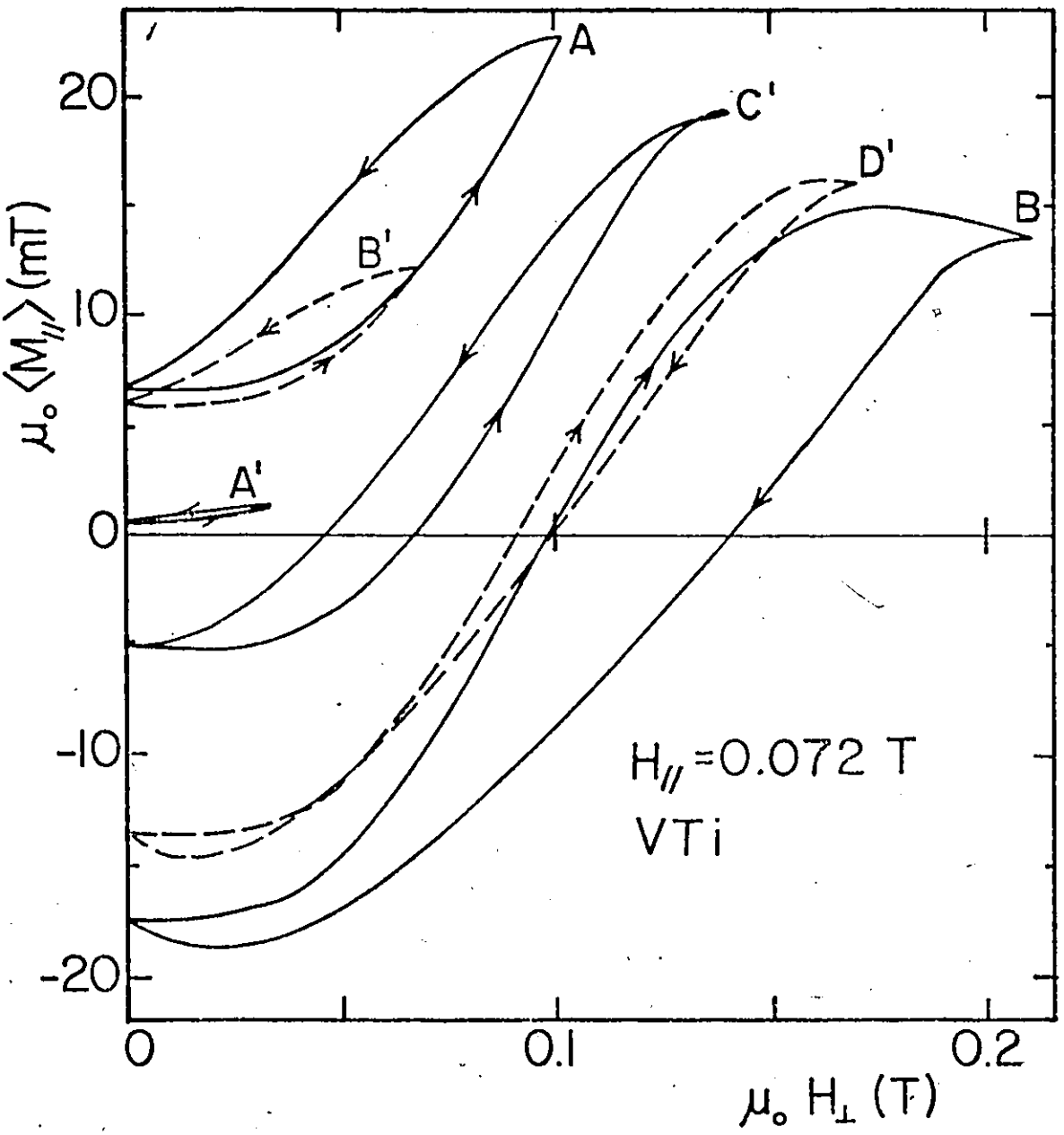

FIG. 4.21 Family of $\mu_o \langle M_{//} \rangle$ vs. $\mu_o H_\perp$ curves observed with the VTi ribbon in a stationary magnetic field $H_{//}$ = 0.72 T. The various amplitudes of these half-wave cycles are: h_o = 0.017, 0.034, 0.051, 0.068, 0.085 and 0.102 T for curves A', B', A, C', D' and B respectively.

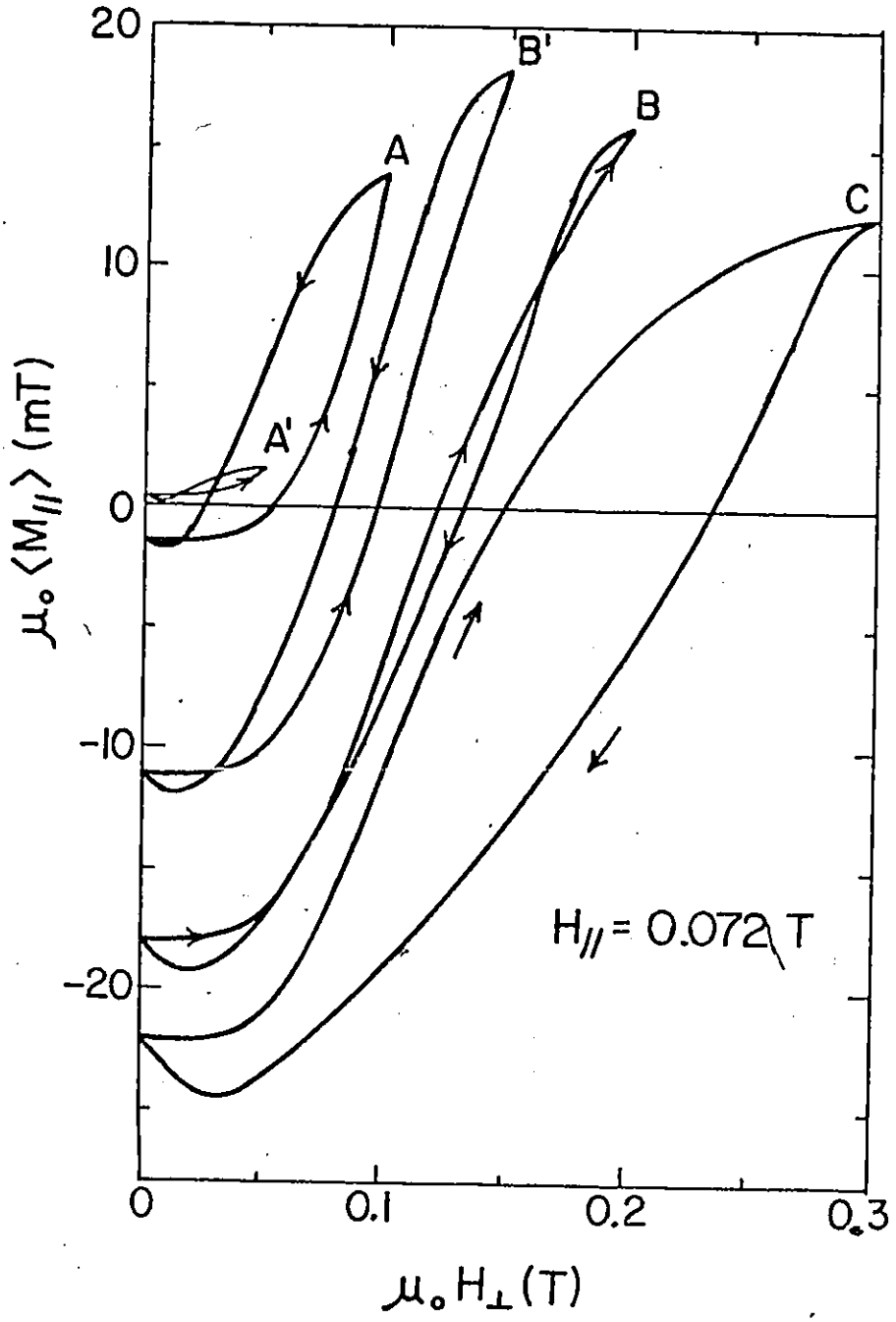

FIG. 4.22 Calculated curves computed with the double critical state model using equations 4.10 and 4.31. Compare "with care" with Fig. 4.21 because the amplitudes are not exactly in correspondence, n_o = 0.025, 0.05, 0.075, 0.10 and 0.15 for curves A', A, B', B and C respectively.

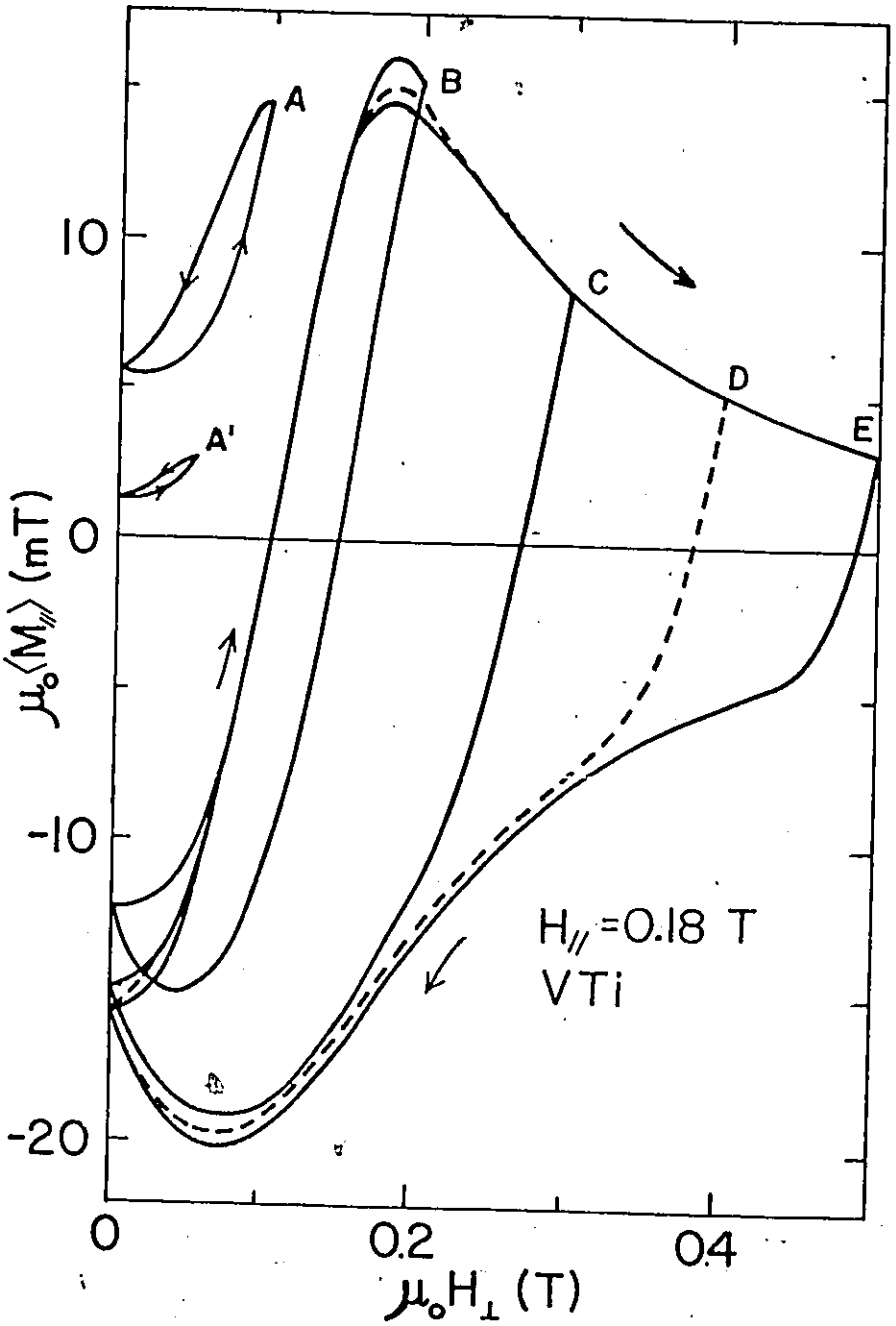

FIG. 4.23 Family of $\mu_o \langle M_{//} \rangle$ vs. $\mu_o H_\perp$ curves observed with the VTi ribbon in a stationary magnetic ffeld $H_{//}$ = 0.18 T. The various amplitudes of these half-wave cycles are: h_o = 0.025, 0.05, 0.10, 0.15, 0.20 and 0.25 T for curves A', A, B, C, D and E respectively.

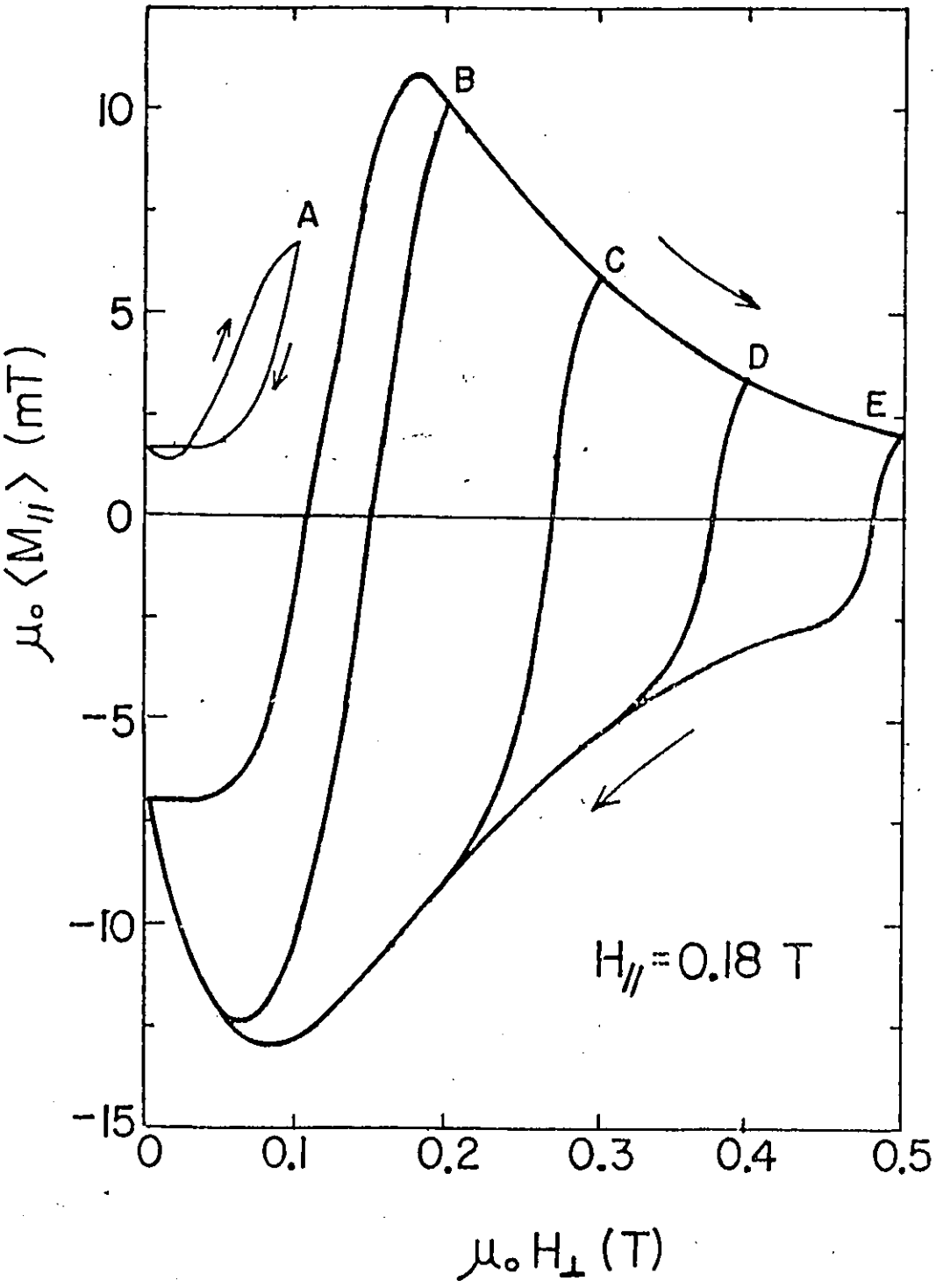

FIG. 4.24 Calculated curves computed with the double critical state model using equations 4.10 and 4.31. Compare with Fig. 4.23.

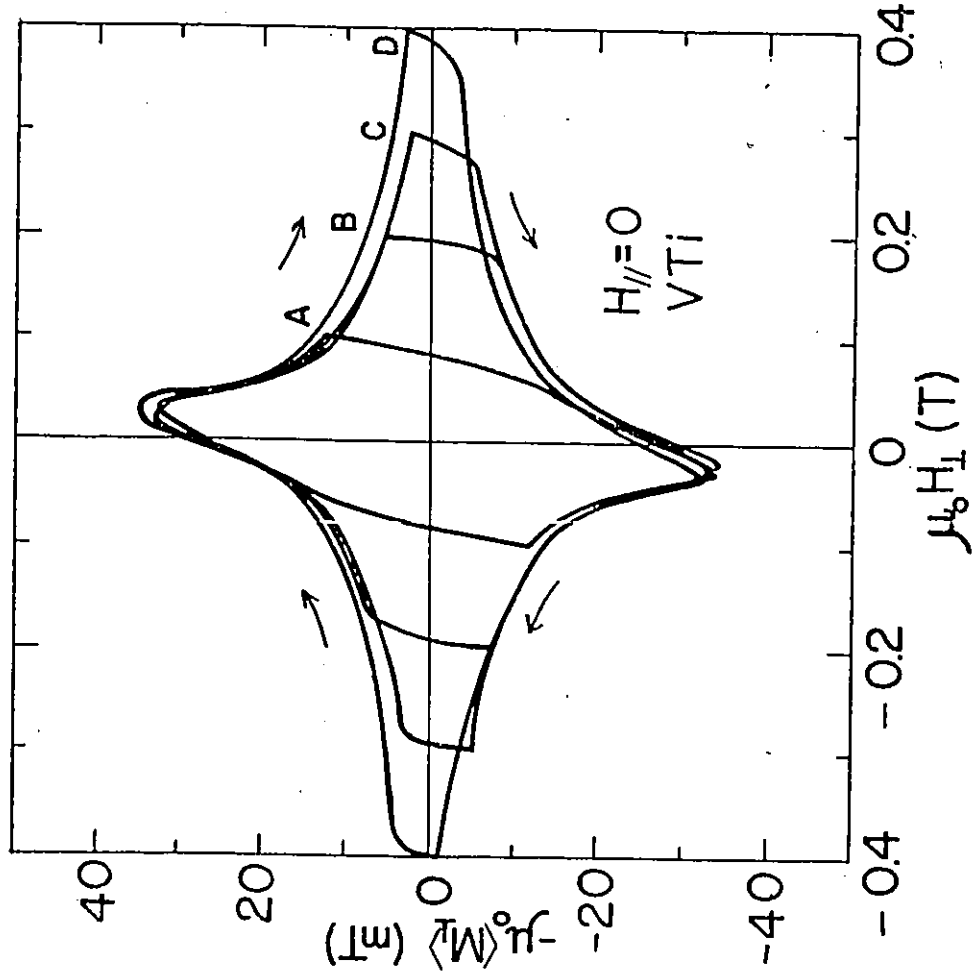

FIG. 4.25 Hysteresis curves $-\mu_o \langle M_\perp \rangle$ vs. $\mu_o H_\perp$ observed with the VTi ribbon in a stationary magnetic field $H_{//} = 0$. The various amplitudes of these full-wave cycles are: h_o = 0.1, 0.2, 0.3 and 0.4 T for curves A, B, C and D respectively.

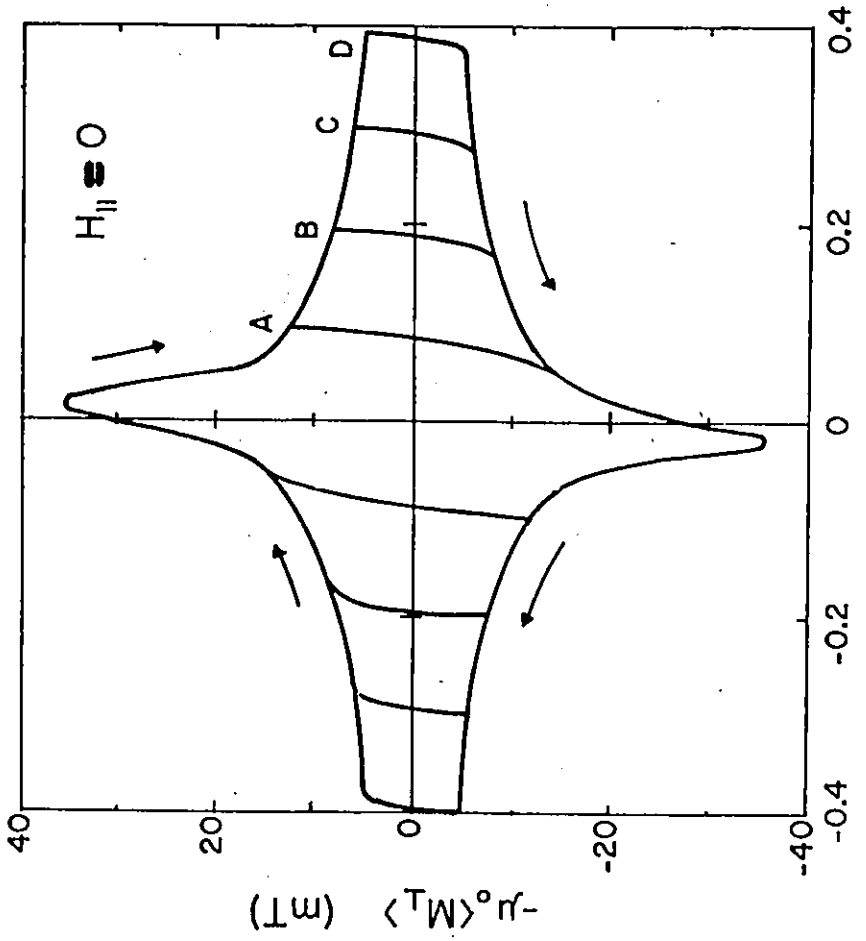

FIG. 4.26 Calculated curves computed with the double critical state model using equation 4.10 and 4.31. Compare with Fig. 4.25.

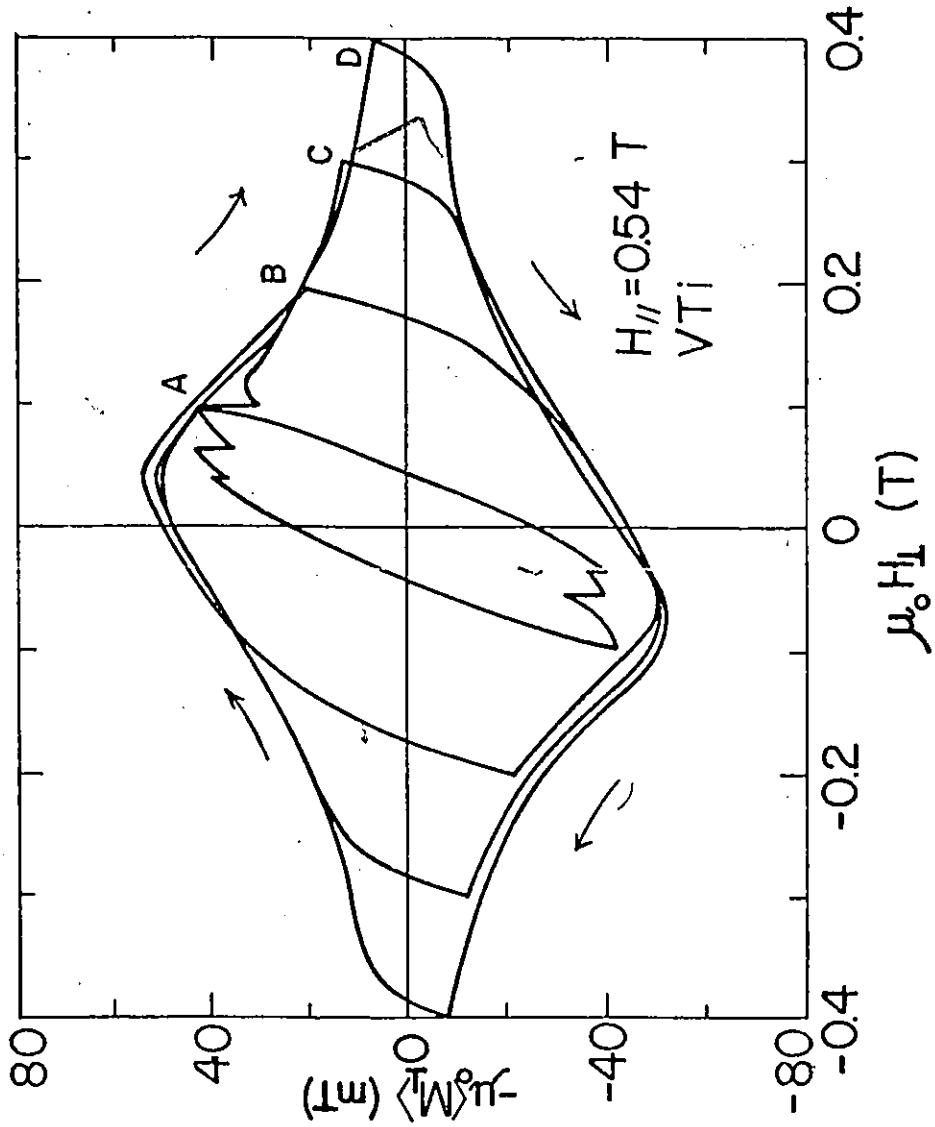

FIG. 4.27 Same as Fig. 4.25 with $H_{//}$ = 0.54 T.

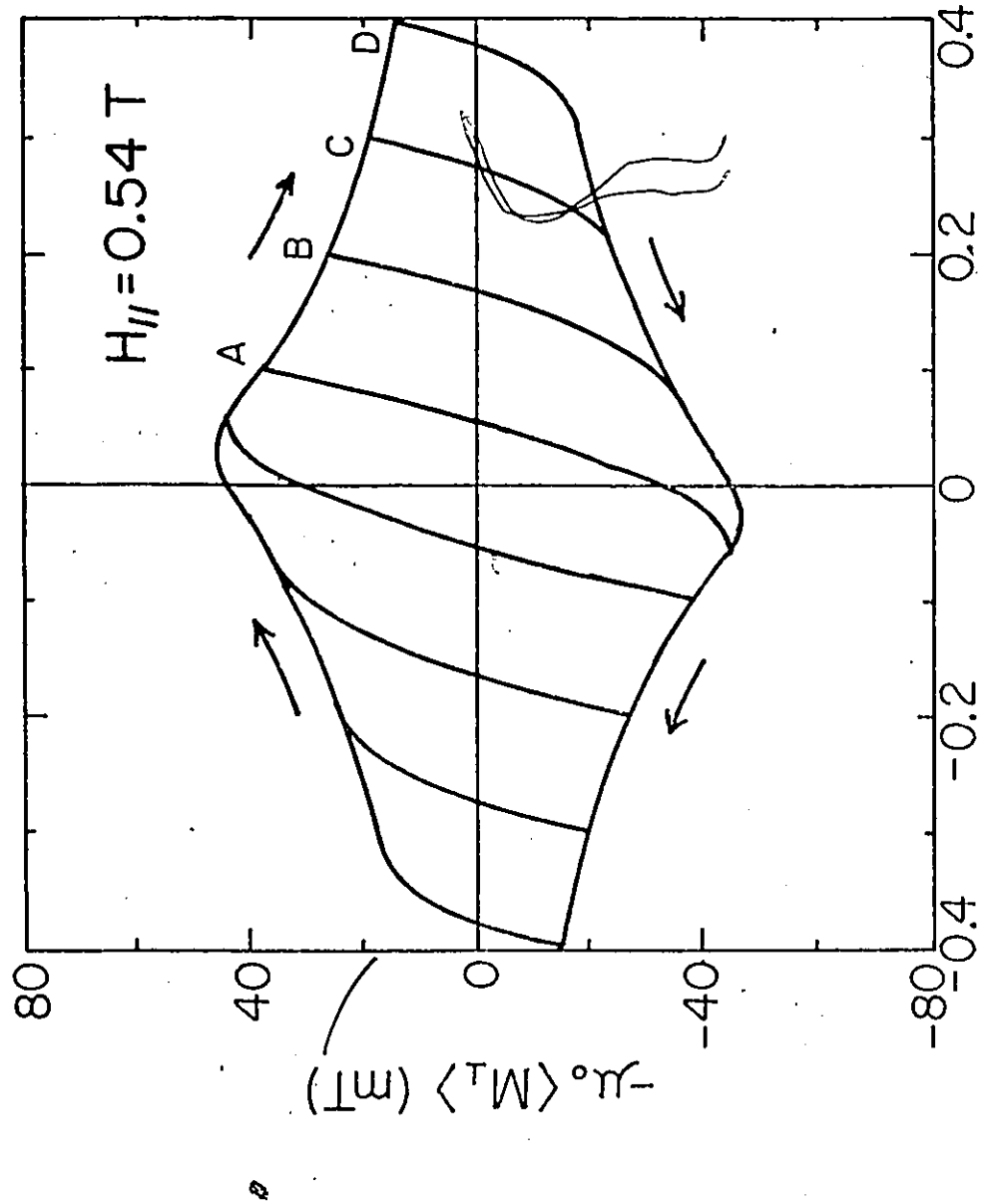

FIG. 4.28 Same as Fig. 4.26 with $H_{//}$ = 0.54 T. Compare with Fig. 4.27.

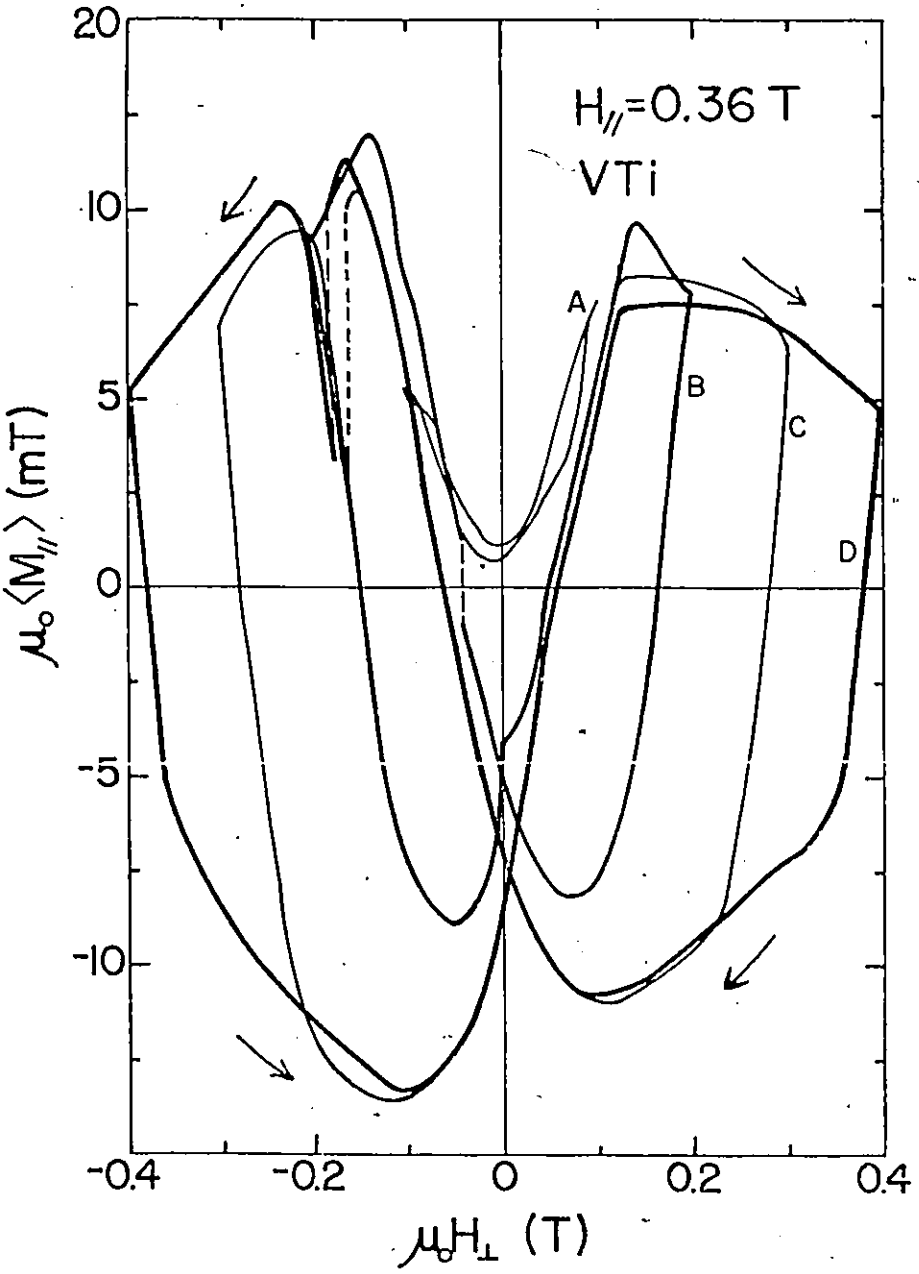

FIG. 4.29 Family of $\mu_o \langle M_{//} \rangle$ vs. $\mu_o H_\perp$ curves observed with the VTi ribbon in a stationary magnetic field $H_{//}$ = 0.36 T. The various amplitudes of these full-wave cycles are: h_o = 0.1, 0.2, 0.3 and 0.4 T for curves A, B, C and D respectively.

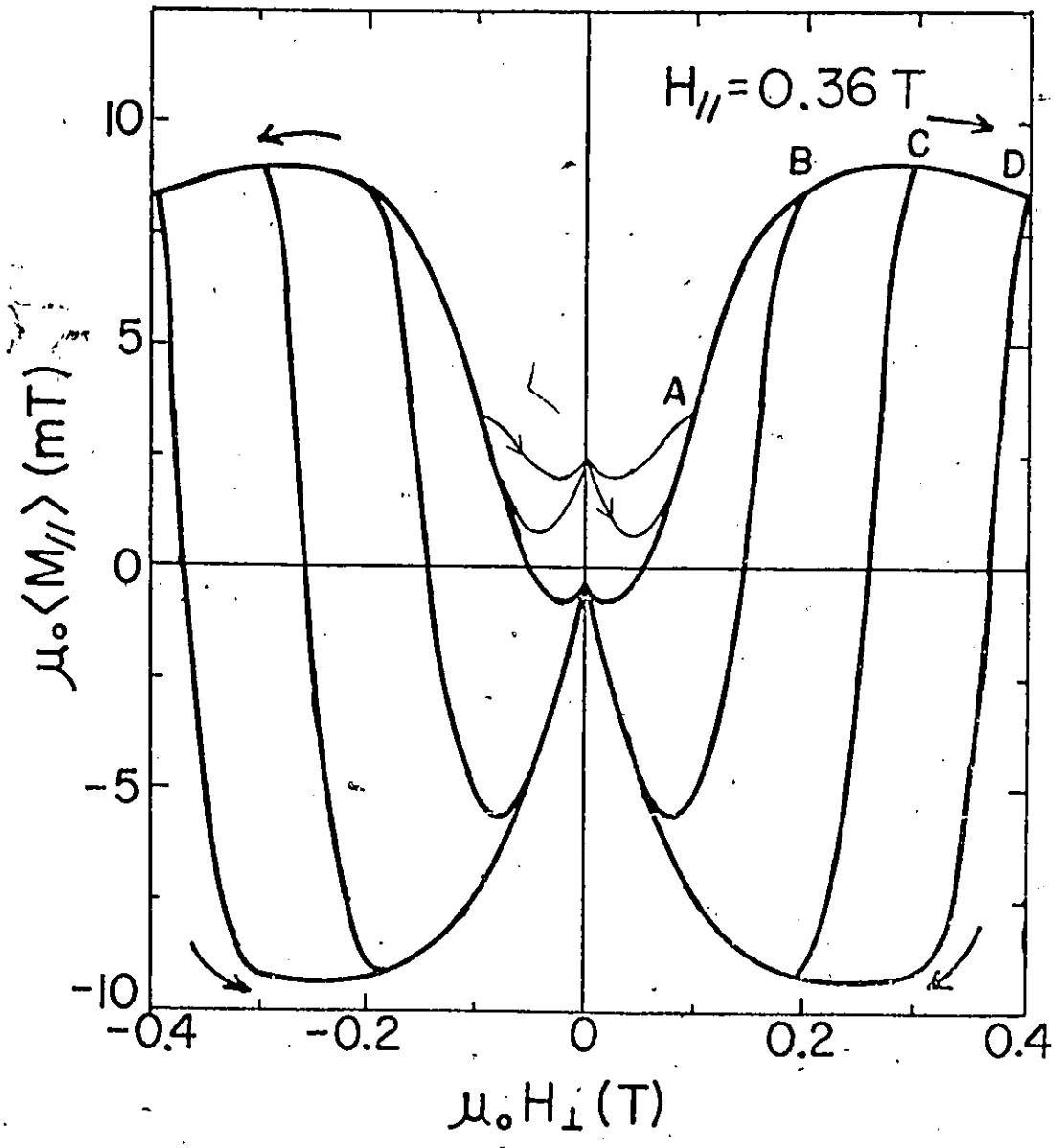

FIG. 4.30 Calculated curves computed with the double critical state model using equations 4.10 and 4.31. Compare with Fig. 4.29.

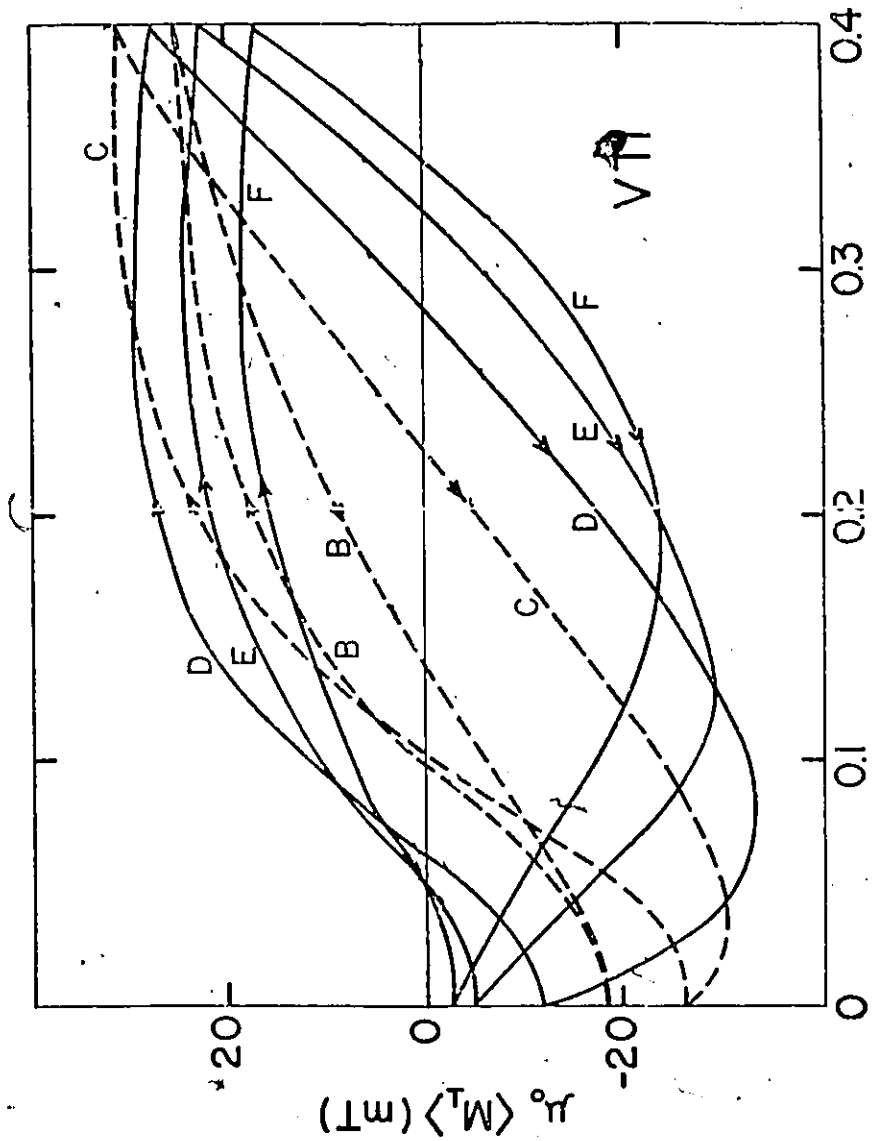

FIG. 4.31 Family of curves $\mu_o \langle M_{\perp} \rangle$ vs. $\mu_o H_{//}$ curves observed with the VTi ribbon. The amplitude of the half-wave cycles is h_o = 0.2 T and the various stationary magnetic fields $H_{\perp}$ = 0.036, 0.072, 0.108, 0.144 and 0.18 T for curves B, C, D, E and F respectively.

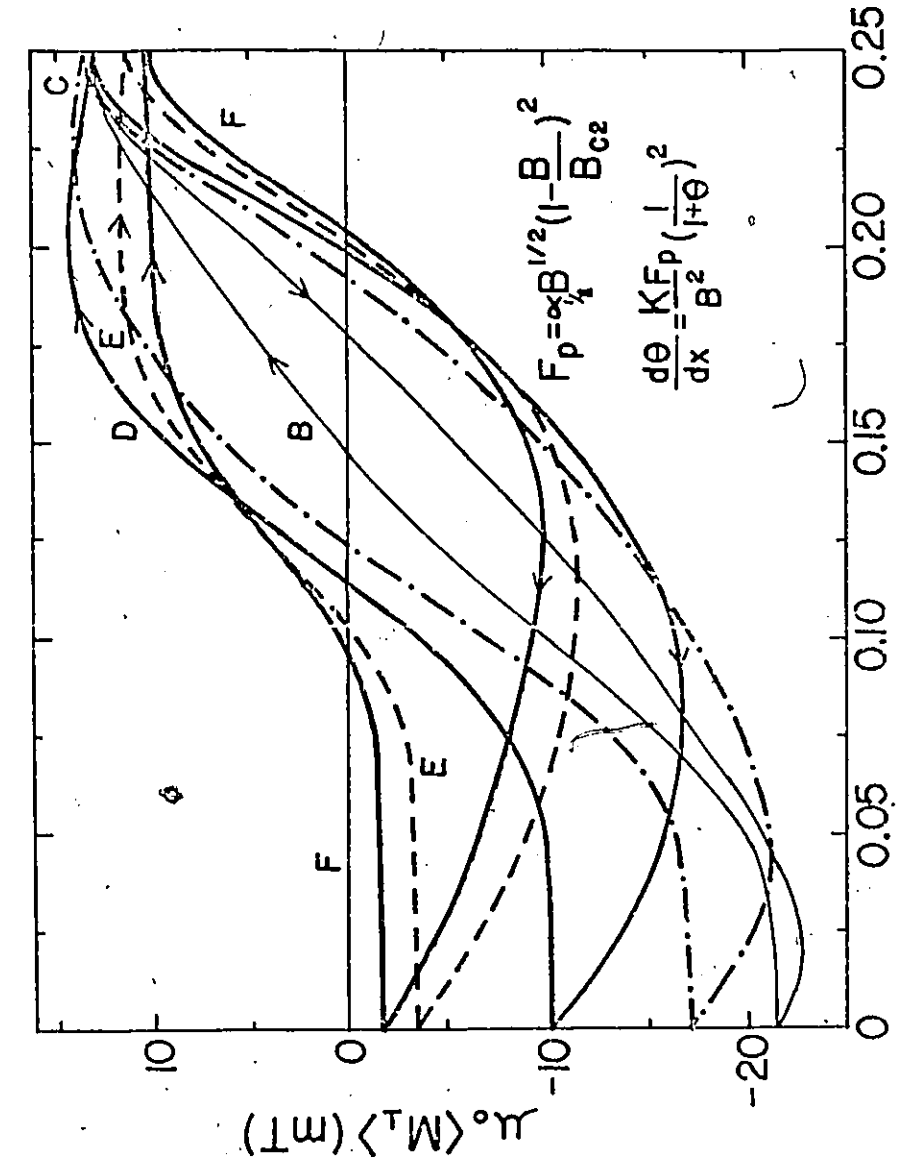

FIG. 4.32 Calculated curves computed with the double critical state model using equations 4.10 and 4.31. Compare "with care" with Fig. 4.31 because the stationary magnetic fields are not in correspondence, H_1 = 0.06, 0.10, 0.15, 0.25 and 0.30 T for curves B, C, D, E and F respectively and the amplitude of the half-wave cycles is h_o = 0.125 T.

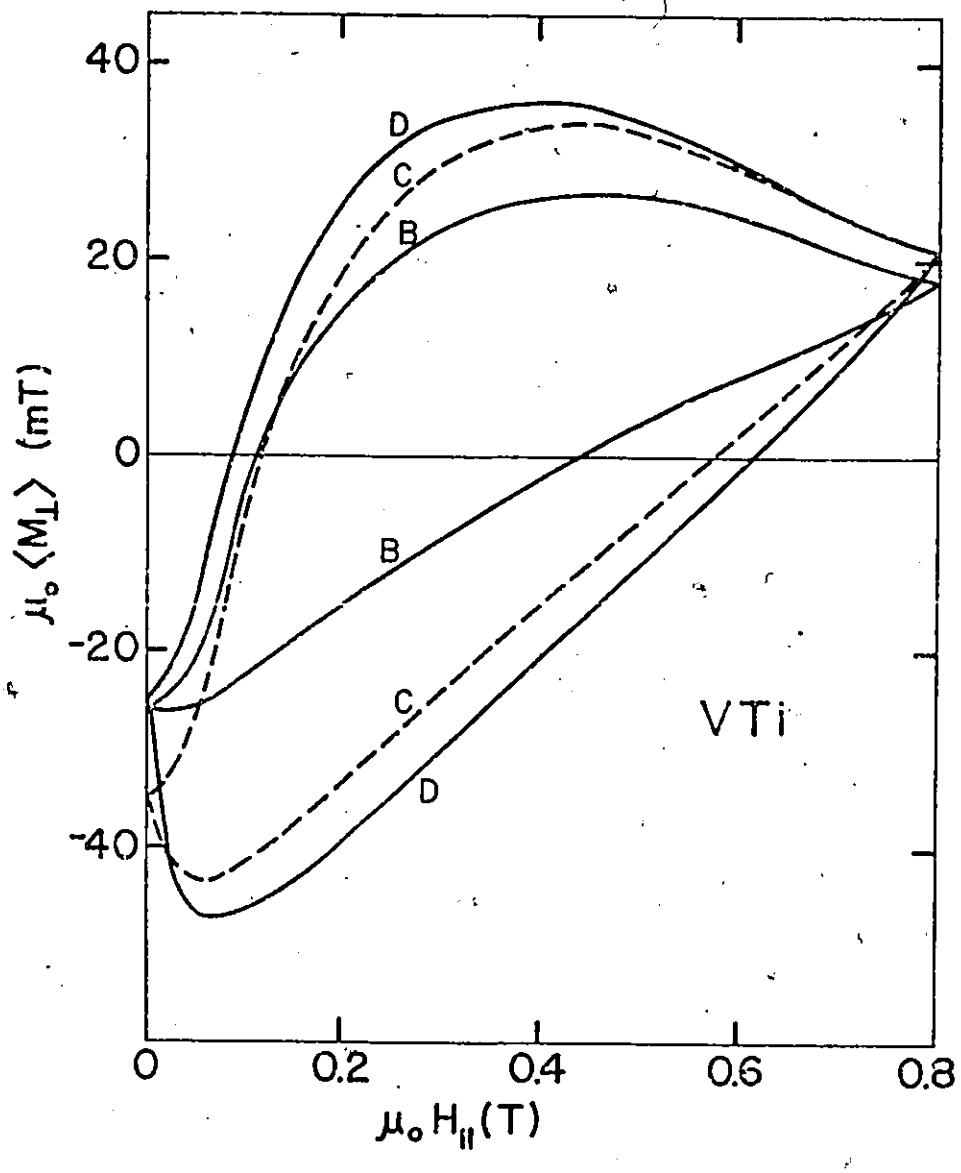

FIG. 4.33 Family of curves $\mu_o \langle M_\perp \rangle$ vs. $\mu_o H_{//}$ curves observed with the VTi ribbon. The amplitude of the half-wave cycles is h_o = 0.4 T and the various stationary magnetic fields are: $H_\perp$ = 0.036, 0.072 and 0.09 T for curves B, C and D respectively.

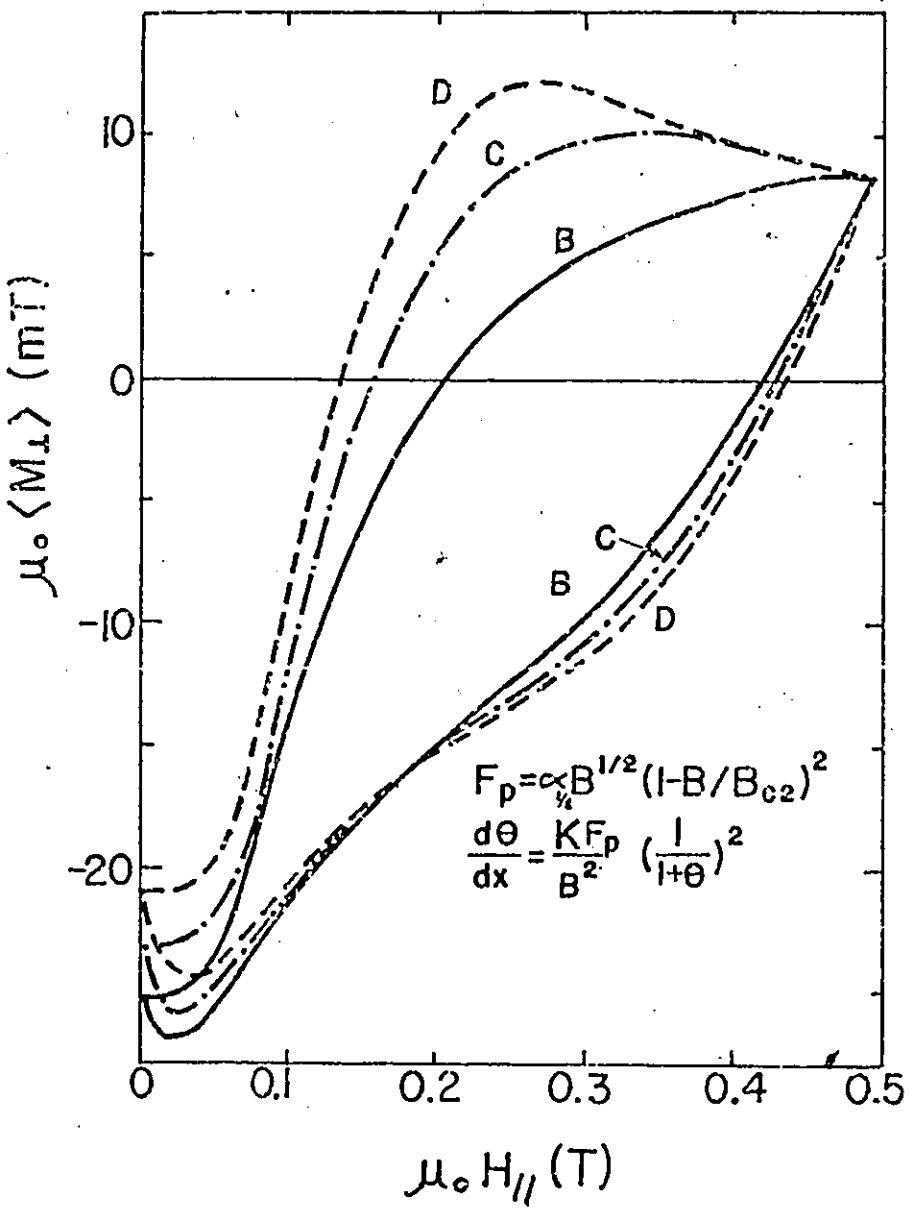

FIG. 4.34 Calculated curves computed with the double critical state model using equations 4.10 and 4.31. Compare "with care" with Fig. 4.33 because the stationary magnetic fields are not in correspondence, H_1 = 0.06, 0.07 and 0.08 T for curves B, C and D respectively and the amplitude of the half-wave cycles is h_o = 0.25 T.

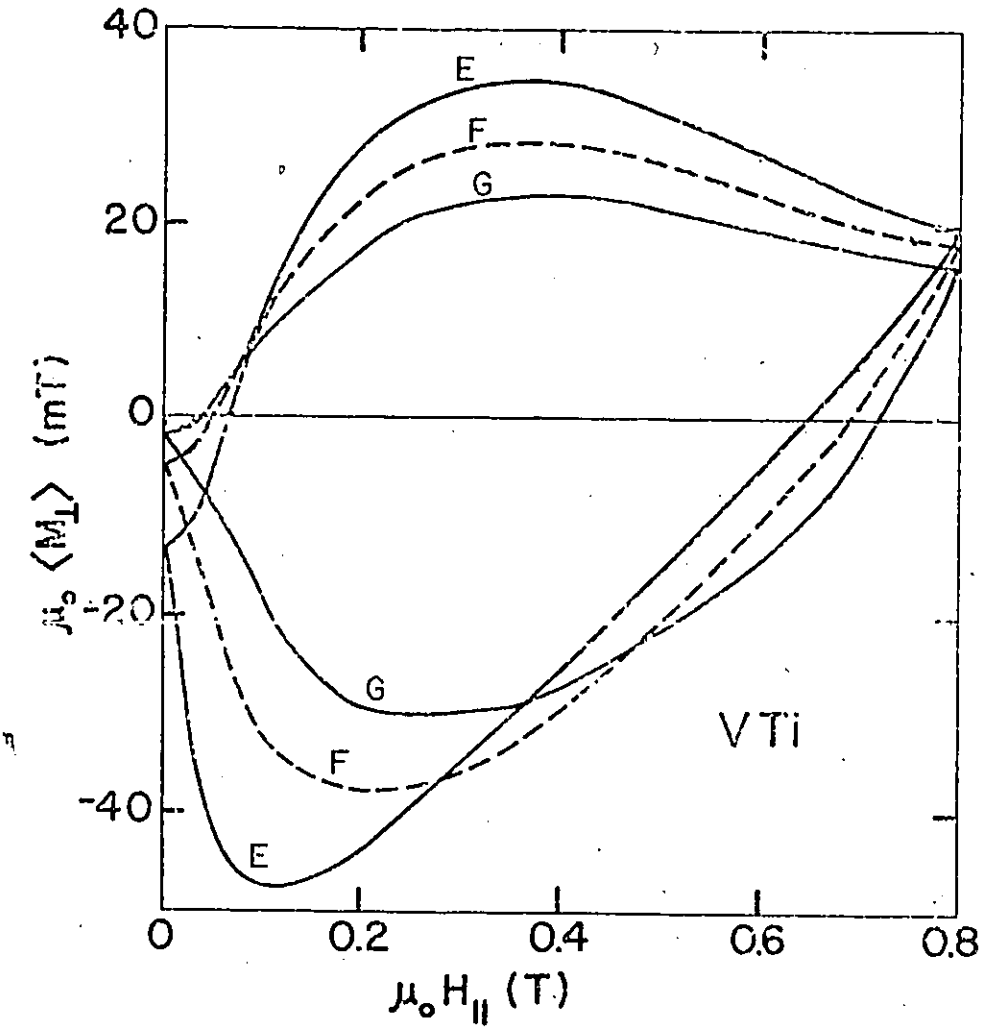

FIG. 4.35 Family of curves $\mu_o \langle M_\perp \rangle$ vs. $\mu_o H_{//}$ curves observed with the VTi ribbon. The amplitude of the half-wave cycles is h_o = 0.4 T and the various stationary magnetic fields are $H_\perp$ = 0.108, 0.144 and 0.18T for curves E, F and G respectively.

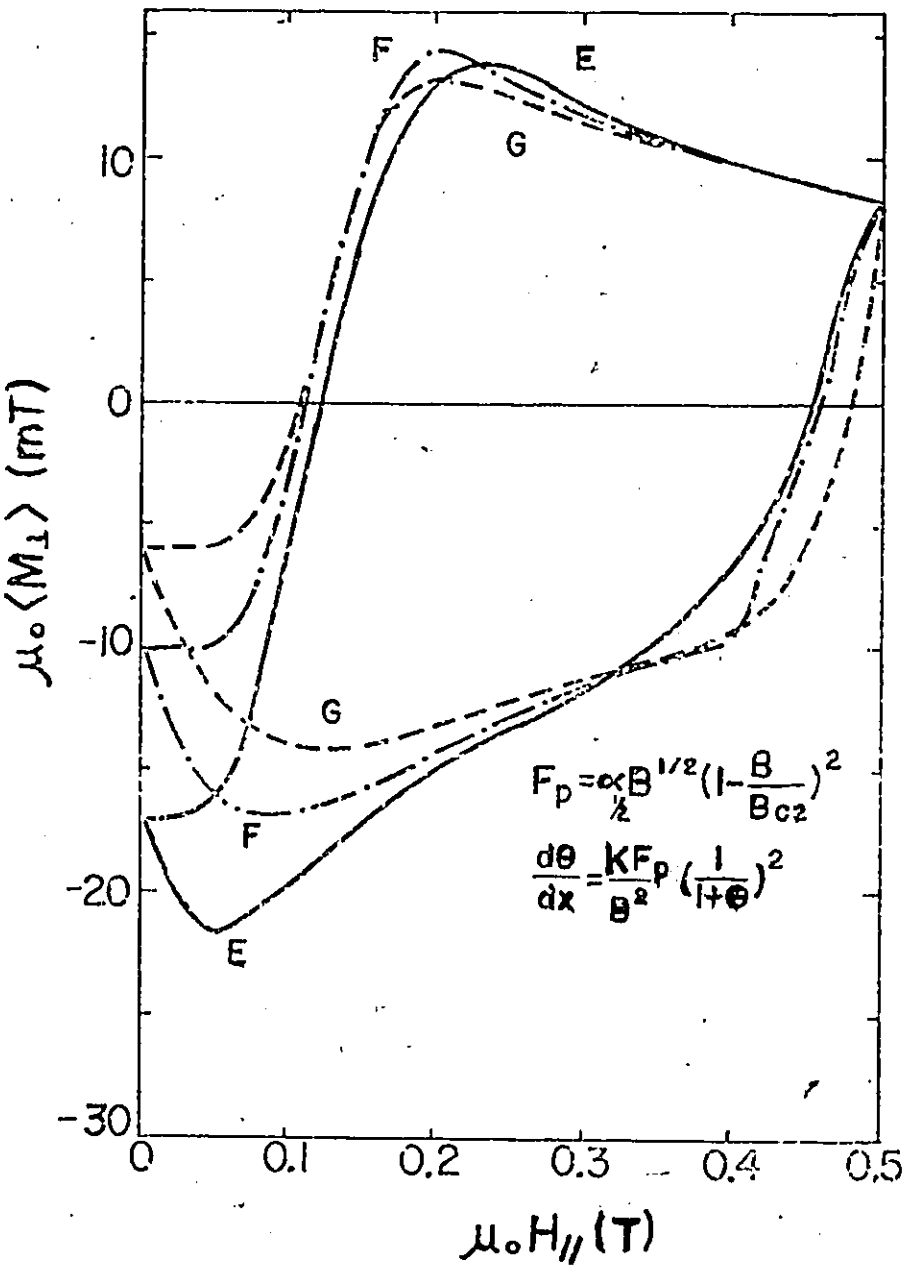

FIG. 4.36 Calculated curves computed with the double critical state model using equation 4.10 and 4.31. Compare "with care" with Fig. 4.35 because the stationary magnetic fields are not in correspondence, H_1 = 0.10, 0.15 and 0.20 T for curves E, F and G respectively and the amplitude of the half-wave cycles is h_o = 0.25 T.

CHAPTER 5

HYSTERESIS LOSSES IN THE COLLINEAR REGIME

5.1 INTRODUCTION

Recently workers have reported the discovery that hysteresis losses in type II superconductors subjected to a periodically varying magnetic field of chosen amplitude h_o, directed parallel to the broad surface of the specimen, initially decrease, traverse a minimum and then rise, hence trace a valley, when a static bias magnetic field H_b is impressed collinearly with h_o. Clem has investigated this phenomenon systematically and phenomenologically in the framework where (i) bulk pinning, (ii) equilibrium diamagnetism and (iii) surface barriers to entry and exit of flux, are taken into account. His survey reveals that a minimum occurs in most circumstances where realistic approximations are exploited to describe these various quantities. In particular, he notes that the B dependence of the bulk pinning alone can yield a minimum. Further, with the pinning function chosen in his study he finds that the minimum occurs when $H_b \approx 2h_o/3$.

In this chapter we report on our measurements of this Clem valley at various amplitudes in our ribbon sample of VTi. Since the specimen shows significant anisotropy, we have explored the behaviour of the hysteresis losses, with the collinearly superimposed h_o and H_b directed along the length of the ribbon and also along its width.

We compare our data with the predictions of the critical state model neglecting surface barriers and reversible shielding currents. This

approach was adopted for simplicity and in view of the success previously achieved in analysing magnetic phenomena in this material in this bare context. In the light of the remarkably good correspondence between data and calculations provided by this rudimentary framework we deemed it instructive to pursue in some detail the behaviour predicted for, a) the structure of the valleys and b) the evolution of H_b where the minimum occurs as a function of (i) the amplitude h_o, (ii) the characteristics of the bulk pinning and (iii) the geometry, always in this simple context.

The results of these computations are of intrinsic interest. Further, a knowledge of the effect of changes in the character of the B profiles and of the choice of geometry should prove useful in assessing the contributions of surface barriers and reversible surface shielding currents to the behaviour encountered in various materials. Our results provide a background for more sophisticated analysis where these additional features, as in Clem's work, are taken into account.

The appearance of a minimum in the A.C. losses may prove significant in the exploitation of these materials in the technological applications of type II superconductors.

5.2 EXPERIMENTAL RESULTS AND DISCUSSION

In Fig. 5.1 we display the magnetization curve of the ribbon of VTi measured when the applied magnetic field increasing from zero is directed along the length and along the width of the ribbon (upper and lower curves respectively). The difference between the two measured curves may be attributed to the demagnetization factors and the material

anisotropy.

Boyer observed anisotropy in the magnetic behaviour of a disk of VTi cut from the same ingot from which our ribbon sample was obtained. In his work the magnetization was measured with the magnetic field directed along various diameters of the disk, hence the demagnetization factor is the same for his several data curves. The maximum and minimum magnetization curves occur for two diameters orthogonal to each other and the deviation he observes is comparable to that which we encounter. We consequently ascribe the deviation between the two solid curves in Fig. 5.1 mainly to anisotropy. The degree to which this assignation is correct, is not germane to the purpose of the present investigation.

The dashed curves in Fig. 5.1 were calculated exploiting the well established idea that wherever a gradient in the magnetic flux density is made to arise, it exists in a critical state. For planar geometry, taking the magnetic induction to be directed along the z-axis, the critical gradients at a constant temperature can be written

$$\frac{dB}{dx} = \pm \frac{F_p(B)}{B} \tag{5.1}$$

where the subscript z is omitted and $F_p(B)$ is regarded as the bulk pinning function characterizing the given sample. For simplicity and as a first approximation we make use of the boundary condition,

$$B_s = \mu_o H_o \tag{5.2}$$

where B_s is the density of flux lines in the vicinity of the surface and

H_o is the applied magnetic field. This means that we ignore the possible existence of a surface step or a discontinuity in the magnetic induction which could arise from the presence of reversible surface shielding (Meissner)currents and the operation of a surface barrier against flux entry.

Guided by other investigations on this material we choose the simple analytic expression

$$F_p(B) = \alpha_{1/2} B^{1/2} \left(1 - \frac{B}{B_{c2}}\right)^2 \tag{5.3}$$

for the pinning function. Equation 5.1 then reads

$$\frac{dB}{dx} = \pm \frac{\alpha_{1/2}}{B^{1/2}} \left(1 - \frac{B}{B_{c2}}\right)^2 \tag{5.4}$$

A useful measure of the magnitude of magnetic inductions in this study is the magnetic induction at the surface of the slab (or cylinder) when the B profile drops to zero exactly at the midplane (or axis). Let $B_* = \mu_o H_*$ denote this quantity. Taking B_{c2} as infinite, equation 5.4 leads to

$$B_* = \left(\frac{3}{2} \alpha X\right)^{2/3} = \left(\frac{3}{2} \alpha R\right)^{2/3} \tag{5.5}$$

where X is the half thickness of the slab and R the radius of the cylinder. The upper and lower dashed curves in Fig. 5.1 were calculated taking $B_* = 0.06$ and 0.05 T respectively and $B_{c2} = 4$ T.

The data points in Figs. 5.2 and 5.3 present hysteresis losses, W, measured at four different amplitudes $h_o \lesssim H_*$ as a function of the collinear bias magnetic field H_b applied along the length and width of the ribbon respectively. The solid curves in Figs. 5.2 and 5.3 were calculated using a simplified version of equation 5.4, namely

$$\frac{dB}{dx} = \pm \frac{\alpha_{1/2}}{B^{1/2}} \tag{5.6}$$

which we refer to as the Yasukochi approximation. For the range of magnetic inductions under consideration here, the term $(1 - B/B_{c2}) \approx 1$ since $B_{c2} \gtrsim 4$ T and the results of the calculations with equations 5.4 and 5.6 almost overlap. The simpler form is more convenient for the investigation we pursued.

Figures 5.4, 5.5 and 5.6 display hysteresis loops observed at one chosen amplitude (h_o = 0.05 T) with the collinear bias field directed along the length of the ribbon and chosen such that the locus of W versus H_b (see upper data curve of Fig. 5.2) is located at the start of the valley (H_b = 0), near its minimum (H_b = 0.04 T) and near the top of the peak on the right hand side (H_b = 0.09 T). The solid curves are experimental and the dashed curves are calculated using equation 5.6.

We have developed a computer program which starting with arbitrary formulae for the B dependence of dB/dx, (i) generates sequences of B profiles as $H_o = H_b + h_o f(t)$ undergoes cyclical sweeps, where f(t) varies between ±1 and ∓1, (ii) computes <B>, the spatial average of the series of B profiles for planar and cylindrical geometry, (iii) determines $\Delta\langle B\rangle/\Delta\mu_o H_o$ versus H_o and (iv) calculates the area enclosed by the

locus of <B> vs. H_o (the hysteresis loop), hence,

$$W(h_o, H_b) = \oint H_o \, \Delta\langle B\rangle = \oint \langle B\rangle \, dH_o. \tag{5.7}$$

The energy dissipated per cycle per unit volume. The computer program has been verified as follows. (a) By comparing its results in the limit where $H_b = 0$ with separate calculations using closed form expressions derived by Dunn and Hlawiczka for pinning functions of the form $F_p = \alpha_n B^n$. (b) By comparing its predictions with calculations using the analytic expression for $W(h_o, H_b)$ developed in appendix III for the case where $dB/dx = \alpha_o/B$ (the Kim-Anderson approximation) and the amplitude of the oscillations does not cause the front of the disturbance in the B profile to penetrate to the midplane. We refer to this range of amplitudes as lying below saturation.

The correspondence between observations and calculations in Fig. 5.2 through 5.6 is remarkable considering that the presence of a surface step has been ignored in the analysis whereas the data spans the low field range where reversible shielding currents and surface barriers are expected to play a significant role.

The agreement is not entirely fortuitous. In principle, $dB(B)/dx$, $\Delta B_{in}(B)$ and $\Delta B_{out}(B)$, the surface steps during flux entry and exit, can be extracted from the magnetization data. In view of the number of unknown quantities, it is necessary to exploit several distinct pieces of information in this analysis; namely (i) <M> versus H_o increasing, (ii) <M> versus H_o decreasing, (iii) <M> versus H_o increasing in a positive (negative) sense after traversing zero and starting from a high

negative (positive) value, and (iv) <M> generated by flux expulsion as the sample cools through T_c to 4.2 K in various stationary H_o. Boyer has pursued this task and extracted these quantities for the VTi disk mentioned above. He finds that dB(B)/dx is well reproduced by equation 5.6 and that the surface steps are only a small fraction of B_* in this material (< 1/10).

It is noteworthy that once the choice for $F_p(B)$ is made in the calculations, the good agreement with the set of data taken along the length of the ribbon and along its width is achieved simply by adjusting the pinning strength parameter α, hence the full penetration magnetic field H_*. This supports the view that the difference between the two sets of data arises mainly from anisotropy in the bulk pinning.

5.3 EFFECT OF $F_p(B)$ AND GEOMETRY ON THE VALLEY

In view of the results just presented where, by exploiting bulk pinning only and neglecting other basic elements of the complete picture, a good description of observation was obtained, we considered it worthwhile to retain this simple format and explore the effect of $F_p(B)$ on the structure of the valley. An important aspect of the structure of the valley is $H_{b\,min}$, the bias magnetic field where the minimum in $W(h_o, H_b)$ versus H_b occurs. Clem has already examined this feature in the same simple framework which we exploit and noted that $H_{b\,min}/h_o \approx 2/3$ when

$$\frac{dB}{dx} = \pm \frac{\alpha}{B + \Delta} \tag{5.8}$$

where Δ is an adjustable parameter. To avoid all complications, in our study, we focus on the simplest form of this formula, namely,

$$\frac{dB}{dx} = \pm \frac{\alpha_o}{B} \tag{5.9}$$

which we will denote as the Kim-Anderson approximation.

Here

$$H_* = \sqrt{2\alpha_o X} = \sqrt{2\alpha_o R}$$

We have calculated the evolution of $H_{b\,min}$ as the amplitude h_o increases (i) for both planar (infinite slab) and cylindrical geometry, (ii) using the Yasukochi (eqn. 5.6) and the Kim-Anderson (eqn. 5.9) approximations. The results of these calculations are displayed in Fig. 5.7 and 5.8. The choice between the two geometries brings about a greater separation between the curves for a given form of pinning than the change in the latter for a chosen geometry. The locus of $H_{b\,min}$ versus h_o is nearly linear, (a) in the range of small amplitudes ($h_o/H_* \gtrsim 0.5$) for slab geometry when the Yasukochi approximation is used and here $H_{b\,min} \approx 0.7\ h_o$ and (b) in the range of large amplitudes ($h_o/H_* \gtrsim 1.0$) for slab and cylinder geometry for both forms of $F_p(B)$ with $H_{b\,min} \gtrsim 0.9\ h_o$. For slab geometry, a noticeable inflection point occurs with both forms of $F_p(B)$ when $h_o/H_* \gtrsim 1.0$.

The contour of the valley is seen to change as the amplitude increases, with the left hand slope becoming steeper and the right hand peak less prominent. Eventually the valley is only a depression on the side of a hill (see Fig. 5.3). This depression becomes imperceptible and

for practical purposes has vanished when $h_o/H_* > 2$ for slab geometry with both forms of $F_p(B)$. The transformation of the valley into a dip on the side of a hill as h_o/H_* increases occurs at smaller h_o/H_* with the Kim-Anderson approximation than with the Yasukochi approximation This can be seen by comparing Figs. 5.2 and 5.9. The transformation of the valley into a dip on the side of a hill also occurs at smaller h_o/H_* for cylindrical geometry than for slab geometry. This is illustrated in Fig. 5.10 where $W(h_o, H_b)/W(h_o, 0)$ versus H_b/H_* is compared at $h_o/H_* = 0.8$ for slab and cylinder geometry, taking $dB/dx = \alpha_{1/2}/B^{1/2}$ (Yasukochi approximation).

An interesting case in the spectrum of pinning functions of the form, $F_p = \alpha_n B^n$ is that where $n = 1$, hence $dB/dx = \pm\alpha_1$. This is denoted the Bean-London approximation. With this approximation, $W(h_o, H_b)$ for a chosen amplitude is independent of H_b, hence no valley occurs. This result can be seen without performing any calculations. The locus of $\langle B \rangle$ versus H_o can be easily sketched from consideration of the sequences of B profiles during the oscillation of H_o when $H_b = 0$. We now note that since dB/dx is constant, the hysteresis loop is simply displaced without alteration when H_b is impressed. A shallow valley will appear however, if the B profiles are given a curvature convex away from the $B = 0$ horizontal line. This can be accomplished by multiplying the Bean-London pinning function by a function of B/B_{c2} which decreases monotonically to zero as B/B_{c2} goes to unity. A straightforward choice is that where

$$F_p(B) = \alpha_1 B\left(1 - \frac{B}{B_{c2}}\right) \tag{5.10}$$

We have pursued this particular case, taking $B_{c2}/B_* = 5$. The results are displayed in Fig. 5.11 where $H_* = \alpha X = \alpha R$. We note that for planar geometry, $H_{b\,min}$ versus h_o is linear when $h_o \lesssim 0.8\ H_*$ and here $H_{b\,min} = h_o/2$. In the range $0.8 < h_o/H_* < 1$, the behaviour of $H_{b\,min}$ versus h_o becomes nonlinear. In this range, as h_o/H_* approaches unity, the valley, however becomes too shallow to be meaningful. For cylindrical geometry, $H_{b\,min}$ versus h_o shows no linear behaviour.

5.4 SUMMARY AND CONCLUSION

The hysteresis losses, $W(h_o, H_b)$, in a VTi ribbon measured at various amplitudes h_o of an oscillating external magnetic field as a function of a static bias magnetic field H_b collinear with h_o, exhibit a valley. The hysteresis loops and the valleys are well accounted for exploiting the simple formula, $dB/dx = \pm\alpha_{1/2}/B^{1/2}$, denoted the Yasukochi approximation, to generate the sequences of critical B profiles. The existence of a B dependent surface step during the entry and exit of flux is ignored in the analysis. In the light of the success of this approach we pursue this simple framework, which focuses only on the role played by the form of the B profiles, to investigate $W(h_o, H_b)$ versus H_b computationally for planar and cylindrical geometry. We examine the behaviour taking $dB/dx = \pm\alpha_o/B$ (the Kim-Anderson approximation) and $dB/dx = \pm\alpha_1(1 - (B/B_{c2}))$ (a modified Bean-London approximation) as well as the Yasukochi approximation. We explore the phenomena for the range of amplitudes and bias fields lying below saturation and also beyond this range. Since experimental workers have sought to extract linear dependences of $H_{b\,min}$, the bias magnetic field where the bottom of a

valley occurs, on h_o, from their data, we scrutinize our computed results for the appearance of such linear behaviour. This occurs over various ranges of $H_{b\,min}$ which depend on the geometry and the bulk pinning function.

In various applications of type II superconductors with alternating fields or alternating currents, it is desirable to operate in the vicinity of the minimum. Our survey provides a rough guide for this purpose.

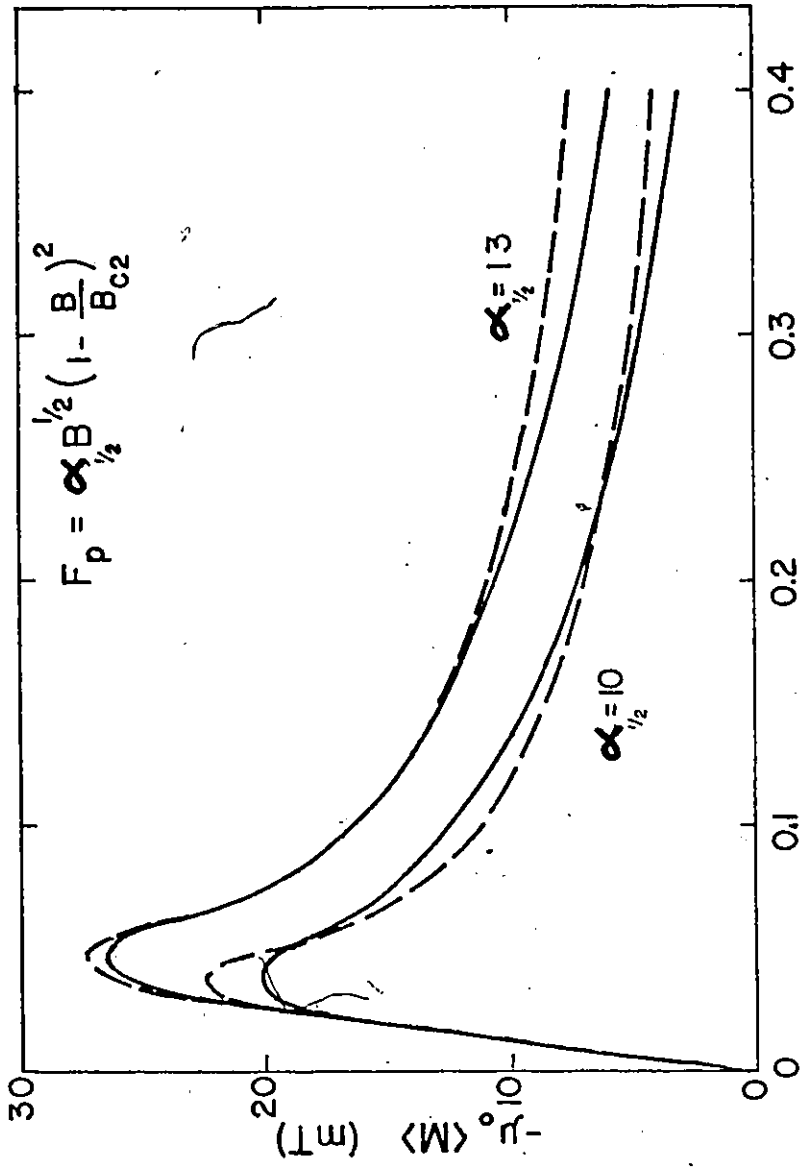

FIG. 5.1 Magnetization curve of the VTi ribbon measured when the applied magnetic field is directed along the length (upper curve) and along the width of the ribbon (lower curve). The dashed curves were calculated using equation 5.3, taking $B_* = 0.06$ and 0.05 T for the upper and lower curves respectively and $B_{c2} = 4$ T.

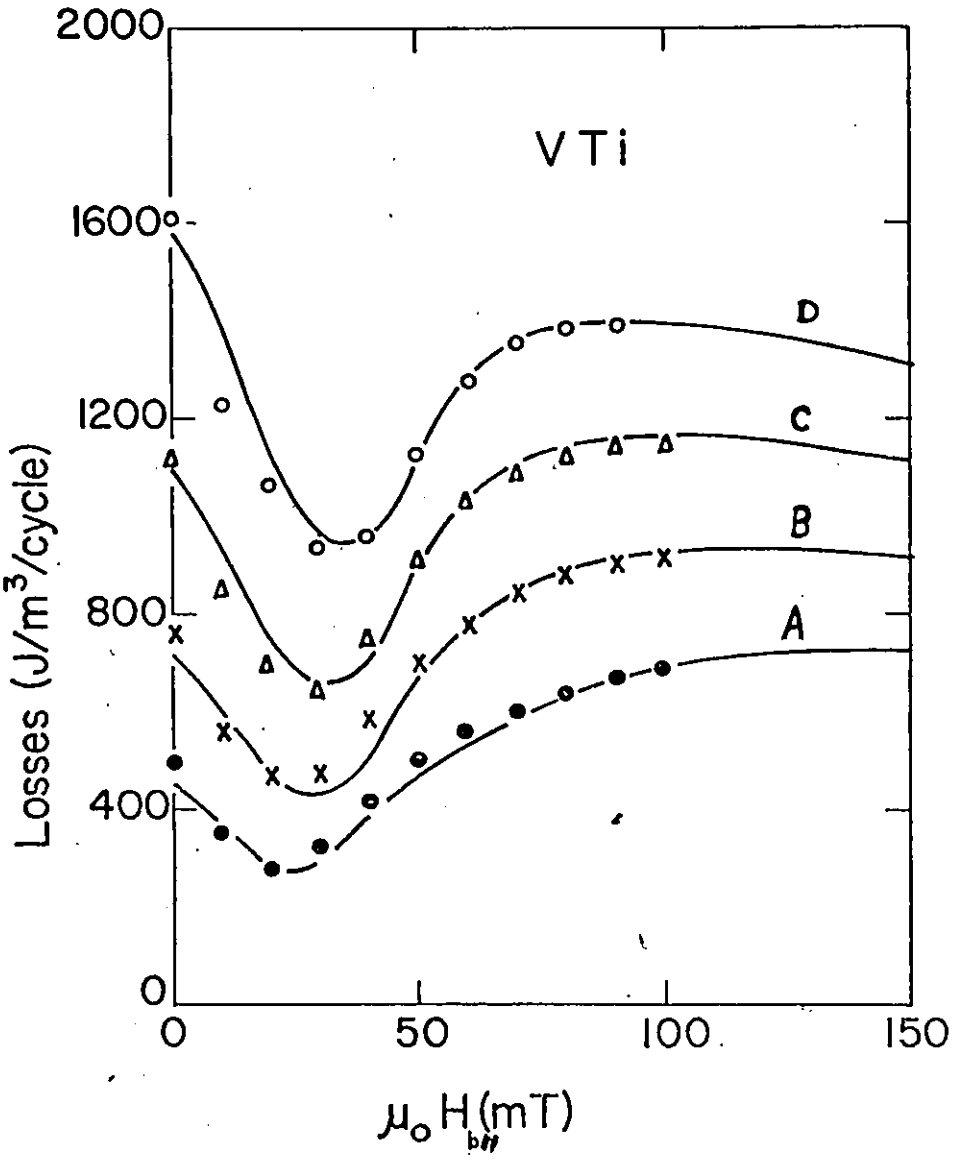

FIG. 5.2 Hysteresis losses measured on the VTi ribbon at four different amplitudes: h_o = 35, 40, 45 and 50 mT for curves A, B, C and D respectively as function of the collinear bias magnetic field applied along the length of the ribbon. The solid curves are calculated using equation 5.6.

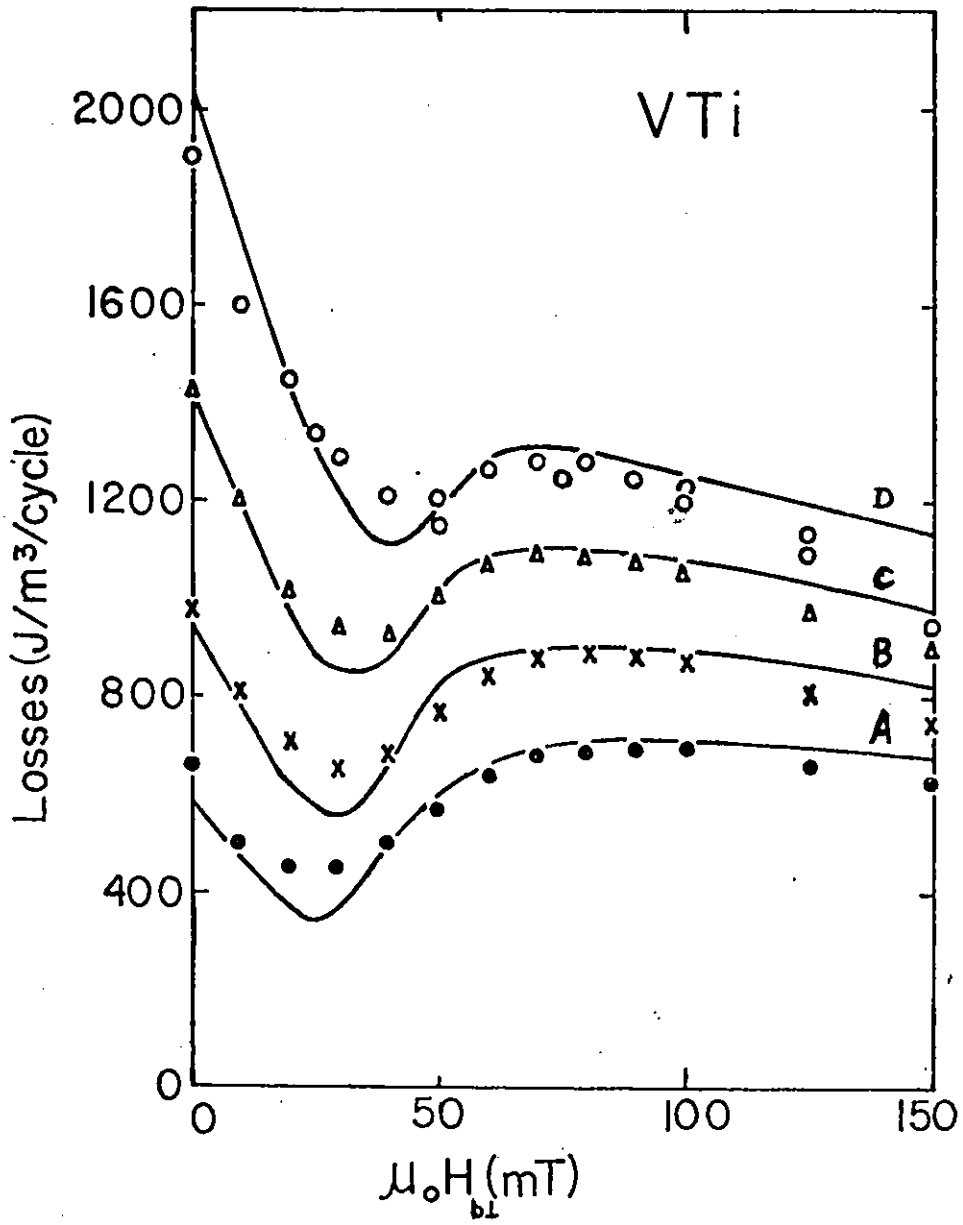

FIG. 5.3 Same as Fig. 5.2, except that the bias magnetic field is now applied along the width of the ribbon.

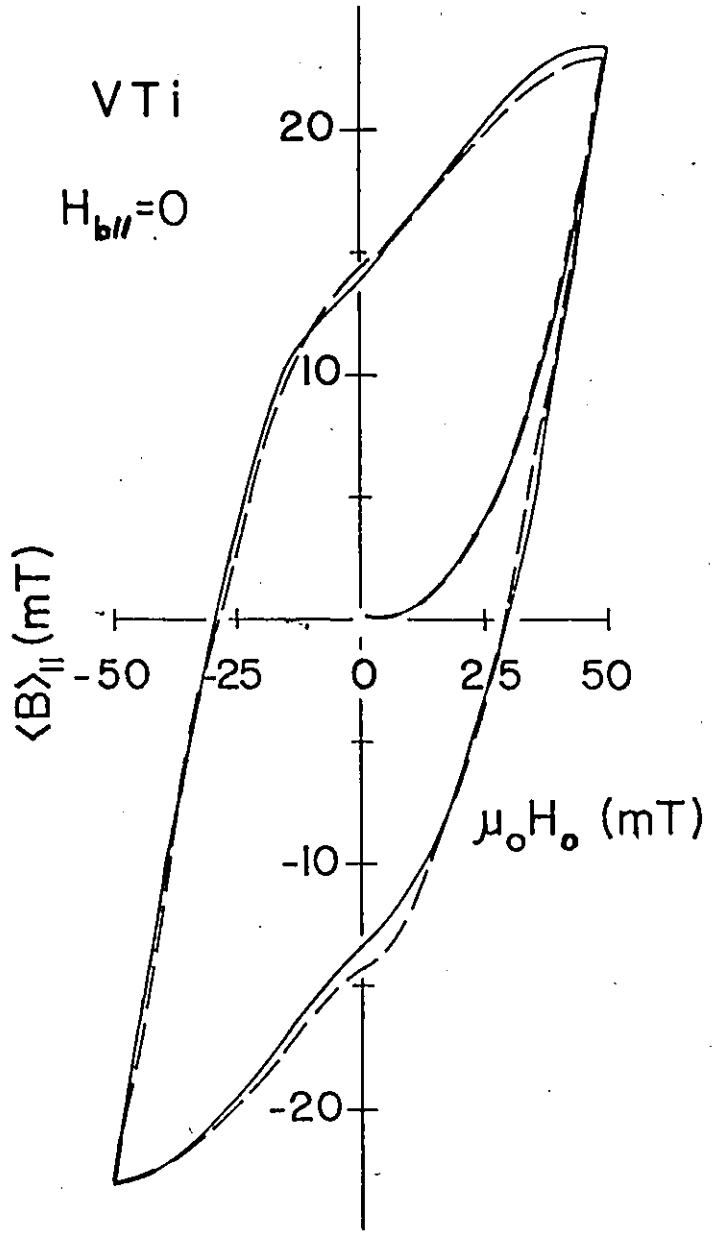

FIG. 5.4 Hysteresis loops observed at an amplitude h_o = 0.05 T with the collinear bias field directed along the length of the ribbon. Here the bias magnetic field is chosen at the start of the valley (H_b = 0) in the upper curve of Fig. 5.2. The solid curve is experimental and the dashed curve is calculated using equation 5.6.

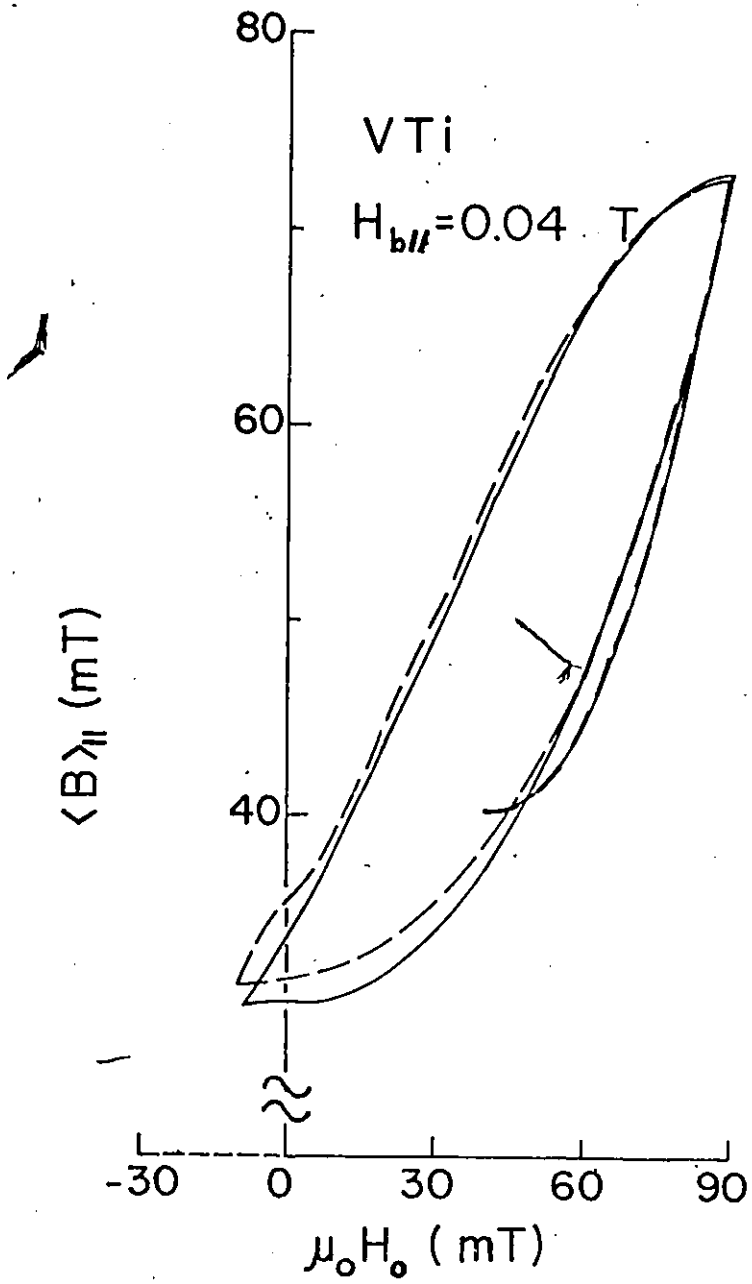

FIG. 5.5 Same as Fig. 5.4 with the collinear bias field chosen near the minimum of the valley, H_b = 0.04 T.

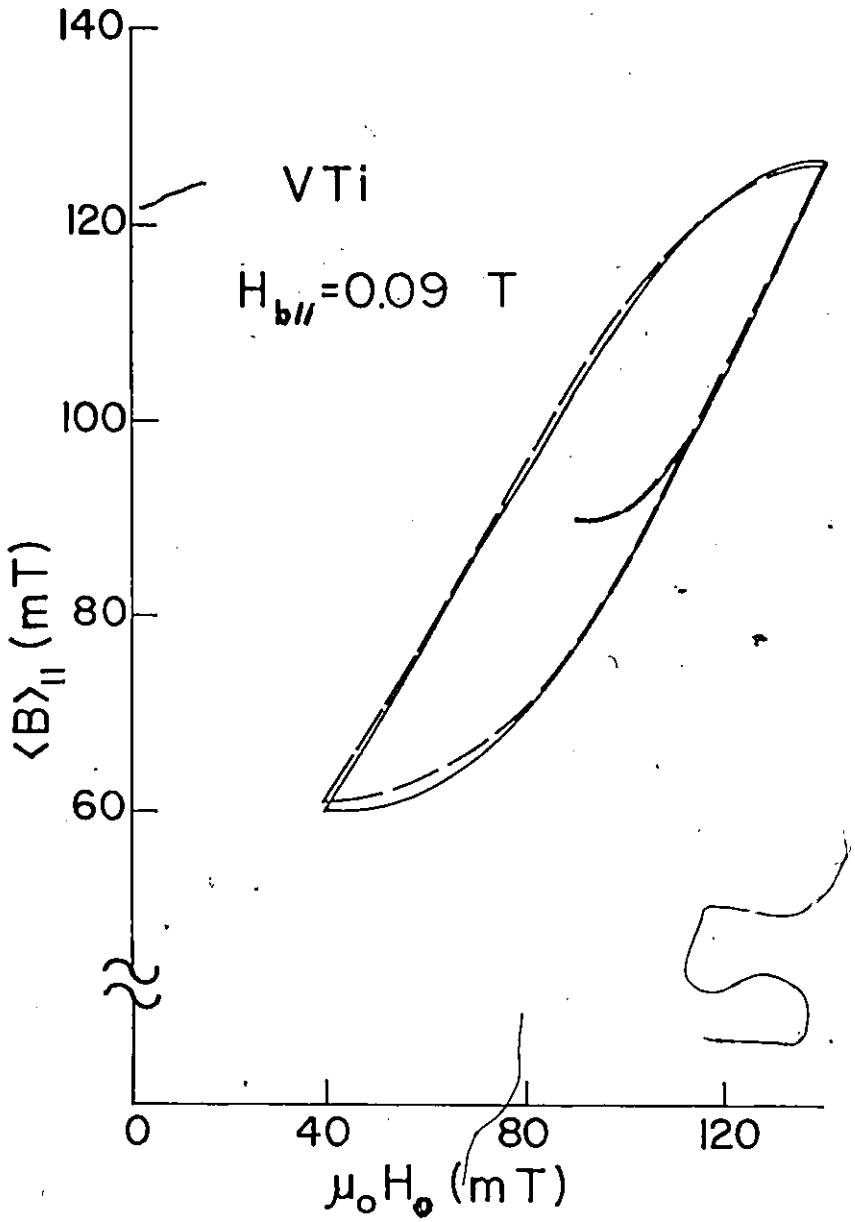

FIG. 5.6 Same as Fig. 5.4 with the collinear bias field chosen near the top of the peak on the right hand side, H_b = 0.09 T.

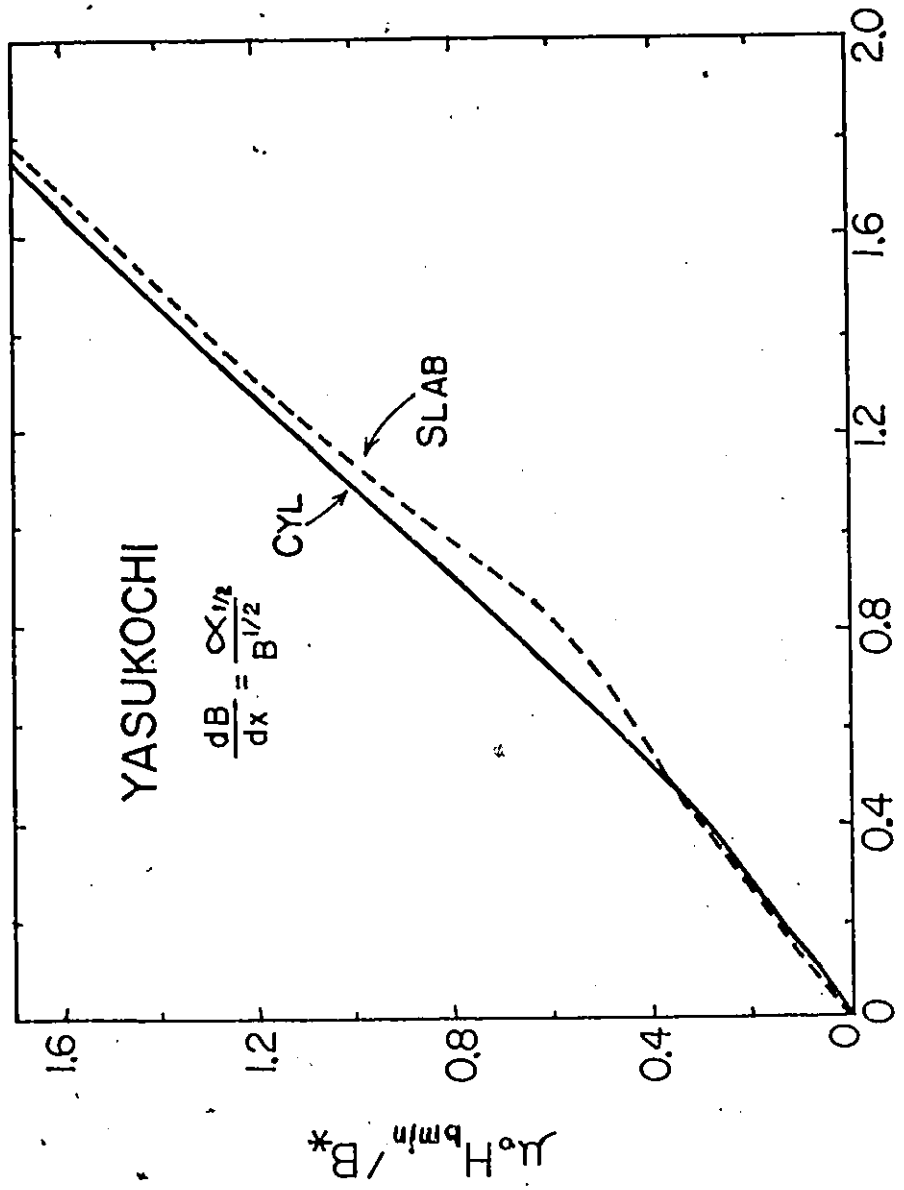

FIG. 5.7 Evaluation of $H_{b\,min}$ as the amplitude h_o increases for both planar (infinite slab) and cylindrical geometry using the Yasukochi approximation (eqn. 5.6).

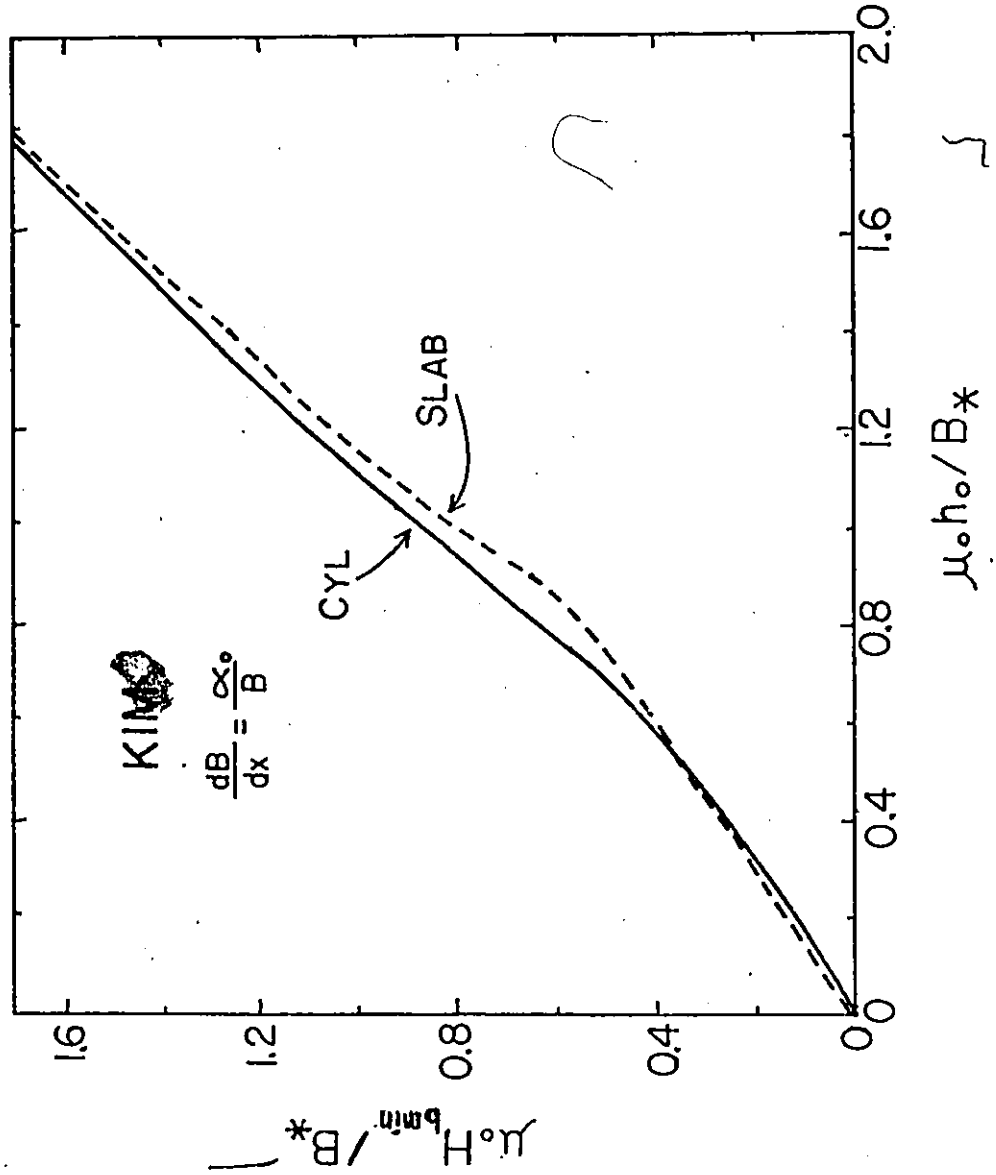

FIG. 5.8 Same as Fig. 5.7 using the Kim approximation (eqn. 5.9).

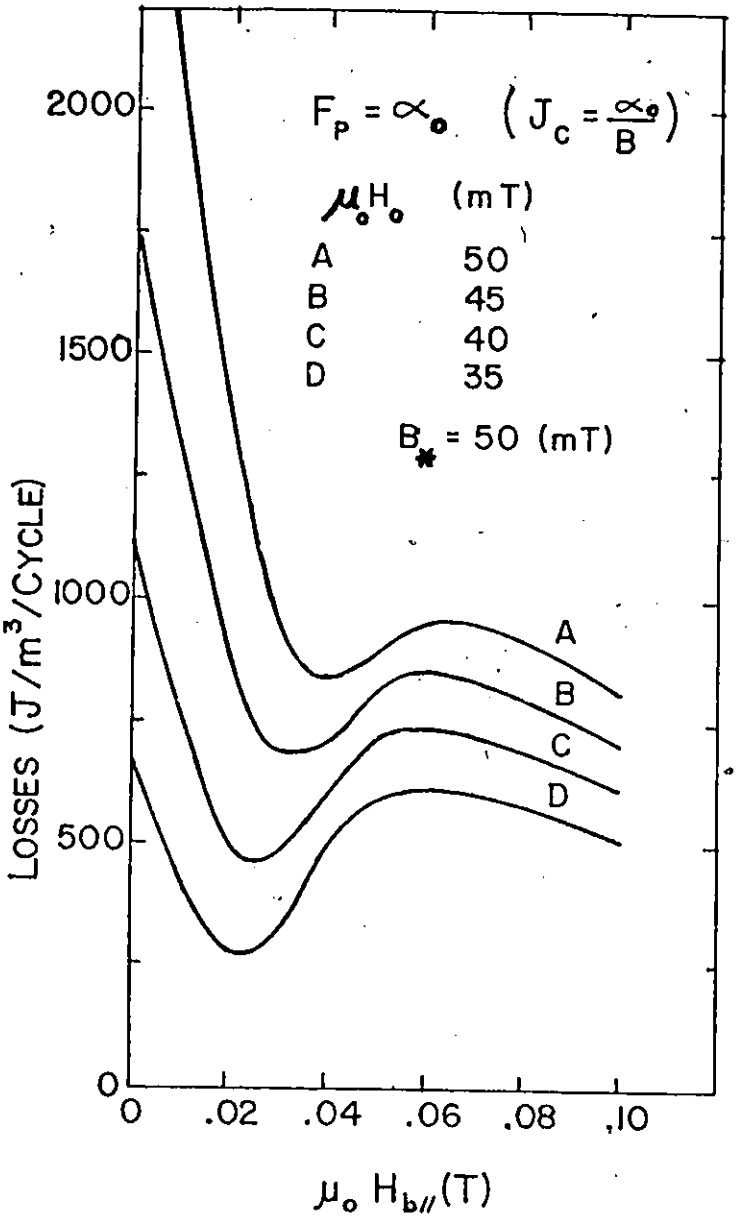

FIG. 5.9 Same as Fig. 5.2 using equation 5.9.

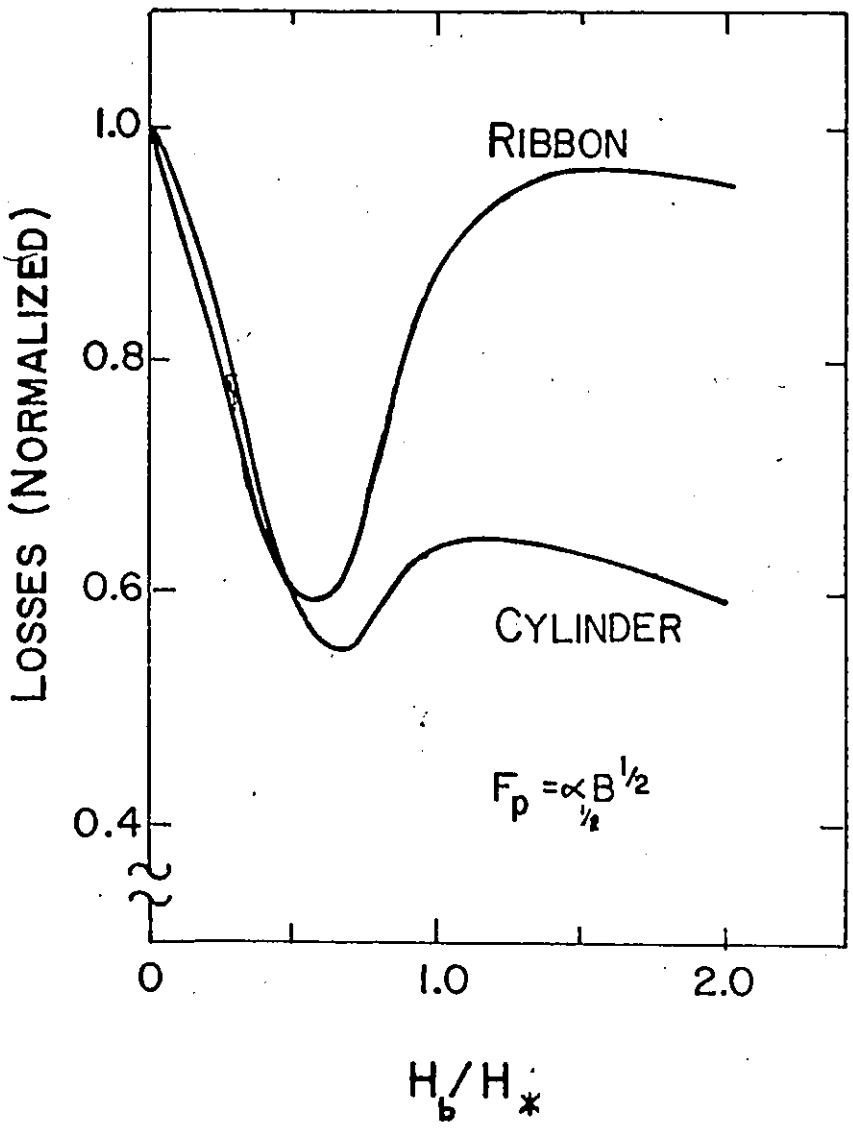

FIG. 5.10 Hysteresis losses (normalized) as function of the bias magnetic field H_b (normalized) at an amplitude h_o = 0.8 H_*, for slab and cylinder geometry using equation 5.6.

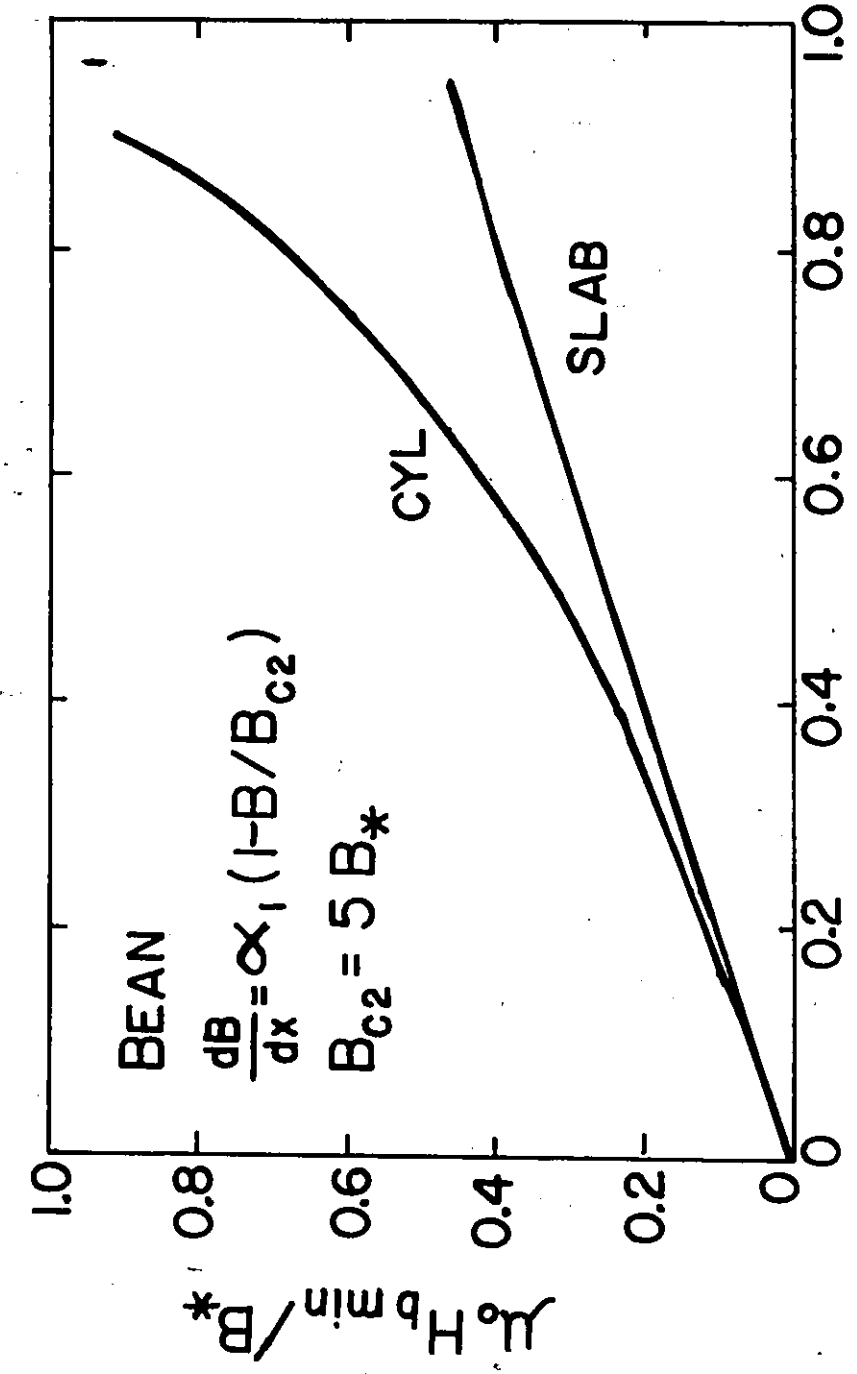

FIG. 5.11 Same as Fig. 5.7 using the Bean-London approximation (eqn. 5.10) taking $B_{c2}/B_* = 5$.

CHAPTER 6

EFFECT OF A FIELD INDEPENDENT SURFACE BARRIER ON HYSTERESIS LOSSES

6.1 INTRODUCTION

Several workers have shown that type II superconductors, below H_{c2}, exhibit a surface barrier to the entry or exit of magnetic flux (E). This barrier can make a significant contribution to the critical current I_c which ribbons and wires of these materials can support (148, 149, 150). Further, the barrier plays a crucial role in dictating the range over which an applied magnetic field, H_o, or an impressed conduction current, I, can be cycled without having energy dissipation occur (76, 77, 78). When the amplitude of the variation in I or H_o exceeds the boundaries set by the surface barrier, displacement of flux in the bulk of the sample takes place and hysteresis losses are generated. These losses then arise from motion of flux, (i) through the barrier and (ii) in the bulk. Consequently surface and bulk contributions to the energy dissipation can be identified, at least theoretically, (Clem (3)).

In some applications, it is desirable and feasible to operate within the limits prescribed by the surface barrier and avoid any changes of flux in the bulk. In this regime, losses are negligible and, ideally, zero at low frequencies. Superconducting power transmission cables are designed to operate in this regime. In many situations, however, this boundary is inevitably surmounted and flux motion takes place in the volume adjacent to the surface. Circumstances must also be envisaged where changes of flux density, hence vortex motion, are made to occur

throughout the entire volume of the sample during some portion of the working cycle. This state of affairs is encountered when superconducting coils and magnets are pulsed or ramped to high fields.

A basic expression for W, the energy dissipation density per cycle, is

$$W = \oint H_o \, d\langle B \rangle \tag{6.1a}$$

where $\langle B \rangle$ is the average of the magnetic flux density over the cross section of the sample. We visualize that H_o and B are collinear and parallel to the surface of the specimen. W can be written

$$W = \oint (\Delta H + \frac{B_{si}}{\mu_o}) \, d\langle B \rangle \tag{6.1b}$$

where ΔH is the difference between the external magnetic field and, B_{si}, is the internal magnetic induction (density of flux or vortices) adjacent to the surface. ΔH is referred to as the surface step or discontinuity and is taken to occupy a negligible element of thickness. Two ingredients enter into the construction of the surface step; a) a surface barrier and b) a reversible surface screening current (the intrinsic or equilibrium Abrikosov diamagnetism). ΔH in equation 6.1b can therefore be rewritten in terms of these two contributions. The critical surface barrier is known to depend on the magnetic field strength and may also depend on whether it is called upon to oppose the entry or exit of flux. The evolution of ΔH during a cycle of H_o can, in practice, be quite complicated. In our work, however, we will invoke only simple but useful modalities. Further, in our work, the "structure" of the surface step plays no role. Consequently we will often, for convenience,

also refer to ΔH as the surface barrier.

In the context of equation 6.1b, the essential quasi-macroscopic elements of calculations of W are; (i) ΔH looked upon as one entity or in terms of its two basic constituents and (ii) the sequence of profiles of the magnetic induction (B profiles) in the bulk. We view these profiles as independent of the rate of change of H_o, hence focus on hysteresis losses only. Several workers have investigated hysteresis losses experimentally and analytic expressions for these losses have been developed using models and functional forms of various degrees of sophistication for the surface step and for the B profiles. These, sometimes elaborate, mathematical formulae have frequently lain dormant and their conversion to families of curves of W versus h_o for various chosen ΔH or W versus ΔH for various chosen h_o has been pursued in only a few instances. We let h_o denote the amplitude of the oscillations of H_o. The purpose of this chapter is to conduct a survey of the effect of ΔH on hysteresis losses and display the results of this survey graphically. This survey reveals interesting, unsuspected and useful physics.

It is indeed possible to extract important conclusions and read the essential message we will convey from simple qualitative considerations without resorting to any mathematical manipulations and computations. In Fig. 6.1a and 6.1b we sketch hysteresis loops (<B> vs. H_o curves) of amplitude, (i) $h_o = H_{c2}/2$ and (ii) $h_o = H_{c2}$ for applied magnetic fields of the form (i) $H_o = h_o + h_o \cos \omega t$ and (ii) $H_o = h_o \cos \omega t$ respectively. We denote (i) as the half-wave and (ii) as the full-wave cases. A sketch

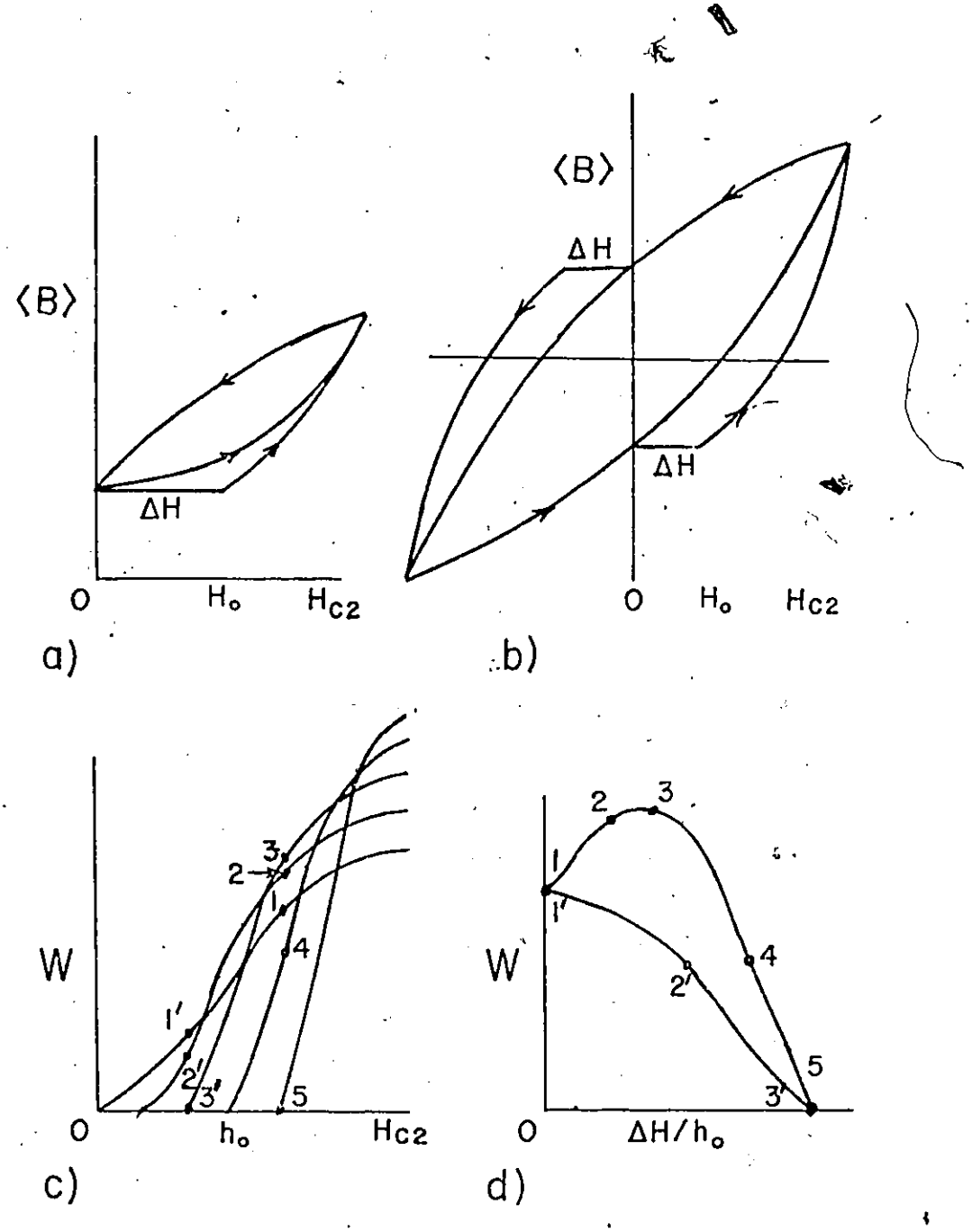

FIG. 6.1 Sketch of hysteresis loops (<B> vs. H_o curves) of amplitude (a) $h_o = H_{c2}/2$ (half-wave) and (b) $h_o = H_{c2}$ (full-wave) showing the hysteresis loop when no barrier exists and also when a barrier is acting. In (c), $W(h_o, \Delta H)$ vs. h_o curves are presented, one with no barrier and the others when barriers of different magnitude operate. Vertical cuts through the family of curves of (c) are shown in (d).

is drawn of the hysteresis loop when no barrier exists and also when a barrier is acting. The barrier is taken to vanish at $H_o \lesssim H_{c2}$. No precisions are required regarding the detailed form of the critical B profiles. For simplicity, in this pictorial exercise, we assume an asymmetric type of barrier. By this we mean that the barrier ΔH opposes entry of flux but does not impede the exit of flux. Indeed, this approximation appears to be fairly realistic. The detailed dependence of the barrier against entry on H_o is immaterial. We note that the enclosed area of the hysteresis loops, hence the maximum W, must increase with increasing ΔH.* Hysteresis loops for intermediate amplitudes need not be drawn. Their enclosed area, however, will fall between 0 and the corresponding maximum. We then sketch curves of $W(h_o, \Delta H)$ versus h_o, one with no barrier and others where barriers of different magnitudes operate as in Fig. 6.1c (See Fig. 6.18 also). The important feature which emerges from this exercise is that pairs of W vs. h_o curves must intersect. There is therefore a threshold amplitude beyond which $W(h_o, \Delta H) > W(h_o, 0)$. Bussière and Clem (22) have indeed already observed this phenomenon. They have also generated behaviour similar to that shown in Fig. 6.1c and Fig. 6.18 by exploiting a strongly magnetic field dependent barrier.

Examining Fig. 6.1c we now focus on $W(h_o, \Delta H)$ at various chosen amplitudes and regard ΔH as the variable, all other things remaining the same. We then plot vertical cuts through the family of curves of Fig. 6.1c. Two modes of behaviour of $W(h_o, \Delta H)$ versus ΔH will be encountered as shown in Fig. 6.1d. For a chosen h_o, as $\Delta H/h_o$ varies from

* In practice, this might be accompanied by plating the surface with an appropriate thickness of a suitable metal (antiferromagnetic, ferromagnetic or a good conductor) or by piercing the surface of the sample with a small static transverse component of the applied magnetic field.

zero to unity, (a) the losses will decline monotonically to zero and (b) the losses will initially rise, traverse a peak and then diminish gradually to zero. The first type of behaviour has been extensively examined in some detail in the literature. Perhaps because of this work, the idea that hysteretic losses should decrease as the barrier is increased seems to have become implicitly accepted generally. To our knowledge, the latter very important regime seems to have been overlooked. Indeed, its existence seems not to have been suspected and the possibility of an initial rise in energy dissipation over the initial range of increase of the barrier may even intuitively appear unacceptable. This rise is particularly surprising in cases where the amplitude is too small to cause the flux disturbance generated during the cycle of H_o to attain the midplane of a ribbon sample or the centreline of a cylindrical specimen. We refer to this as the regime below saturation.

In this chapter, we investigate the effect of a magnetic field independent surface barrier on hysteretic losses for two basic geometries readily amenable to analysis and also of practical interest; the infinite slab and the infinitely long cylinder. The external magnetic field is directed parallel to the surfaces of the slab or the axis of the cylinder. We examine the hysteresis loops occurring for both half-wave ($H_o = h_o + h_o \cos \omega t$) and full-wave ($H_o = h_o \cos \omega t$) variations of the external field. The rate of change of H_o is regarded as sufficiently slow so that viscous flow of vortices makes a negligible contribution to the energy dissipation. Since we are concerned only with the form of the hysteresis loops and the area they enclose, the specific time dependence of H_o is immaterial, and the expressions just introduced for

$H_o(t)$ are used only for convenience. In particular these provide brief and clear statements of the meaning of the expressions half-wave and full-wave oscillations, and other terms we need to introduce such as amplitude, bias field, maximum and minimum external field etc.

In this study we introduce two radically different types of behaviour for the surface barrier: (i) the symmetric case, where the entry and exit of flux are equally opposed and (ii) the asymmetric case, where the entry of flux only is opposed. Both of these barrier configurations have already been exploited in the literature and there is some evidence that examples of both forms can be encountered in nature.

The detailed sequence of configurations of the magnetic induction inside the specimen plays an important role in hysteretic losses since this prescribes $\Delta\langle B\rangle$ in equation 6.1. Consequently, to better delineate the influence of the surface barrier we explore the phenomena exploiting two extremal types of bulk pinning, namely, the Bean-London (2, 13) approximation where $F_P = \alpha_1 B$ (hence $j_c = \alpha_1$) and the Kim-Anderson (120, 151) approximation where $F_P = \alpha_o$ (hence $j_c = \alpha_o/B$). For brevity we will refer to these simply as the Bean and Kim approximations.

Finally we pursue the evolution of the losses for (i) the range of amplitudes below that needed for penetration of the flux profile to the midplane or centreline of the specimen (below saturation) and (ii) the range of amplitudes where the B profile changes throughout the cross section of the sample during some portion of each cycle of H_o (above saturation).

Each of the modalities we investigate may, taken individually, be regarded as artificial and crude. The pattern of behaviour which

emerges from our study of the collection of cases we have mapped out may, however, be useful in outlining basic features of the real phenomena and stimulate as well as guide experimental exploration of these model predictions.

6.2 RESULTS AND DISCUSSION

A. General Description

It is instructive and useful to present the set of sixteen situations we have investigated in tabular form. We will see that some cases yield identical results. The reasons for this readily emerge from qualitative considerations of these particular cases. As a consequence, the set of sixteen, in effect reduces to twelve distinct cases.

Table 6.1

Geometry		Infinite Slab				Infinite Cylinder			
Cycle		Half-Wave		Full-Wave		Half-Wave		Full-Wave	
Barrier		Sym	Asym	Sym	Asym	Sym	Asym	Sym	Asym
Pinning	Bean	1a	1b	1c	2	3a	3b	3c	4
	Kim	5	6	7	8	9	10	11	12

Situations numbered 1a, 1b and 1c generate the same results, and, similarly, situations 3a, 3b and 3c.

In Figure 6.5 through 6.16 we present the results of our computations of $W(h_o, \Delta H)$ for this assortment of situations in a perspective where we regard the amplitude h_o as fixed and the barrier ΔH as a variable

parameter whose magnitude can be adjusted to span the range from zero to a height which allows no flux motion in the bulk, hence, the extinction of hysteresis losses (ideally). This occurs when $\Delta H'$, the height of the symmetric type of barrier becomes equal to the amplitude ($\Delta H' = h_o$) and when $\Delta H''$, the height of the asymmetric type of barrier becomes equal to h_o for the full-wave cycle but twice the amplitude ($\Delta H'' = 2h_o$) for the half-wave cycle. These limits follow from our definitions of these two types of barriers as will be seen below.

For a chosen amplitude it is convenient to display the evolution of the energy dissipation $W(h_o, \Delta H)$ versus ΔH by normalizing $W(h_o, \Delta H)$ for a specified choice of geometry, cycle, barrier and bulk pinning to the corresponding dissipation, $W(h_o, 0)$ when no barrier is present.

A convenient and meaningful unit for measuring the amplitude (and therefore the barrier) is the magnetic field $H_* = B_*/\mu_o$, where B_* is the magnetic induction just inside the surface when a critical B profile exists over the entire cross section of the sample and declines to zero at the midplane or centreline. Alternatively the "mirror image" can be envisaged, where B = 0 just inside the surface and the critical B profile rises from there to B_* at the midplane of centreline.

We display the evolution of W, normalized as just indicated, versus ΔH, also normalized, for various fixed amplitudes expressed relative to H_*. We let C indicate the latter ratio. We choose C such that when C = 1, and no barrier is acting, the cycle of the applied field H_o between the specified limits ($H_o = h_o \cos \omega t$ or $H_o = h_o + h_o \cos \omega t$), causes the disturbance in the B profile to reach the midplane or centreline

but produces no change in the magnetic induction at that inner boundary. Consequently we take $C = C' = h_o/H_*$ for half-wave and full-wave cycles when the Bean approximation is introduced and also for the full-wave cycle when the Kim approximation is used. For the half-wave cycle when the Kim approximation is exploited we, however, let $C = C'' \sqrt{2}\ (h_o/H_*)$. The reason for the latter choice emerges from consideration of the appropriate limiting B profiles sketched below. The $\sqrt{2}$ factor results from integration of $dB/dx = \alpha_o/B$ from $x = 0$ where $B = 0$ to $x = 2X$ and taking $B_* = \sqrt{2\alpha_o X}$.

When the Bean approximation is being used, $C \leq 1$ also serves as a direct indicator of the fractional depth of penetration of the flux front into the slab or cylinder since the B profiles are linear. With the Kim approximation, however, because of the B dependence of the gradient of the flux density, C is no longer a linear measure of the penetration. For infinite slab geometry, when $0 < C \leq 1$, the curves of W (normalized) vs. ΔH (normalized) are independent of the normalized amplitude h_o/H_*. The "universal" curve for each of these instances is labelled C = 1.0 in the Figures. This independence on C over the range $0 < C \leq 1$, is a consequence of the geometry and of our scaling of the hysteresis losses for a given amplitude to the situation where there is no barrier. This feature can be qualitatively understood from consideration of sequences of B profiles for situations below saturation ($C \leq 1$). We note that $\Delta\langle B\rangle/\Delta B_{si}$ for planar geometry is unaffected by displacements of the midplane away from the surface (enlarging the half thickness X of the slab). For cylindrical geometry, however, the normalized curves of W versus ΔH do depend on C even in the range $C \leq 1$.

This arises from the presence of the radius r in the element of area $\Delta A = 2\pi r \Delta r$ in the evaluation of $\langle B \rangle$ and hence in the determination of $\Delta\langle B \rangle$.

When C approaches zero, the depth of penetration of the B profiles becomes small compared to the radius R of the cylinder. The normalized results for cylinder geometry then merge with that for the corresponding case, below saturation, for the infinite slab. Therefore the curve, labelled C = 0 for the cylinder, corresponds to that labelled C = 1 for the slab, all other features (type of cycle, barrier, pinning) being the same.

The B profiles depicted by solid lines in Fig. 6.2 represent the limiting flux configurations of a cycle which we denote as saturated (or saturation cycle). Limiting B profiles lying inside these boundaries correspond to cycles which we denote as below saturation. Limiting B profiles which embrace these boundaries correspond to cycles denoted as above saturation. It is important to note in scrutinizing the graphs of W (normalized) versus ΔH (normalized) that the sequence of limiting B configurations when C > 1, progresses from above saturation, to saturation, to below saturation as ΔH grows. This progression occurs because it is the sweep of B_{si}, the magnetic induction just inside the surface which determines the limiting B profiles. Clearly, with the amplitude kept fixed (relative to H_*), the range traversed by B_{si}/μ_o must shrink as ΔH is made to increase. This feature is illustrated schematically by the dashed profiles in Fig. 6.2 where ΔH is taken to be symmetric.

B. Types of Surface Barriers (Surface Steps)

Qualitatively, four surface barrier regimes can be envisaged;

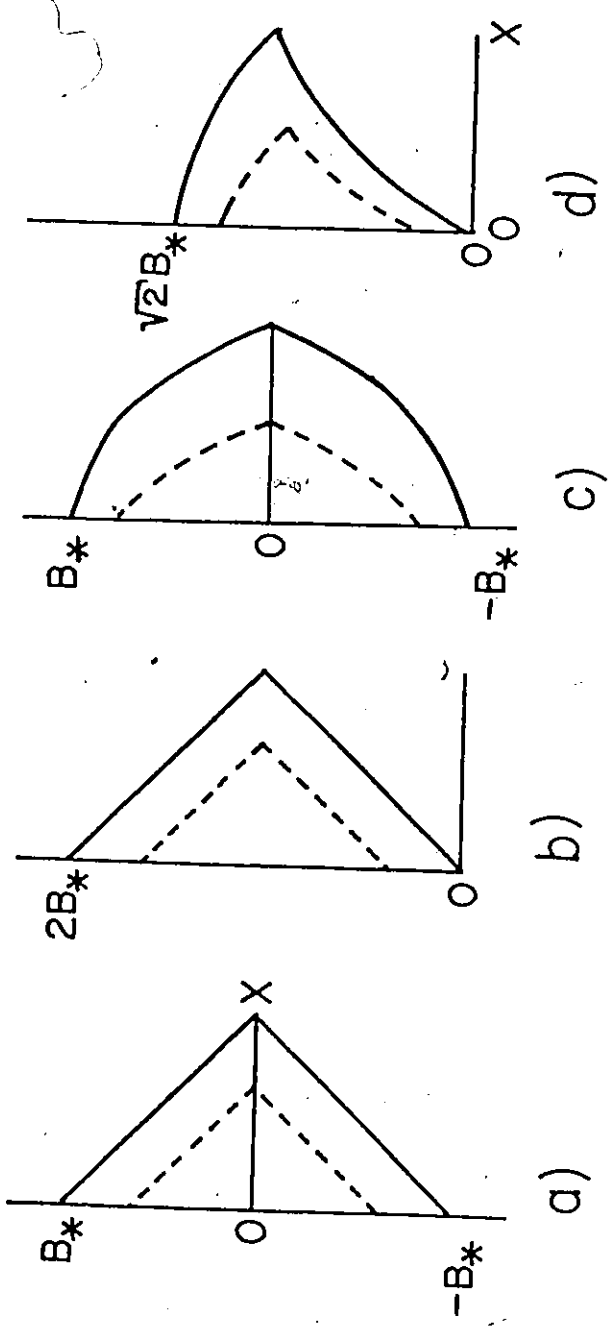

FIG. 6.2 Sketch of limiting B profiles at saturation (solid lines) and below saturation (dashed lines).

(i) no barrier either to entry or to exit of flux, (ii) a barrier against entry but none against exit (we refer to this as the asymmetric case), (iii) a barrier against entry and also against exit, and finally, (iv) a barrier against exit but none against entry. We set the last option aside since it appears unphysical in view of image force interactions and is not supported by any experimental evidence. For simplicity, we take the critical magnitude of the barrier (s) to be independent of the magnetic induction. Among the multitude of possibilities embraced by the third category we select the special case where flux entry and exit are equally opposed. This situation, which we denote as the symmetric case, presumably constitutes a limiting or extreme configuration since image force interactions make it unlikely that flux exit can be as stronly opposed as flux entry. Further, when equilibrium (Meissner) screening currents are taken into account, it is even less plausible that such an equality in magnitude of the surface steps can occur. The surface step is regarded as the resultant of the operation of the barrier and the presence of reversible surface shielding currents. Evidently a large variety of barrier or surface step arrangements, other than the two simplistic configurations we have chosen, can be visualized. The two regimes we exploit, however, bracket the spectrum of possibilities and serve as useful benchmarks. Intermediate and alternative situations can be semi-quantitatively mapped out from interpolation and extrapolation of the results we present.

For clarity and completeness we supplement the verbal statements of the two types of barriers with detailed mathematical descriptions and pictorial representations. A quantity of much importance in the deter-

mination of $\Delta\langle B\rangle$ is B_{si}, the magnetic induction just inside the surface. Consequently we describe the surface barrier and its behaviour by writing explicit expressions for B_{si} for the variety of situations encountered during the half-wave and full-wave oscillations of H_o.

A convenient starting point is the end of the initial increase in $|H_o|$ to $|2h_o|$ (half-wave case) or to $|h_o|$ (full-wave case) where the sense of the sweep of H_o reverses direction. We often abbreviate full-wave case to f.w and half-wave case to h.w. We refer the reader to Fig. 6.3 for aid in visualizing the following.

a) Symmetric Barrier, $\Delta H'$.

i) Half-wave cycle, $H_o = h_o + h_o \cos \omega t$

$|B_{si}|$ remains constant at the value attained during the initial sweep of $|H_o|$, namely, $|B_{si}/\mu_o| = 2|h_o| - |\Delta H'|$, while $|H_o|$ decreases from $2|h_o|$ to $2(|h_o| - |\Delta H'|)$. Subsequently, $|B_{si}/\mu_o| = |H_o| + |\Delta H'|$ as $|H_o|$ continues to diminish to zero. At this juncture, upon reversal of the sence of the sweep of $|H_o|$, $|B_{si}|$ remains constant at the value $|B_{si}/\mu_o| = |\Delta H'|$ as $|H_o|$ rises from zero to $2|\Delta H'|$. Then, throughout the rise of $|H_o|$ from $2|\Delta H'|$ to $2|h_o|$, $|B_{si}/\mu_o| = |H_o| - |\Delta H'|$. The sequence just described repeats as H_o oscillates between the specified limits.

ii) Full-wave cycle, $H_o = h_o \cos \omega t$

$|B_{si}/\mu_o| = |h_o| - |\Delta H'|$ while $|H_o|$ decreases from $|h_o|$ to $|h_o| - 2|\Delta H'|$. Subsequently $|B_{si}/\mu_o| = |H_o| + |\Delta H'|$ as $|H_o|$ is reduced to zero. After reversal of the sign of H_o, $|B_{si}| = |H_o| - |\Delta H'|$, hence diminishes to zero while $|H_o|$ increases from 0 to $|\Delta H'|$. Then $|B_{si}| = |H_o| - |\Delta H'|$ while $|H_o|$ increases from $|\Delta H'|$ to $|h_o|$. The

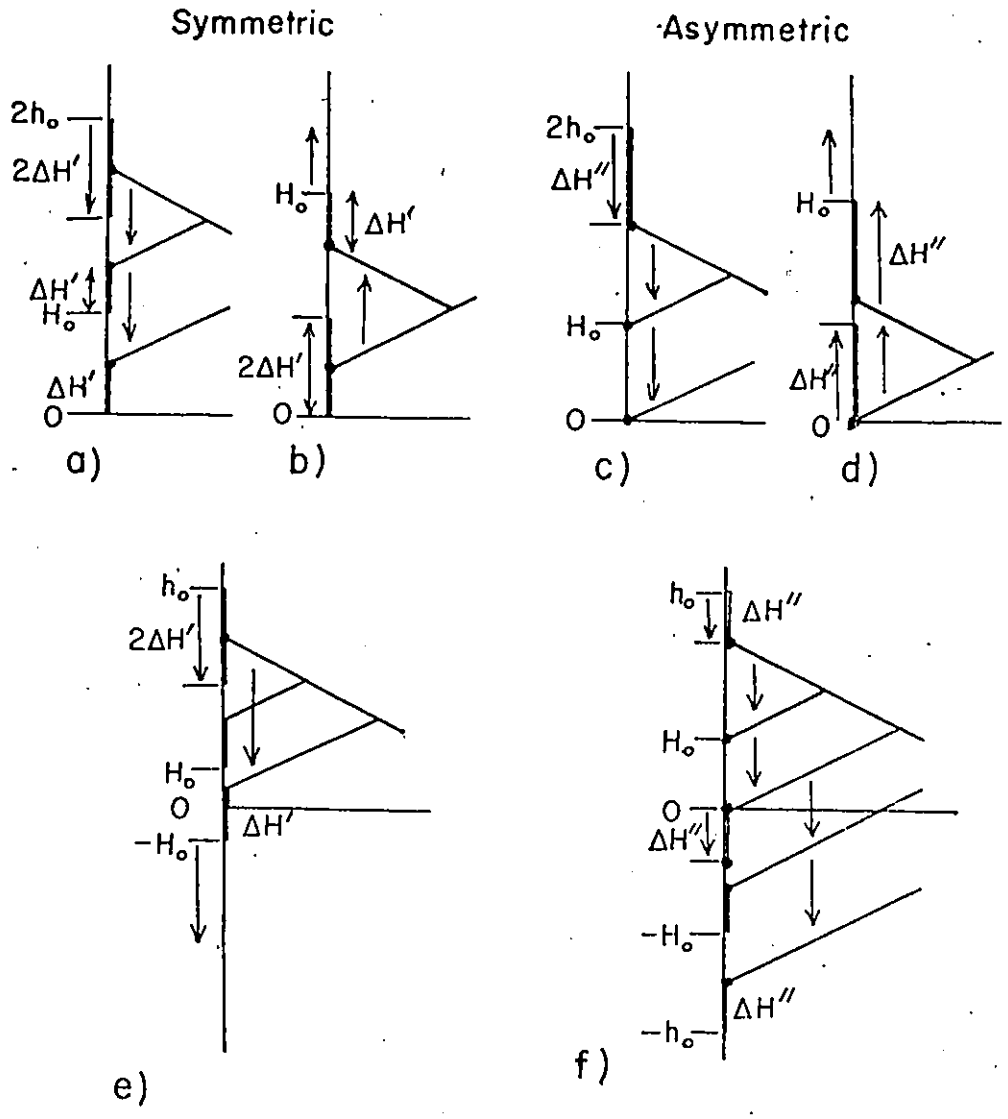

FIG. 6.3 Sketch of a half-wave cycle (a and b) and of a a full-wave cycle (e) when a symmetric barrier is acting and when an asymmetric barrier is in operation (c, d and f).

sequence just described now repeats as H_o swings through subsequent half cycles.

From consideration of (i) and (ii) it ensues that B_{si}, hence $\langle B \rangle$ will remain constant during the entire cycle and hysteresis losses vanish when $\Delta H' = h_o$.

We note that with this type of barrier (surface step), $|\langle B \rangle|$ decreases continuously, albeit with variations in the slope, $|\Delta\langle B \rangle/\Delta H_o|$, during the traversal of H_o through the range straddling zero. In other words, no region is encountered in this portion of the hysteresis curve where $\langle B \rangle$ remains constant. This is the behaviour, puzzling as the absence of such a region may be, which is encountered experimentally.

Aside from the simplifying stipulation that the critical ΔH is independent of the magnetic induction, the symmetric $\Delta H'$ we have just described is fundamentally unrealistic. It neglects the existence of equilibrium (Meissner) flux shielding surface currents even when $H_o \gtrsim H_{cl}$. The latter by aiding the barrier to flux entry and counteracting the barrier to flux exit will introduce some degree of asymmetry in the surface steps for $|H_o|$ increasing and decreasing. Nevertheless, the perfectly symmetric $\Delta H'$ we envisage above, provides a useful, simple, extremum situation for purpose of comparison or reference.

b) Asymmetric Barrier, $\Delta H''$

i) Half-wave cycle, $H_o = h_o + h_o \cos \omega t$.

$|B_{si}|$ remains constant at the value attained during the initial sweep of $|H_o|$, namely, $|B_{si}/\mu_o| = 2|h_o| - |\Delta H''|$, while $|H_o|$ decreases from $2|h_o|$ to $2|h_o| - |\Delta H''|$. Subsequently, $|B_{si}/\mu_o| = |H_o|$ as $|H_o|$ continues to diminish to zero. Now upon reversal of the sense of the

sweep of $|H_o|$, $|B_{si}| = 0$ as H_o rises from zero to $|\Delta H''|$. Then, during the rise of $|H_o|$ from $|\Delta H''|$ to $2|h_o|$, $|B_{si}/\mu_o| = |H_o| - |\Delta H''|$. The sequence then repeats. In order that B_{si}, hence $\langle B \rangle$, remain constant during the entire cycle and hysteresis losses vanish, H" must grow to $2h_o$. This can be seen from the first sentence of this paragraph. It follows also that $B_{si} = 0$ under these circumstances, although $\langle B \rangle$ need not vanish.

ii) Full-wave cycle, $H_o = h_o$

$|B_{si}/\mu_o| = |h_o| - |\Delta H''|$ while $|H_o|$ decreases from $|h_o|$ to $|h_o| - |\Delta H''|$. Then $|B_{si}/\mu_o| = |H_o|$ as $|H_o|$ is reduced to zero. After reversal of the sign of H_o, $|B_{si}| = 0$ while $|H_o|$ grows from zero to $|\Delta H''|$. Next, $|B_{si}| = |H_o| - |\Delta H''|$ while $|H_o|$ continues to increase from $|\Delta H''|$ to $|h_o|$. The sequence now repeats as H_o completes the full cycle. Here the limiting barrier for extinction of the losses is $\Delta H'' = h_o$.

In terms of equilibrium (Meissner) shielding currents and critical surface currents, the asymmetric $\Delta H''$ just described implies that, when $|H_o|$ is decreasing, these two counterflowing currents effectively cancel each other. In practice, such an exact cancellation appears unlikely and variations on the degree of asymmetry are expected. The simple, extreme case envisaged here, however, has heuristic merit.

C. Sequences of B profiles, $\Delta\langle B \rangle$ and Losses

The accepted picture of the evolution of the magnetic flux configuration in irreversible type II superconductors as the magnetic induction at the boundaries undergoes changes and traverses one of a variety of possible cycles, starting from different initial states (B

profiles), has now been presented in many articles in the literature. The different categories of B profiles encountered during half-wave and full-wave cycles of amplitudes lying above and below saturation are displayed schematically in Fig. 6.19.

In this chapter we exploit two basic and radically different forms for the B profiles. These ensue from the stipulation that the gradients of the flux density are (i) independent of B, hence $dB/dx = \alpha_1$ and (ii) inversely proportional to B, hence $dB/dx = \alpha_o/B$. These modalities are often referred to as the Bean-London (2, 13) and Kim-Anderson (120, 151) approximations. They are chosen for their simplicity and because they conveniently bracket the spectrum of expected flux configurations.

In appendix IV we present analytic expressions for $d\langle B\rangle/dB_{si}$ and $W(h_o, \Delta H)$ for many of the twelve different cases enumerated in table 6.1, both below and above full penetration. Case 1a (or equivalently 1b) of table 6.1 (half-wave oscillations) has been examined in detail by Ullmaier (83) and also by Sekula and Barrett (16). Although the latter consider a cylindrical arrangement, they pursue this geometry in the limit of superficial flux penetration, hence, they are actually addressing infinite slab (planar) geometry. Case 1c (which is equivalent to 1a and 1b)constitutes a special limit of the general expressions developed by Dunn and Hlawiczka (5) for full-wave oscillations with planar geometry. These authors also envisage a wide variety of field independent surface steps. Closed form expressions for case 1c and also for case 7 have been derived as particular examples by Fournet and Mailfert (6) who explored full-wave oscillations applied to an infinite slab with arbitrary pinning and symmetric barriers (surface steps). All of the above authors confine

their analysis to amplitudes below full penetration. The equivalence of cases 1a, 1b and 1c is not explicitly indicated in the papers just referenced. It is noteworthy that $W(h_o, \Delta H)$ vs ΔH exhibits no initial rise, for the two (non-equivalent) cases just mentioned when the amplitude falls below saturation (C = 1, in our nomenclature). As a consequence, an important feature which emerges from our extensive exploration, was not encountered nor intimated in these previous studies.

The equivalence of cases 1a, 1b and 1c of table 6.1 and also, of cases 3a, 3b and 3c as another distinct group, can be seen without mathematical manipulation. We consider hysteresis loops of corresponding amplitudes and note that here, (i) the B profiles are taken independent of B (hence linear) and (ii) the barriers are also independent of B. Choosing identical (+ and -) slopes for the B profiles in all cases, and identical sample dimensions, it follows that <B> versus B_{si} will trace a "basic" curve as B_{si} is cycled over a selected range, whether this range lies below or extends beyond saturation. Clearly, due to the $2\pi r$ factor, the form of <B> vs B_{si}, for cylindrical geometry, will differ from that for the infinite slab. We now note that when <B> is evolving as B_{si} varies, $\Delta B_{si}/\Delta (\mu_o H_o) = 1$ since ΔH is taken independent of B, consequently, the form of the "basic" curve of <B> vs H_o is not affected by the presence of the barrier. Finally, introducing <B> constant over equal ranges of H_o for all cases ($\Delta H'' = 2\Delta H'$), generates three identical hysteresis loops, displaced horizontally and/or vertically with respect to the <B> and H_o axes as shown schematically in Figs. 6.4a, 6.4b and 6.4c.

The broad matrix of situations tabulated and investigated by Clem (3) overlaps with a portion of the cases we have pursued in compu-

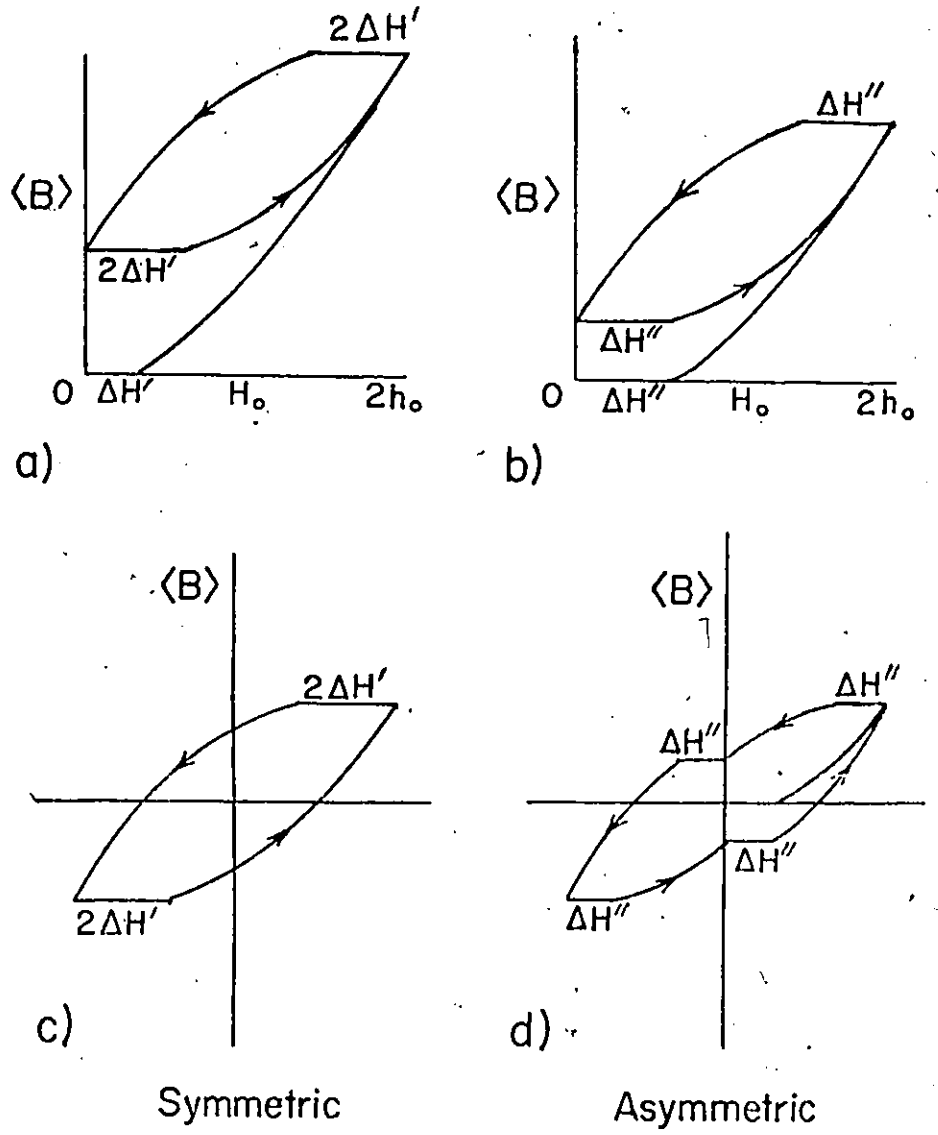

FIG. 6.4 Hysteresis loops showing schematically the equivalence of cases 1a, 1b and 1c of table 6.1 (with $\Delta H'' = 2\Delta H'$).

tational detail. This author focuses on several interesting aspects of hysteretic losses, in particular, (i) the relative contribution of different processes (barrier, pinning, flux annihilation) to the energy dissipation and (ii) the occurrence of a valley when $W(h_o, \Delta H, H \text{ bias})$ is plotted as a function of H bias. A rise in W ensuing from an initial increase in the barrier does not explicitly emerge from this encyclopedic survey. Clem, however does envisage the possibility that strongly B-dependent surface barriers, can lead to larger losses in a superconductor when compared to those occurring in an identical sample without a surface barrier.

Bussière and Clem (22) have investigated hysteresis losses in samples subjected to full-wave oscillations for amplitudes lying below saturation. Although their arrangement is cylindrical, the penetration of flux is peripheral, hence, the situation corresponds to planar geometry. In their calculations, they exploit a symmetric B-dependent surface barrier where

$$\Delta H(B) = (\Delta^2 + (B_{si}/\mu_o)^2)^{1/2} - B_{si}/\mu_o \tag{6.2}$$

where Δ, an adjustable parameter, is the height of the critical barrier when $B_{si} = 0$ (first entry field). These workers indeed find, both experimentally and theoretically that, above a threshold amplitude, larger losses occur when a barrier is present (as sketched in Fig. 6.1c) This cross over behaviour is encountered in their analysis when they exploit the Bean approximation for the B profile and also when they use a standard modification of the Kim approximation, namely,

$dB/dx = \alpha_o/(B + B')$, where B' is an adjustable parameter. They choose $B' = 2\Delta$ and examine the behaviour over the range $\Delta < h_o \lesssim 2\Delta$. In the light of their analysis, Bussière and Clem view a cross over in the curves of W vs h_o, hence an increase in losses by a barrier, as requiring a rapid decrease of ΔH with B. The lowermost curves of Fig. 6.5 and of Fig. 6.11 have a bearing on their investigation since, aside from the B dependence of the barrier, the other set of conditions are in correspondence (planar geometry, $C \leq 1$, Bean and Kim approximations, full-wave oscillations, symmetric barrier). We note that these two curves exhibit a continuous decline of W vs ΔH. In these circumstances the cross over in W vs h_o (a rise in W vs ΔH) which they calculate, must then indeed arise from the introduction of a B dependence on the symmetric barrier.

In our work we developed a computer program which calculates numerically:

i) sequence of B profiles for arbitrary functional choices of $dB(B)/dx$, (or equivalently of pinning function $F_p(B)$) as B_{si} is cycled through full-wave or half-wave oscillations of amplitude below and beyond saturation.

ii) the corresponding sequences of the average magnetic induction $\langle B \rangle$ and of $\Delta\langle B \rangle/\Delta B_{si}$ for planar and cylindrical geometry and

iii) the integral of $H_o(B_{si})\ \Delta\langle B \rangle$ for the chosen cycle of H_o and barrier regime (symmetric or asymmetric).

Aside from internal consistency of the families of curves of $W(h_o, \Delta H)$ vs ΔH, and overlap of the results at the appropriate limits (eg. superficial penetration for cylindrical geometry corresponding to

$C \leq 1$ for planar geometry), the computer program has been verified in two ways. Firstly, by graphical and planimeter integration of the computer output for <B> versus B_{si} and H_o in a sampling of cases. Secondly, by comparing the final results of the computer program with the corresponding computer calculations using the analytic expressions for $W(h_o, \Delta H)$ given in appendix IV.

For purpose of illustration of the phenomenon in a different perspective, in Fig. 6.17 we display three hysteresis loops calculated for case 9 of table 6.1 where a particularly impressive increase in W vs. ΔH is encountered even when $C \leq 1$. We show a hysteresis loop with no barrier, one where the barrier height $\Delta H'/h_o = 0.25$ which yields the peak in energy dissipation, and one where $\Delta H'/h_o \approx 0.6$, where the losses again correspond to that encountered with no barrier.

Finally in Fig. 6.18 we show W vs h_o calculated for case 9.

6.3 SUMMARY AND CONCLUSION

An irreversible type II superconductor subjected to a periodically varying external magnetic field H_o whose amplitude is too small to overcome the surface barrier will exhibit negligible hysteresis losses. If the amplitude h_o is augmented or the barrier ΔH is somehow lowered, a situation is reached where movement of flux in the body of the specimen will take place. This shuttling of flux in and out of the bulk will cause energy dissipation. We focus on the hysteretic regime, where the losses, by definition, are independent of the velocity of flux line motion, hence on the rate of change of the external magnetic field.

All other things being the same, the hysteresis losses will initially increase as the surface barrier shrinks and/or the amplitude grows. We find that, in many circumstances, the hysteretic losses do not grow continuously to attain their maximum when the barrier vanishes. Rather, the losses, in numerous cases, traverse a peak when the barrier is still finite and then decline monotonically to a value smaller than the maximum when the barrier is made to vanish.

This type of behaviour has already been reported by Bussière and Clem (22). These authors examined the growth of the losses as a function of amplitude, for a specimen with and without a surface barrier. They observe that the two curves intersect at a certain amplitude and beyond this cross over amplitude, the former curve lies above the latter (see Fig. 6.18 for illustration). They attribute this phenomenon to the presence of a surface barrier whose height diminishes rapidly as a function of magnetic field. They visualize that such a dependence is crucial for the inversion to occur and explore two cases theoretically which exhibit this feature.

We have investigated the effect of a magnetic-field-independent surface barrier on hysteresis losses for a representative set of sixteen cases, twelve of which are truly distinct. The conditions we select for our survey are chosen to sample and span the spectrum of physical possibilities. We examine two basic geometries, that of the infinite slab and the cylinder, subjected to an external magnetic field directed parallel to the length of the ribbon or wire which undergoes either full-wave ($H_o = h_o \cos \omega t$) or half-wave oscillations ($H_o = h_o + h_o \cos \omega t$). We explore the behaviour over an extensive range of amplitudes which,

when no barrier exists, cause the B profile to change over only part of the cross section of the sample (below saturation, $C \leq 1$) and over all of the cross section during part of the cycle (beyond saturation, $C > 1$). The latter regime has generally been neglected in the pertinent literature and cylindrical geometry has been usually pursued in the context of superficial flux penetration, hence in the limit where it corresponds to planar geometry. We exploit two radically different forms for the gradients of the sequences of B profiles, namely, the Bean-London approximation ($dB/dx = \alpha_1$) and the Kim-Anderson approximation ($dB/dx = \alpha_o/B$). We visualize two special types of barrier actions or discontinuities between the external magnetic induction and the magnetic induction just inside the surface, B_{si}. A symmetric type, where the entry and exit of flux are equally opposed; and an asymmetric situation, where only the entry of flux is impeded and no discontinuity occurs after $|\mu_o H_o|$ decreasing becomes equal to B_{si}.

We find that an initial rise in hysteretic losses caused by the growth of the barrier, is a frequently occurring feature. Our survey reveals that this phenomenon is promoted by a change from

i) slab to cylindrical geometry,

ii) asymmetric to symmetric barrier,

iii) full-wave to half-wave oscillations and,

iv) Kim-Anderson to Bean-London B profiles.

These trends or rules emerge from comparing Figures where all of the elements are the same except the item under consideration. It is also clear from all of the families of curves and emerges from qualitative considerations that increasing the effective depth of penetration (the

parameter $C \alpha h_o/H_*$), pushes the peak in losses to higher levels and larger barriers.

We are currently extending this investigation to the situation where the strength of the magnetic field reduces the height of the barrier(s), exploring the effect of different rates and functional forms for the decrease in height. Our preliminary survey confirms and extends the conclusion reached by Bussière and Clem. We find that a barrier which diminishes with magnetic field intensity promotes the occurrence of a cross over of the curves of W vs. h_o with and without a barrier. Further, the separation of the two curves beyond the point of inversion becomes more pronounced as the decline of the barrier versus magnetic field becomes steeper.

It is worthwhile to note that all the results developed for planar geometry also apply to the case of special practical interest of a long straight cylindrical wire where a varying transport current I is fed from an external supply via leads suitably connected to its ends. Here, in equation 6.1, $H_o = I/2\pi R$ (S.I. units) with R, the radius of the wire and

$$\langle B \rangle = \int_o^R B_\theta \, d\left(\frac{r}{R}\right)$$

where $B_\theta(r)$ is the azimuthal magnetic induction inside the wire. Under these circumstances, $d\langle B \rangle/dt$ can be monitored by measuring the potential difference along the length of the wire with attached voltage leads in the range where I is smaller than I_c, the critical current for the onset of flux flow voltages. It is well known that intricate configurations of the magnetic induction are encountered as I is varied when a

stationary longitudinal magnetic field $H_{//}$ is present. The complicated configurations will influence the hysteresis losses only through their effect on the sequences of the B profiles when $H_{//}$ is kept constant. The curves where $C > 1$ will, however, not apply to the case of the current carrying wire whether in a static longitudinal magnetic field or not, since, by symmetry, the azimuthal magnetic induction at the centreline must remain $B_\theta = 0$ as I is cycled below or even above I_c.

Hysteresis losses can be viewed as proportional to the difference between, (i) the total energy entering the specimen during the portion of the cycle where $|H_o|$ increases from zero (or a minimum) to a maximum and (ii) the total energy leaving during the portion of the cycle where $|H_o|$ decreases from the maximum to zero (or a minimum). For the full-wave and half-wave oscillations which we consider, the minimum is zero. Part of the energy flowing into (out of) the specimen during the ascending (descending) portion of the cycle can be assigned to the barrier, $(\int \Delta H \, \Delta\langle B\rangle)$, and the remainder to the bulk, $(\int B_{si} \, \Delta\langle B\rangle)$. At a fixed amplitude for a given sample, a rise in the total "barrier" contribution generated by a growth in ΔH, must be accompanied by a decrease in the "bulk" contribution. A rise in the combination, requires that the net dissipation associated with the barrier has increased more than the concomitant bulk dissipation has decreased.

Due to the complexity of the variation of the sequences of the contributions during each portion of the cycle (particularly when descriptions of the B profiles other than the Bean-London approximation are used), it is extremely difficult to predict whether in a given situation, the growth of a barrier will cause a rise in the total losses,

without resorting to computational or analytic development.

An alternative approach, outlined in the introduction and illustrated in Fig. 6.1c, predicts, quite generally, that for asymmetric types of barriers, regardless of the form of the B dependence, a cross over of W vs. h_o curves will occur with an increase in barrier. These considerations, however, impart no information on the relative amplitudes where the intersections will occur.

The results we have presented in this chapter can prove to be useful in practical situations. We can visualize an arrangement where the amplitude is set by various considerations and causes the system to operate in the vicinity of the maximum in W vs. ΔH. Two solutions can be envisaged. The losses may be reduced by either increasing or decreasing the barrier by known techniques. We expect that the latter avenue will usually prove easier and less costly.

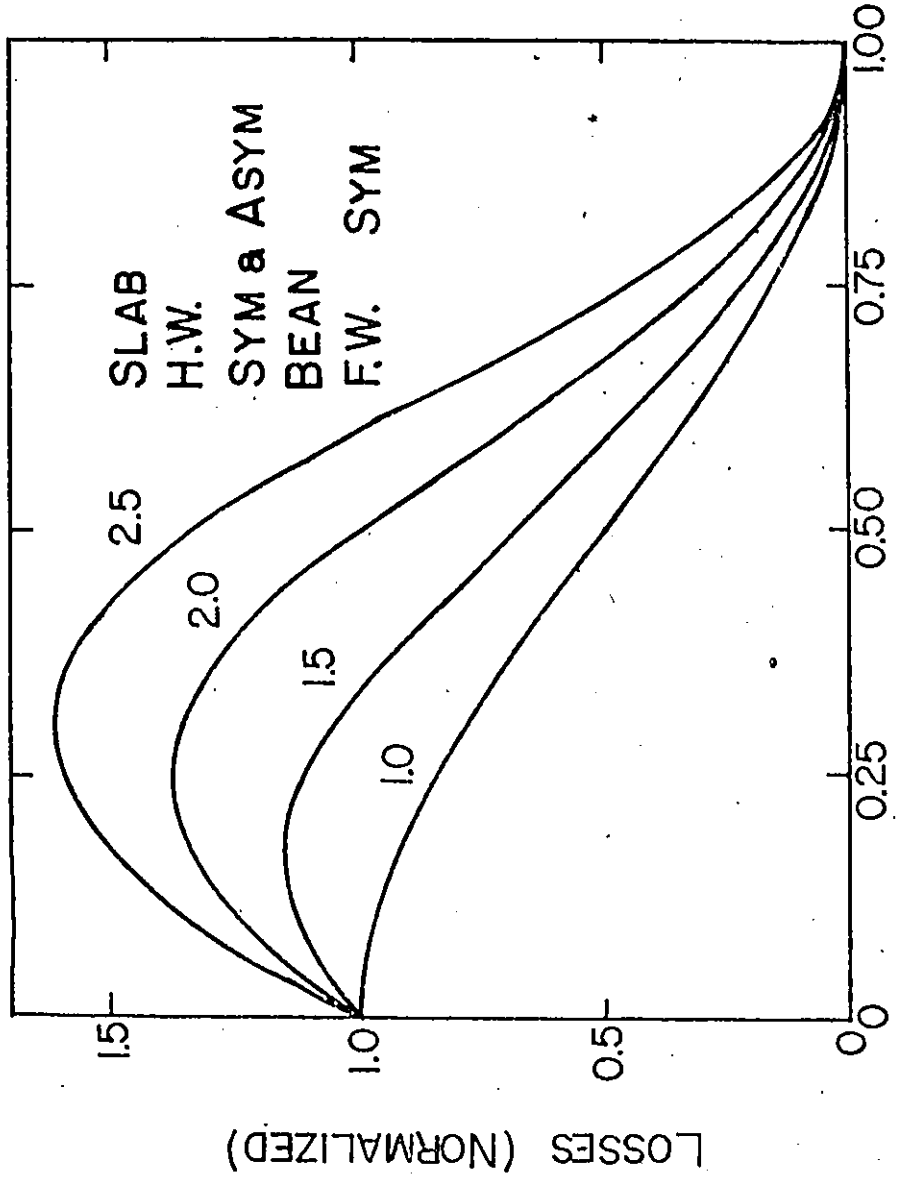

FIG. 6.5 Calculations of hysteresis losses (normalized vs. the height of the constant symmetric barrier normalized to the amplitude of oscillation $\Delta H'/h_o$ (or $\Delta H''/2h_o$ for an asymmetric barrier) for cases 1a, 1b and 1c of table 6.1 with c = 1.0, 1.5, 2.0 and 2.5.

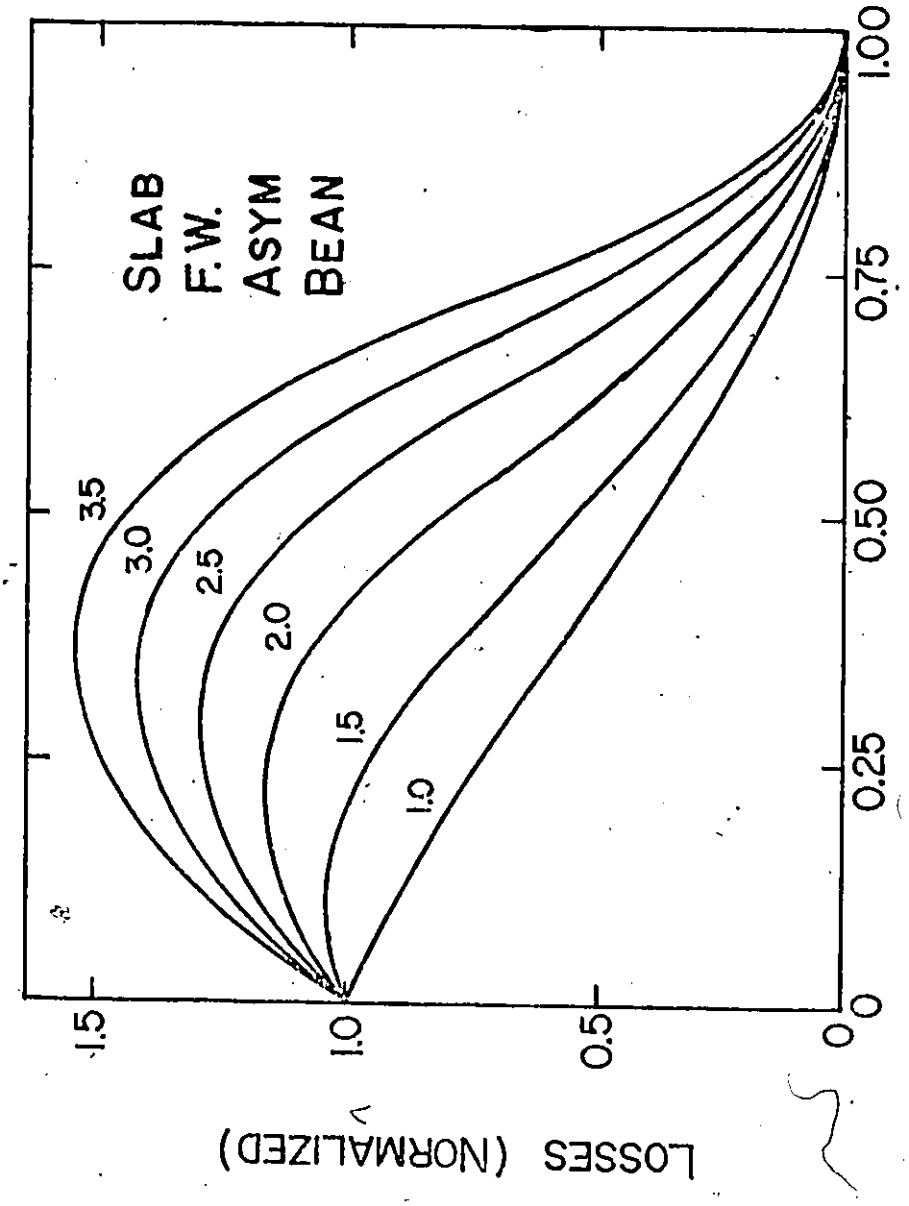

FIG. 6.6 Calculations of hysteresis losses (normalized) vs. the height of the constant asymmetric barrier (normalized) for case 2 of table 6.1 with c = 1.0, 1.5, 2.0, 2.5, 3.0 and 3.5.

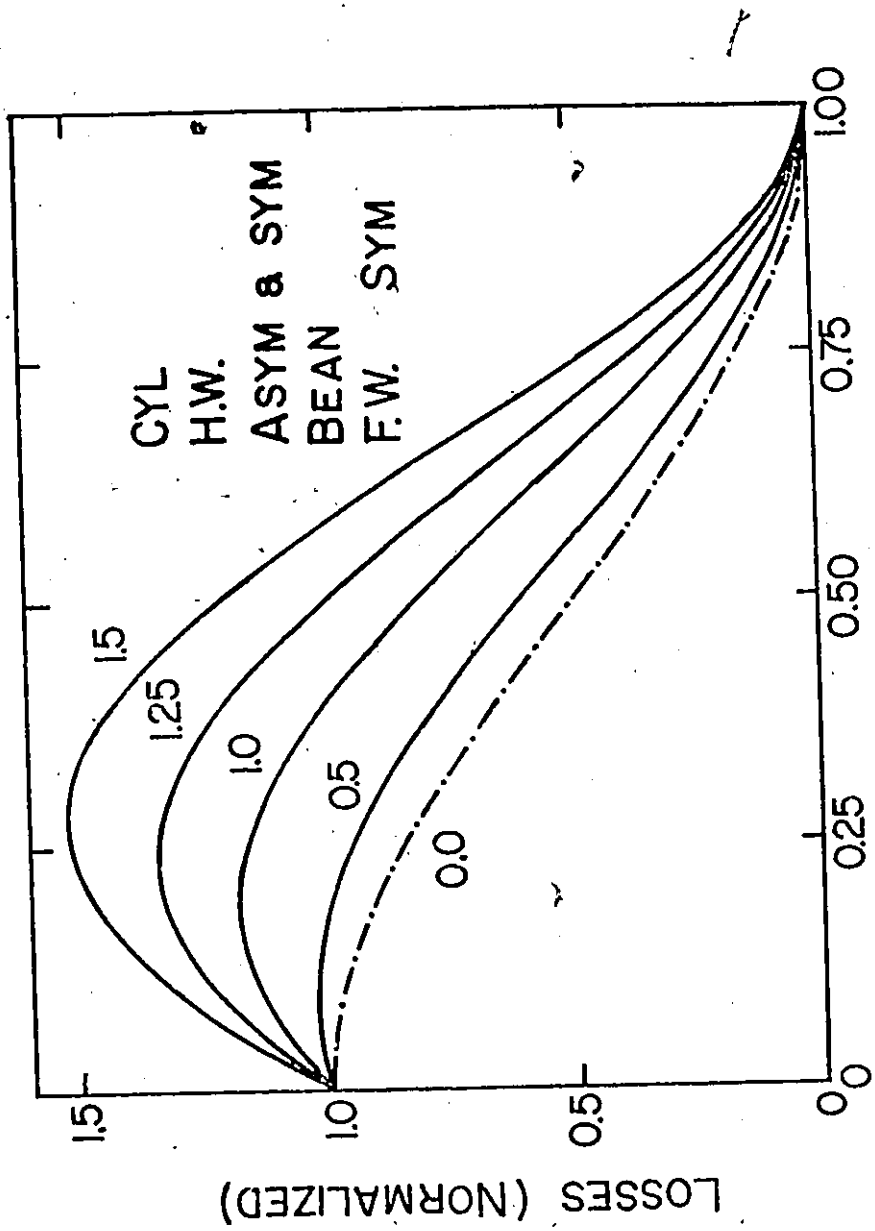

FIG. 6.7 Same as Fig. 6.5 for cases 3a, 3b and 3c of table 6.1 with c = 0, 0.5, 1.0, 1.25 and 1.5. The dashed curve indicates superficial penetration for cylindrical geometry (c = 0) corresponding to c ≤ 1 for planar geometry.

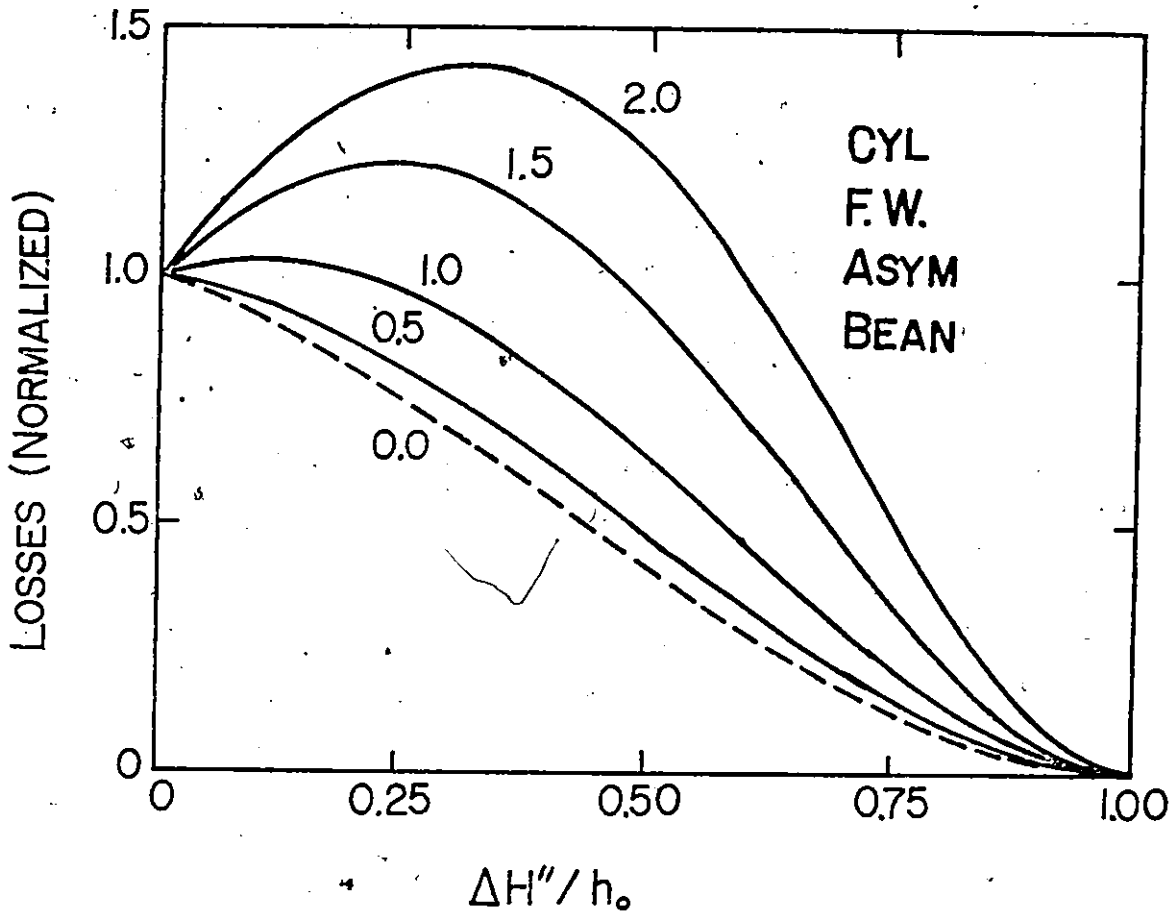

FIG. 6.8 Same as Fig. 6.6 for case 4 of table 6.1 with c = 0, 0.5, 1.0, 1.5 and 2.0. The dashed curve indicates superficial penetration for cylindrical geometry (c = 0) corresponding to c ≤ 1 for planar geometry.

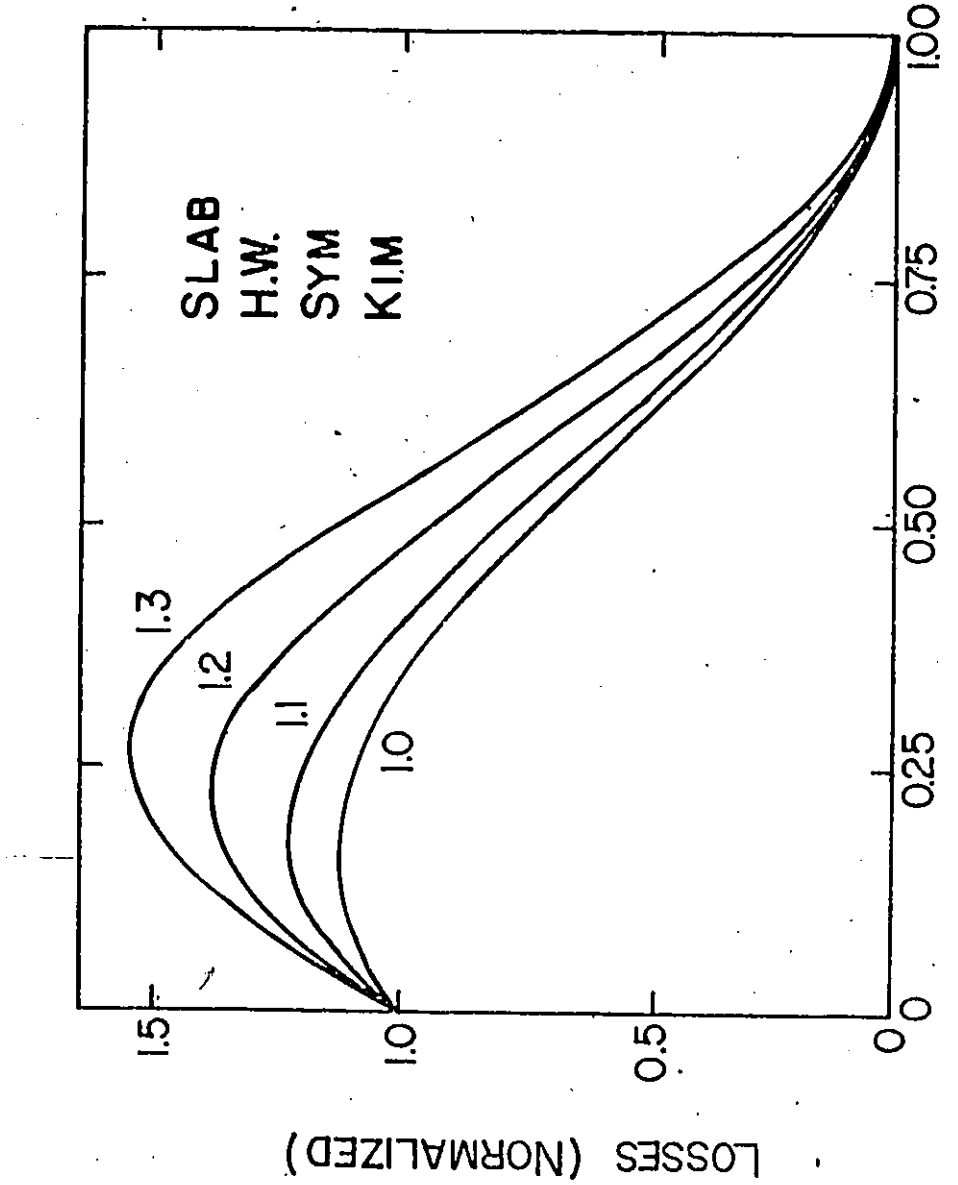

FIG. 6.9 Calculations of hysteresis losses (normalized) vs. the height of the constant symmetric barrier (normalized) for case 5 of table 6.1 with c = 1.0, 1.1, 1.2 and 1.3.

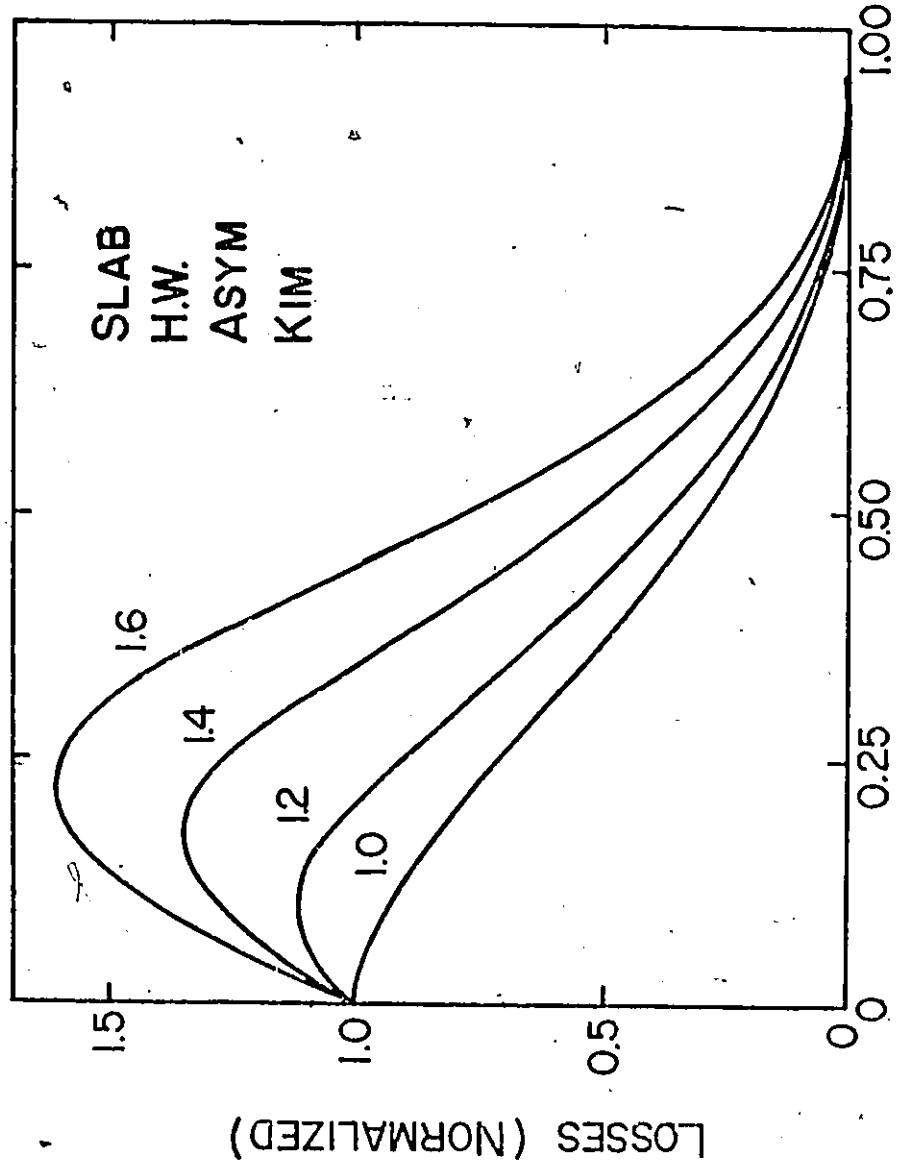

FIG. 6.10 Calculations of hysteresis losses (normalized) vs. the height of the constant asymmetric barrier (normalized) for case 6 of table 6.1 with c = 1.0, 1.2, 1.4 and 1.6.

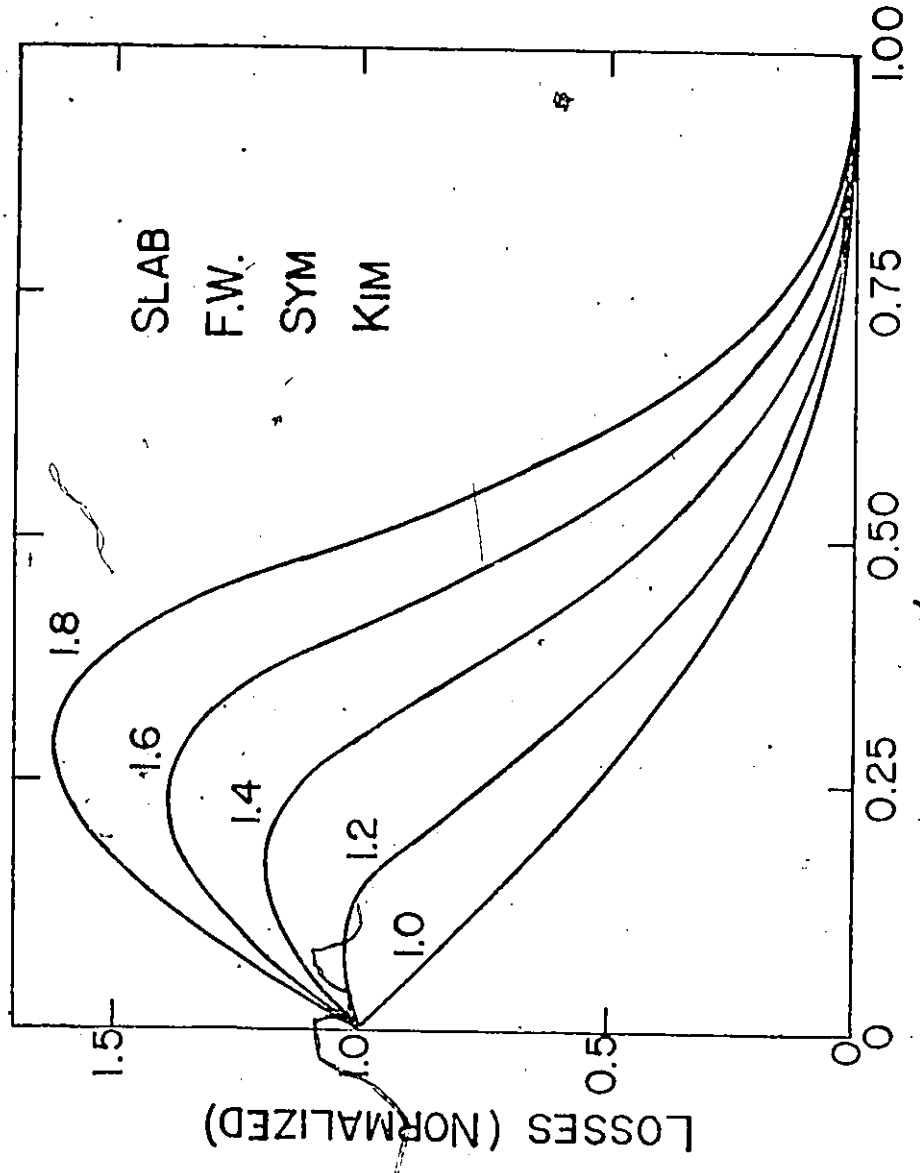

FIG. 6.11 Same as Fig. 6.9 for case 7 of table 6.1.with c = 1.0, 1.2, 1.4, 1.6 and 1.8.

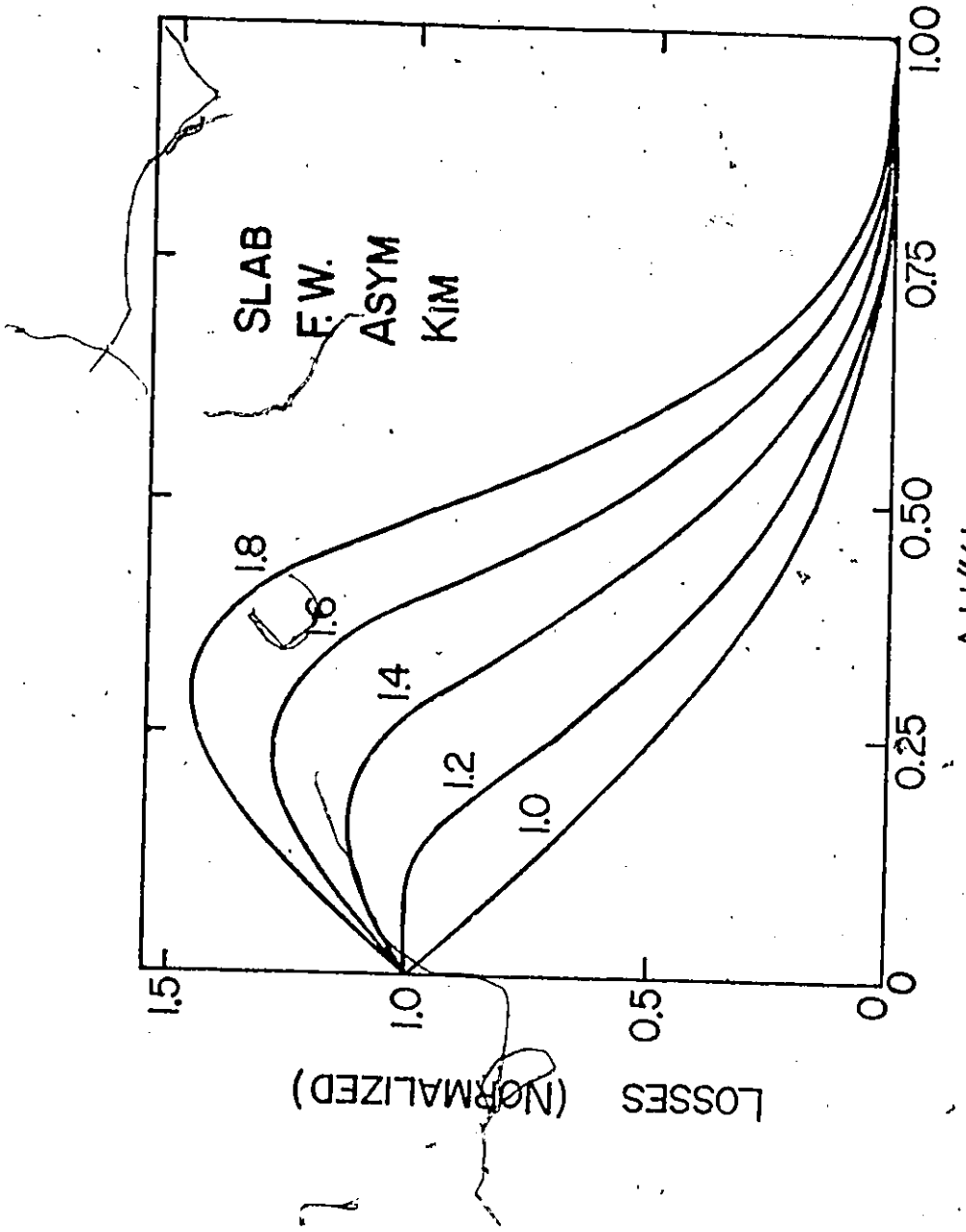

FIG. 6.12 Same as Fig. 6.10 for case 8 of table 6.1 with c = 1.0, 1.2, 1.4, 1.6 and 1.8.

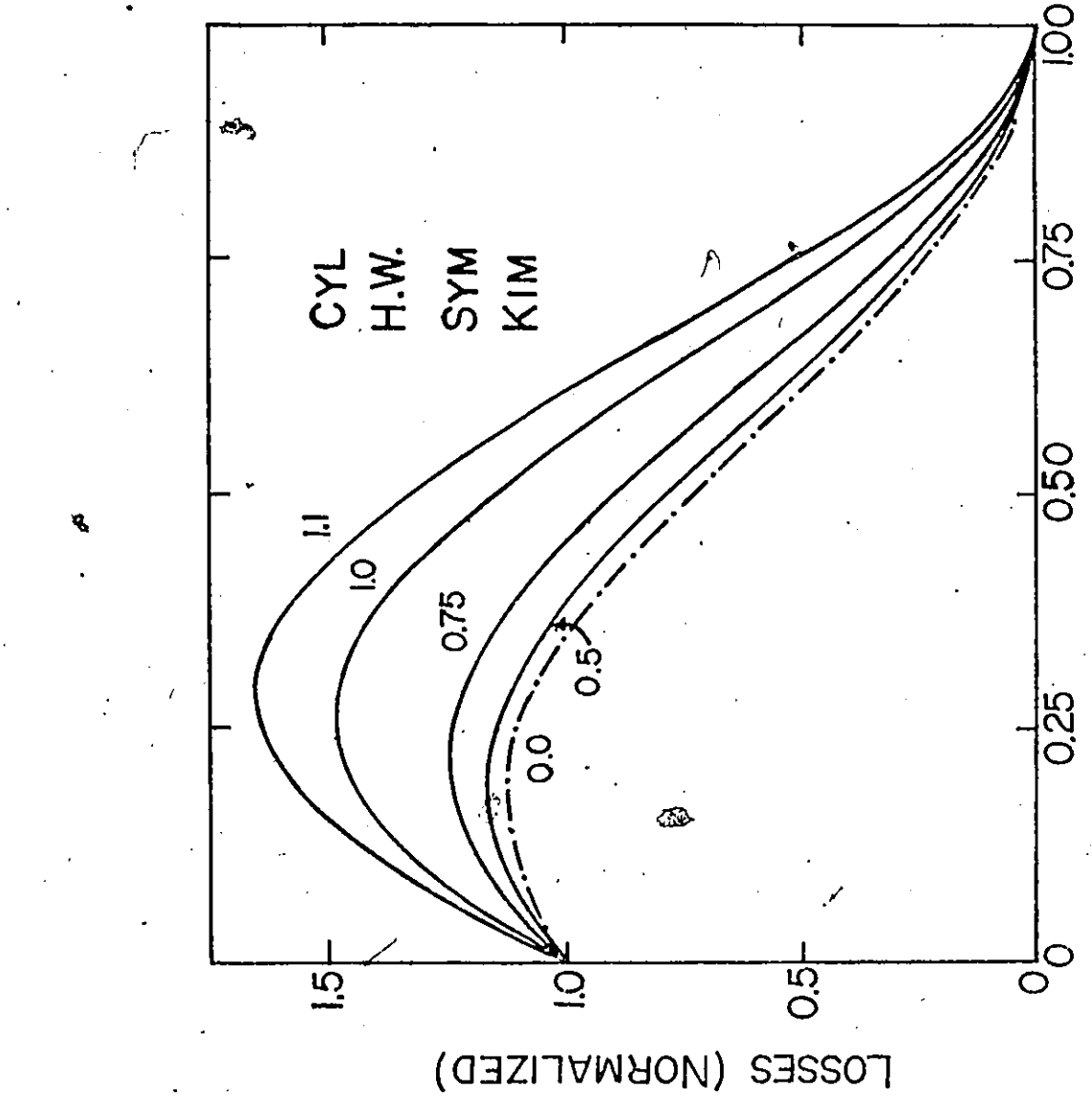

FIG. 6.13 Same as Fig. 6.9 for case 9 of table 6.1 with c = 0, 0.5, 0.75, 1.0 and 1.1. The dashed curve has the same meaning as in Fig. 6.7.

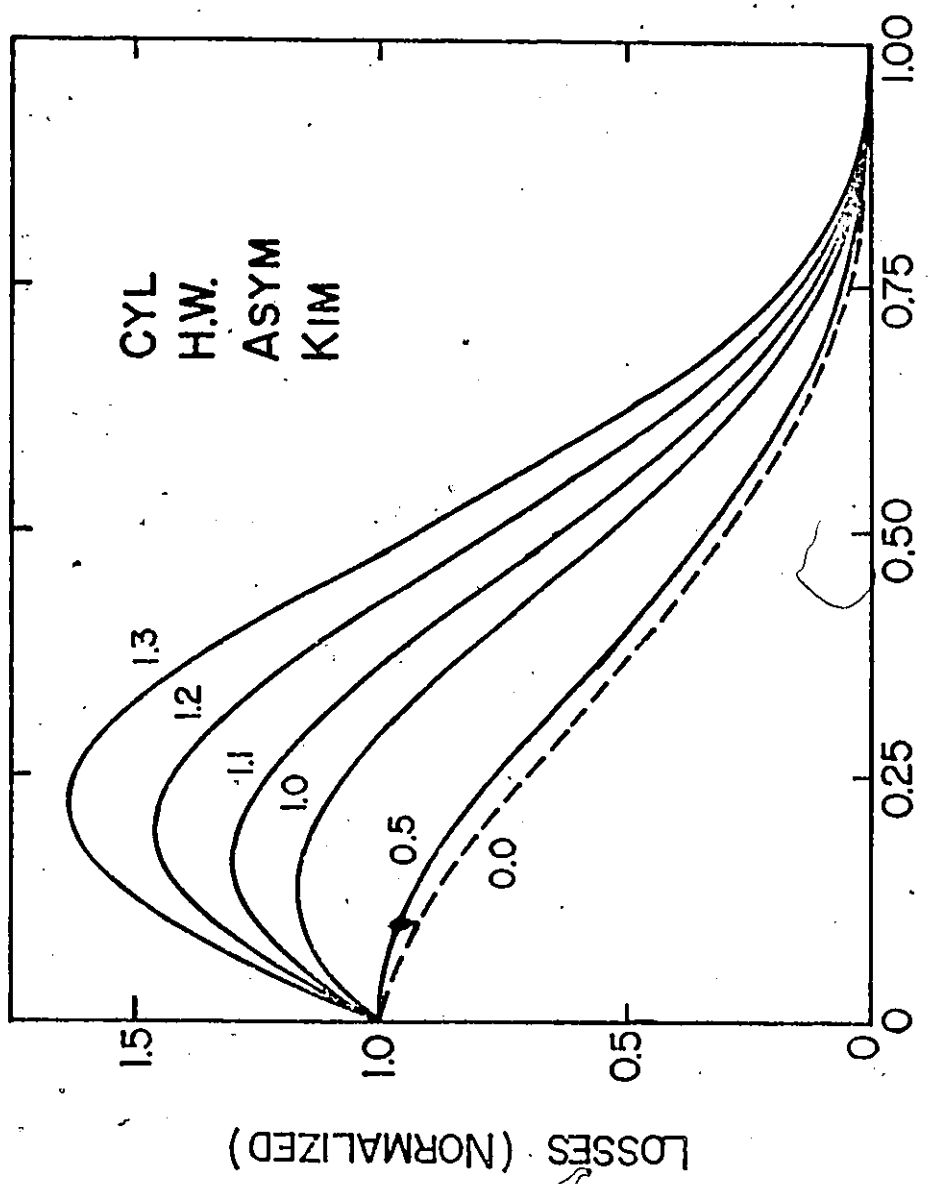

FIG. 6.14 Same as Fig. 6.10 for case 10 of Table 6.1 with c = 0, 0.5, 1.0, 1.1, 1.2 and 1.3. The dashed curve has the same meaning as in Fig. 6.7.

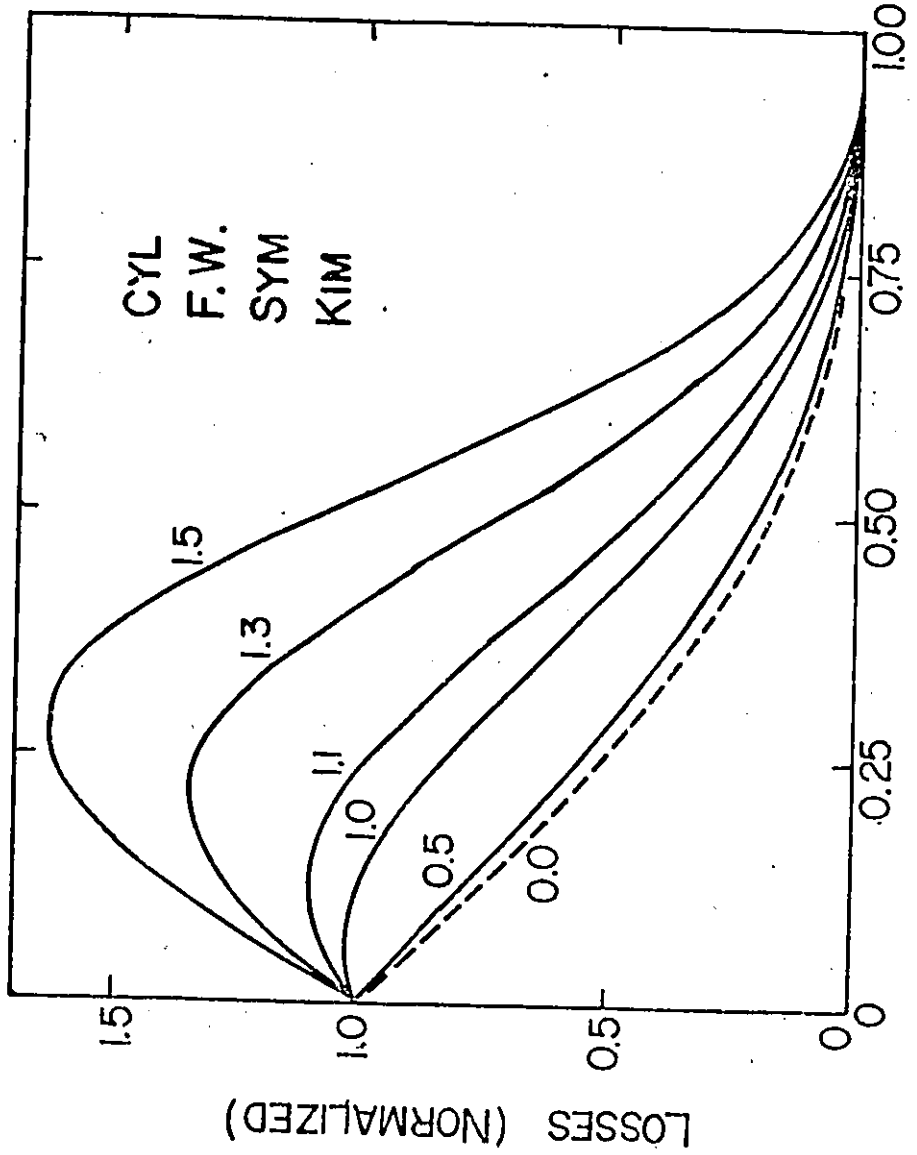

FIG. 6.15 Same as Fig. 6.11 for case 11 of table 6.1 with c = 0, 0.5, 1.0, 1.1, 1.3 and 1.5. The dashed curve has the same meaning as in Fig. 6.7.

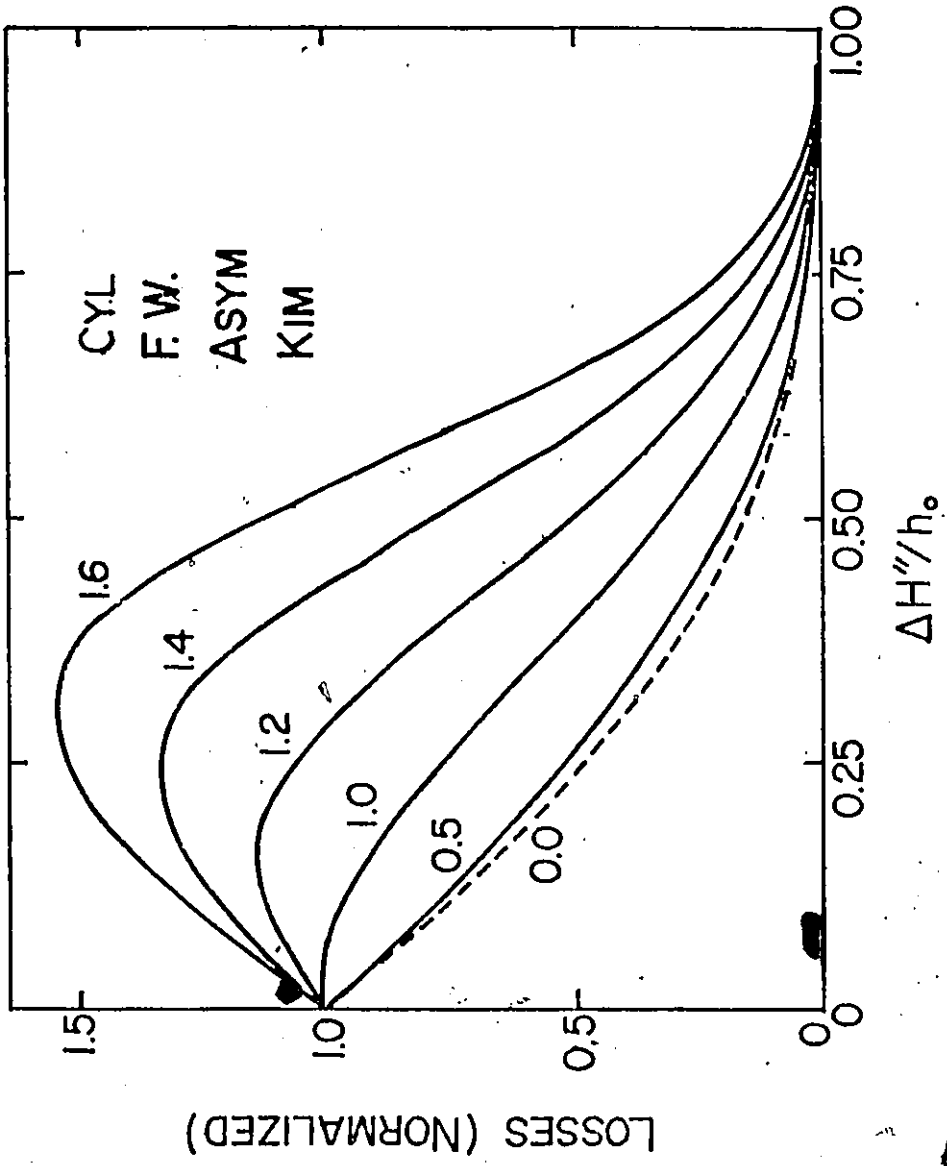

FIG. 6.16 Same as Fig. 6.12 for case 12 of table 6.1 with c = 0, 0.5, 1.0, 1.2, 1.4 and 1.6. The dashed curve has the same meaning as in Fig. 6.7.

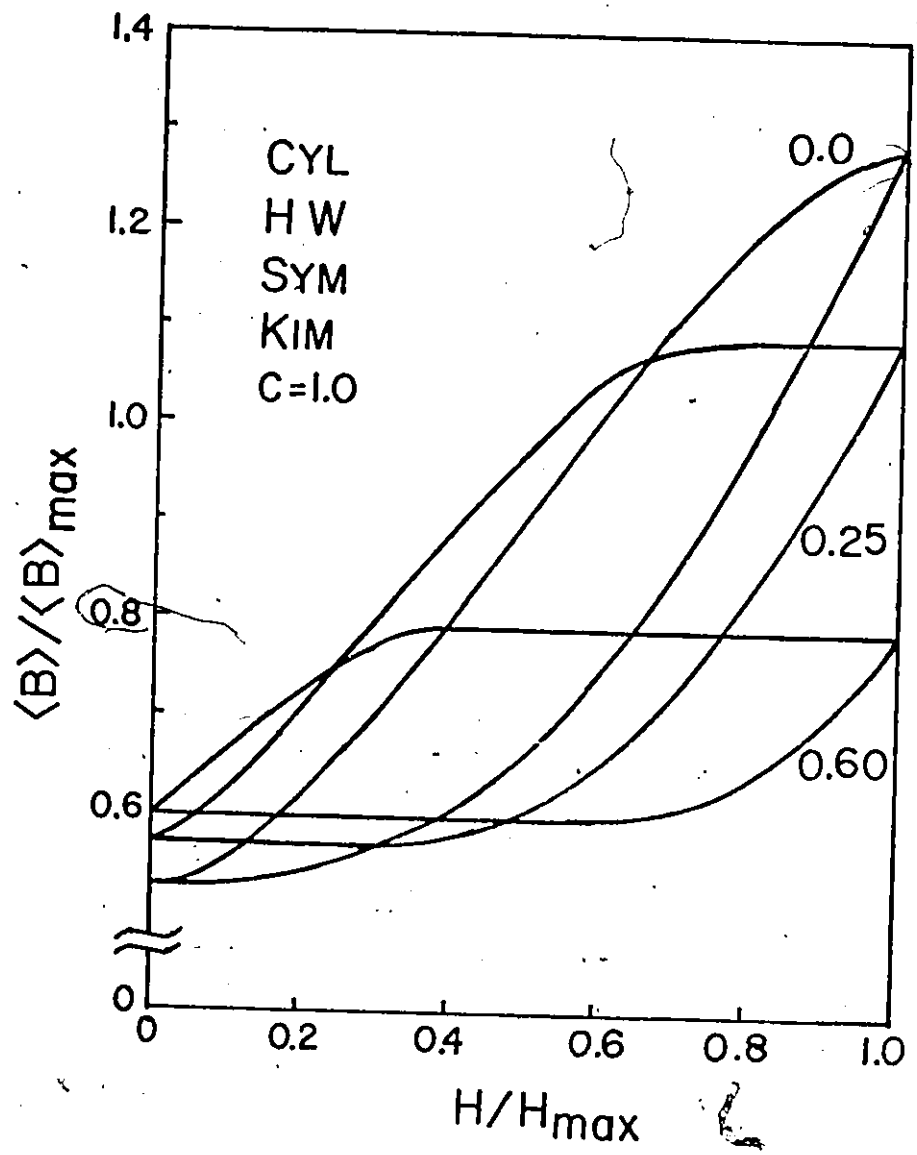

FIG. 6.17 Hysteresis loops calculated for case 9 of table 6.1 with $\Delta H'/h_o$ = 0, 0.25 and 0.60.

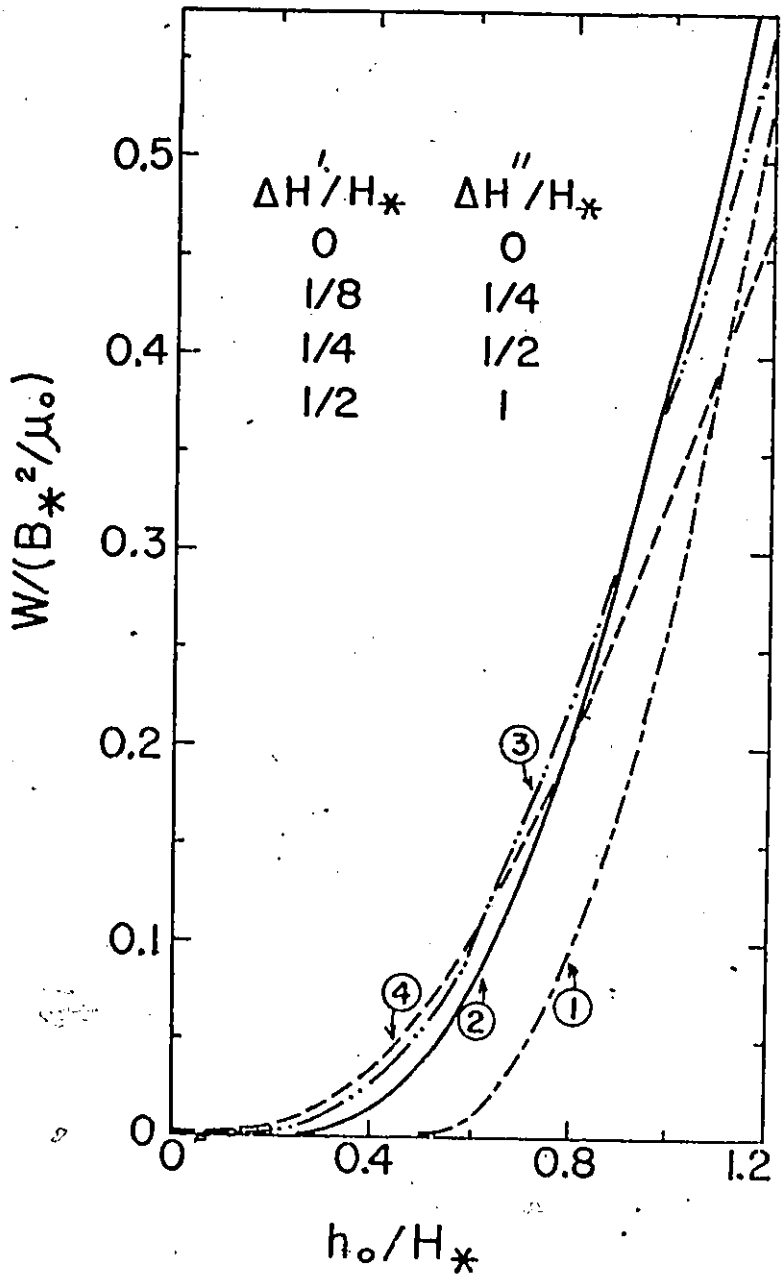

FIG. 6.18 W vs. h_o calculated for case 9 of table 6.1.

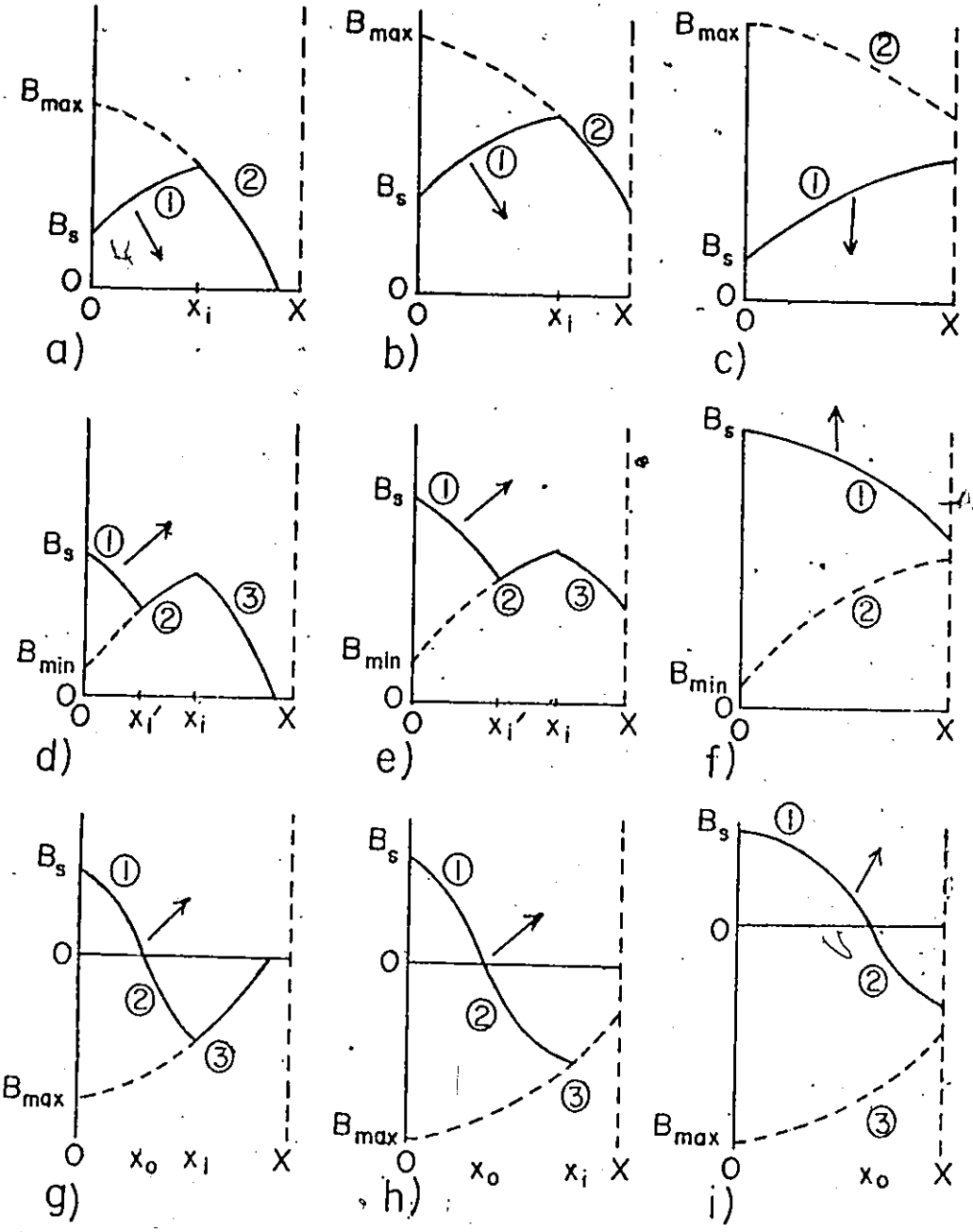

FIG. 6.19 Schematic of different categories of B profiles encountered during half-wave and full-wave cycles of amplitudes lying above and below saturation.

SUMMARY AND FUTURE DIRECTION

We have investigated magnetic behaviour and hysteresis losses in type II superconductors in the classical arrangement where a time varying magnetic field, h_o f(t), is superimposed upon and directed along a static bias magnetic field H_b. We denote this as the collinear regime. We have also pursued these phenomena in the less familiar but very fundamental situation where $\vec{h}_o$ f(t) is directed perpendicularly to $\vec{H}_b$ or tilted with respect to the latter. The latter arrangements are denoted the noncollinear regime. In both regimes, flux lines undergo compression or decompression as they are made to enter or leave the specimen and are displaced within its bulk. In the noncollinear regime however, the experimental observations indicate unambiguously that a significant rearrangement in the orientation of the flux lines takes place during their migrations. Flux line cutting is believed to be the mechanism whereby these changes in configuration can occur. Our measurements therefore provide insight into the sequence of intricate flux configurations which ensue from the operation of this intriguing and novel process.

We examine the magnetic response of ribbon samples where $\vec{H}_b$ and $\vec{h}_o$ f(t) are directed along the flat surfaces of the specimens. For expediency $\vec{h}_o$ f(t) is directed either along the length or along the width of the ribbon. Also for simplicity, we let the main component of the fixed bias magnetic field be directed either along the width

or length of the ribbon and perpendicular to $\vec{h}_o$ f(t). Our arrangement is not only convenient experimentally but corresponds to the situation encountered when a ribbon carries a transport current in a stationary longitudinal magnetic field.

In chapter 3 we compare our observations with the predictions of a model originally proposed by Campbell and Evetts. They put forward the idea that in the noncollinear regime, the flux lines migrate within the sample at the angle they possessed when they were created and when they entered the sample at its surfaces. We show that as the total external magnetic field $\vec{H}_s$ increases in magnitude and changes its orientation θ_s, this concept does provide an adequate description of the initial behaviour but that the data and the predictions progressively diverge as the change in θ_s and H_s becomes significant. We show that these deviations cannot be attributed to any B dependence of the bulk pinning but are an intrinsic feature of the model. Essentially then the model fails because its basic premise that the flux lines maintain their initial orientation is invalid.

Consequently the idea that vortices do not rotate as they are made to migrate and are caused to undergo changes in density is abandoned.

In chapter 4 a vast assortment of observations of hysteresis losses and magnetic responses of ribbons of VTi and Nb in the noncollinear regime is analyzed exploiting an alternate proposal of Lachaine, referred to as the double critical state concept. According

to this idea, the gradients in the density of the flux lines and in the spatial variation of their orientation exist in critical configurations whenever changes in these quantities have occurred. We pursue this idea in the simple context that the density gradient dB/dx may depend on B but not on $\theta(x)$, the orientation configuration of the sheets of flux lines. We present the major milestones in our empirical search for a simple analytic prescription for the critical orientation gradient $d\theta/dx$. We find that the formula

$$\frac{d\theta}{dx} = \pm \frac{k\, F_P}{B^2\, (1 + |\theta|)^2}$$

in tandem with the standard critical state expression

$$\frac{dB}{dx} = \pm \frac{F_P}{B}$$

provide the most satisfactory description of our extensive data. We regard $\theta = 0$ to be determined by the stationary component of $\vec{H}_s$. This view is tested and supported by performing two sets of measurements, one where the stationary component of $\vec{H}_s$ lies along the length and another where it lies along the width of the samples.

A profound modification of our simple double critical state approach has recently been developed by Clem from fundamental considerations. His framework examines $\vec{E}(x)$, the electric fields generated as the configuration of flux lines and the associated quasi-macroscopic persistent current density pattern are caused to change. The model

visualizes critical levels (possibly B dependent) exist separately for $j_\perp$ and $j_{//}$, the critical current densities perpendicular and parallel to B(x). We note that $j_\perp$ corresponds to dB/dx and $j_{//}$ to B $d\theta/dx$. A crucial consequence of the model is that two additional types of regions, ignored in our approach, can be encountered, namely, regions where (i) dB/dx is critical but B $d\theta/dx$ is subcritical and (ii) B $d\theta/dx$ is critical but dB/dx is subcritical. Which of the three possible types of region occurs and the level of the subcritical quantity which arises are determined by a systematic and basic consideration of $\vec{E}(x)$, $\vec{B}(x)$ and $\vec{j}(x)$, the angle subtended by these various quantities as well as the requirement that the components of $\vec{E}(x)$ and $\vec{B}(x)$ be continuous. Clearly our data need to be reexamined in the light of this model. This formidable task has already been launched.

Another difficult, but basic and technologically important problem which awaits scrutiny is the behaviour of the surface step in the noncollinear regime.

In chapter 5 we focus on the contribution of bulk pinning alone to the valley in hysteresis losses, $W(h_o, H_b)$ versus H_b, predicted by Clem for the collinear regime and first reported by him and co-workers. We show that this contribution alone can account for our data on a VTi ribbon. In the light of this result we pursue computationally the influence of distinct types of B profiles, which bracket the range generally envisaged, and the role of geometry on the structure of the valley.

In chapter 6 we conduct an extensive computational investigation of the effect of a surface step (surface barrier) on hysteresis losses in the collinear regime. To obtain a complete picture we construct an inventory of basic cases. We accomplish this by introducing two radically different and extreme types of surface steps (denoted symmetric and asymmetric). We also examine the behaviour when the sample is subjected to full-wave ($H_b = 0$) and half-wave ($H_b = h_o$) oscillations.

We explore the full range of amplitudes causing the B disturbance to penetrate only partially into the sample and also those large enough to considerably exceed full penetration levels. We bracket the spectrum of accepted B profiles by exploiting two well established but extremal approximations, namely $dB/dx = \pm\alpha$ and $dB/dx = \pm\alpha/B$. Further we pursue the problem for both infinite slab and cylinder geometry. For simplicity, however, we have chosen a B independent surface step. A startling and important message which emerges from this thorough study is that very frequently the hysteresis losses can be diminished by lowering the surface barrier.

Evidently this work should be extended to the more realistic situation where the barrier diminishes as B increases. Of course, a variety of B dependences incorporating this basic feature need to be envisaged. A preliminary study reveals the dramatic result that the decrease in losses by a lowering of the barrier is accentuated.

APPENDIX I

We list expressions for $\langle B \rangle$ and $d\langle B \rangle / dB_s$ applicable to an infinite slab in various initial magnetic states and where the pinning can be described by $F_p = \alpha_n B^n$ with n = 0 or 1. The evolution of the B profiles for the different configurations are sketched in Figure I - 1 of this appendix. The expressions for $d\langle B \rangle / dB_s$ can be obtained by differentiation of $\langle B \rangle$ or by exploiting equation (3.30).

A) Before saturation

i) Diamagnetic Initial State

a) n = 1

$$B(x) = B_s - B_*\left(\frac{x}{a}\right) \quad \text{for} \quad 0 \le \frac{x}{a} \le \frac{x_i}{a} = \frac{B_s}{B_*}$$

$$B(x) = 0 \quad \text{for} \quad \frac{B_s}{B_*} = \frac{x_i}{a} \le \frac{x}{a} \le 1$$

$$\text{(I - 1)} \qquad \langle B \rangle = \frac{B_s^2}{2B_*}$$

$$\text{(I - 2)} \qquad \frac{d\langle B \rangle}{dB_s} = \frac{B_s}{B_*}$$

which apply when $0 < B_s \le B_*$ where $B_* = \alpha_1 a$

b) n = 0

$$B(x) = \left(B_s^2 - B_*^2\left(\frac{x}{a}\right)\right)^{1/2} \quad \text{for} \quad 0 \le \frac{x}{a} \le \frac{x_i}{a} = \left(\frac{B_s}{B_*}\right)^2$$

$$B(x) = 0 \quad \text{for} \quad \left(\frac{B_s}{B_*}\right)^2 = \frac{x_i}{a} \le \frac{x}{a} \le 1$$

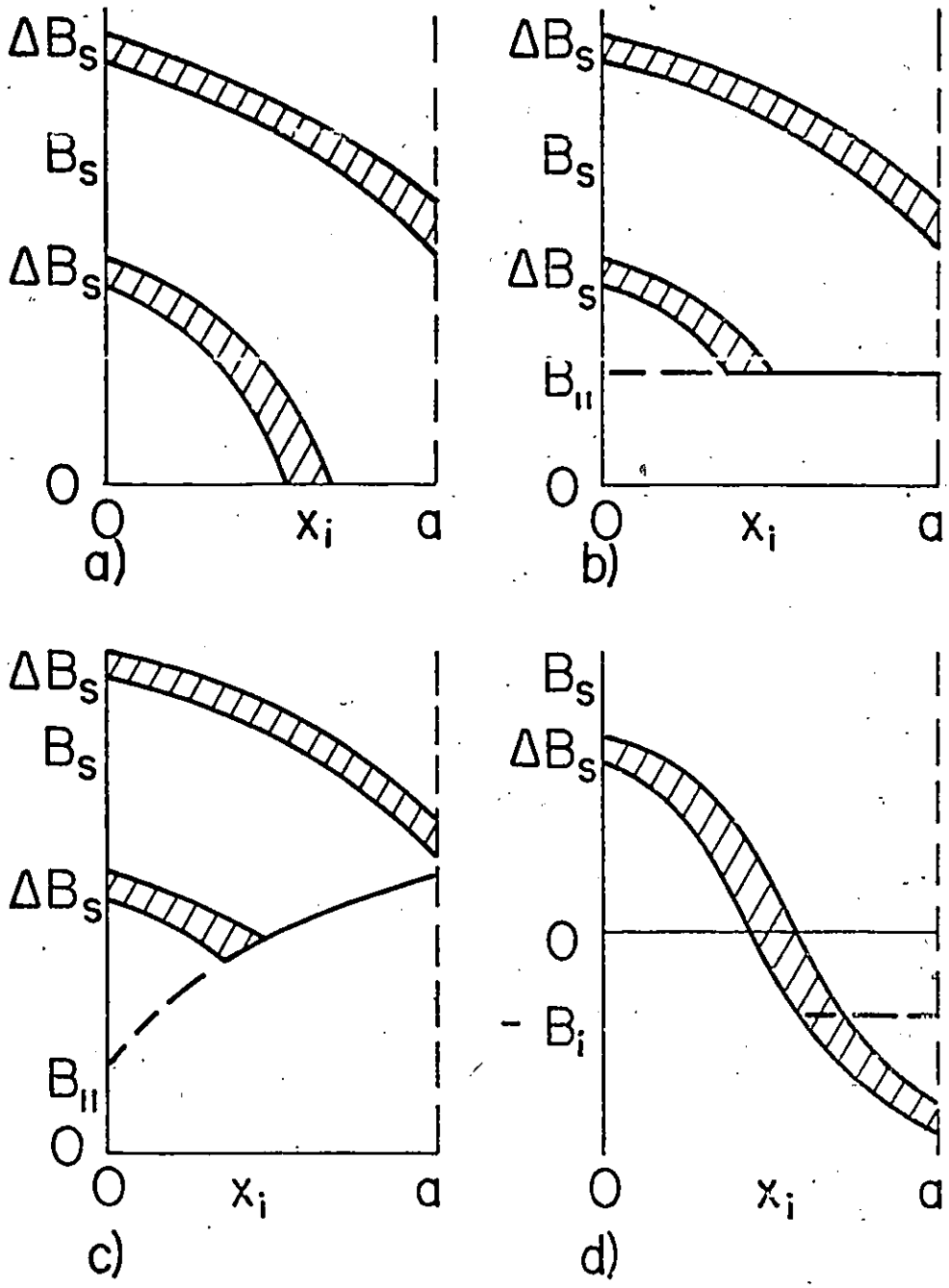

FIG. I - 1 Schematic of increments of B profiles before and after saturation where the initial configuration or state is a) diamagnetic, b) nonmagnetic c) paramagnetic and d) hybrid.

$$(I - 3) \qquad \langle B \rangle = \frac{2}{3} \frac{B_s^3}{B_*^2}$$

$$(I - 4) \qquad \frac{d\langle B \rangle}{dB_s} = 2\left(\frac{B_s}{B_*}\right)^2$$

which apply when $0 < B_s \leq B_*$ where $B_* = (2\alpha_o a)^{\frac{1}{2}}$

ii) Nonmagnetic Initial State

a) n = 1

$$B(x) = B_{//} \text{ for } \frac{(B_s - B_{//})}{B_*} = \frac{x_i}{a} \leq \frac{x}{a} \leq 1$$

$$(I - 5) \qquad \langle B \rangle = \frac{(B_s - B_{//})^2}{2B_*} + B_{//}$$

$$(I - 6) \qquad \frac{d\langle B \rangle}{dB_s} = \frac{B_s - B_{//}}{B_*}$$

which apply when $B_{//} \leq B_s \leq (B_* + B_{//})$

b) n = 0

$$B(x) = B_{//} \text{ for } \frac{B_s^2 - B_{//}^2}{B_*^2} = \frac{x_i}{a} \leq \frac{x}{a} \leq 1$$

$$(I - 7) \qquad \langle B \rangle = \frac{2}{3} \frac{(B_s^3 - B_{//}^3)}{B_*^2} - B_{//} \frac{(B_s^2 - B_{//}^2)}{B_*^2} + B_{//}$$

$$(I - 8) \qquad \frac{d\langle B \rangle}{dB_s} = 2 \frac{B_s}{B_*} \left(\frac{B_s - B_{//}}{B_*}\right)$$

which apply when $B_{//} \leq B_s \leq (B_*^2 + B_{//}^2)^{\frac{1}{2}}$

iii) Paramagnetic Initial State

a) n = 1

$$B(x) = B_{//} + B_*\left(\frac{x}{a}\right) \quad \text{for} \quad \frac{B_s - B_{//}}{2B_*} = \frac{x_i}{a} \leq \frac{x}{a} \leq 1$$

$$(I - 9) \quad \langle B \rangle = \frac{1}{4}\frac{(B_s - B_{//})^2}{B_*} + \frac{B_*}{2} + B_{//}$$

$$(I - 10) \quad \frac{d\langle B \rangle}{dB_s} = \frac{B_s - B_{//}}{2B_*}$$

which apply when $B_{//} \leq B_s \leq (B_{//} + 2B_*)$

b) n = 0

$$B(x) = \left(B_{//}^2 + B_*^2\left(\frac{x}{a}\right)\right)^{1/2} \quad \text{for} \quad \frac{B_s^2 - B_{//}^2}{2B_*^2} = \frac{x_i}{a} \leq \frac{x}{a} \leq 1$$

$$(I - 11) \quad \langle B \rangle = \frac{2}{3B_*^2}\left\{ B_s^3 - 2\left(\frac{B_s^2 + B_{//}^2}{2}\right)^{3/2} + \left(B_{//}^2 + B_*^2\right)^{3/2} \right\}$$

$$(I - 12) \quad \frac{d\langle B \rangle}{dB_s} = 2\frac{B_s}{B_*^2}\left\{ B_s - \left(\frac{B_s^2 + B_{//}^2}{2}\right)^{1/2} \right\}$$

which apply when $B_{//} \leq B_s \leq \left(B_{//}^2 + 2B_*^2\right)^{1/2}$

iv) Hybrid Initial State

a) n = 1

$$B(x) = -B_i \quad \text{for} \quad \frac{B_s + B_i}{B_*} = \frac{x_i}{a} \leq \frac{x}{a} \leq 1$$

$$(I-13)\quad \langle B\rangle = \frac{(B_s + B_i)^2}{2B_*} - B_i$$

$$(I-14)\quad \frac{d\langle B\rangle}{dB_s} = \frac{B_s + B_i}{B_*}$$

which apply when $0 \le B_s < (B_* - B_i)$ and $B_i < B_*$.

If $x_i/a = 1$ (see Fig. 3.35(d)), there is no region with $B(x) = -B_i$

$$(I-15)\quad \langle B\rangle = B_s - \frac{B_*}{2}$$

$$(I-16)\quad \frac{d\langle B\rangle}{dB_s} = 1$$

b) $n = 0$

$$B(x) = -(B_*^2(\frac{x}{a}) - B_s^2)^{\frac{1}{2}}$$

for $$(\frac{B_s}{B_*})^2 = \frac{x_o}{a} \le \frac{x}{a} \le \frac{x_i}{a} = \frac{B_i^2 + B_s^2}{B_*^2}$$

$$B(x) = -B_i \quad \text{for} \quad \frac{x_i}{a} \le \frac{x}{a} \le 1$$

$$(I-17)\quad \langle B\rangle = \frac{2}{3B_*^2}(B_s^3 - B_i^3) + \frac{B_i}{B_*^2}(B_s^2 - B_*^2 + B_i^2)$$

$$(I-18)\quad \frac{d\langle B\rangle}{dB_s} = \frac{2}{B_*^2} B_s(B_s + B_i)$$

which apply when $0 < B_s \le (B_*^2 - B_i^2)^{\frac{1}{2}}$.

If there is no region with $B(x) = -B_i$ then $x_i/a = 1$ and

$$(I - 19) \qquad \langle B \rangle = \frac{2}{3B_*^2} \left\{ B_s^3 - (B_*^2 - B_s^2)^{3/2} \right\}$$

$$(I - 20) \qquad \frac{d\langle B \rangle}{dB_s} = \frac{2}{B_*^2} B_s \left\{ B_s + (B_*^2 - B_s^2)^{1/2} \right\}$$

which apply when $0 \leq B_s \leq B_*$.

B) After saturation

When the front of the advancing disturbance in the B profile has attained the midplane, the initial configuration has been erased and ceases to play any role.

a) $n = 1$

$$(I - 21) \qquad \langle B \rangle = B_s - \frac{B_*}{2}$$

$$(I - 22) \qquad \frac{d\langle B \rangle}{dB_s} = 1$$

b) $n = 0$

$$(I - 23) \qquad \langle B \rangle = \frac{2}{3B_*^2} \left\{ B_s^3 - (B_s^2 - B_*^2)^{3/2} \right\}$$

$$(I - 24) \qquad \frac{d\langle B \rangle}{dB_s} = 2 \frac{B_s}{B_*^2} \left\{ B_s - (B_s^2 - B_*^2)^{1/2} \right\}$$

APPENDIX II

In many instances equations (3.28) and (3.29) can be integrated analytically. We list expressions for $\mu_o \langle M_{//} \rangle = \langle B_z \rangle - B_{//}$ and $\mu_o \langle M_{\perp} \rangle = \langle B_y \rangle - B_{\perp}$ for the case where $F_p = \alpha_n B^n$ with $n = 0$ or 1 where $B_* = \alpha_1 a$ and $(2\alpha_o a)^{\frac{1}{2}}$ respectively. We consider only the situation where the initial state is nonmagnetic and $B_{//}$ is maintained constant as B_s increases.

A) Before saturation

a) $n = 1$

$$(II - 1) \quad \mu_o \langle M_{//} \rangle = \frac{B_{//}}{B_*} \{ (B_s - B_{//}) - B_{//} \ln \frac{B_s}{B_{//}} \}$$

$$(II - 2) \quad \mu_o \langle M_{\perp} \rangle = \frac{1}{B_*} \{ \frac{B_{\perp} B_s}{2} - \frac{B_{//}^2}{2} \ln \left(\frac{B_{\perp} + B_s}{B_{//}} \right) - B_{//} B_{\perp} + B_{//}^2 \cos^{-1} \frac{B_{//}}{B_s} \} - B_{\perp}$$

b) $n = 0$

$$(II - 3) \quad \mu_o \langle M_{//} \rangle = \frac{B_{//}}{B_*^2} (B_s - B_{//})^2$$

$$(II - 4) \quad \mu_o \langle M_{\perp} \rangle = \frac{1}{B_*^2} \{ 2 \frac{B_{\perp}^3}{3} - B_{\perp} B_{//} B_s + B_{//}^3 \ln \left(\frac{B_{\perp} + B_s}{B_{//}} \right) \} - B_{\perp}$$

B) After saturation

a) $n = 1$

$$(II - 5)\quad \mu_o \langle M_{//} \rangle = B_{//} \{1 - \frac{B_{//}}{B_*} \ln (1 + \frac{B_*}{B_{//}}) + \ln (\frac{B_s}{B_{//} + B_*})\}$$

$$(II - 6)\quad \mu_o \langle M_{\perp} \rangle = \frac{1}{B_*} \{ \frac{B_{\perp}^{*}(B_{//} + B_*)}{2} - \frac{B_{//}^{2}}{2} \ln (\frac{B_{\perp}^{*} + B_{//} + B_*}{B_{//}})$$

$$- B_{//} B_{\perp}^{*} + B_{//}^{2} \cos^{-1} (\frac{B_{//}}{B_{//} + B_*}) \}$$

$$+ \{B_{//} (\cos^{-1} \frac{B_{//}}{B_{//} + B_*} - \cos^{-1} \frac{B_{//}}{B_s}) \} - B_{\perp}^{*}$$

where $B_{\perp}^{*} = \{ B_*(2 B_{//} + B_*) \}^{\frac{1}{2}}$

b) $n = 0$

$$(II - 7)\quad \mu_o \langle M_{//} \rangle = \frac{B_{//}}{B_*^{2}} \{ B_s^{2} + B_{//}^{2} - B_{//} \sqrt{B_{//}^{2} + B_*^{2}} - B_s \sqrt{B_s^{2} - B_*^{2}}$$

$$+ B_*^{2} \ln (\frac{B_s + \sqrt{B_s^{2} - B_*^{2}}}{B_{//} + \sqrt{B_{//}^{2} + B_*^{2}}}) \}$$

$$(II - 8)\quad \mu_o \langle M_{\perp} \rangle = \frac{1}{B_*^{2}} \{ \frac{2}{3} B_*^{3} - B_* B_{//} \sqrt{B_{//}^{2} + B_*^{2}}$$

$$+ B_{//}^{3} \ln \frac{B_* + \sqrt{B_{//}^{2} + B_*^{2}}}{B_{//}} \}$$

$$- B_{\perp} - \frac{2}{B_*^{2}} \int_{(B_{//}^{2} + B_*^{2})^{\frac{1}{2}}}^{B_s} \sqrt{(B_s^{2} - B_{//}^{2})(B_s^{2} - B_*^{2})}\, dB_s$$

Analytic expressions for the latter integral involve elliptic integrals of the first and second kind. We refer the reader to the Table of Integrals, Series, and Products by I.S. Gradshteyn and I.M. Ryzhik, 4th Ed. p. 248 Equation 3.155 (2).. Academic Press 1965.

APPENDIX III

We develop an expression for $W(h_o, H_b)$, the hysteresis losses per cycle per unit volume when a static magnetic field H_b collinear with an oscillating magnetic field of amplitude h_o are applied along the surfaces of an infinite slab of thickness 2X. We write

III-1 $$H_o(t) = H_b + h_o f(t)$$

where f(t) varies between +1 and -1. We take the sequence of B profiles to be prescribed by

III-2 $$B \frac{dB}{dx} = B_y \frac{dB_y}{dx} + B_z \frac{dB_z}{dx} = \pm\alpha$$

where α is a temperature dependent parameter characterizing the sample.

In chapter 4 we focus on a situation where a uniform stationary magnetic induction, B_{static}, is present and directed orthogonal to h_o, hence H_b. In chapter 5, we examine the simpler limiting situation where only h_o and a collinear H_b are applied and the orthogonal $B_{static} = 0$. In both instances, without loss of generality, we take h_o and H_b to be directed either along the y or the z axis. When $B_{static} \neq 0$, it is useful to focus only on the component of the B profile which is changing rather than on the total magnetic induction $B = (B_{static}^2 + B_y^2)^{1/2}$ or $B = (B_{static}^2 + B_z^2)^{1/2}$. In the formulae given below, we ignore the subscripts y and z but it is implied that we are considering either B_y or B_z with $dB_y/dx = 0$ or $dB_z/dx = 0$.

The surfaces of the infinite slab are located at x = 0 and x = 2X. We focus on the half width between x = 0 and x = X.

We ignore the possible existence of surface steps and use the boundary condition

III-3 $$B_s = B(0) = \mu_o H_o$$

Let the magnetic induction at the surface swing from B_{max} to B_{min}. To fix ideas we consider that B_{max} is positive and B_{min} is negative. Let

III-4 $$B_{max} = \mu_o (H_b + h_o)$$

III-5 $$B_{min} = \mu_o (H_b - h_o)$$

III-6 $$B_b = \mu_o H_b$$

III-7 $$B_* = (2 \alpha X)^{1/2}$$

Energy flows out of the slab during the swing of B_s from B_{max} to 0 and from B_{min} to 0. We refer to this as the descending portions of the cycle. Energy flows into the slab during the swing of B_s from 0 to B_{max} and from 0 to B_{min}. We refer to this as the ascending portions of the cycle. The spatial average of the magnetic induction during the descending portions of the cycle can be written

III-8 $$\langle B \rangle = \int_0^{x_i(B_s)} \left(B_s^2 + B_*^2 \frac{x}{X}\right)^{1/2} d\left(\frac{x}{X}\right) + \int_{x_i(B_s)} \left(B_{max}^2 - B_*^2 \frac{x}{X}\right)^{1/2} d\left(\frac{x}{X}\right)$$

and a similar expression where x_i' replaces x_i, B_{min} replaces B_{max} and the sign in front of the two integrals is changed to negative.

We confine our derivation to amplitudes where $0 < x_i < X$, $(0 < x_i' < X)$, a situation denoted as lying below saturation. Since we are ultimately interested in $d\langle B\rangle/dB_s$, the upper limit to the second integral in equation 8 and the area under the B profile in the region $x_i < x \leq X$ $(x_i' < x \leq X)$ are immaterial here.

Integrating equation 8 and its analog with B_{min} and taking the derivatives with respect to B_s, noting that

III-9 $$x_i = \frac{B_{max}^2 - B_s^2}{2B_*^2}, \qquad x_i' = \frac{B_{min}^2 - B_s^2}{2B_*^2}$$

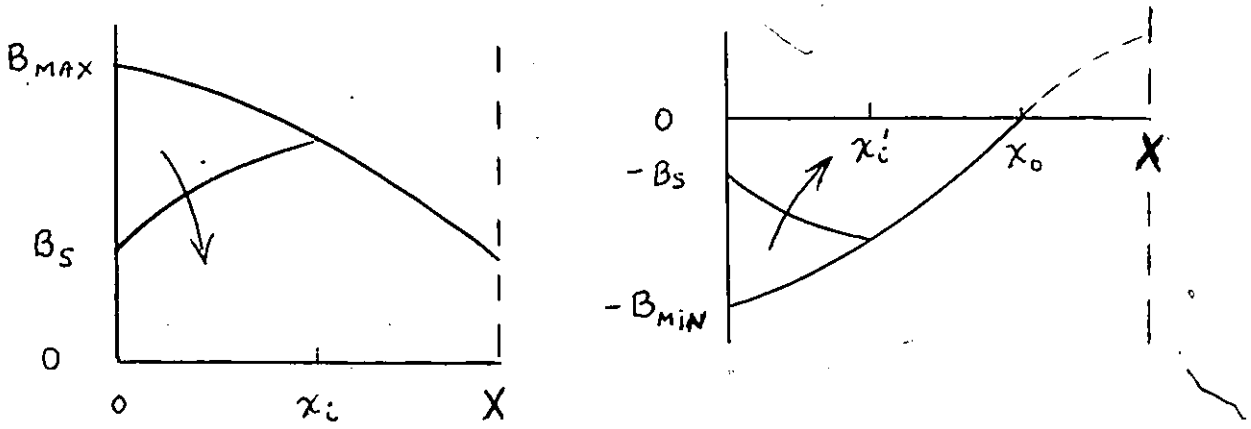

we obtain

III-10(a) $$\frac{d\langle B\rangle}{dB_s} = \frac{\sqrt{2}}{B_*^2}\left(B_s\left(B_s^2 + B_{max}^2\right)^{1/2} - \sqrt{2}\,B_s^2\right)$$

III-10(b) $$\frac{d\langle B\rangle}{dB_s} = -\frac{\sqrt{2}}{B_*^2}\left(|B_s|\left(B_s^2 + B_{min}^2\right)^{1/2} - \sqrt{2}\,B_s^2\right)$$

Turning our attention to the ascending portions of the cycle we refer the reader to the sketches below.

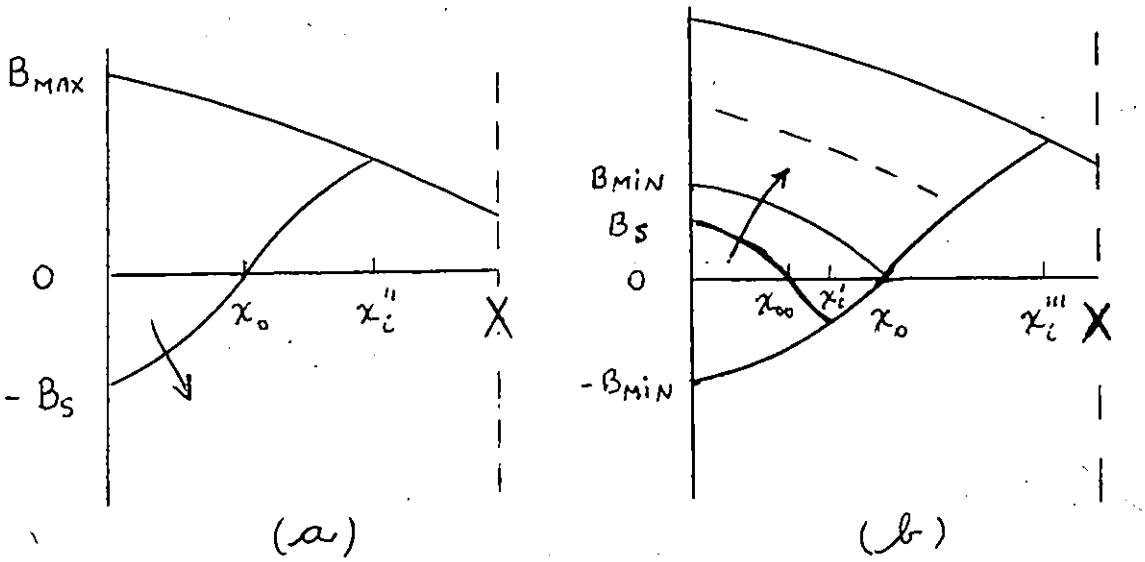

Focussing first on the situation where B_s is changing from 0 to $-B_{min}$ (sketch (a) above) we write

III-11
$$\langle B \rangle = -\int_0^{x_o(B_s)} \left(B_s^2 - B_*^2 \frac{x}{X}\right)^{\frac{1}{2}} d\left(\frac{x}{X}\right) + \int_{x_o(B_s)}^{x_i''(B_s)} \left(B_*^2 \frac{x}{X} - B_s^2\right)^{\frac{1}{2}} d\left(\frac{x}{X}\right) + \int_{x_i''(B_s)} \left(B_{max}^2 - B_*^2 \frac{x}{X}\right) d\left(\frac{x}{X}\right)$$

where the upper limit on the third integral and the area under the B profile in the region $x_i'' < x \leq X$ are of no concern here and,

III-12
$$x_o = \frac{B_s^2}{B_*^2}, \qquad x_i'' = \frac{B_{max}^2 + B_s^2}{2B_*^2}$$

Integrating equation 11 and taking the derivative with respect to B_s leads

$$\text{III-13(a)} \qquad \frac{d\langle B\rangle}{dB_s} = -\frac{\sqrt{2}}{B_*^2}\left(|B_s|\ (B_{max}^2 - B_s^2)^{\frac{1}{2}} + \sqrt{2}\ B_s^2\right)$$

The swing from 0 to B_{max} consists of two stages (see sketch (b) above). Firstly the increase from 0 to B_{min} where equation 11 applies with the sign in front of the integrals changed and B_{min} replacing B_{max}. This leads to

$$\text{III-13(b)} \qquad \frac{d\langle B\rangle}{dB_s} = \frac{\sqrt{2}}{B_*^2}\left(B_s\ (B_{min}^2 - B_s^2)^{\frac{1}{2}} + \sqrt{2}\ B_s^2\right)$$

In the second stage where B_s is increasing from B_{min} to B_{max},

$$\text{III-14} \qquad \langle B\rangle = \int_0^{x_i''(B_s)} (B_s^2 - B_*^2\,\frac{x}{X})^{\frac{1}{2}}\, d(\frac{x}{X})$$

$$+ \int_{x_i'''(B_s)} (B_*^2\,\frac{x}{X} - B_{min}^2)^{\frac{1}{2}}\, d(\frac{x}{X})$$

where the upper limit on the second integral and the area under the B profile in the region $x_i''' < x \leq X$ is not pertinent and

$$\text{III-15} \qquad x_i''' = \frac{B_{max}^2 + B_{min}^2}{2B_*^2}$$

Integrating equation 14 and taking the derivative with respect to B_s leads to

III-16 $$\frac{d\langle B\rangle}{dB_s} = \frac{\sqrt{2}}{B_*^2}\left(\sqrt{2}\,B_s^2 - B_s\,(B_s^2 - B_{min}^2)^{\frac{1}{2}}\right)$$

Introducing equations 10, 13 and 16 for the appropriate range of variation of B_s into the standard expression

III-17 $$W(h_o, H_b) = \frac{1}{\mu_o}\oint B_s \frac{d\langle B\rangle}{dB_s}\, dB_s$$

and integrating leads to,

III-18 $$W(h_o, H_b) =$$

$$\frac{\mu_o}{H_*^2}\left[\frac{\sqrt{2}}{8}(H_b + h_o)^4\left\{\log(1+\sqrt{2}) - \sqrt{2} - \sin^{-1}\left(\frac{H_b - h_o}{H_b + h_o}\right)\right\}\right.$$

$$+ \frac{(H_b - h_o)^4}{2} + 2\sqrt{2}\,(H_b - h_o)\,(H_b\ \ h_o)^{3/2}$$

$$\left. - \frac{\sqrt{2}}{4}(H_b^3 + H_b^2 h_o - H_b h_o^2 - h_o^3)\,(H_b h_o)^{\frac{1}{2}}\right]$$

$$+ \frac{\mu_o}{H_*^2}\left[\frac{\sqrt{2}}{8}(H_b - h_o)^4\left\{\log(1+\sqrt{2}) - \sqrt{2} + \frac{\pi}{2}\right\}\right.$$

$$+ \frac{(H_b + h_o)^4}{2} - 2\sqrt{2}\,(H_b + h_o)\,(H_b h_o)^{3/2}$$

$$- \frac{\sqrt{2}}{4}(H_b^3 - H_b^2 h_o - H_b h_o^2 + h_o^3)\,(H_b h_o)^{\frac{1}{2}}$$

$$\left. - \frac{\sqrt{2}}{8}(H_b - h_o)^4 \log\frac{|H_b - h_o|}{H_b + h_o + 2(H_b h_o)^{\frac{1}{2}}}\right]$$

where we have introduced equations 4 and 5. In equation 18, the set of terms contained in the first and second pair of rectangular brackets pertain to the net energy flow

(i) as B_s swings from B_{max} to $-B_{min}$ (the downsweep portion of the cycle) and

(ii) as B_s swings from $-B_{min}$ to B_{max} (the upsweep portion of the cycle).

We verify that equation 18 reduces to the well known full-wave limit when $H_b = 0$, hence $|B_{max}| = |B_{min}|$.

III-19 $$W(h_o, 0) = \frac{\mu_o h_o^4}{H_*^2} \left(\frac{\sqrt{2}}{4} \log(1 + \sqrt{2}) + \frac{1}{2} + \frac{\sqrt{2}}{8} \pi\right)$$

$$= 1.367 \frac{\mu_o h_o^4}{H_*^2}$$

Indeed we find that the two groups of terms of equation 18 become equal, as they should, in this limit.

For the special case, $H_b = h_o$, which we refer to as the half-wave case, equation 18 reduces to

III-20 $$W(h_o, h_o) = \frac{\mu_o h_o^4}{H_*^2} \left(2\sqrt{2} \log(1 + \sqrt{2}) - 4(\sqrt{2} - 1)\right) = 0.836 \frac{\mu_o h_o^4}{H_*^2}$$

Equation 19 (full-wave oscillations) has been obtained by several workers focusing on that particular case. Equation 18 and also equation 20, the expression for the half-wave oscillations are new results. The latter can of course be obtained much less tediously by focusing on that particular situation.

Ohmer and Heinrich have developed analytic expressions for <M>, hence <B>, versus H_o for cylindrical geometry exploiting the Kim-Anderson approximation (equation 2) for the B profiles and ignoring the surface step. They obtain $W(h_o, H_b)$ from graphical or numerical integration of the hysteresis loops calculated using their formulae for <M> vs. H_o. Since the focus on large amplitudes, where the valley in W versus H_b has consequently vanished, they report a monotonic decrease of W vs. H_b. They examine, in particular, the ratio of W for half-wave ($H_b = h_o$) and full-wave oscillations ($H_b = 0$) and find that

$$\frac{W(h_o, h_o)}{W(0, h_o)} = 0.345$$

when $h_o = 5\ H_*$.

APPENDIX IV

In this appendix we present analytic expressions for hysteresis losses for eight of the sixteen cases listed in table 6.1 of chapter 6. These expressions can be intrinsically useful. Further they provide a means of checking the computer program we have developed for computing hysteresis losses for arbitrary bulk pinning functions and B dependences of the surface barrier against entry and exit.

We consider;

a) i) infinite slab and ii) infinite cylinder geometry,

b) i) amplitudes h_o lying below and ii) extending above full penetration (saturation),

c) i) half-wave and ii) full-wave oscillations, and

d) i) symmetric and ii) asymmetric types of surface steps (surface barriers).

We exploit the Bean-London approximation

IV-1 a) $$\frac{dB}{dx} = \pm\alpha \qquad \text{b)} \quad \frac{dB}{dr} = \pm\alpha$$

to describe the B profiles. The magnetic induction B_* for full penetration (saturation) can be written

$$B_* = \alpha X$$

We refer the reader to Fig. IV-1 which schematically displays the various basic sequences of B profiles which are encountered during the cycle. With the Bean-London approximation, the B profiles are linear.

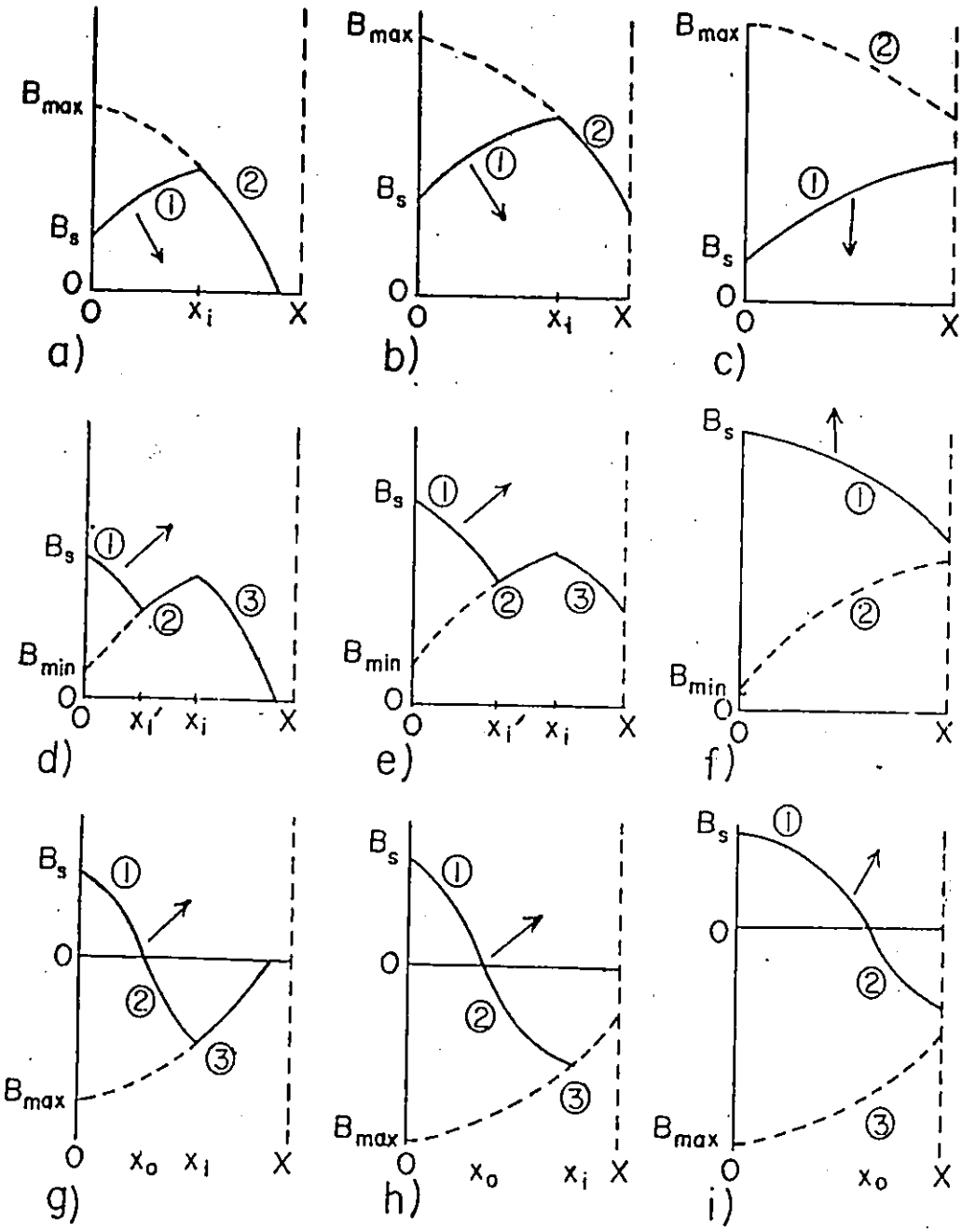

FIG. IV-1 Schematic of different categories of B profiles encountered during half-wave and full-wave cycles of amplitudes lying above and below saturation.

These profiles are drawn curved in Fig. IV-1, in order to present the more general and realistic configuration.

In presenting our results it is useful to identify all the pertinent features in each instance. Consequently it is convenient to introduce the following abbreviations;

Slab for infinite slab geometry.

Cyl for infinite cylindrical geometry.

H.W. for half-wave oscillations (between 0 and $2h_o$).

F.W. for full-wave oscillations (between $\pm h_o$ and $\mp h_o$).

Sym for symmetric type of surface step or surface barrier ($\Delta H'$ against flux entry $\Delta H'$ against flux exit).

Asym for asymmetric type of surface step or surface barrier ($\Delta H'' = 2\Delta H'$ against flux entry, $\Delta H = 0$ against flux exit).

Bean for Bean-London approximation for the B profiles.

Kim for the Kim-Anderson approximation for the B profiles.

Saturation instead of full penetration.

W denotes the hysteresis losses per cycle per unit volume in S.I. units.

h_o is the amplitude.

$H_* = B_*/\mu_o = \alpha X/\mu_o$ is the magnetic field for full penetration.

Infinite Slab Geometry

The B profiles are constructed from two solutions of equation IV-1. $x = 0$ and $x = X$ locate a surface and the midplane of the slab. For the descending portions of cycles,

IV-2 $$B(x) = B_{max} - B_*(\frac{x}{X}) \quad \text{where} \quad x_i \leq x \leq X$$

IV-3 $$B(x) = B_s + B_*(\frac{x}{X}) \quad \text{where} \quad 0 \leq x \leq x_i$$

IV-4 with $$\frac{x_i}{X} = \frac{B_{max} - B_s}{2B_*}$$

Finding the average area under the B profile and its derivative with respect to B_s leads to

IV-5 $$\frac{d<B>}{dB_s} = \frac{B_{max} - B_s}{2B_*} \quad \text{where } x_i < X$$

IV-6 $$\frac{d<B>}{dB_s} = 1 \quad \text{when } x_i > X$$

For the ascending portion of cycles, the profiles are constructed using,

IV-7 $$B(x) = B_{min} + B_*(\frac{x}{X}) \quad \text{where } x_i' \leq x \leq x_i$$

IV-8 $$B(x) = B_s - B_*(\frac{x}{X}) \quad \text{where } 0 \leq x \leq x_i', \text{ with}$$

IV-9 $$\frac{x_i'}{X} = \frac{B_s - B_{min}}{2B_*}$$

and equation 2 where $x_i \leq x \leq X$ with $x_i/X = \frac{(B_{max} - B_{min})}{2B_*}$

IV-10 $$\frac{d<B>}{dB_s} = \frac{B_s - B_{min}}{2B_*} \quad \text{when } x_i' < X$$

IV-11 $$\frac{d<B>}{dB_s} = 1 \quad \text{when } x_i' < X$$

Case 1a): Slab, H.W., Sym, Bean

i) Below saturation; $h_o \leq H_* + \Delta H'$

IV-12 $$W = \frac{2}{3} \frac{\mu_o h_o^3}{H_*} \cdot \{ 1 - 3 (\frac{\Delta H'}{h_o})^2 + 2 (\frac{\Delta H'}{h_o})^3 \}$$

ii) Above saturation; $h_o \geq H_* + \Delta H'$

IV-13 $$W = 2\mu_o h_o^2 \{ \frac{H_*}{h_o} - \frac{2}{3} (\frac{H_*}{h_o})^2 + 2 \frac{\Delta H'}{h_o} (1 - \frac{H_*}{h_o} - \frac{\Delta H'}{h_o}) \}$$

Case 1b): Slab, H.W., Asym, Bean

i) Below saturation, $h_o \leq H_* + \frac{\Delta H''}{2}$

IV-14 $$W = \frac{2}{3} \frac{\mu_o h_o^3}{H_*} \{ 1 - \frac{3}{4} (\frac{\Delta H''}{h_o})^2 + \frac{1}{4} (\frac{\Delta H''}{h_o})^3 \}$$

ii) Above saturation, $h_o \geq H_* + \frac{\Delta H''}{2}$

IV-15 $$W = 2\mu_o h_o^2 \{ \frac{H_*}{h_o} - \frac{2}{3} (\frac{H_*}{h_o})^2 + \frac{\Delta H''}{h_o} (1 - \frac{H_*}{h_o} - \frac{\Delta H''}{2h_o}) \}$$

We note that equations 14 and 15 are identical to equations 12 and 13 respectively with $\Delta H'' = 2\Delta H'$

Case 1c): Slab, F.W., Sym, Bean

i) Below saturation, $h_o \leq H_* + \Delta H'$

Same as equation 12

ii) Above saturation, $h_o \geq H_* + \Delta H'$

Same as equation 13

Case 2: Slab, F.W., Asym, Bean

i) Below saturation, $h_o \leq H_* + \Delta H''$

IV-16 $$W = \frac{2}{3} \frac{\mu_o h_o^3}{H_*} \left\{ 1 - \frac{3}{4} \frac{\Delta H''}{h_o} \left(1 + 2 \frac{\Delta H''}{h_o} - \frac{5}{3} \left(\frac{\Delta H''}{h_o}\right)^2\right) \right\}$$

ii) Above saturation, $h_o \geq H_* + \Delta H''$

Two ranges of the amplitudes above saturation must be considered separately. The reason for this state of affairs is presented schematically below and in Fig. IV-2.

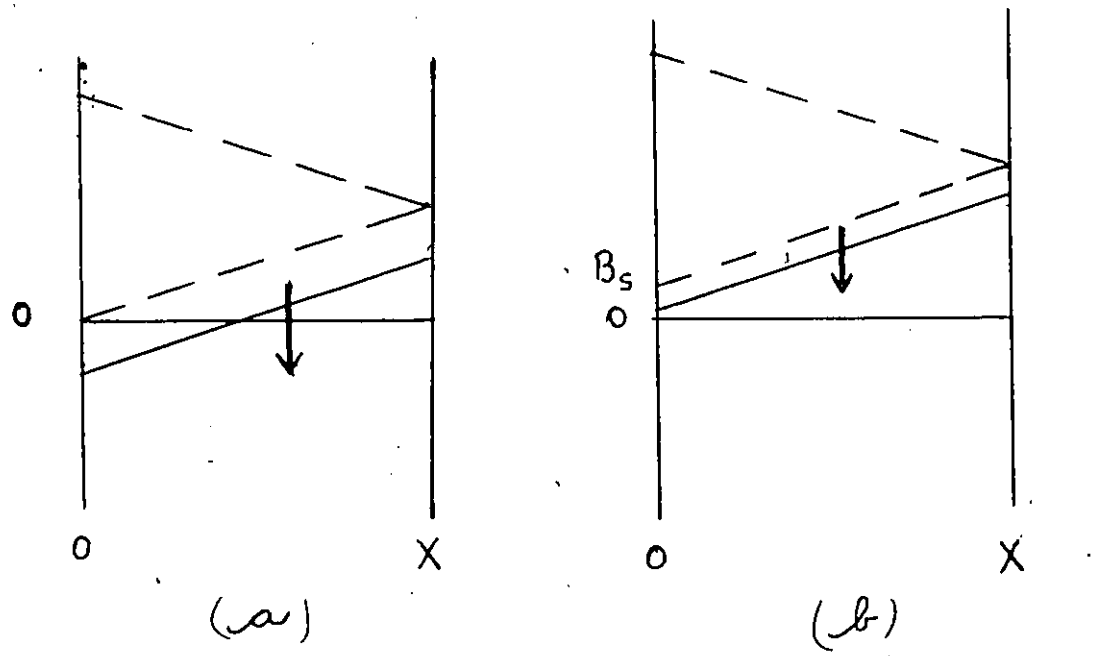

The configuration depicted by the solid line in sketch (b) which is encountered during the descending quarter cycles in the range of the larger amplitudes must be taken into account in deriving the appropriate expression for W.

a) $H_* + \Delta H'' \leq h_o \leq 2H_* + \Delta H''$

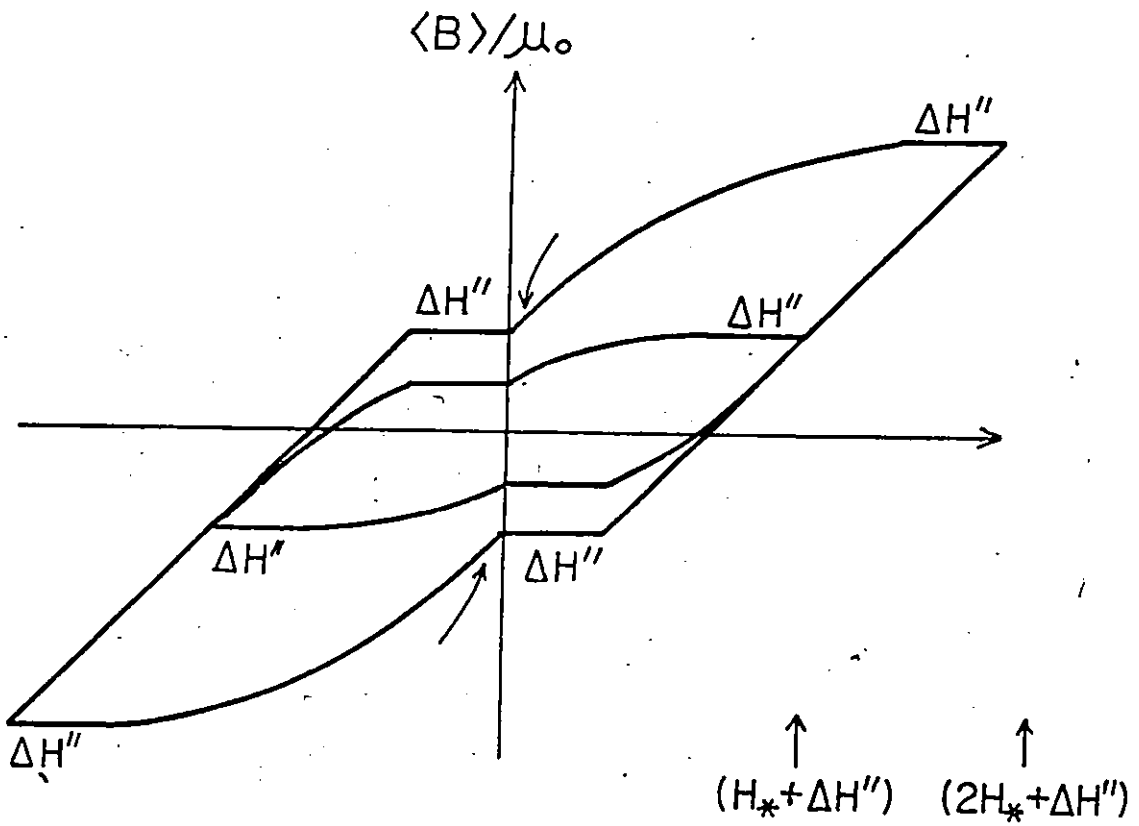

FIG. IV-2 Illustrates that as the amplitude grows beyond $H_* + \Delta H''$, a linear sloping portion of $\langle B \rangle$ vs. H_o first appears at the extremes of the hysteresis loop. When $h_o > 2 H_* + H''$, this linear portion extends to the regions indicated by the arrows. As a consequence, different formulae are required to describe W in these two saturation regimes.

IV-17 $$W = \frac{2}{3}\frac{\mu_o h_o^3}{H_*}\left\{3\left(\frac{H_*}{h_o}\right)^2 - 2\left(\frac{H_*}{h_o}\right)^3 - \frac{3}{4}\frac{\Delta H''}{h_o}\left(1 - 2\left(\frac{\Delta H''}{h_o}\right) + \left(\frac{\Delta H''}{h_o}\right)^2\right)\right.$$

$$\left. + 6\frac{\Delta H''}{h_o}\frac{H_*}{h_o}\left(1 - \frac{H_*}{h_o} - \frac{\Delta H''}{h_o}\right)\right\}$$

b) $h_o \geq 2H_* + \Delta H''$

IV-18 $$W = 2\mu_o h_o^2\left\{\frac{H_*}{h_o} - \frac{2}{3}\left(\frac{H_*}{h_o}\right)^2 + \frac{\Delta H''}{h_o}\left(1 - \frac{\Delta H''}{h_o} - \frac{H_*}{h_o}\right)\right\}$$

Infinite Cylinder Geometry

The magnetic induction is directed along the cylinder axis $r = 0$ and $r = R$ locate the centreline and the surface of the cylinder. The B profiles are constructed from two solutions to equation 1(b). For the descending parts of cycles,

IV-19 $$B(r) = B_{max} - B_*\left(1 - \frac{r}{R}\right) \quad \text{where} \quad 0 \leq r \leq r_i$$

IV-20 $$B(r) = B_s + B_*\left(1 - \frac{r}{R}\right) \quad \text{where} \quad r_i \leq r \leq R$$

IV-21 $$\frac{r_i}{R} = 1 - \frac{1}{2}\left(\frac{B_{max} - B_s}{B_*}\right)$$

The spatial average of the magnetic induction is determined introducing these into the definition

IV-22 $$\langle B \rangle = 2\int_0^R B(r)\frac{r}{R}\,d\left(\frac{r}{R}\right)$$

Taking the derivative with respect to B_s leads to

IV-23 $$\frac{d<B>}{dB_s} = \frac{B_{max} - B_s}{B_*} \left\{ 1 - \frac{1}{4} \left(\frac{B_{max} - B_s}{B_*}\right)\right\} \text{ when } r_i > 0 \text{ and}$$

IV-24 $$\frac{d<B>}{dB_s} = 1 \quad \text{when} \quad r_i = 0$$

For the ascending parts of cycles, the profiles are constructed using

IV-25 $$B(r) = B_{min} + B_* \left(1 - \frac{r}{R}\right) \quad \text{where} \quad r_i \le r \le r_i' \quad \text{and}$$

IV-26 $$B(r) = B_s - B_* \left(1 - \frac{r}{R}\right) \quad \text{where} \quad r_i' \le r \le R \quad \text{with}$$

IV-27 $$\frac{r_i'}{R} = 1 - \frac{1}{2} \left(\frac{B_s - B_{min}}{B_*}\right) \quad \text{and}$$

equation 19 when $0 \le r \le r_i$ with $r_i/R = 1 - \frac{1}{2}(B_{max} - B_{min})/B_*$.

Calculating <B> and taking its derivative with respect to B_s leads to

IV-28 $$\frac{d<B>}{dB_s} = \frac{B_s - B_{min}}{B_*} \left\{ 1 - \frac{1}{4} \left(\frac{B_s - B_{min}}{B_*}\right)\right\} \text{ when } r_i > 0 \text{ and}$$

IV-29 $$\frac{d<B>}{dB_s} = 1 \quad \text{when} \quad r_i = 0$$

Case 3a): Cyl, H.W., Sym, Bean

i) Below saturation, $h_o \le H_* + \Delta H'$

IV-30 $$W = \frac{4}{3}\frac{\mu_o h_o^4}{H_*^2}\left\{\frac{H_*}{h_o}\left(1 - 3\left(\frac{\Delta H'}{h_o}\right)^2 + 2\left(\frac{\Delta H'}{h_o}\right)^3\right) - \frac{1}{2}\right.$$

$$\left. + \frac{\Delta H'}{h_o}\left(1 - \left(\frac{\Delta H'}{h_o}\right)^2 + \frac{1}{2}\left(\frac{\Delta H'}{h_o}\right)^3\right)\right\}$$

ii) Above saturation; $h_o \geq H_* + \Delta H'$

IV-31 $$W = \frac{4}{3}\mu_o h_o^2\left\{\frac{H_*}{h_o} - \frac{1}{2}\left(\frac{H_*}{h_o}\right)^2 + 3\frac{\Delta H'}{h_o}\left(1 - \frac{2}{3}\frac{H_*}{h_o} - \left(\frac{\Delta H'}{h_o}\right)\right)\right\}$$

Case 3b): Cyl, H.W., Asym, Bean

i) Below saturation; $h_o \leq H_* + \frac{\Delta H''}{2}$

IV-32 $$W = \frac{4}{3}\mu_o \frac{h_o^4}{H_*^2}\left\{\frac{H_*}{h_o}\left(1 - \frac{3}{4}\left(\frac{\Delta H''}{h_o}\right)^2 + \frac{1}{4}\left(\frac{\Delta H''}{h_o}\right)^3\right) - \frac{1}{2}\right.$$

$$\left. + \frac{1}{2}\frac{\Delta H''}{h_o}\left(1 - \frac{1}{4}\left(\frac{\Delta H''}{h_o}\right)^2 + \frac{1}{16}\left(\frac{\Delta H''}{h_o}\right)^3\right)\right\}$$

ii) Above saturation; $h_o \geq H_* + \frac{H''}{2}$

IV-33 $$W = \frac{4}{3}\mu_o h_o^2\left\{\frac{H_*}{h_o} - \frac{1}{2}\left(\frac{H_*}{h_o}\right)^2 + \frac{3}{2}\frac{\Delta H''}{h_o}\left(1 - \frac{2}{3}\frac{H_*}{h_o} - \frac{1}{2}\left(\frac{\Delta H''}{h_o}\right)\right)\right\}$$

We note that equations 32 and 33 are identical to equations 30 and 31 respectively with $\Delta H'' = 2\Delta H'$.

Case 3c): Cyl, F.W., Sym, Bean

i) Below saturation; $h_o \leq H_* + \Delta H'$

Same as equation 30

ii) Above saturation; $h_o \geq H_* + \Delta H'$

Same as equation 31

Case 4: Cyl, F.W., Asym, Bean

i) Below saturation; $h_o \leq H_* + \Delta H''$

$$\text{IV-34} \quad W = \frac{4\mu_o h_o^4}{3H_*^2} \left\{ \frac{H_*}{h_o} - \frac{1}{2} + \frac{9}{8}\frac{\Delta H''}{h_o}\left(1 - \frac{1}{3}\frac{\Delta H''}{h_o} + \frac{5}{9}\left(\frac{\Delta H''}{h_o}\right)^2 + \frac{1}{3}\left(\frac{\Delta H''}{h_o}\right)^3\right) \right.$$

$$\left. - \frac{3}{4}\frac{H_*}{h_o}\frac{\Delta H''}{h_o}\left(1 + 2\frac{\Delta H''}{h_o} - \frac{5}{3}\left(\frac{\Delta H''}{h_o}\right)^2\right) \right\}$$

ii) Above saturation; $h_o \geq H_* + \Delta H''$

As in case 2, two ranges of amplitudes above saturation must be considered separately and lead to different expressions.

a) $H_* + H'' \leq h_o \leq 2H_* + \Delta H'$

$$\text{IV-35} \quad W = \frac{4}{3}\frac{\mu_o h_o^4}{H_*^2} \left\{ 3\left(\frac{H_*}{h_o}\right)^2 \frac{\Delta H''}{h_o}\left(1 - \frac{\Delta H''}{h_o} - \frac{2}{3}\frac{H_*}{h_o}\right) \right.$$

$$+ \left(\frac{H_*}{h_o}\right)^3 \left(1 - \frac{1}{2}\frac{H_*}{h_o}\right)$$

$$\left. + \frac{1}{8}\frac{\Delta H''}{h_o}\left(1 - \frac{\Delta H''}{h_o}\right)^3 - \frac{3}{4}\frac{H_*}{h_o}\left(\frac{\Delta H''}{h_o}\right)\left(1 - \frac{\Delta H''}{h_o}\right)^2 \right\}$$

b) $h_o \geq 2H_* + \Delta H''$

$$\text{IV-36} \quad W = \frac{2\mu_o h_o^2}{3} \left\{ 2\frac{H_*}{h_o} - \left(\frac{H_*}{h_o}\right)^2 + 3\frac{\Delta H''}{h_o}\left(1 - \frac{2}{3}\frac{H_*}{h_o} - \frac{\Delta H''}{h_o}\right) \right\}$$

Case 1(b), below saturation (equation 14) has been developed, by a different approach, by Sekula and Barrett. Fournet and Mailfert and Dunn and Hlawiczka have independently developed general formulae for hysteresis losses under full-wave oscillations below situation in planar geometry. Fournet and Mailfert derive equation 12 and an explicit expression for case 7 as illustrative examples. Dunn and Hlawiczka focus on pinning functions of the form $F_p = \alpha B^n$ and introduce a field independent surface step, comprising a reversible (Meissner) shielding contribution and a barrier, thereby providing surface steps of different degrees of asymmetry. Equations 12 and 16 are generated by the general formula of Dunn and Hlawiczka when the Bean-London approximation is introduced and the parameters are chosen to yield symmetry and asymmetric surface steps. Their general formulae also yield explicit expressions for cases 5 and 7, below saturation. Equations 13, 15, 17, 18 and 30 through 36 of this appendix constitute new results.

Bibliography

A. Hysteretic losses

(i) Theoretical

1. ASHKIN M., J. Appl. Phys., 50, 7060 (1979).
2. BEAN C.P., Rev. Mod. Phys., 36, 31 (1964).
3. CLEM J.R., J. Appl. Phys., 50, 3518 (1979).
4. CLEM J.R., Autumn School on Metal Physics, November 26 - December 1, 1979, Piecowise, Poland.
5. DUNN W.I., HLAWICZKA P., Brit. J. Appl. Phys. (J. Phys. D), 1, 1469 (1968).
6. FOURNET G., MAILFERT A., Journal de Physique, 31, 35 (1970).
7. GREEN M., HLAWICZKA P., Proc. IEE, 114, 1329 (1967).
8. HANCOX R., Proc. IEE, 113, 1221 (1966).
9. IRIE F., YAMAFUJI K., Phys. Lett., 24A, 30 (1967).
10. IRIE F., YAMAFUJI K., J. Phys. Soc. Japan, 23, 255 (1967).
11. KAWASHIMA T., EZAKI T., YAMAFUJI K., Japanese Journal of Applied Physics, 17, 551 (1978).
12. KAWASHIMA T., SUEYOSHI T., YAMAFUJI K., Japanese Journal of Applied Physics, 17, 699 (1978).
13. LONDON H., Phys. Lett., 6, 162 (1963).
14. MELVILLE P.H., Advances in Physics, 21, 647 (1972).
15. NORRIS W.T., J. Phys. D: Appl. Phys., 4, 1358 (1971).
16. SEKULA S.T., BARRETT J.H., Appl. Phys. Lett., 17, 304 (1970).
17. URBAN E.W., Phys. Rev. B, 5, 3530 (1972).

18. WISCHMEYER C.R., Phys. Rev., 154, 323 (1967).

(ii) Experimental

19. ALAIS P., SIMON Y., Phys. Rev., 158, 426 (1967).

20. BEALL W.T. JR., MEYERHOFF R.W., J. Appl. Phys., 40, 2052 (1969).

21. BUCHHOLD T.A., Cryogenics, 3, 141 (1963).

22. BUSSIERE J.F., CLEM J.R., IEEE Trans. Magn. Mag-15, 264 (1979).

23. CISZEK M., KOZLOWSKI G., TEKIEL P., GIJSBERTSE E.A., VAN DE KLUNDERT L.J.M., Phys. Lett., 77A, 271 (1980).

24. CISZEK M., et al., IEEE Trans. Magn. Mag-17, 975 (1981).

25. CLEM J.R., KERCHNER H.R., SEKULA S.T., Phys. Rev. B, 14, 1893 (1976).

26. DEIS D.W., CAVALER J.R., JONES C.K., J. Appl. Phys., 42, 5710 (1971).

27. EASSON R.M., HLAWICZKA P., Brit. J. Appl. Phys., 18, 1237 (1967).

28. EASSON R.M., HLAWICZKA P., Brit. J. Appl. Phys. (J. Phys. D), 1, 1477 (1968).

29. EZAKI T., IRIE F., KLIPPING G., LUDERS K., MATSUSHITA T., RUPPERT U., TAKEO M., Cryogenics, 19, 97 (1979).

30. FURTADO C.S., Cryogenics, 12, 129 (1972).

31. GRASMEHR T.W., FINZI L.A., IEEE Trans. Magn. Mag-2, 334 (1966).

32. KAMPER R.A., Phys. Lett., 2, 290 (1962).

33. KERCHNER H.R., J. Low Temp. Phys., 34, 33 (1978).

34. KOVACHEV V.T., J. Appl. Phys., 51, 3812 (1980).

35. MCCONNELL R.D., CRITCHLOW P.R., J. Appl. Phys., 46, 426 (1975).

36. OGASAWARA T., TAKAHASHI Y., KANBARA K., KUBOTA Y., YASOHAMA K., YASUKOCHI K., Cryogenics, 19, 736 (1979).

37. OHMER M.C., HEINRICH J.P., J. Appl. Phys., 44, 1804 (1973).

38. RHODES R.G., ROGERS E.C., SEEBOLD R.J.A., Cryogenics, 4, 206 (1964).

39. ROCHER Y.A., SEPTFONDS J., Cryogenics, 7, 96 (1967).

40. THOMPSON J.D., MALEY M.P., CLEM J.R., J. Appl. Phys., 50, 3531 (1979).

41. ZAR J.L., J. Appl. Phys., 35, 1610 (1964).

(iii) Longitudinal Case

42. GAUTHIER R., LEBLANC M.A.R., IEEE Trans. Magn. Mag-13, 560 (1977).

43. LACHAINE A., LEBLANC M.A.R., LORRAIN J.P., Physica, 107B, 433 (1981).

44. NAKAYAMA N., Proc. 4th Int. Cryogenic Engr. Conf. 133 (1972).
NAKAYAMA N., KOIKE Y., TOYADA T., Proc. 5th Int. Cryogenic Engr. Conf. 129 (1974).

45. SUGAHARA M., KATO S., Appl. Phys. Lett., 19, 111 (1971).

46. TAYLOR H.F., Appl. Phys. Lett., 11, 169 (1967).

B. Flux cutting

47. BOYER R., Ph.D. Thesis University of Ottawa. Ottawa, Ont., Canada 1977.

48. BOYER R., LEBLANC M.A.R., Solid State Commun., 24, 261 (1977).

49. BOYER R., FILLION G., LEBLANC M.A.R., J. Appl. Phys., 51, 1692 (1980).

50. BRANDT E.H., CLEM J.R., WALMSLEY D.G., J. Low Temp.Phys., 37, 43 (1979).

51. BRANDT E.H., Phys. Lett., 79A, 207 (1980).

52. BRANDT E.H., J. Low Temp. Phys., 39, 41 (1980).

53. BRANDT E.H., J. Low Temp. Phys. 42, 557 (1981).

54. BRANDT E.H., J. Low Temp. Phys., 44, 33 (1981).

55. BRANDT E.H., J. Low Temp. Phys., 44, 59 (1981).

56. BRANDT E.H., Physica, 107B, 459 (1981).

57. CAVE J.R., EVETTS J.E., CAMPBELL A.M., J. de Physique, Colloque C6, 39, C6-614 (1978).

58. CLEM J.R., Phys. Rev. Lett., 38, 1425 (1977).

59. CLEM J.R., J. Low Temp. Phys., 38, 353 (1980).

60. CLEM J.R., Physica, 107B, 453 (1981).

61. CLEM J.R., YEH S., J. Low Temp. Phys., 39, 173 (1980).

62. FILLION G., GAUTHIER R., LEBLANC M.A.R., Phys. Rev. Lett., 43, 86 (1979).

63. NICHOLSON J.E., SIKORA P.T., J. Low Temp. Phys., 17, 275 (1974).

64. TIMMS W.E., WALMSLEY D.G., J. Phys. F6, 2107 (1976), Phys. Stat. Sol. (B), 71, 741 (1975).

65. WALMSLEY D.G., TIMMS W.E., J. Phys. F3, L203 (1973), J. Phys. F5, 287 (1975), J. Phys. F6, 2107 (1976), J. Phys. F7, 2373 (1977).

C. Conduction current in $H_{//}$.

66. CULLEN G.W., CODY G.D., J. Appl. Phys., 44, 2838 (1973).

67. GAUTHIER R., LEBLANC M.A.R., BELANGER B.C., Low Temp. Phys. LT13. Edited by K.D. Timmerhaus, W.J. O'Sullivan, E.F. Hammel. Plenum, New York, N.Y. Vol. III, 241 (1974).

68. GAUTHIER R., Ph.D. Thesis. University of Ottawa, Ottawa, Ont., Canada 1976.

69. GRASSMAN P.G., RINDERER L., Helv. Phys. Acta, 27, 309 (1954).

70. HEATON J.W., ROSE-INNES A.C., Phys. Lett., 9, 112 (1964).

Cryogenics, 4, 85 (1964).

71. KARASIK V.R., VERESCHAGIN, Soviet Phys. JETP, 32, 20 (1971).

72. LEBLANC M.A.R., BELANGER B.C., FIELDING R.M. Phys. Rev. Lett., 14, 704 (1965).

73. LEBLANC M.A.R., Phys. Rev., 143, 220 (1966).

74. SEKULA S.T., BOOM R.W., BERGERON C.J. JR., Appl. Phys. Lett., 2, 102 (1963).

75. YAMAFUJI K., KAWASHIMA T., ICHIKAWA H., J. Phys. Soc. Japan, 39, 581 (1975).

D. Various contributions of Clem

(i) Hysteretic Losses

CLEM J.R., KERCHNER H.R., SEKULA S.T., Phys. Rev. B, 14, 1893 (1976).

CLEM J.R., J. Appl. Phys., 50, 3518 (1979).

CLEM J.R., Autumn School on Metal Physics, November 26 - December 1, 1979, Piecowice, Poland.

THOMPSON J.D., MALEY M.P., CLEM J.R., J. Appl. Phys., 50, 3531 (1979).

(ii) Flux Cutting

CLEM J.R., Phys. Rev. Lett., 38, 1425 (1977).

CLEM J.R., J. Low Temp. Phys., 38, 353 (1980).

CLEM J.R., Physica, 107B, 453 (1981).

CLEM J.R., YEH S., J. Low Temp. Phys., 39, 173 (1980).

E. Surface barriers

(i) Review

MELVILLE P.H., Advances in Physics, 21, 647 (1972).

(ii) Reduction of barrier vs. H

76. BUSSIERE J.F., Phys. Lett., A58, 343 (1976).

77. BUSSIERE J.F., SUENAGA M., J. Appl. Phys., 47, 707 (1976).

78. BUSSIERE J.F., KOVACHEV V.T., J. Appl. Phys., 49, 2526 (1978).

79. CHANG C.T.M., LEBLANC M.A.R., Appl. Phys. Lett., 10, 344 (1967).

80. LOVE G.R., J. Appl. Phys., 37, 3361 (1966).

81. SUENAGA M., KLAMUT C., BUSSIERE J.F., IEEE Trans. Magn. Mag-13, 436 (1977).

THOMPSON J.D., MALEY M.P., CLEM J.R., J. Appl. Phys., 50, 3531 (1979).

82. ULLMAIER H.A., GAUSTER W.F., J. Appl. Phys., 37, 4519 (1966).

83. ULLMAIER H.A., Phys. Stat. Solidi, 17, 631 (1966).

(iii) Reduction of barrier vs. angle

84. DAS GUPTA A., KRAMER E.J., Phil. Mag., 26, 779 (1972).

85. GASCON F., LOWELL J., MUÑOZ J.S., Phys. Lett., 24A, 257 (1967).

86. GOOD J.A., KRAMER E.J., Phil. Mag., 24, 339 (1971).

87. HART H.R. JR., SWARTZ P.S., Phys. Rev., 156, 403 (1967).

88. JOINER W.C.H., KUHL G.E., Phys. Rev., 168, 413 (1968).

89. JONES R.G., Solid State Commun., 5, 375 (1967).

90. LOWELL J., J. Phys. C (Solid State Phys.), 2, 372 (1969).

91. LOWELL J., Solid State Commun., 5, 323 (1969).

92. SCHARTZ P.S., HART H.R. JR., Phys. Rev., 137A, 818 (1965).

93. SCHARTZ P.S., HART H.R. JR., Phys. Rev., 156, 412 (1967).

(iv) Other evidence of barrier

94. CARDONA M., GITTLEMAN J., ROSENBLUM B., Phys. Lett., 17, 92 (1965).

95. DUNN W.I., HLAWICZKA P., J. Phys., D1, 1469 (1968).
EASSON R.M., HLAWICZKA P., Brit. J. Appl. Phys. (J. Phys. D), 1, 1477 (1968).

96. HECHT R., RCA Rev., 25, 453 (1964).

97. LEBLANC M.A.R., GRIFFITHS D.J., Phys. Lett., 21, 150 (1966).

98. LEBLANC M.A.R., GRIFFITHS D.J., MATTES H.G., Appl. Phys. Lett., 11, 143 (1967).

99. LEBLANC M.A.R., GRIFFITHS D.J., BELANGER B.C., Phys. Rev. Lett., 18, 844 (1967).

100. LEBLANC M.A.R., CHANG C.T.M., Solid State Commun., 6, 617 (1968).

101. LEBLANC M.A.R., MATTES H.G., J. de Physique (Paris) Colloq. 39, C6-654 (1978).

102. LEBLANC M.A.R., FILLION G., TIMMS W.E., ZARADNITSKY A., CAVE J.R., Cryogenics, 21, 491 (1981).

103. MOORE D.F., BEASTLEY M.R., Appl. Phys. Lett., 30, 494 (1977).

104. SCHWEITZER D.G., BERTMAN B., Phys. Rev., 153, 293 (1966).

105. SHAW R., ROSENBLUM B., BRIDGES F., IEEE Trans. Magn. Mag-13, 494 (1977).

106. SUTTON J., Proc. Phys. Soc., 87, 791 (1966).

(v) Exit barrier (theoretical)

107. BEAN C.P., LIVINGSTON J.D., Phys. Rev. Lett., 12, 14 (1964).

108. CLEM J.R., Low Temp. Phys. LT-13. Edited by K.D. Timmerhaus, W.J. O'Sullivan and E.F. Hammel. Plenum, N.Y., 3, 102 (1974).

109. DE GENNES P.G., Solid State Commun., 3, 127 (1965).

110. TERNOVSKII F.F., SHEKHATA L.N., Sov. Phys. JETP, 35, 1202 (1972).

111. ABRIKOSOV A.A., Sov. Phys. JETP, 5, 1174 (1957).

F. Empirical B vs. H expressions

112. EVETTS J.E., CAMPBELL A.M., DEW HUGHES D., J. Phys., C1, 715 (1968).
MELVILLE P.H., Advances in Physics, 21, 647 (1972).

113. SCHAFER R., HEIDEN C., IEEE Trans. Magn. Mag-13, 201 (1977).

G. jc vs. B extracted from data

114. COFFEY H.T., Phys. Rev., 166, 447 (1968).

115. FIETZ W.A., WEBB W.W., Phys. Rev., 178, 657 (1969).

116. KRAMER E.J., J. Appl. Phys., 44, 1360 (1973).

H. Empirical jc vs. B

117. BEAN C.P., Phys. Rev. Lett., 8, 250 (1962).
BEAN C.P., Rev. Mod. Phys., 36, 31 (1964).

118. FIETZ W.A., BEASLEY M.R., SILCOX J., WEBB W.W., Phys. Rev., 136, A 335 (1964).

IRIE F., YAMAFUJI K., J. Phys. Soc. Japan, 23, 255 (1967).

119. KIM Y., HEMPSTEAD C., STRNAD A., Phys. Rev. Lett., 9, 306 (1962).

Phys. Rev., 131, 2486 (1963).

120. KIM Y., HEMPSTEAD C., STRNAD A., Phys. Rev., A, 139, 1163 (1965).

Phys. Rev., 129, 528 (1963).

LONDON H., Phys. Lett., 6, 162 (1963).

121. URBAN E., J. Appl. Phys., 42, 115 (1971).

URBAN E., Phys. Rev. B, 5, 3530 (1972).

122. YAMAFUJI K., et al., J. Phys. Soc. Japan, 26, 315 (1969).

123. YASUKOCHI K., OGASAWARA T., USUI N., KOBAYASHI H., USHIO S., J. Phys. Soc. Japan, 19, 137 (1964).

J. Phys. Soc. Japan, 19, 1649 (1964).

J. Phys. Soc. Japan, 21, 89 (1966).

I. Effect of surface conditions on barrier

124. CAMPBELL A.M., EVETTS J.E., DEW HUGHES D., Phil. Mag., 18, 313 (1968).

125. CHANG C.C., ROSE-INNES A.C., Low Temp. Phys. LT12, (ed) E. Kanda. (Academic Press of Japan), 381 (1971).

126. DE BLOIS R.W., DE SORBO W., Phys. Rev. Lett., 12, 499 (1964).

127. FLIPPEN R.B., Phys. Lett., 24A, 588 (1967).

128. GOOD J.A., KRAMER E.J., Phil. Mag., 22, 329 (1970).

129. JONES R.G., ROSE-INNES A.C., Phys. Lett., 22, 271 (1966).

130. JOSEPH A.S., TOMASCH W.J., Phys. Lett., 12, 219 (1964).

131. LEBLANC M.A.R., Phys. Lett., 21, 266 (1966).

132. LOWELL J., Phys. Lett., 26A, 111 (1968).

133. MORRISON D.D., ROSE R.M., Phys. Rev. Lett., 25, 356 (1970).

J. Effect of metallic coating on barrier

134. BARNES L.J., FINK H.J., Phys. Lett., 20, 583 (1966).

135. BERTMAN B., SCHWEITZER D.G., LIPSHULTZ F.P., Phys. Lett., 21, 260 (1966).

136. EVETTS J.E., Phys. Rev. B2, 95 (1970).

137. HAUSER J.J., Phys. Lett., 22, 378 (1966).

K. Miscellaneous references

138. COFFEY H.T., Cryogenics, 7, 73 (1967).

139. DUBASOV B.G., MYMRIKOV V.V., SEREDA G.E., TROKHACHEV G.V., Cryogenics, 19, 114 (1979).

140. FORSYTH E.B., Cryogenics, 14, 316 (1974).

141. CAMPBELL A.M., EVETTS J.E., Adv. Phys., 21, 199 (1972).

142. TIMMS W.E., LEBLANC M.A.R., J. Phys. F, 4, 136 (1974).

143. LACHAINE A., LEBLANC M.A.R., Low Temp. Phys. LT13. Edited by K.D. Timmerhaus, W.J. O'Sullivan and E.F. Hammel. Plenum, N.Y., Vol. III, 247 (1974).

144. LACHAINE A., Ph.D. Thesis University of Ottawa, Ottawa, Ont., Canada (1976).

145. WALMSLEY D.G., J. Phys. F, 2, 510 (1972).

146. BEAN C.P., J. Appl. Phys., 41, 2482 (1970), J. de G. Gilchrist, J. Phys. D, 5, 2282 (1972).

147. LEBLANC M.A.R., CHANG C.T.M., Solid State Commun., 6, 679 (1968).

148. BELANGER B.C., Ph.D. Thesis, University of Southern California, Los Angeles, USA (1968).

149. MATTES H.G., Ph.D. Thesis, University of Southern California, Los Angeles, USA (1969).

150. LEBLANC M.A.R., MATTES H.G., Appl. Phys, Letters, 4, 267 (1966).

151. ANDERSON P.W., KIM Y.B., Rev. Mod. Phys., 36, 39 (1964).